Thermomechanical investigations of thin polymer films with scanning force microscopy

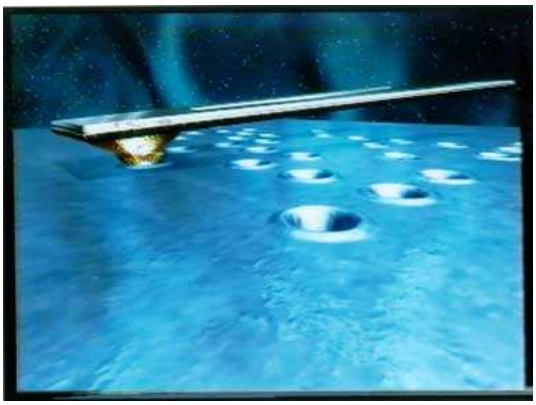

Dissertation zur Erlangung des Doktorgrades Dr. rer. nat. der Fakultät für Naturwissenschaften der Universität Ulm

vorgelegt von

Martin Hinz
aus Bonn

Abteilung Experimentelle Physik
2006

Amtierender Dekan:	Prof. Dr. Klaus–Dieter Spindler
1. Gutachter:	Prof. Dr. Othmar Marti
2. Gutachter:	
Tag der Promotion:	

Titelbild: Darstellung einer rasterkraftmikroskopischen Spitze beim Schreibvorgang im "Millipede". Mit freundlicher Genehmigung von IBM, Zurich Research Laboratory. Quelle: www.zurich.ibm.com

Contents

1 Introduction and motivation **1**
1.1 Introduction 1
1.1.1 "Millipede" project of IBM 3
1.2 Motivation and scope of the present work 7
1.3 Dissertation overview 10

2 Nanoscale mechanical properties of thin polymer films at elevated sample temperatures **11**
2.1 Introduction 11
2.2 Force distance curves with the SFM 12
2.2.1 Conversion of FDCs into FPCs 13
2.3 Experimental setup 16
2.3.1 The SFM and the heating stage 16
2.3.2 The SFM tips 17
2.4 Sample preparation 18
2.4.1 PMMA films on silicon 19
2.4.2 Epoxy photoresist SU8 films on silicon 20
2.5 Nanoindentation experiments 22
2.5.1 Experimental details 22
2.5.2 Results and discussion 23
2.5.3 Discussion of the nanoindentation experiments 30
2.6 Thermal stability of nanoindentations 32
2.7 Chapter summary 37

3 Heatable SFM cantilevers **39**
3.1 Introduction 39
3.2 Design and functionality of heatable cantilevers 40
3.3 Temperature calibration of the heater 43
3.4 Chapter summary 45

4 High frequency nanoindentation of thin polymer films with pulse-heated SFM tips at elevated sample temperatures **47**

4.1 Introduction . . . 47
4.2 Experimental setup . . . 48
4.2.1 Adaption of the heatable cantilevers to the D3000 SFM . . 49
4.3 Topography imaging under ambient conditions . . . 51
4.4 Nanoindentations on the micro-second scale . . . 51
4.4.1 Experimental implementation . . . 53
4.4.2 Cantilever performance during pulsed indentation . . . 56
4.4.3 Electro-static force calibration . . . 59
4.4.4 High frequency nanoindentation at room temperature . . . 62
4.4.5 High frequency nanoindentation at elevated sample temperatures . . . 65
4.5 Chapter summary . . . 79

5 Heat transfer measurements on the nanoscale: Scanning Thermal Microscopy in vacuum 83
5.1 Introduction . . . 83
5.2 Heat transfer mechanisms . . . 84
5.3 Experimental setup of the vacuum SFM . . . 86
5.4 Heatable cantilevers in vacuum . . . 89
5.5 Heat transfer measurements with the vacuum SFM . . . 90
5.5.1 Thermal approach curves . . . 90
5.5.2 Data analysis of approach curves in vacuum . . . 93
5.5.3 Thermal approach curves on PMMA and silicon . . . 98
5.5.4 Adhesion dependence of thermal contact resistances . . . 111
5.5.5 Thermal contact resistances with different tips . . . 114
5.5.6 Surface analysis of the silicon sample . . . 117
5.5.7 Discussion and conclusions of this section . . . 119
5.5.8 Radiative heat transfer . . . 122
5.6 Thermal imaging with the vacuum SFM . . . 124
5.6.1 Experimental setup for the thermal vacuum imaging . . . 125
5.6.2 Experimental results of thermal vacuum imaging . . . 126
5.6.3 Rescaling of thermal vacuum imaging . . . 128
5.6.4 Material contrast in the thermal image . . . 133
5.7 Chapter summary . . . 140

6 Outlook 143

7 Summary 149

A Proof for the penetration of the PMMA film by the tip 157

B Estimation of the deformation energy with the Hertzian model 159

Chapter 1

Introduction and motivation

1.1 Introduction

In the last decades the capability of electronic applications such as computers, communication devices or entertainment equipment has steadily increased. Especially new products for mobile applications like MP3-players, digital cameras, cellular phones, personal digital assistants (PDA), memory sticks or laptops have been developed and rushed into the market. These devices are steadily developed further leading to smaller and more powerful devices. This trend, however, increases the demand for larger data memories: For example in the beginning of digital photography the cameras were equipped with charge coupled devices (CCD) chips of 1-2 Mega pixels. Nowadays 10 Mega pixel cameras are available leading to large amounts of data to be stored. Although for mobile music players the MP3 file format is widely used because of the high compression rate, the trend to store large amounts of data in this format is unbroken: Whereas in the beginning the memory sizes of 64 or 128 MByte were typical, nowadays MP3 players and memory sticks with up to 1-2 GBytes Flash memory and more than 50 GByte hard disk capacity are available.

For all these devices storage of digital data in non-volatile memories is essential. Different data storage techniques are used for this purpose: CD and DVD drives as well as hard disk drives are built into every laptop or desktop computer. These devices store data in an opto-electronical way, i.e. a laser beam reads and writes data on the storage medium. In digital cameras or MP3-player the so-called mini-disk (a hard disk drive with a very small form factor as small as a matchbox) or memory cards like the smart digital (SD) card or the XD card are used. The latter devices store the data in so-called Flash memories, which are litographically manufactured highly integrated circuits (ICs).

Although all these devices have reached a remarkable high data capacity in a small volume and are steadily further developed, the demand for even larger (and faster) techniques for data storage memories is still present. This is nevertheless due to the fact that fundamental physical effects limit the data densities achievable with these devices: In CD and DVD drives the size of the data bits on the disk is limited by the laser wavelength used for data reading and writing because of diffraction effects. The data density of magnetic recording devices (like hard disk drives and the mini disks) cannot exceed the so-called super-paramagnetic limit. And finally flash memory based devices (like memory cards) are limited by the fundamental structure size producable with lithographic techniques. In addition with further miniaturization of the structure size tunneling effects become relevant leading to undesired leakage currents.

Thus, basic research focuses on further miniaturization of the devices and on increase of the data densities. In recent years holographic storage techniques have been discussed and storage techniques based on addressable and switchable molecules are under investigations. Another technique under discussion for data storage application is scanning probe microscopy: Soon after the invention of the scanning tunneling microscope (STM) [1] and the scanning force microscope (SFM) [2] in the 1980s it has been realized that these techniques can not only image surfaces with ultra-high resolution (down to the atomic scale) but also provide the possibility to modify and structure the sample surface. One of the most popular example of this techniques are the letters "IBM" written with a STM tip by positioning individual Xenon atoms [3], which demonstrates that indeed single atoms can be moved and surfaces can be structured in a targeted way. This gave rise to speculations concerning data storage devices with single atoms or molecules which would result in ultra-high data densities.

Whereas these examples are rather basic research and demonstrate what in principle could be possible one day, different other probe based data storage technologies are investigated such as Magnetic Probe Recording [4], Resistive Probe Storage [5] or Atomic Resolution Storage [6]. One concept for probe based data storage is a technology called "Millipede" [7–11], which is currently developed at the IBM Zurich Research Laboratory (ZRL) in Switzerland. Since the work of this study is closely related to this concept and has partially been conducted at the ZRL, the "Millipede" project shall be presented in detail in the next section.

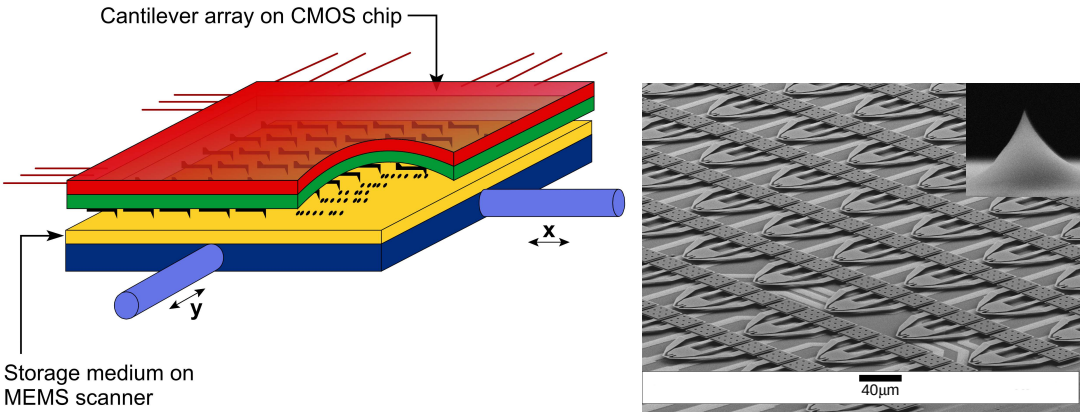

Figure 1.1: *Left:* Concept of the "Millipede": An array of 64×64 SFM tips is processed and transferred onto a single CMOS chip. These tips press indentations of 10-100 nm diameter into a polymer film, which acts as data storage medium.*Right:* Scanning Electron Microscope (SEM) image of the "Millipede" cantilever array chip. The inset on the top right corner shows a single tip located at the end of each cantilever. The size of the inset frame is 1 μm. Graphs from [12].

1.1.1 "Millipede" project of IBM: Thermomechanical data-storage with ultra-high data density

1.1.1.1 The "Millipede" concept

The "Millipede" concept is based on a completely new data storage technology and in contrast to established systems it is not based on opto-electronics like CDs or DVDs, magnetic recording like HDDs or electronic data storage with integrated circuits like Flash memory. Instead, it uses cantilevers and tips known from Scanning Force Microscopy integrated on a single CMOS chip and the data are stored by thermomechanical writing and reading [13]. These tips can thermomechanically write, read and erase tiny indentations in a thin polymer film, which acts as the data storage medium. One huge benefit resulting from this concept is that the tips can nowadays be manufactured with a very small size in the order of 10 nm resulting in very large realizable data densities: 1.0 Tera Bit/inch^2 have been demonstrated with single cantilevers using this technique [8, 9], which means that the equivalent of 25 DVDs could be stored on the area of a stamp.

Figure 1.1 (*left*) shows the concept of the "Millipede": Digital data are stored using a large number of cantilever tips in parallel in order to achieve the data rates required for a commercial product. Chips have been designed with more than 4,000 of these tips on an area of 6.4 mm ×6.4 mm. These dimensions enable to pack an entire high-capacity storage system into an SD Flash memory format package.

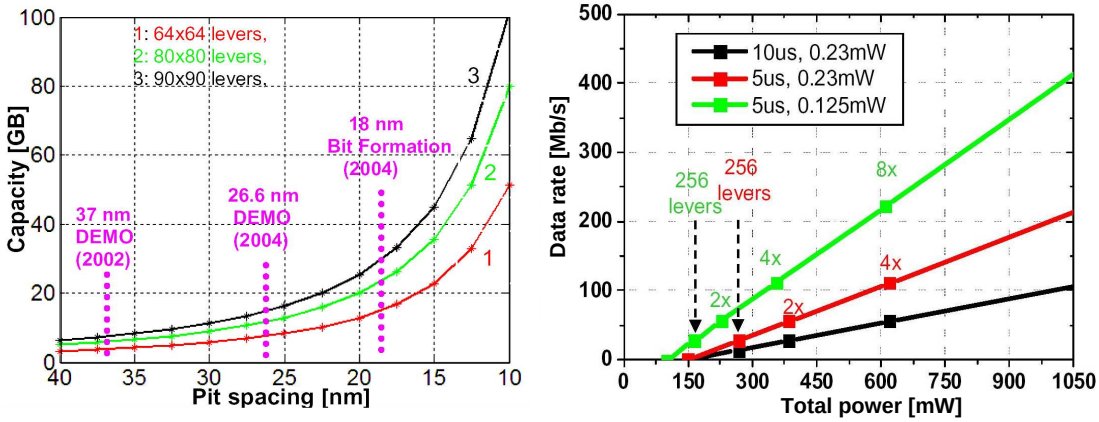

Figure 1.2: *Left:* "Millipede" capacity as function of pit spacing for different cantilever array sizes. *Right:* "Millipede" data rates of the write process as function of total power consumption for different write pulse durations, write powers of the heaters and number of simultaneously active cantilevers. Both graphs from [14].

The cantilever tips are arranged in an array like structure on a single CMOS chip (see figure 1.1, *right*). The device works similar like a punch card known from the early days of data storage. Data writing is performed by pressing the probe tips into a polymer films, which acts as the storage medium, leaving behind small indentations. These indentations represent the data bits and their diameter is in the range of the tip size (10-100 nm). A scanner moves the tip array relative to the storage medium in order to reach a significant capacity. Thus, every cantilever tip has its own storage field, where it reads and writes data bits. These data fields are approximately $100 \times 100\,\mu$m large, which is equal to the scan size of the scanner. The required accuracy of the scanner for positioning is of the order of the bit size, i.e. 10-100 nm.

The total capacity of a potential "Millipede" device depends very much on the specific implementation of the device: Figure 1.2 shows the calculated capacity as function of the pit spacing for different numbers of cantilever. Additionally, the pit spacings demonstrated so far are plotted. For example a "Millipede" device consisting of 90×90 cantilevers packed in a Secure Digital (SD) card format would reach a capacity of 100 GByte, if a pit spacing of 10 nm is applied. This would mean, that the capacity of this device would be 50-100 times larger than that of an SD card available today based on the Flash memory technology. The right diagram in figure 1.2 shows the achievable data rates of the write process as function of the total power consumption for different write pulse durations, write powers of the heaters and number of simultaneously active cantilevers (as multiple of 256). The SD card specifications, however, require a maximum total device power of 300 mW showing the necessity of an efficient and fast writing process.

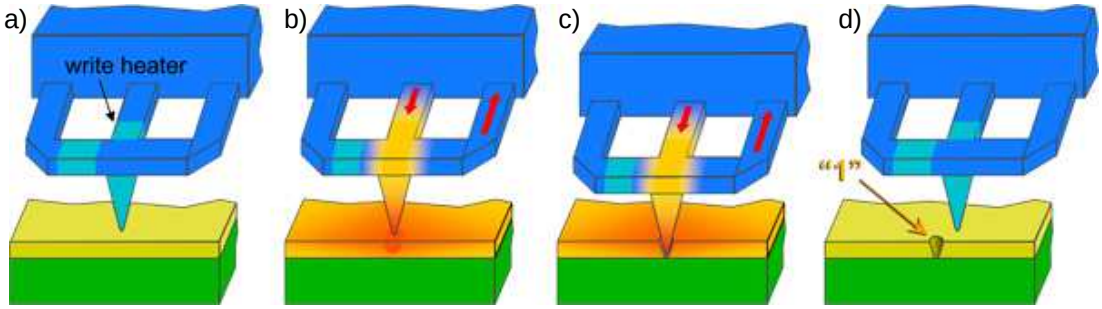

Figure 1.3: Schematic sketch of the thermomechanical bit writing process. Graphs from [12].

1.1.1.2 Thermomechanical bit writing and reading

We will now have a closer look to the thermomechanical write and read process. The data bits are written by pressing the tip into the polymer storage medium. In order to avoid tip wear the write process is assisted by heating the tip to soften the polymer medium around the tip. Figure 1.3 shows a schematic sketch of the bit writing process: A tip heater is placed near the tip within the cantilever. This heater is made up of a low doped region whereas the rest of the cantilever consists of highly doped silicon. Before the writing process the tip is moved by the scanner to a particular location, where the bit shall be written (a). By passing an electrical current through the heater, it is heated up to a writing temperature of about 300 °C (b). Thus, the temperature of the tip as well as the polymer medium around the tip is also heated and the tip can easily create an indentation, because the polymer medium becomes soft due to the increased temperature (c). The indentation process is assisted by an electro-static force acting between cantilever and polymer data storage medium by applying a bias voltage between cantilever and the substrate of the polymer film. As soon as the heater current is switched off, the heater and the polymer medium cool down and the polymer material hardens leaving behind a stable bit (d). The complete writing process of a single bit is performed within in several micro-seconds, because the time constant of the cantilever is in this range. Writing times, however, as short as 300 ns have been demonstrated with this technique [15].

Figure 1.4 shows an array of indentations written with the thermomechanical bit writing technique on a 35 nm thin Polymethylmethacrylate (PMMA) film on silicon. Since the writing parameters have been changed along both axis the bit sizes vary significantly. The bit writing performance at elevated sample temperature has been studied in this thesis and in chapter 4 a detailed investigation of the writing process will be presented.

The read process is illustrated in figure 1.5: A second heater ("reader") is placed aside from the tip and is heated to relatively moderate temperatures of about

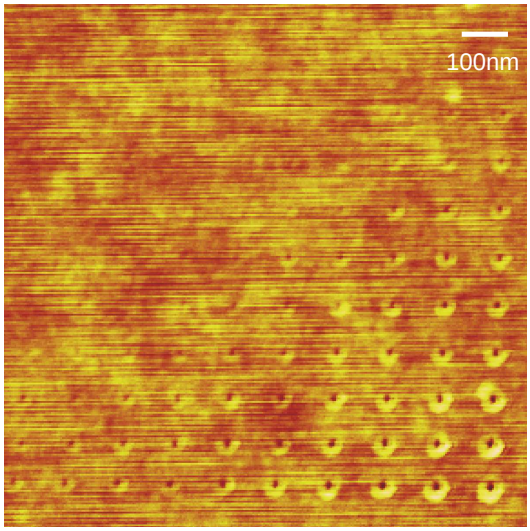

Figure 1.4: Example of bits written with a heatable cantilever on a 35 nm thin Polymethylmethacrylate (PMMA) film on silicon using 10 μsec pulses. The different bit sizes result from variations of the writing parameters: In horizontal direction the heater temperature has been varied and in vertical direction the electro-static force was changed. Image Size: 2 μm, Zscale: 10 nm.

200-300 °C. As the tip moves into an previously written indentation the distance between reader and sample decreases resulting in an increased cooling effect of the reader. This in turn leads to a decrease of the electrical resistance of the reader and thus, to a measurable change of the electrical current running through the reader. Besides reading and writing, erasing of individual bits has also been demonstrated [8, 9].

Although the "Millipede" project has already reached a remarkably stage and a prototype has been demonstrated by IBM on the CeBit 2005 basic research concerning the bit writing process and the cantilever performance has to be conducted: The requirements for the storage medium and the cantilever tips are enormous. Whereas the polymer medium should be easily deformable during the writing process to minimize or avoid tip wear, it should not degrade at the elevated temperatures being present around the tip. Furthermore, the data bits should be stable for at least 10 years even at elevated surrounding temperatures of up to 80 °C. For commercial products like e.g. Flash memories 10^5-10^6 write/read/erase cycle are required. Thus, for a potential product the "Millipede" also has to demonstrate this without significant tip and polymer wear.

However, the writing procedure is not well understood in detail: Especially the heat transfer from the heater through the tip to the polymer medium has not been investigated so far and thus, the temperature of the tip and of the polymer medium during the indentation process are unknown. This is of large interest for

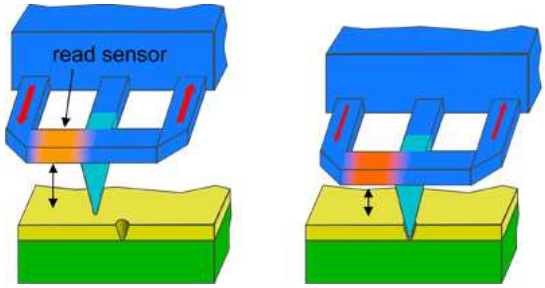

Figure 1.5: Schematic sketch of the thermomechanical bit reading process. Graphs from [12].

the choice of the best polymer medium and possible improvements. Furthermore, mechanical as well as thermal properties of thin polymer films used in the "Millipede" have only been investigated rarely and surface effects as well as influences of the substrate are likely to appear making it difficult to transfer bulk polymer properties to thin films.

1.2 Motivation and scope of the present work

In the present study questions concerning the thermomechanical properties of thin polymer films on the nanometer scale and the thermal performance of heatable scanning force microscopy cantilevers are addressed. Both topics are on the one hand of scientific interest and are on the other hand important for the development of the "Millipede". The subjects of this thesis can be divided into the following items:

- Thermomechanical properties of thin polymer films
- Heat transfer measurements on the nanoscale and further development of Scanning thermal microscopy (SThM) technique

Thermomechanical properties of thin polymer films

The mechanical and thermal properties of bulk polymer materials are both experimentally and theoretically well investigated and understood [16–21]. Typical polymer properties like the glass transition, frequency-temperature superposition principle or relaxation processes are well known and analyzed. Polymer materials are widely used in a huge amount of applications and products. However, thin polymer films with a film thickness of the order of the radius of gyration have gained increasing attention in the last years because they play an important role as photoresists in the fabrication of micro-electronic devices and as lubricant coatings in hard disk drives. Thus, a trend can be recognized, that the

focus of the polymer science has moved away from bulk samples towards thin films. Therefore, new measurement techniques for the investigation of thin polymer films have been developed such as ellipsometry, different X-ray techniques or scanning force microscopy. Nevertheless, there is still a lack of fundamental understanding of thin polymer films.

Thermomechanical properties of thin ($<$100 nm) polymer films on silicon substrates are investigated on the nanometer scale with Scanning Force Microscopic techniques. Two different polymers are investigated, which have completely different constitutions: Polymethylmethacrylate (PMMA), which consists of linear unbranched polymer chains forming a physically linked network and SU8 epoxy photo-resist, which forms a chemically highly cross-linked network. The consequences of these different molecular structures on the thermomechanical properties of the thin films is also addressed in this study. The following topics are treated in particular:

- The deformation behavior of the polymer film indented by an SFM tip is investigated in the glass transition range at moderate frequencies ($\approx$ 1 Hz). The forces necessary to create permanent impressions are measured as function of the sample temperaure and the elastic, plastic and visco-elastic deformation of the polymer films are of special interest.
- The thermal stability of the indentations is investigated as function of the sample temperature and reveals relaxation processes on the molecular level.
- "Millipede" bit writing experiments (i.e. high speed nanoindentation experiments with pulse-heated cantilever tips on a time scale of micro-seconds) are performed at elevated sample temperatures in order to investigate the influence of the sample temperature on the indentation topography. Furthermore, the performance of the heatable cantilevers at elevated surrounding temperature is of interest.

These topics are also of fundamental interest for the development of the "Millipede": The thermal stability of the indentations is important in terms of data reliability, but also in order to understand the data erasing procedure. The investigation of the deformation behavior of the thin polymer films is closely related to the "Millipede" bit writing procedure. The high speed indentation experiments with a heated SFM tip at elevated sample temperatures are important in order to determine the data densities, which are possible to achieve with the "Millipede" and to investigate possible data storage media.

Heat transfer measurements on the nanoscale and further development of Scanning thermal microscopy

During the "Millipede" write process the write heater is brought to a temperature of several hundred degree Celsius in order to soften the polymer temperature of the material underneath the tip. Whereas the temperature of the heater can be determined with a calibration procedure, the tip temperature and the temperature of the polymer material around the tip are unknown. These temperatures, however, determine the mechanical properties of the polymer material. Simulations or theoretical models cannot address this question with sufficient precision, because several material properties like the thermal conductivity of thin polymer films under high pressure acting during the writing process and of the SFM tip itself are unknown. The experiments presented in this study address specially the question of the heat transfer from the tip to the sample.

The tip-sample heat transfer measurements are not only interesting for the "Millipede" bit writing but also in the field of Scanning thermal microscopy (SThM): Knowing the amount of energy transferred into the sample enables to determine thermal properties of the sample material leading to a more quantitative analysis method than applied so far in SThM. Thus, the measurements presented in this study contribute to further development of the SThM technique.

The following topics concerning the heat transfer measurement on the nanoscale are addressed in this study:

- Heatable cantilevers manufactured at the IBM Zurich Research Laboratory are used to investigate the heat transfer from the heater located in the cantilever through the tip to the sample. The measurements are performed under vacuum conditions, where heat conduction through air is absent and the tip-sample heat transfer can be measured.

- The dependence of the heat transfer on the sample material, the tip size (tip radius and apex angle) and the adhesion force (which is proportional to the tip-sample contact radius) is investigated.

- Thermal properties of ultra-thin oxide films (2 nm thin silicon oxide and 3 nm thin hafnium oxide) are investigated by thermally imaging a sample, which consists of two phases of these materials. Hafnium oxide is of technical importance because it is a possbile material for future gate dielectrics in highly integrated electronic circuits [22].

1.3 Dissertation overview

This dissertation describes three different types of experiments, which all address questions concerning thermomechanical properties of thin polymer films on the nanometer scale. The first type of experiment is discussed in chapter 2: Nanoindentation experiments with the Scanning Force Microscope (SFM) using unheated conventional SFM tips at elevated sample are presented and the thermal stability of these impressions is investigated. Chapter 3 introduces the functionality of the heatable cantilevers manufactured at the IBM Zurich Research Laboratory for the "Millipede", which are used in the experiments of the chapters 4 and 5 and the mechanical and electro-thermal properties of these devices are discussed in detail. The second type of experiment is presented in chapter 4: High frequency nanoindentation experiments similar to the "Millipede" bit writing procedure are conducted at sample temperatures between room temperature and 130 °C. The aim of these experiments is to investigate the influence of the sample temperature on the performance of the heatable cantilevers and to analyze the topographic dimensions of indentation produced at elevated sample temperatures. The third type of experiment is described in chapter 5: The heat transfer from the cantilever heater through the tip to the sample is investigated under vacuum conditions with by means of approach curves. Furthermore, Scanning thermal microscopy imaging under vacuum conditions is presented with high lateral and thermal resolution. Chapter 6 describes possible future research on the topic of thermo-mechanics on the nanoscale and chapter 7 summarises the thesis.

Chapter 2

Nanoscale mechanical properties of thin polymer films at elevated sample temperatures

2.1 Introduction

The Scanning Force Microscope (SFM) [2, 23, 24] provides the possibility to image sample surfaces with resolutions ranging from a few nanometers down to the atomic scale. This is realized by raster-scanning the sample surface with a nanometer-sized tip attached to the end of a cantilever. During scanning a constant force acting between the tip and the sample (contact mode) or a constant amplitude of the excited cantilever oscillating in resonance (Tapping Mode^{TM1}) is maintained. The cantilever deflection is typically measured using an optical deflection system as shown in figure 2.1 (*right*). The force or the oscillation amplitude are kept constant by a feed back loop adjusting the vertical displacement of the piezo during the scan. The vertical displacement of the piezo reflects the sample topography and is used for the image, which is displayed in a computer using color-coded three-dimensional representation.

Besides imaging the sample topography with ultra-high resolution, mechanical measurements on the nanoscale can be conducted. Different operation modes have been developed to combine both capabilities: In friction force microscopy the lateral forces acting on the SFM tip are measured to determine tribological effects between tip and sample surface [26–29]. The Pulsed Force Mode (PFM) [30–32] and the further development the Digital Pulsed Force Mode (DPFM) [33, 34] enable to measure topography, sample compliance and adhesion forces

[1] Tapping Mode is a trademark of Veeco [25]

simultaneously. Additionally, force modulation techniques have been developed to measure viscoelastic properties of polymer surfaces [35, 36].

Whereas all these techniques are performed while scanning the tip over the sample surface and thus, images of the topography and maps the particular quantities (e.g. stiffness or adhesion) are obtained, the so-called force distance curve measurement is performed at one single location. Force distance curves (FDC) are nowadays a SFM operating mode applied to investigate mechanical material properties of samples surfaces or to perform force spectroscopy with extremely high accuracy in the Piconewton range [37–44]. Force distance curves are used to investigate the mechanical properties of samples at room temperature in the elastic range [37–41] and in the viscoelastic-plastic range [42–44]. Thermal properties, especially the glass transition of polymer surfaces and thin polymers films have been studied with lateral force microscopy [45–49] and force distance curves on heated samples [50, 51].

In this chapter experiments are presented, which investigate the thermal properties of thin polymer films (film thicknesses smaller than 100 nm) on silicon substrates at elevated sample temperatures with the SFM. Force distance curve measurements with maximum forces of $4\,\mu$N have been conducted to measure forces necessary to create permanent impressions on thin polymer films. Quantities like the indentation depth of the SFM tip during the indentation process into the polymer film, the remaining indentation depth after the indentation process (remanence depth) and the dissipated energy during the process among others have been measured as a function of the cantilever force and the sample temperature. The lateral dimensions of the indentations are between 100 and 300 nm and were determined by Tapping Mode imaging. Additionally, the thermal stability of the structures has been investigated by continuously imaging revealing a strong temperature dependent relaxation process.

2.2 Force distance curve measurements

Figure 2.1 shows a measurement of a force distance curve schematically. The initial starting point of the tip for a FDC measurement is several hundred nanometer above the sample surface. Starting from that point the cantilever chip is displaced towards the sample with a constant velocity (1) until the tip comes into contact with the sample (2). The piezo is further displaced and the tip exerts a certain force to the sample (3). Afterwards, the cantilever chip is retracted by contracting the piezo until the tip snaps off the surface (4) and finally reaches the initial position above the sample surface again (5). As shown in figure 2.1 *right* the piezo displacement $\delta_{\text{Piezo,Polymer}}$ and the top minus bottom signal $U_{\text{T-B,Polymer}}$ of the four quadrant photo diode in Volts are measured and recorded during this

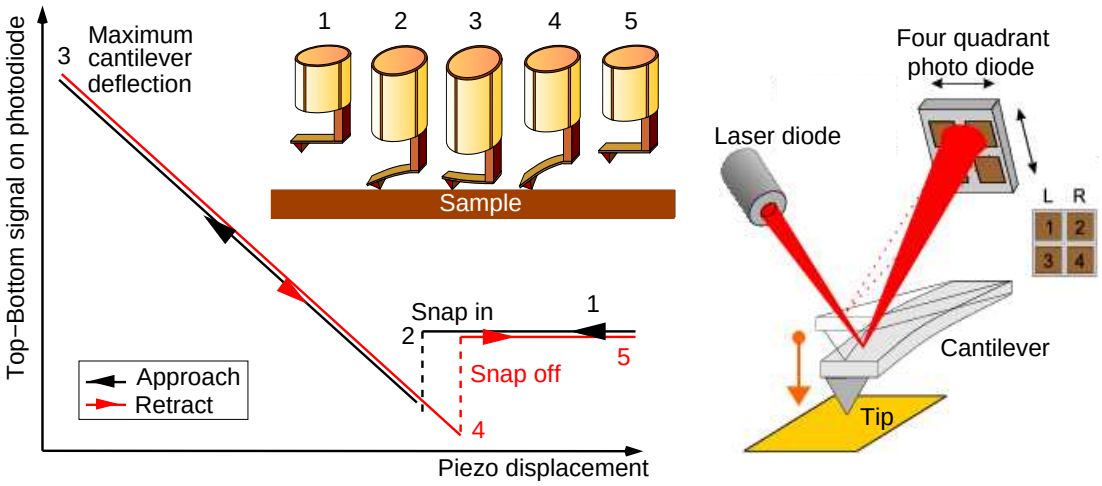

Figure 2.1: *left:* Schematic sketch of a force distance measurement on the a hard rigid surface such as silicon. Significant points are the approach part (1), the snap-in (2), the point of maximum cantilever deflection (3), the snap off (4) and the off-contact region (5); *right:* Laser detection system for the cantilever deflection.

cycle. However, the quantities of interest are the force exerted by the tip to the sample and the penetration depth of the tip into the sample. A calibration measurement (calibration force curve, CFC) on a hard rigid sample (e.g. silicon) enables to determine the cantilever deflection and the Hook's law is used to calculate the force provided the spring constant of the cantilever is known (see section 2.2.1).

Experimentally two different ways are possible to define the point of maximum force during the FDC: In the untriggered mode the user can preset the piezo displacement whereas in the triggered mode the maximum cantilever deflection (maximum force) is predetermined. In the first case the maximum cantilever force is unknown and the measurement is performed in an rather uncontrolled way, whereas in the latter case the maximum force is known and tip and sample damage respectively can be avoided. However, one has to know the sensitivity of the detection system (i.e. the signal measured on the photodiode as function of the cantilever deflection, see section 2.2.1), which is in turn dependent on the particular adjustment of the laser on the cantilever. Thus, at least one CFC has to be conducted in an untriggered mode.

2.2.1 Conversion of FDCs to FPCs

Figure 2.2 shows examples for an FDC measured on a thin polymer film and a CFC obtained on a silicon substrate. Now, the conversion of these two curves to

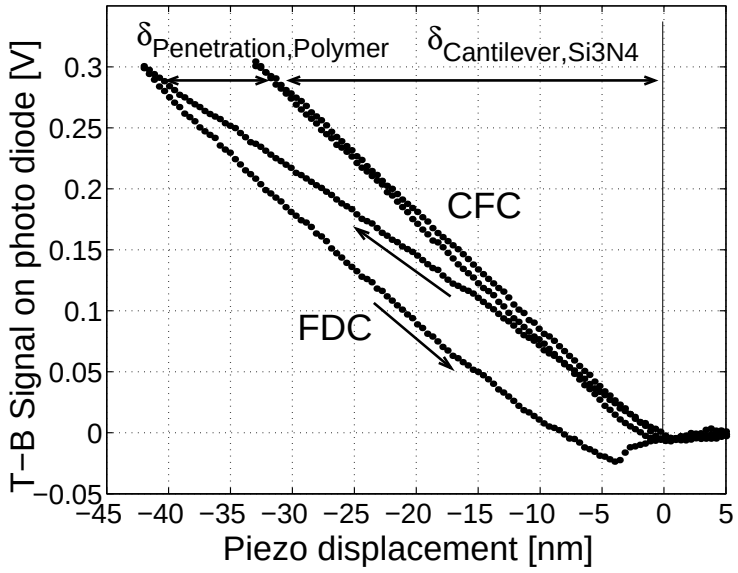

Figure 2.2: Example for an FDC and a CFC. The penetration (loading) and retraction (unloading) parts are denoted by the arrows.

a force-penetration curve (FPC) shall be discussed. The FPC is more meaningful for the analysis of the indentation process because it relates the force exerted by the tip and the indentation depth of the tip into the polymer film.

Assuming that the deformation of the silicon nitride substrate and the compression of the tip can be neglected, the cantilever deflection $\delta_{\text{Cantilever,Si}_3\text{N}_4}$ is equal to the piezo displacement by the tip $\delta_{\text{Piezo,Si}_3\text{N}_4}$ in the CFC. The dependence of the detector voltage $U_{\text{T-B,Si}_3\text{N}_4}$ on the cantilever deflection $\delta_{\text{Cantilever,Si}_3\text{N}_4}$ is given as the slope of the CFC in the repulsive region and is called sensitivity S:

$$S = \frac{\partial U_{\text{T-B,Si}_3\text{N}_4}}{\partial \delta_{\text{Piezo,Si}_3\text{N}_4}}. \tag{2.1}$$

S is used to calculate the cantilever deflection $\delta_{\text{Cantilever,Polymer}}$ in the FDC

$$\delta_{\text{Cantilever,Polymer}} = \frac{U_{\text{T-B,Polymer}}}{S} \tag{2.2}$$

The force $F_{\text{Tip,Polymer}}$ applied by the tip to the polymer film can be calculated with Hook's law:

$$F_{\text{Tip,Polymer}} = \delta_{\text{Cantilever,Polymer}} \cdot k_{\text{Cantilever}} \tag{2.3}$$

where $k_{\text{Cantilever}}$ is the spring constant of the cantilever.

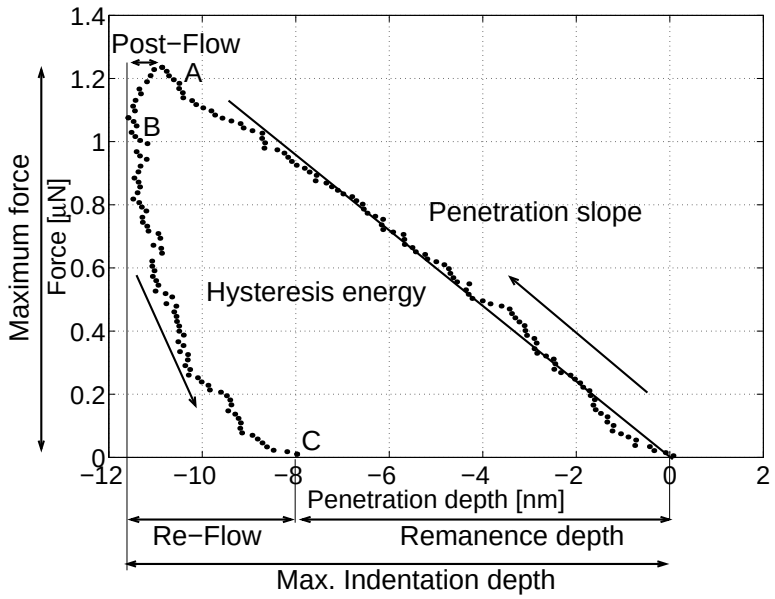

Figure 2.3: Example for an FPC with the quantities of interest, which can be deduced from the curve. Point A: Point of maximum force exerted by the tip, Point B: Point of maximum indentation depth of the tip, Point C: Remanence depth of the indentation at the point where the cantilever force is zero after the indentation cycle. The penetration (loading) and retraction (unloading) parts are denoted by the arrows.

The piezo displacement $\delta_{\text{Piezo,Polymer}}$ in the FDC is the sum of the cantilever bending $\delta_{\text{Cantilever,Polymer}}$ and the penetration depth of the tip into the polymer film $\delta_{\text{Penetration,Polymer}}$. Thus, the penetration depth $\delta_{\text{Penetration,Polymer}}$ can be calculated as:

$$\delta_{\text{Penetration,Polymer}} = \delta_{\text{Piezo,Polymer}} - \delta_{\text{Cantilever,Polymer}} \tag{2.4}$$

The penetration depth of the tip into the polymer $\delta_{\text{Penetration,Polymer}}$ can be worked out with equation 2.2. Thus, the force exerted by the tip and the indentation depth can be calculated and the FPC can be plotted as shown in figure 2.3.

Besides the indentation depth several characteristic quantities can be determined from the FPC as shown in figure 2.3:

- The point of maximum penetration depth (Point B) does not coincide with the point of maximum cantilever bending (Point A). This means, that the tip further penetrates into the polymer film, even though the force applied by the tip to the polymer is reduced. We will call this effect "post-flow" in the following.
- The penetration depth at zero force (Point C) is called remanence depth. The difference of the maximum penetration depth and the remanence depth

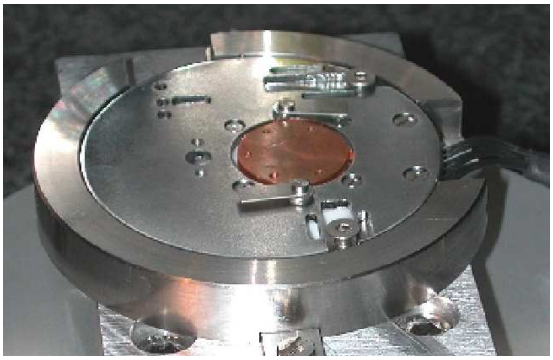

Figure 2.4: The heating platform used for the measurement of force-distance curves at elevated sample temperature

is named "re-flow" in the following and can be related to elastic recovery of the material during unloading.

- The area between the penetration and retraction part in the repulsive regime of the FPC is the hysteresis energy $E_{\text{Hysteresis}}$. This is the energy dissipated into the polymer during the deformation and is the sum of different contributions such as the plastic deformation energy, viscoelastic deformation energy and friction energy among others.
- The slope of the FPC's indentation part is given by

$$g = \frac{\partial F_{\text{Tip,Polymer}}}{\partial \delta_{\text{Penetration,Polymer}}} \tag{2.5}$$

and can be related to the compliance of the material. Since the slope is constant only at the beginning of the FPC, we have calculated this slope g by a linear regression fit on the first 10 nm penetration depth.

2.3 Experimental setup

2.3.1 The SFM and the heating stage

A commercial Scanning Force Microscope (Dimension 3100 with Nanoscope IIIa Controller from Veeco) was equipped with a heating stage from Molecular Imaging [52] and a controller from LakeShore (Model 330) [53]. The heating platform is a circular copper disc with a diameter of 2 cm. The temperature accuracy of the heating platform is 0.1 °C as stated by the manufacturer. With this setup SFM measurements (imaging and force distance curves) at temperatures between 100 °C and 130 °C were carried out.

To estimate the temperature difference between the heater platform and the sample, an external thermocouple device was placed on top of a sample. The thermal contact between the thermocouple and the silicon substrate was enhanced by using heat-conductive paste. A temperature deviation of 1.4 °C at 120 °C controller setpoint was measured. Thus, a deviation between sample temperature and controller set point temperature of at most 2 °C at the highest sample temperature of 130 °C is derived.

The influence of the sample temperature on the piezo calibration was investigated by measuring a standard silicon calibration grid at room temperature and at elevated temperatures: The lateral sizes did not change within the error margin. In vertical direction the measured values at 130 °C were about 2 % smaller than the values measured at room temperature and thus the deviation is neglectable compared to the other uncertainties involved in the measurement.

2.3.2 The SFM tips

The indentation process and the subsequent imaging in Tapping Mode^{TM} was conducted using commercially available cantilevers from Olympus. The cantilevers have a length, width and thickness of 160 μm, 50 μm and 4.6 μm respectively and are reflex coated with Aluminum. The typical resonance frequency of 300 kHz and a spring constant of typically 40 N/m is stated by the manufacturer. However, the spring constants of different cantilevers have a large variation between 12 and 103 N/m also stated by the manufacturer. This is obviously a large range and thus the force and energy values presented in this study are afflicted with large absolute errors of up to 50 % (error bars are omitted in the diagrams for reasons of clarity). However, the essence of the experiments is not afflicted, since the focus is on the relative change of the indentation behavior as a function of the sample temperature and all measurements in this chapter were conducted with the same cantilever.

The appropriate choice of the cantilever's spring constant is a crucial point in order to obtain best possible results: As figure 2.2 shows the cantilever should have the same stiffness as the polymer material. In this case the penetration depth of the tip into the sample $\delta_{\text{Penetration,Polymer}}$ and the cantilever deflection $\delta_{\text{Cantilever,Si}_3\text{N}_4}$ are equal. If the cantilever is much weaker than the polymer material the tip does not indent into the sample and the signal-to-noise ration becomes bad. On the other hand if the cantilever is too stiff the force becomes extremely large even though the cantilever deflection is relatively small. This would result in very high forces and possibly significant tip damage.

The tip radius of unused tips is less than 20 nm as investigated by Scanning Electron Microscopy (see figure 2.5). It is observed that new unused tips break

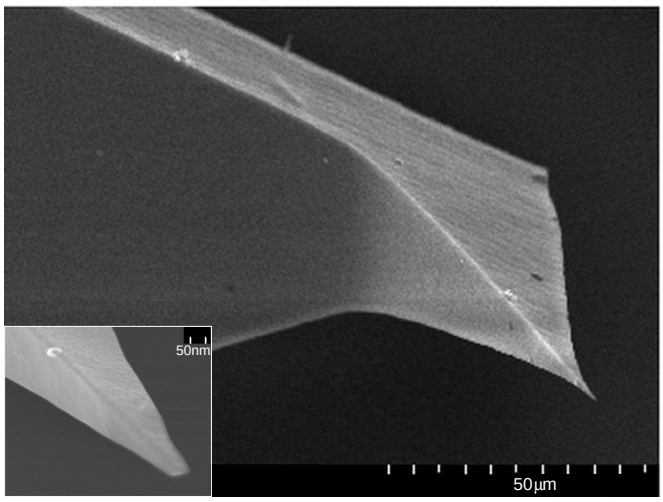

Figure 2.5: SEM image of a commercial Tapping Mode tip. The inset shows that the tip radius is smaller than 20 nm.

at 1.5-2 μN in the first FDC, but in all subsequent FDCs the tip remains stable and reproducible measurements can be performed [54].

Since the tip is thermal contact with the heated sample and the cantilever is only about 10 μm away from the sample the influence of the sample temperature on the cantilever spring constant was investigated. This was done by measuring the cantilever's resonance frequency at each sample temperature with the tip 100 μm away from the sample surface. In the measurement it turned out that the resonance frequency decrease from 321.95 kHz to 321.7 kHz. Since the the resonance frequency ν is proportional to the spring constant $k^{1/3}$ this decrease of the resonance frequency would correspond to a decrease of the spring constant of 0.2 %.

2.4 Sample preparation

The samples under investigation in this study were a 35 nm thin PMMA film on silicon and a 80 nm thin SU8 Epoxy photoresist on silicon. Both polymers are used in the lithography technique as photoresists and are possible candidates for the storage medium in the "Millipede". The two polymer materials have very different constitutions: PMMA is built up of unbranched chain molecules and is physically crosslinked by entanglements. Bulk PMMA samples produced from the same material as the film samples exhibit a clear glass transition between 100 and 120 °C. SFM nanoindentation experiments performed in the same way as the ones presented here show that the glass transition temperature of the thin film samples is in the same region [54].

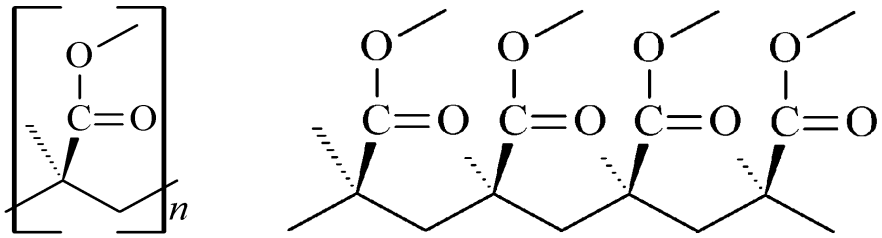

(a) (b)

Figure 2.6: Molecular structure of PMMA: (a) Monomer unit of PMMA (b) Section of a PMMA chain

On the other hand the SU8 epoxy photoresist consists of monomers which have the capability to form a chemically highly cross-linked network. It does not show a glass transition up to 200 °C. These two differently built-up polymers were chosen in order to investigate the thermomechanical differences arising from the different molecular composition. The temperature range of most interest in this study was the glass transition region of the PMMA (100 to 130 °C). Thus the change of the material properties of a polymer film in the glass transition region (PMMA) was investigated in comparison to SU8 which is not in the glass transition range at these temperatures.

These sample systems were also studied in the nanoindentation experiments with pulse-heated SFM tip presented in chapter 4 and in heat transfer measurements of chapter 5.

2.4.1 PMMA films on silicon

Although it is possible to crosslink PMMA chemically with covalent bonds, the sample investigated in this study were physically crosslinked by entanglements. The molecular structure of the PMMA is shown in figure 2.6. The thin Polymethylmethacrylate (PMMA) films were produced on dehydrated (200 °C for 30 minutes) silicon substrates by spin coating (2200 rpm) from the solution of chlorobenzene (1 % concentration). Afterwards the samples were annealed for 30 minutes at 180 °C.

The film thickness was determined by wiping away the PMMA film partially and imaging the step edge between PMMA and silicon in the SFM. As a result the film thickness turn out to be at 35±5 nm. The molecular weights (M_w) are distributed between 5×10^4 and 1×10^6 g/mol with a broad maximum at M_w=3.5×10^5 g/mol. The radius of gyration is calculated by $R_{\text{Gyration}} = \sqrt{K \cdot M_W}$ [16]. Given $K = 5.2 \times 10^{-18}$ cm^2 mol/g [20], the radius of gyration is calculated

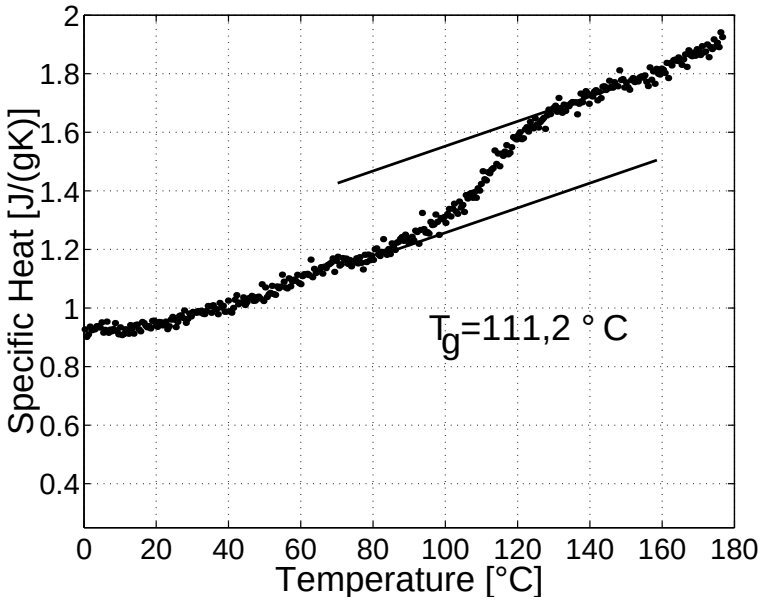

Figure 2.7: DSC-Curve of bulk PMMA

to be 13 nm, which means that the film thickness is in the range of the diameter of gyration.

To measure the bulk glass temperature of this specific PMMA, a differential scanning calorimetry (DSC) measurement was performed with a DSC2 device from Perkin Elmer at a heating rate of 10 K min^{-1}. A bulk sample was produced by solution casting from the same solution as the thin film sample. The glass transition temperature of this bulk sample is at 111 °C as deduced from the DSC data in figure 2.7.

For the SFM measurement the PMMA film sample was attached onto a copper plate of 17×10×1 mm (length × width × height) using a highly thermal conducting epoxy glue (H74 by Polytech) with T_G above 130 °C. To perform calibration force curve measurements (see section 2.2) on a hard rigid surface, a piece of silicon nitride was glued on the copper plate additionally.

2.4.2 Epoxy photoresist SU8 films on silicon

Besides the PMMA film a SU8 Epoxy photoresist film of 80 nm thickness on a silicon substrate was investigated in this study. The SU8 resist is based on Epoxy resin technology and the monomer units are shown in figure 2.8. It consists of eight Epoxy groups which can form chemical crosslinks to other monomer units resulting in a chemically highly crosslinked network.

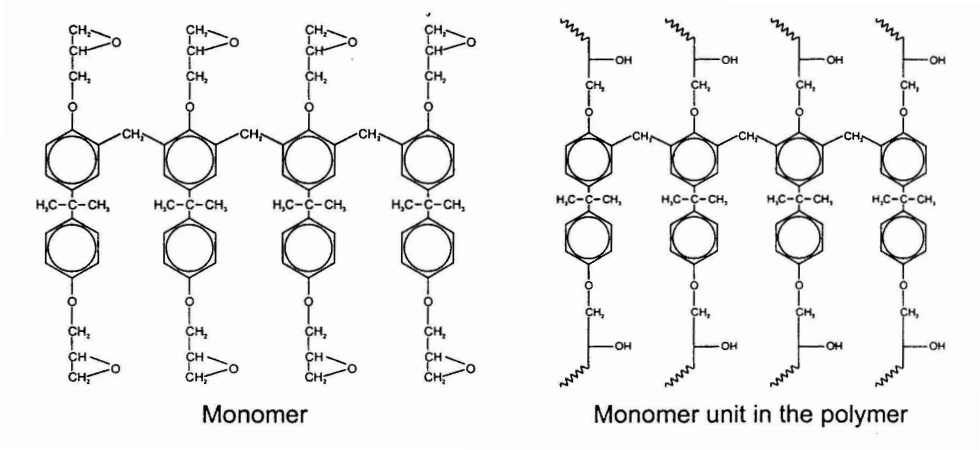

Figure 2.8: *Left:* Individual monomer unit of SU8; *Right:* Monomer unit of SU8 in the polymer

The film was produced from the monomers in a solution of Butyrolacton of 2-4 % concentration by spin-coating at 4000 rpm. A prebake of 5 minutes at 95 °C and an exposure with 250-300 mJ UV radiation followed. Then the post exposure bake (15 minutes at 95 °C) and the hard bake (30 minutes at 200 °C) were conducted. The film thickness of 80 nm was measured in the same way as the thickness of the PMMA film.

As for the PMMA a DSC measurement of a SU8 bulk sample was performed to investigate if thermal phase changes are observable (figure 2.9 *left*). It turns out that there is are strong differences between the first and second run of the DSC measurement: In the first run a decrease of the specific heat at temperatures higher than 80 °C and a strong increase at temperatures higher than 110 °C are observed. In the second run the curve shows a smooth increase with no indication

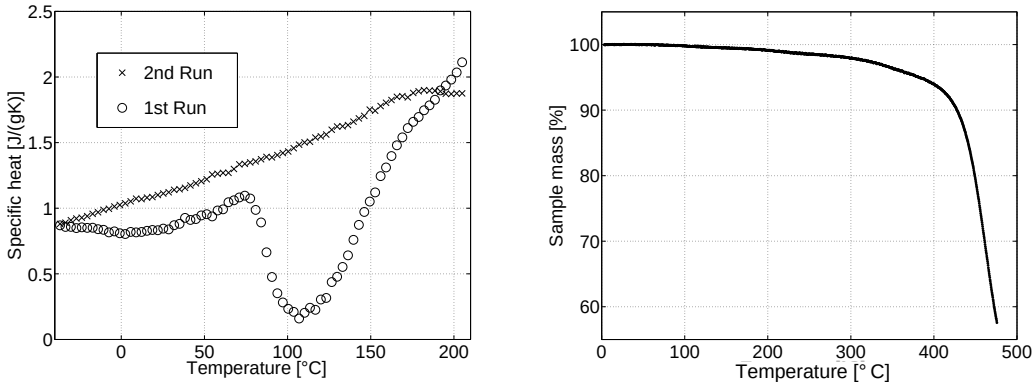

Figure 2.9: DSC (*left*) and TGA measurement (*right*) of SU8

of a phase transition (e.g. glass transition) up to 200 °C. The strong differences between first and second run could possibly be explained by annealing processes during the first run.

Besides the DSC measurement a TGA (thermo gravimetry) measurement of bulk SU8 samples was performed (figure 2.9 *right*). The material is thermally stable up to temperatures of 150 °C and starts to degrade when further heated.

2.5 Nanoindentation experiments

2.5.1 Experimental details

Force penetration curves haven been measured on the 35 nm PMMA film on silicon at temperatures ranging from 100 °C to 130 °C and on the 80 nm SU8 film on silicon at temperatures between 100 °C and 120 °C. At each sample temperature calibration force curves on silicon nitride were taken additionally. Performing quantitative SFM measurements at elevated sample temperature requires to minimise thermal drift effects. Thus, a waiting time at each sample temperature before conducting the indentation measurements was necessary. E.g. at a sample temperature of 130 °C the conditions were stable after approx. 40 minutes.

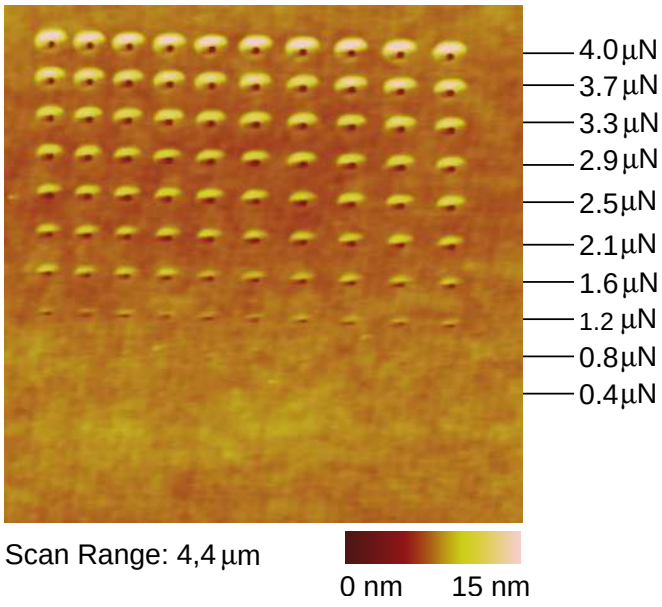

Figure 2.10: Example of an array of 10×10 indentations in a 35 nm PMMA film on silicon at 100 °C sample temperature. The averaged maximum force exerted by the tip for each line is given.

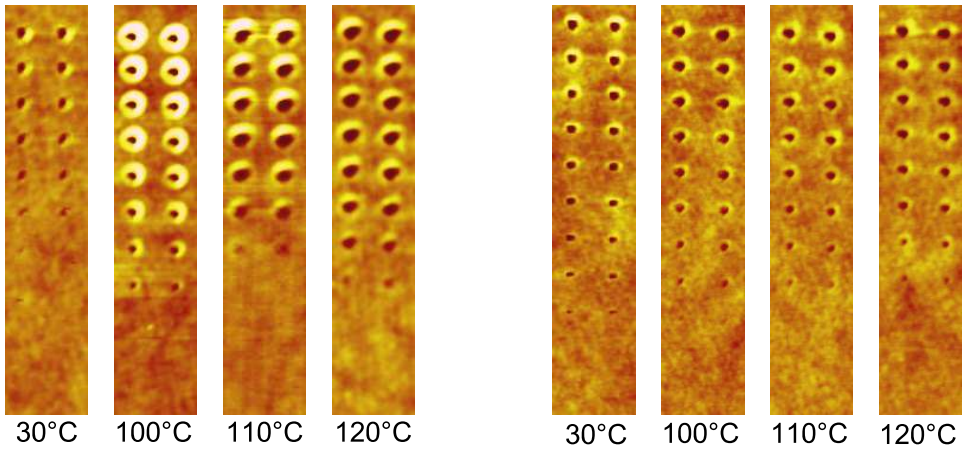

Figure 2.11: Comparison of the topography of indentations created with constant maximum force at different sample temperatures on the PMMA film (*left*) and on the SU8 film (*right*). Image size: $0.7 \times 3{,}4\,\mu$m; height scale: 10 nm

Arrays of 10×10 indentations were created with a constant force in each row and decreasing force in each column. Figure 2.10 shows an example of an array produced with this method at 100 °C sample temperature. The average maximum forces during the FDC cycle for each line of 10 indentations are denoted. Only eight lines are visible in this Tapping Mode^{TM} image which was taken after the indentation process, because for forces smaller than 1,2 nN (lower two lines) no permanent indentations were created. The lateral size (horizontal diameter) of the indentations ranges from 270 nm in the first line to 120 nm in the last visible line.

All force curves were measured at a constant velocity of the piezo displacement. Since the maximum cantilever force and thus the piezo displacement decreases within an array column (see figure 2.10) the duration of a FDC measurements changed from approx. 1 second to 0.1 second. This span of time includes the part when the tip is not in contact with the sample during the approach and retract part as well as the time for the indentation process (FPC) which is only 20-40% of the time needed for the entire FDC cycle.

2.5.2 Results and discussion

2.5.2.1 Comparison of indentation topography in PMMA and SU8 at different temperatures

Before the force penetrations curves on PMMA and SU8 are analyzed separately in the following sections 2.5.2.2 and 2.5.2.3 respectively, the indentation topogra-

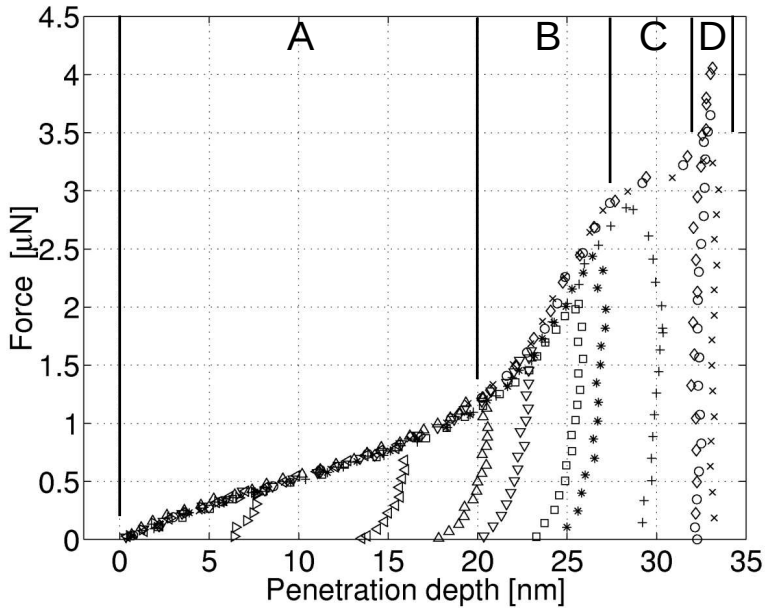

Figure 2.12: 10 FPC measured at 130 °C sample temperature with maximum forces exerted by the tip between 0.4 and 4.0 μN.

phy on the two polymer samples shall be compared in this section. Figure 2.11 shows the topography of indentations on PMMA and SU8 at different sample temperatures measured with Tapping Mode. The variation of the maximum force during the indentation process were identical, which makes it possible to compare the images directly.

The influence of the sample temperature is clearly observable on PMMA: The lateral size of the indentations increases clearly with temperature and a large rim formation on PMMA stands out at 100 °C. This pile-up effect is smaller at 110 °C and 120 °C and hardly observable at 30 °C. On SU8 the influence of the sample temperature is very small. Neither the lateral nor the vertical dimensions of the indentations are affected by the increase of the temperature. This observation is in accordance with the FPC measurements in the section 2.5.2.3. There it will turn out that the temperature influence on the indentation behavior is much smaller on SU8 than on PMMA.

2.5.2.2 Force penetration curves on the PMMA film

To point out the differences of the FPCs above and below T_G, curves taken with different maximum forces ranging from 0.4 μN to 4.0 μN are plotted in figure 2.12 and 2.13. Shown are examples of FPCs measured above T_G at 130 °C (Figure 2.12) and below T_G at 100 °C (Figure 2.13). In both figures the penetration parts of the curves match well showing that measurements are well reproducible and

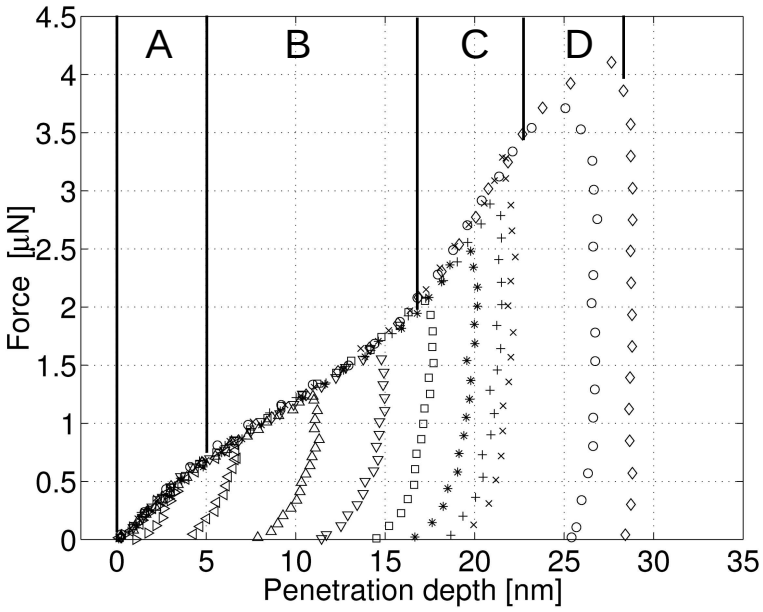

Figure 2.13: 10 FPC measured at 100 °C sample temperature with maximum forces exerted by the tip between 0.4 and 4.0 μN.

the film is homogeneous on a length scale of at least the array size (approx. 4 μm). During this measurements no significant tip contamination or tip wear occurred, or, if it had occurred, it had no influence on the FPCs.

The FPCs in figure 2.12 exhibit different slopes in the indentation part of the curve: The slope is relatively small at the forces up to 1.2 μN (region A). For higher forces up to 3 μN the curve becomes steeper (region B) followed by a very flat region between 3 and 3.3 μN (region C). For forces larger than 3.3 μN the slope is vertical (region D) showing that the tip has penetrated the PMMA film down to the silicon substrate. This interpretation is confirmed by the penetration depth of 33 nm, which is comparable to the film thickness. Additionally, a further experiment, where the indented PMMA film has been used as a mask to produce gold clusters, is discussed in detail in Appendix A, which shows that the tip indeed penetrates the polymer film and reaches the silicon substrate. Region C is presumably caused by the rupture of the PMMA film just before the tip reaches the silicon substrate. Figure 2.12 also reveals that the re-flow is dependent on the forces exerted to the polymer film: The three FPCs with high forces (Symbols $\circ, \times$ and $\Diamond$) show no detectable re-flow because of the penetration of the PMMA film, while the curves with smaller maximum forces show significant re-flow behavior.

Figure 2.13 shows 10 FPCs with the same maximum forces as in figure 2.12, but taken below T_G at 100 °C sample temperature: Similar to figure 2.12 the maximum indentation depths as well as the remanence depths increase with increasing

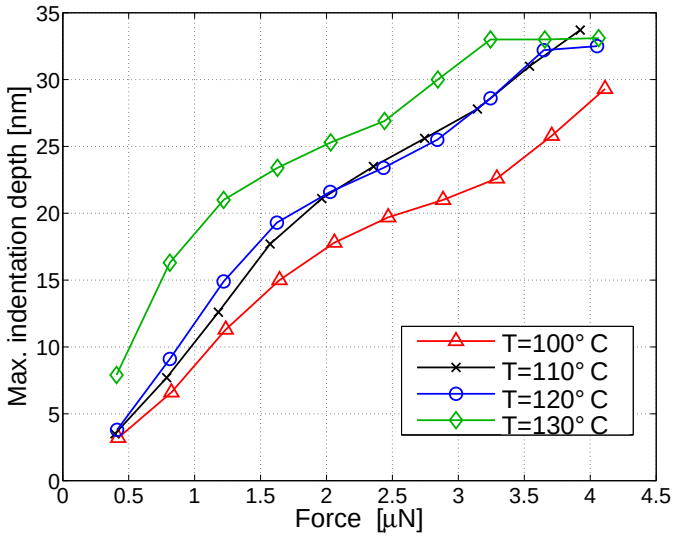

Figure 2.14: Penetration depth as function of the cantilever force.

maximum force and different gradients emerge: For forces smaller than 0.7 μN a relatively steep slope occurs (region A) followed by a region of smaller slope between 0.7 and 2 μN (region B). Then the curve becomes steeper again between 2 and 3.5 μN (region C). For even higher forces the gradient decreases again (region D). The retraction part of the FPCs shows different behaviors depending on the maximum penetration depth: The re-flow decreases with increasing penetration depth. The post-flow effect is clearly recognizable in the FPC with large indentation depths (Symbols $\circ$) and is small at low indentation depths (Symbols $\triangle$ $\triangleleft$ $\triangleright$). Note, that even for small forces of 0.4 and 0.8 μN hysteresis occurs in the FPC of figure 2.13, but in the Tapping Mode image of figure 2.10 no remanent indentations are detectable for these forces. Presumably, the hysteresis is caused by viscoelasticity and the impressions recover completely during the time between the force curve measurement and the completion of the image (approx. 10 minutes).

The influence of the sample temperature can be seen by comparing figures 2.12 and 2.13: Above T_G the indentation slope is smaller than below T_G showing that the polymer is softer. This is confirmed by comparing the indentation depths and remanence depths resulting from constant forces at different temperatures: For instance, for a force of 2 μN an indentation depth of 17 nm is measured at 100 °C but at 130 °C the indentation depth is 25 nm. The vertical peak in figure 2.12 at forces larger than 3.3 μN (region D) shows that the tip penetrates the film down to the silicon substrate above T_G. However, below T_G the tip does not reach the substrate and the peak does not occur in region D of figure 2.13.

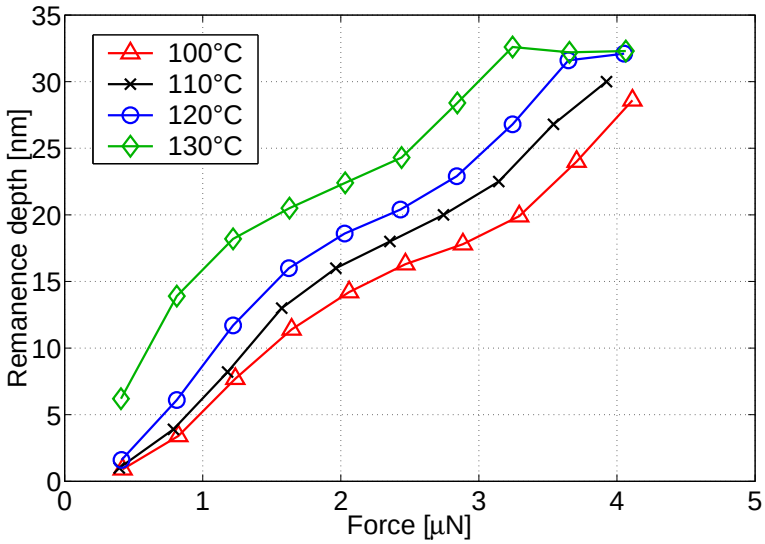

Figure 2.15: Remanence depth as function of the cantilever force at different temperatures.

So far examples of single FPCs have been considered. In the following averaged data will be presented. These sets of data were obtained by calculating the quantities of interest for each FPC of an array. Since the maximum forces in an array line are kept constant, it is possible to average 10 FPCs in the horizontal direction of figure 2.10 and calculate data for the indentation depth, remanence depth, hysteresis energy and penetration gradient.

In figure 2.14 the data of the maximum penetration depths are plotted as a function of the force for temperatures ranging from 100 °C to 130 °C. As in the FPCs of figure 2.12 and 2.13, the indentation depth increases with higher temperature due to the softening of the polymer. The penetration depths at 110 °C and 120 °C are in the same range. A plateau is identified for forces larger than 3.2 μN at 120 °C and 3.6 μN at 130 °C , which occurs due to the penetration of the tip through to PMMA film down to the silicon substrate. For the same forces exerted by the tip the plateau does not appear at 100 °C and 110 °C, because the PMMA is harder below the glass transition temperature.

The remanence depth as a function of the applied force at different temperatures is plotted in figure 2.15. In contrast to the penetration depth in figure 2.14, the remanence depths at 110 °C are smaller than those at 120 °C due to the re-flow effect. The remanence depths increase with increasing temperature by at most a factor of 2 at a force of 1.5 μN.

The hysteresis energy is plotted in figure 2.16 ranging up to 350 keV, which is comparable to results obtained in other studies [43]. A rough estimation using the Hertz model shows that the energies involved in this experiment are in the

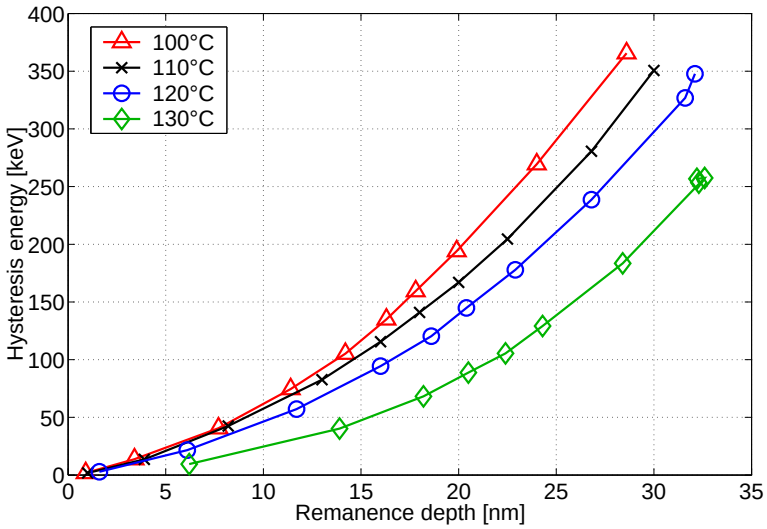

Figure 2.16: Hysteresis energy as function of the penetration depth.

range of several hundred keVs (see appendix B for the calculation). For higher temperatures the hysteresis energies decrease for a given remanence depth, which means that less energy is needed to produce a certain remanent deformation of the polymer film.

The slope of the loading curve as a function of the temperature is shown in figure 2.17 and decrease with increasing temperature by a factor of 3. This confirms the softening of the polymer and is in accordance with other studies [50, 51].

Even though all data show the softening of the polymer film at higher temperature, it is interesting that the hysteresis energy decreases only by a factor of approx. 2. Additionally, the change in the indentation slope by a factor of 3 is rather small considering the drop of the Young's modulus by a factor of 10^3 for bulk samples at T_G. Since the indentation slope is determined on the first 10 nm indentation depth, the Hertz model should describe the behavior well, because the deformation in this part of the FPC is mainly elastic: A decrease of the Young's modulus by a factor of 10^3 would lead to a decrease of the reduced effective modulus K by a factor of 10^3 assuming that Poison's ration remains constant. Since the indentation depth δ is proportional to $K^{-2/3}$ and thus, the penetration depth as well as the the indentation slope is expected to increase by a factor of 10^2. This deviation of the observed indentation depth from the calculated depth according to Hertz theory is also reported in other studies [55].

Different effects could decrease the observed softening effect of the polymer film at T_G. One has to consider the pressure under the SFM tip: In our experiments the SFM tip generates pressures between 0.3 and 3 GPa. For bulk PMMA it is known that the glass transition temperature increases at higher pressures [56]. This

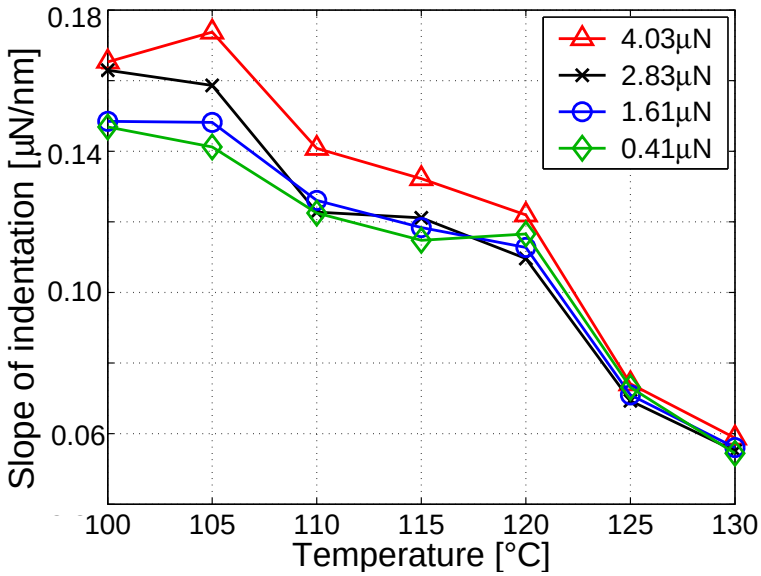

Figure 2.17: Slope of the loading curve as function of the temperature at different maximum cantilever deflections.

means that at 130 °C sample temperature the polymer beneath the tip could still be below the glass transition and this would lead to a reduced penetration depth of the tip. A further effect can be that the polymer is more flexible above the glass transition temperature and wetting of the tip could be enhanced. Thus, the contact area is increased, which would also lead to a reduction of the penetration depth. Finally polymer viscosity above T_G is discussed to decrease the expected indentation depth [57].

2.5.2.3 Force penetration curves on the SU8 film

In this section the results of the nanoindentation measurements on a heated 80 nm thin SU8 films will be presented and discussed in comparison with the measurements on PMMA shown in the previous section. In section 2.3.2 it has been shown that nanoindentation measurements are well comparable and reproducible although not identical tips have been used. The influence of the individual tip shape, wear and contamination has been found to be not detectable.

Figure 2.18 shows single FDCs performed at sample temperatures of 100 °C and 120 °C. Compared with the curves on PMMA (figure 2.12 and 2.13) two fundamental differences stand out: The loading part of the SU8 curves show a straight linear behavior and the elastic recovery during the unloading part on SU8 is much larger than on PMMA.

Whereas the re-flow on PMMA is smaller than 5 nm in all cases it reaches values

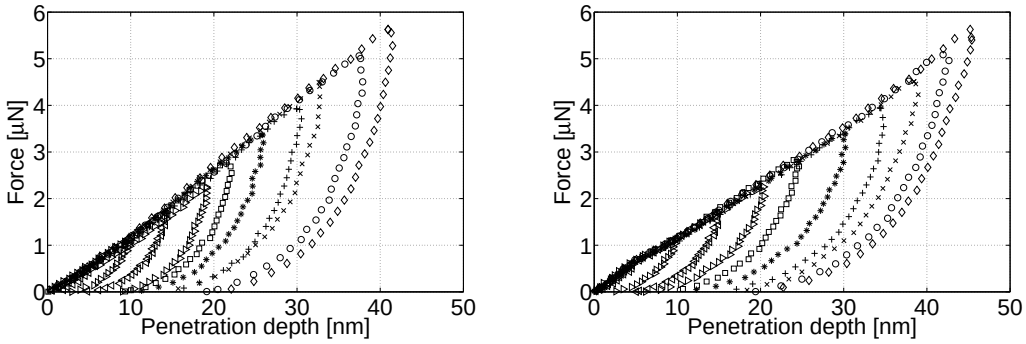

Figure 2.18: Example for FPCs measured on SU8 at a sample temperature of 100 °C (*left*) and 120 °C (*right*).

of more than 20 nm on SU8. Consequently the remanence depth is less than 50 % of the indentation depth at maximum force. Furthermore the remanence depth of the indentations on SU8 is about 50 % smaller than on PMMA when applying the same maximum force at the same temperature.

The large elastic recovery is confirmed by the averaged values shown in figure 2.19. The data are obtained by measuring 10 FPCs and averaging the values of each indentation process (see section 2.5.2.2). It turns out that the maximum indentation depths on PMMA and SU8 are comparable (see figures 2.19 and 2.14) as table 2.1 summarises. From this observation one deduces similar material compliances of PMMA and SU8. The temperature dependence on SU8 is much weaker than on PMMA as one can deduce from figure 2.19: The indentation slope as well as the maximum indentation depths at maximum force differ only slightly, whereas in the case of the PMMA both the shape of the curves as well as the indentation depths changed significantly.

In figure 2.20 the hysteresis energies are plotted as function of the remanence depth. Compared to the PMMA much more energy is needed to create an indentation of the same remanence depth on SU8 . For instance to produce an indentation of 10 nm remanence depth the hysteresis energy accounts for 180 keV whereas on PMMA 25-60 keV are measured (figure 2.16). This reflects the fact that on SU8 higher maximum forces are needed to create an indentation of the same remanence depth. In the example mentioned above for the indentations of 10 nm remanence depth a maximum force of 3.0 μN on SU8 and 0.6-1.5 μN were necessary on PMMA respectively.

2.5.3 Discussion of the nanoindentation experiments

The different indentation behavior can be understood considering the different constitution of the two samples: As discussed in section 2.4 in more detail PMMA

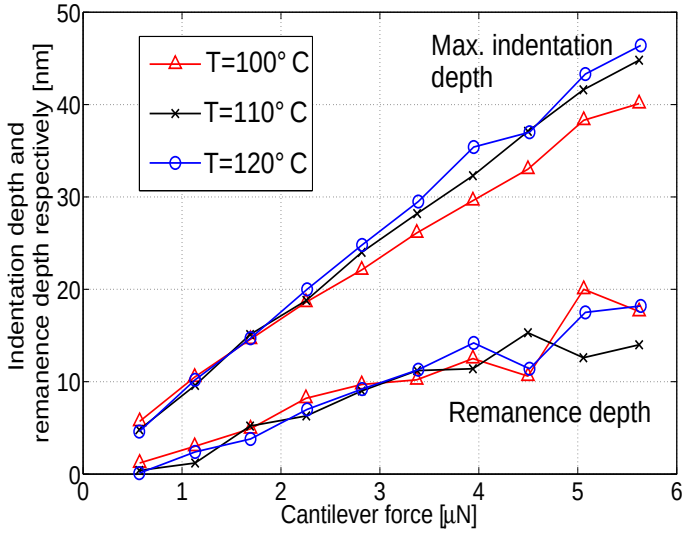

Figure 2.19: Maximum penetration depth and remanence depth as function of cantilever force on SU8.

consists of polymer chains which are physically cross-linked by entanglement. SU8 on the other hand builds up are chemically highly crosslinked network, which can cause the strong re-flow effect: The entire network can be elastically deformed by the tip but the deformation degrades to some extend when the cantilever force is released. Additionally the stress field building up underneath the tip can possibly be smeared out because the polymer segments in the network are better linked together than the chains of the PMMA.

For the interpretation of the FPC one also has to take the different film thicknesses of 35 nm (PMMA) and 80 nm (SU8) into account. The FPCs on PMMA at 130 °C show clearly that the tip penetrates the film and reaches the silicon substrate for cantilever forces higher than 3.5 μN. This is indicated by the vertical part of the FPC and the relatively small gradient just before reaching the substrate, which is presumably originated from the rupture of the polymer film. On SU8 neither a vertical part of the FPC nor the decrease of the indentation slope are observed, because even at the highest maximum forces and resulting indentation depth of

Force [μN]	PMMA [nm]	SU8 [nm]
1.0	8-18	9
2.0	18-25	18
3.0	21-31	24-27
4.0	28-33	30-36

Table 2.1: Comparison of maximum indentation depths on SU8 and PMMA.

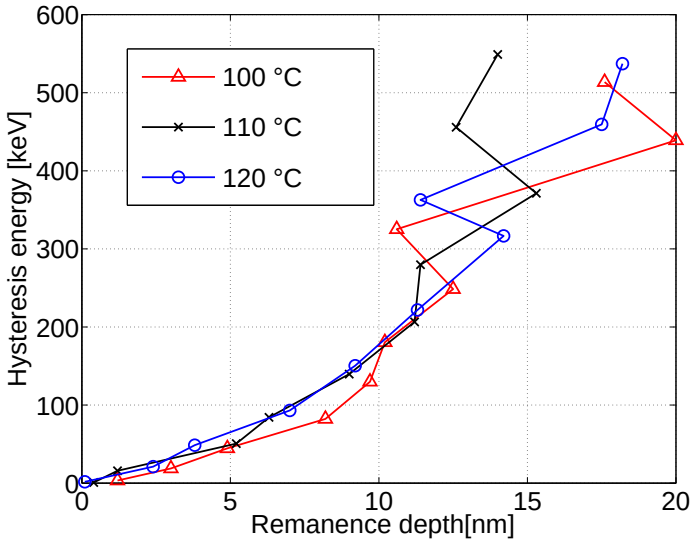

Figure 2.20: Hysteresis energy as function of remanence depth on SU8.

45 nm the tip is approx. 35 nm far away from the substrate. The smaller film thickness of the PMMA film could also lead to an increased confinement effect of the stress field.

The temperature dependence of both polymer films turns out to be significantly different: While PMMA shows a clear temperature dependens of all parameters, the temperature influence for SU8 is found to be much smaller in the investigated temperature range of 100 °C and 130 °C. This was expected because PMMA undergoes the glass transition in this temperature range and the material properties should significantly change. The astonishing observation is that the change of the parameters is much weaker than one would expect from the fact that the Young's modulus drops by 3 orders of magnitude. Viscous flow comes into play above T_G making it possible to displace material and to damp the indentation process. The shape of the FDCs on PMMA (figures 2.12 and 2.13) supports this hypothesis.

2.6 Thermal stability of permanent impressions at elevated sample temperatures

Besides the nanoindentation measurements shown in the previous section the thermal stability of the impressions is of large interest. For a potentially commercial data storage product using thermomechanical write and read mechanisms as discussed in section 1.1.1 the thermal stability of the bits is important for both the long term bit stability and the erasing procedure. On the other hand in poly-

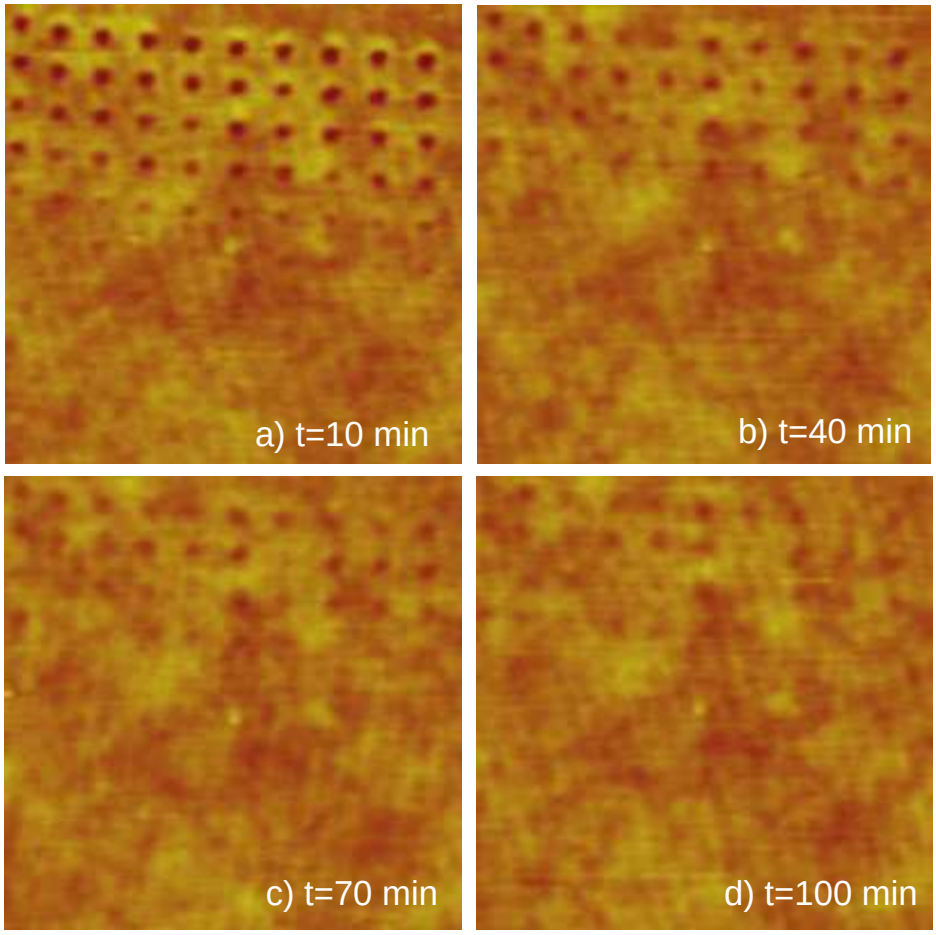

Figure 2.21: Sequence of four Tapping Mode images measured at 120 °C (a) 10 min (b) 40 min (c) 70 min and (d) 100 min after the indentations were created. Image size: 1,8 μm; Height Scale: 10 nm; Sample: 35 nm PMMA on silicon

mer science properties of bulk polymers have been studied for a long time and are known to be determined by mobility of the polymer chains and relaxation processes on the microscopic scale. The question arises if the results of the bulk measurements can also be applied to thin film polymer samples where substrate and interface effects could possibly influence the properties much more than in bulk samples. With the type of experiments shown in this setion both topics are being addressed.

The thermal stability has been investigated by continuously imaging the indentation topography in Tapping Mode after the FDC process. Imaging and indenting have been conducted at the same sample temperature. The topography (especially the depth of the indentations) has been analyzed for the complete set of images making it possible to determining the time evolution of the bit topography. A special software tool for the analysis of the image sequences has been developed and will be described in detail in section 4.4.5.2.

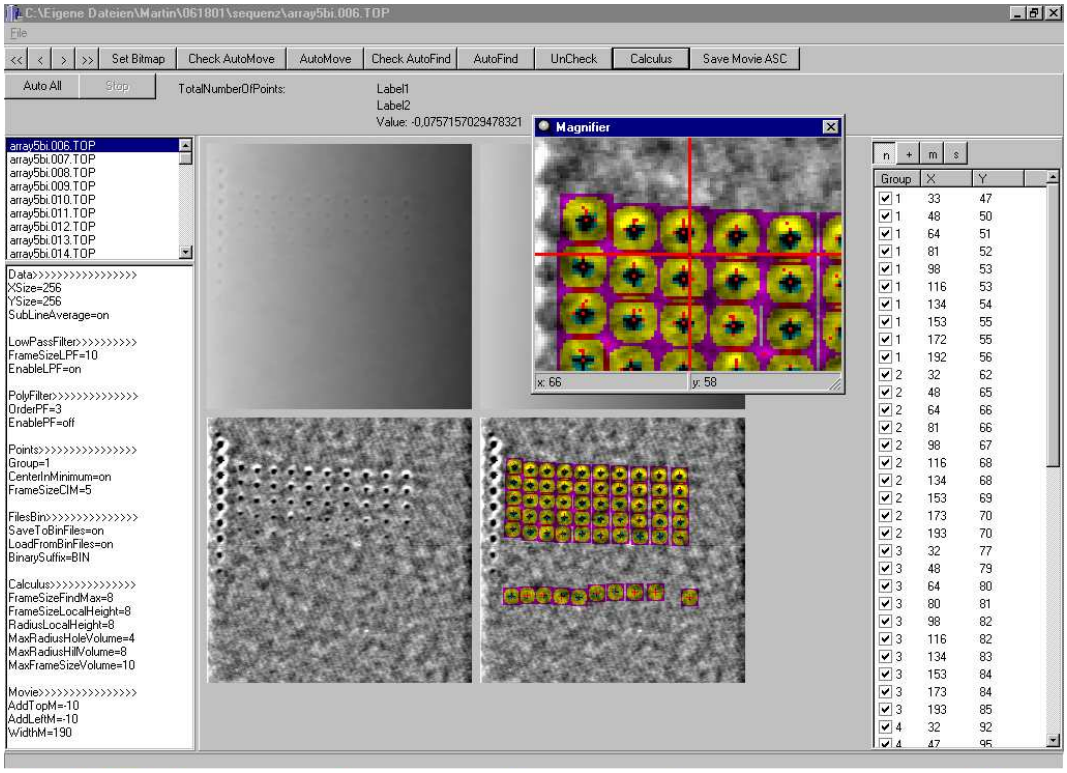

Figure 2.22: User interface of the topography analysis program.

Figure 2.21 shows four selected images scanned at 120 °C 10 min (a) 40 min (b) 70 min (c) and 100 min (d) after the indentations were created with a force distance curve measurement. It is obvious that the indentations are not stable and degenerate at this temperature.

To analyze the indentation topography a program especially designed for the topography analysis has been developed, which enables to measure characteristic quantities of interest, which are typical for the indentation topography, e.g. the indentation depth. The interface of the program is shown in figure 2.22. This program carries out the following image processing steps and determines the quantities of interest in the following way:

- At first the typical tilt of the sample with respect to the piezo tube axis and low-frequency surface variations are removed. This is done by low-pass filtering the image with a mean filter. The mean filter works by averaging n×n pixels around a specific point. This point is shifted pixel by pixel through the image and the averaged data are stored to result in the processed image. The original image is shown in figure 2.22 at the top left, whereas the averaged image is situated at the top right (partially covered

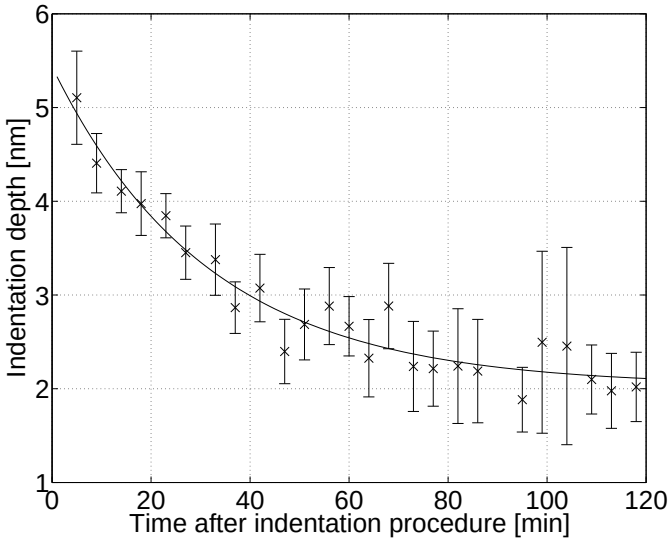

Figure 2.23: Time evolution of indentation depth at 115 °C on 35 nm PMMA on silicon. Shown are the measured data point with standard deviation as error bars and an exponential data fit.

by the "Magnifier" window). Both images are subtracted and the result is shown at the bottom left. The size of the averaging window is chosen by the user and should be significantly larger than the indentation size in order to avoid artefacts of the topography.

- Each indentation of an array has to be identified by a mouse click of the user in the image at the bottom right of figure 2.22. Within a certain window of size m×m defined by the user the minimum is determined and defined as the center of the specific indentation.
- The indentation itself consists of the hole, the rim and a reference area in the surrounding of the indentation defining a local height of the undeformed surface (see "Magnifier" window in figure 2.22).
- The program automatically calculates the following quantities: Deepest point of the indentation (indentation depth), highest point of the rim (rim height), volume of hole and rim, over-all indentation surface.
- The program additionally provides the possibility to automatically analyze a sequence of several images.

The quantitative analysis (figure 2.23) reveals a relaxation process of the indentations. The indentation depths as function of time are plotted. Note, that the indentation depths measured from the Tapping Mode image are smaller than the values obtained from the FPCs due to convolution effects of the tip and the sam-

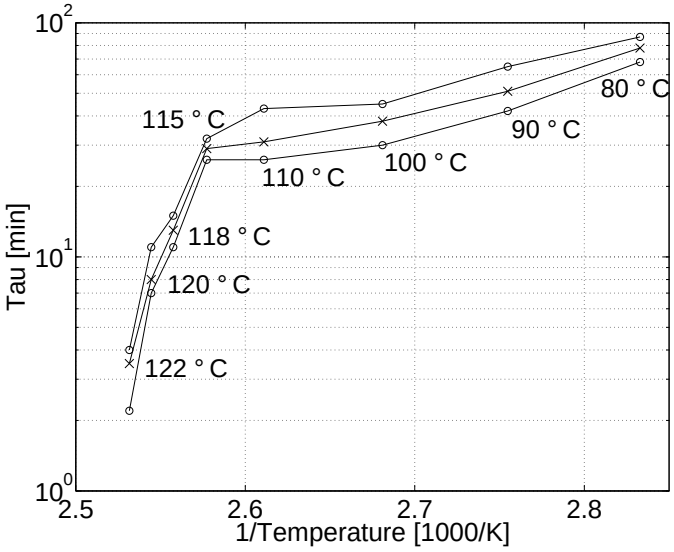

Figure 2.24: Relaxation time constants τ at different temperatures (Symbols $\times$). The kink at 115 °C shows the glass transition. The data plotted with symbols $\circ$ denote the maximum variations for indentations created with different maximum forces. Sample: 35 nm PMMA on silicon.

ple. Nevertheless, the relative change of the depth with time can be quantified. The data are fitted with an exponential decay function:

$$d(t) = d_\circ \cdot e^{-\frac{t}{\tau}} + d_{\text{offset}} \tag{2.6}$$

The fit parameters are the time constant of the relaxation τ, the over-all decrease of the indentation depth $d_\circ$ and the final indentation depth d_{offset} for t $\rightarrow \infty$. The relaxation constant for the 35 nm PMMA film at 115 °C in the example of figure 2.23 has been calculated to be 29 ± 3 min and the relative decrease of the indentation depth $1 - (d_{\text{offset}}/d_\circ)$ was found to be 59%.

To investigate the temperature dependence of the relaxation process the measurements have been performed at various sample temperatures between 80 and 122 °C. Figure 2.24 shows the temperature dependence of the relaxation constant τ. The data plotted with the symbols $\circ$ denote the maximum variations for indentations created with different maximum forces. The kink at 115 °C reveals the glass transition and the mobility of the polymer chains becomes very high, which enable the fast relaxation process. Below T_G the relaxation is also measurable, but the time constants are significantly smaller and only slightly temperature dependent.

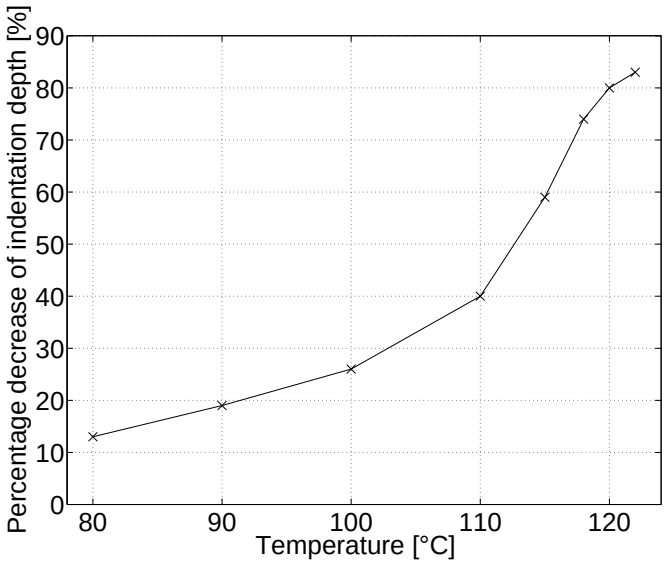

Figure 2.25: Percentage decrease of the indentation depth at different sample temperatures. Sample: 35 nm PMMA on silicon

Assuming Arrhenius-like behavior of the form

$$\tau = \tau_\circ \cdot e^{\frac{E_A}{RT}} \tag{2.7}$$

where T denotes the temperature and $R = N_A \cdot k_B$ the molar gas constant, the activation energy of the relaxation E_A process can be determined. For the temperature range between 80 and 100 °C E_A is 39 kJ/mol and 22 kJ/mol for temperatures between 100 and 115 °C respectively. Literature values for bulk PMMA sample state an activation energy of 67 kJ/mol [58] measured with dielectric and dynamic-mechanical methods and 440 kJ/mol measured with by the recovery of impressions created with a nanoindenter [59]. This suggests a larger mobility in the film sample than in the bulk PMMA.

The relative loss of indentation depth $1 - (d_{\text{offset}}/d_\circ)$ is plotted in figure 2.25 as function of the sample temperature: Additionally to the faster relaxation the indentations are less stable: At 122 °C for instance the indentation depth decreases by 83 %.

2.7 Chapter summary

In this chapter the thermomechanical properties of a 35 nm thin PMMA film in comparison with a 80 nm SU8 epoxy photo resist both on a silicon substrate were

investigated with force distance curve measurements using a commercial microscope (D3100 from Veeco) and conventional Tapping Mode SFM cantilever tips. The indentation experiments were performed at elevated sample temperatures between 100 and 130 °C using a heating stage. The maximum forces were in the range of up to 4 μN leading to permanent impressions in the polymer films of lateral diameters between 100 and 300 nm.

From the force penetration curves, which were calculated by combining force distance curves and a calibration measurement on silicon (calibration force curve, CFC) characteristic quantities like the indentation depth, remanence depth, hysteresis energy and penetration slope among others were analyzed as function of the sample temperature and of the applied force. Whereas PMMA undergoes the glass transition in this specific temperature range and all quantities are clearly temperature dependent, the temperature dependence on the SU8 sample is significantly smaller. Nevertheless, the observed temperature dependence on PMMA is smaller than expected from the change of the mechanical properties in the glass transition.

The thermal stability of the permanent indentations created on PMMA with the force distance curve measurements was investigated by continuously scanning of the indentations in Tapping Mode and anaylsis of the indentation depth. A clear temperature dependent relaxation process was identified, which clearly shows the glass transition of the polymer between 115 and 118 °C.

Chapter 3

Heatable SFM cantilevers

3.1 Introduction

Whereas the first SFM cantilevers were manmade [2] nowadays they are commercially available with a large variety of different mechanical and geometric properties: The cantilever's spring constants range from 0.01 N/m up to 100 N/m and resonance frequencies between 10 kHz and 1 MHz. The tip is typically made out of silicon or silicon nitride with a radius between 10 and 20 nm, but sharp and ultra-sharp tips are on the market with high aspect ratios ("nano-whiskers") and tip radii in the order of 1 nm. Addionally, special wear resistive tips are available, which consist of diamond or are diamond-coated and are used for the application in indentation experiments on hard sample such as metals.

Dependent on the measuring mode the appropriate cantilever is chosen: Weak cantilevers with a spring constant of less than 0.5 N/m are used for Contact Mode measurements, whereas in for Pulsed-Force Mode the spring constant used ranges between 1 and 40 N/m depending of the stiffness of the surface. For Tapping Mode measurements hard cantilevers with spring constants of 40 N/m are usually used. If electrical or magnetic sample properties are of interest, electrical conductive and magnetic cantilevers respectively are used in electrical force microscopy (EFM), Kelvin probe microscopy or magnetic force microscopy (MFM).

Although a large variety of different cantilever / tips is commercially available there are numerous applications of SFM techniques, where the appropriate cantilever is purpose-designed. E.g. for SFM high-speed imaging special cantilevers of high resonance frequency and low spring constant have been designed and fabricated, which are not commercially purchasable.

In the field of thermal analysis of small structures probes have been manufactured with the capability to measure thermal properties of the sample [60]. Different

kinds of thermal probes have been designed using various techniques. The so-called Wollaston probes consist of a V-shaped platinum/10 % rhodium wire of 5 μm diameter and can be used as a resistive heater (active mode) and as thermometer (passive mode) by passing a small electrical current through the probe. These devices were hand-crafted in the beginning, but in the meantime there is also a high-resolution micromachined version [60].
High resolution scanning thermal probes with a filament length of 2-5 μm and a wire diameter of 30-100 nm have been also produced by the use of focused electron beam deposition [61]. Furthermore, micromachined batchfabricated thermal probes with a thermocouple at the tip end have been successfully fabricated and are used e.g. to measure thermal properties of carbon nano-tubes [62].

As discussed in chapter 1.1.1 the most important part of the "Millipede" are heatable SFM cantilevers, which act as a read/write head for data storage and read-out and are equipped with a heating element. In contrast to the "Millipede", where several thousand cantilever/tips are operated simultaneously in a single device, in this study individual cantilevers have been used, which were mounted a chip body. Nevertheless, the operating principle is exactly identical and the fundamental properties like bit writing performance and heat transfer can be studied with the single cantilevers. In this section the design and functionality as well as the electrical and thermal properties of these probes fabricated at the IBM Zurich Research Laboratory are discussed.

3.2 Design and functionality of the heatable SFM cantilevers

The heatable cantilevers discussed in this section are produced with lithographic means and consist of silicon [10, 11]. Two different types of heatable cantilever were used in this study, which are shown in the Scanning Electron Microscope (SEM) images of figure 3.1: a simple design consisting of two legs (so-called 2-leg cantilever SL1 type) [10] and one heater platform and a more sophisticated design with three legs [11], two heaters and an electro-static platform.

Let's first focus on the 2-leg SL1 cantilever: The heater region is artificially marked in the image and is located at the end of the two cantilever beams. It consists of a low-doped region of $4\times6\,\mu\mathrm{m}^2$. The tip is located on top of the heater platform. The heating capability originates from the fact that the heater platform is lower phosphorous-doped ($5\times10^{17}\,\mathrm{cm}^{-3}$) than the highly doped ($10^{20}\,\mathrm{cm}^{-3}$) silicon beams. By passing an electrical current ($<1\mathrm{mA}$) through the heating platform it is heated up to several hundred degrees Celsius. In this simple design the heat platform is used for the bit writing and reading.

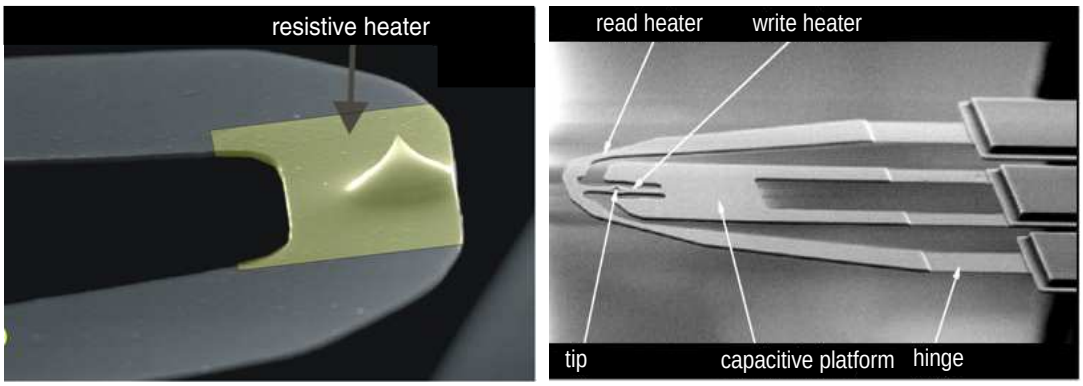

Figure 3.1: The two different types of heatable cantilevers used in this study: *Left:* Simple design consisting of one heater platform and two legs (so-called 2-leg cantilever); *Right:* More sophisticated design with three legs, two heaters and an electro-static platform.

The more sophisticated so-called 3-leg cantilevers of 3LD type (figure 3.1, *right*) have two heater platforms: one for the bit writing and one for the bit reading operation. This is because of the fact that the read procedure relies on the strong distance dependent heat transfer through the heater-sample gap. During the write operation on the other hand the tip should be heated as efficiently as possible to heat the polymer locally best possible. Thus, the write heater is placed close to the tip and the read heater is located aside in the outer cantilever beam. Additionally, an electrostatic platform is included, which makes in possible to apply a bias between cantilever and sample resulting in an electrostatic force. This force supports the writing process and reduces the heater temperatures necessary for bit writing (see chapter 4). The platform has also been used in the experiments presented in chapter 4 to adjust a laser beam of the optical detection system. Thus, it was possible to use the 3LD cantilevers in a commercial SFM (Dimension 3100 from Veeco) and established measurement techniques like Contact Mode imaging, force distance curves measurements and resonance frequency sweep could be performed in this way (see chapter 4).

The beams of the 3-leg 3LD cantilever are 66 μm long and 500 nm thick. The thickness of the beams near the chip is reduced so that a hinge is formed with a thickness of 250 nm (see figure 3.1). The cantilever spring constant has been calculated to be 0.15 N/m with finite element methods [63] and the resonance frequency has determined to be 70 kHz with an resonance experiment using an Tapping Mode SFM (see chapter 4). The write heater is $2\times4.5\,\mu m^2$ (width$\times$length) and the read heater is $2\times4\,\mu m^2$ respectively. The tip has a conical shape and is 500-700 nm high. Thus, the heater is about 500-700 nm away from the sample surface when the tip is in contact with the sample. A scanning electron microscopy image of a tip is shown in figure 3.2.

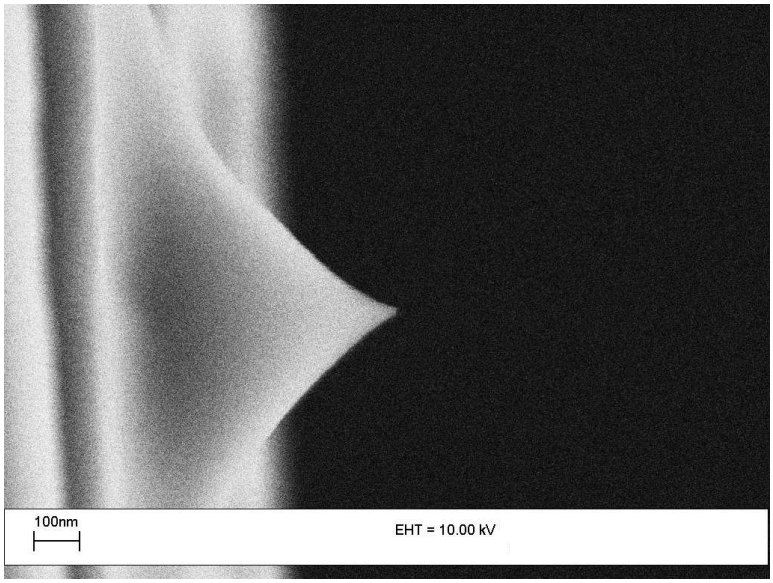

Figure 3.2: Scanning electron microscope (SEM) image of a tip

The 2-leg SL1 type cantilever are 50 μm long and 200-250 nm thick resulting in a spring constant of 0.05..0.1 N/m. The spring constant of cantilevers from every wafer are determined by measuring the thickness of the cantilever with the Scanning Electron Microscope and calculating the spring constant with finite element methods. The tip is conically shaped and $\approx$500 nm high (as the 3LD tips). The heater has a size of $4\times6\,\mu m^2$ and table 3.1 summarises the properties of both types of cantilever / tip.

	3LD (3-leg)	SL1 (2-leg)
Length [μm]	66	50
Thickness [nm]	500	200-250
Spring constant [N/m]	0.15	0.05..0.1
Resonance frequency [kHz]	$\approx$70	not measured
Tip height [nm]	500-700 (conical)	$\approx$500 (conical)
Tip radius [nm]	5-10 (typical value)	5-10 (typical value)
Number of heaters	2	1
Size of heaters [μm^2]	2×4.5 (writer) 2×4 (reader)	6×4
Doping concentration of heater [cm^{-3}]	5×10^{17} (writer) phosphorous 5×10^{17}(reader) phosphorous	5×10^{17} phosphorous
Doping concentration of beams [cm^{-3}]	10^{20} phosphorous	10^{20} phosphorous

Table 3.1: Summary of the properties of the 3LD and SL1 type cantilever / tip

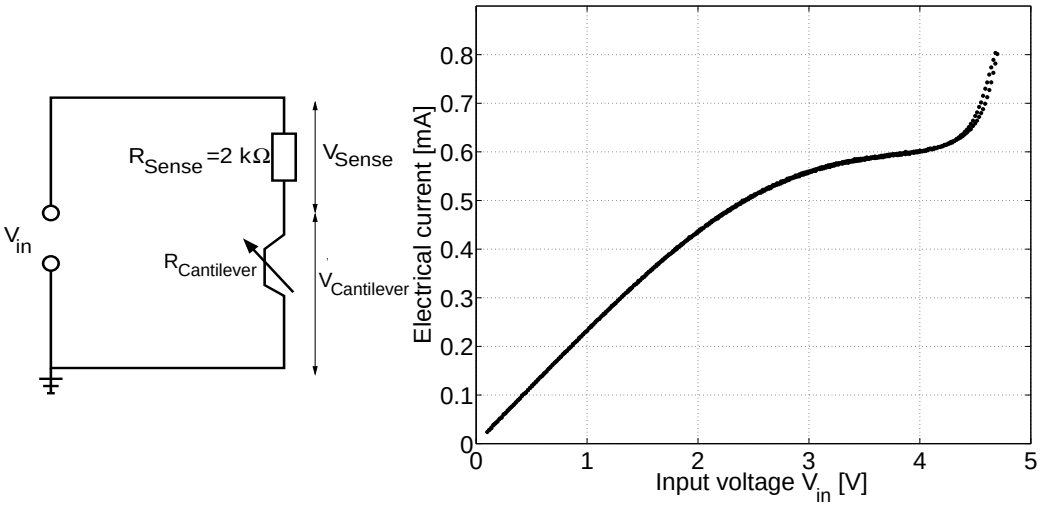

Figure 3.3: Electrical circuit (*left*) for measuring the cantilever IV characteristics (*right*).

3.3 Electrical characteristics and temperature calibration of the heatable cantilevers

For the interpretation and the data analysis of experiments performed with the heatable cantilevers it is essential to determine the heater temperature. This can be done by making use of the strong temperature dependence of the electrical resistance of the heater. Thus, an IV measurement using an electrical circuit sketched in figure 3.3 with the tip being far away from the sample surface is performed for each individual cantilever. A 2 kΩ resistor in series with the cantilever is used to measure the voltages V_{Sense} and $V_{\mathrm{Cantilever}}$ respectively. Thus, the electrical current I running through the heater platform is given by $I = (V_{\mathrm{in}} - V_{\mathrm{Cantilever}})/2\,k\Omega$. The electrical current as function of the input voltage $\mathrm{V_{in}}$ is plotted in figure 3.3. For input voltages higher than 4.3 V a strong increase of the current is observed, which means that the resistance of the cantilever decreases significantly. For the doping level used, the resistance is known to have a maximum at 550 °C [64]. Thus, it is possible to calibrate the heater temperature: Assuming that the heater temperature is proportional to the power, the heater temperature T_{Heater} is given by

$$T_{\mathrm{Heater}} = \mathrm{RT} + \frac{P \cdot (550\,^{\circ}\mathrm{C} - \mathrm{RT})}{P_{\mathrm{Rmax}}} \tag{3.1}$$

where RT is the room temperature and P_{Rmax} is the heater power at the maximum resistance. A resulting heater temperature versus resistance curve is shown in

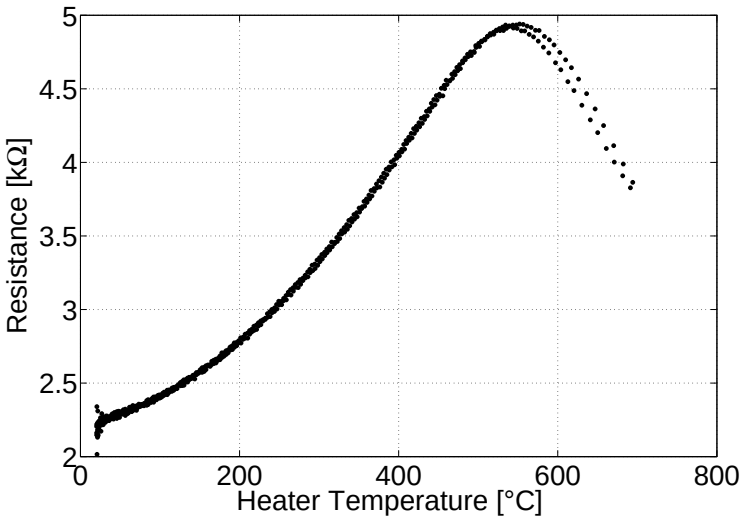

Figure 3.4: Typical temperature dependence of the heater resistance.

figure 3.4. Although many cantilevers are batch microfabricated on one wafer, the dimensions of the cantilevers beam (especially the thickness) and the doping concentration can vary resulting in slightly different IV characteristics. Thus, an IV curve has to be measured for each cantilever and its resistance-temperature curve has to be derived.

It is important to note, that the IV characteristics change with different cooling mechanisms of the cantilever, e.g. with the tip in contact with the sample or under vacuum conditions: With the tip in contact with the sample the cooling through the small air gap between heater and sample and through the tip-sample contact reduces the heater temperature, which in turn leads to a changed electrical resistance of the heater. Consequently the electrical current will change as well. This effect, however, can be used to investigate the cooling mechanisms in detail: Since the electrical resistance versus temperature curve remains unchanged and is a characteristic function of each cantilever, it is possible to measure the heater temperature as e.g. it approaches the sample surface and is cooled through the air.

In order to determine the heater temperature, the input voltage and the cantilever voltage are measured, which enables one to calculated the electrical resistance of the heater. The heater temperature can then be deduced from the R-T curve obtained with the above mentioned calibration process. This procedure has been used in the bit writing experiments (chapter 4) and the vacuum experiments (chapter 5) . With the method the absolute error in the temperature determination of the heater of about $\approx 30\,\%$ for a temperature difference $\Delta T = T_{\mathrm{Heater}} - \mathrm{RT}$ is estimated, but relative measurements can be conducted with a resolution of 0.1 K.

Both in figure 3.3 and figure 3.4 for high values of the input voltage and the heater temperature the curve splits up into two branches. The origin of this kind of hysteresis effect is, that the data are measured while first ramping up the input voltage to a certain maximum (in this case up to 4.7 V) and then decreasing the voltage again. Obviously the data while ramping up and down split up for input voltages larger than 4.5 V and heater temperatures larger than 550 °C respectively, while both branches match very well below these values. It is observed, that this hysteresis effect is especially large for new unused cantilevers, when the IV curve measurement is conducted for the first time and becomes smaller after several heating cycles. An explanation for this behavior is, that annealing effects occur within the heater. Especially the implanted phosphorous atoms become mobile and can diffuse at high temperatures.

3.4 Chapter summary

In this chapter the design and functionality of heatable SFM cantilevers manufactured with lithographic methods at the IBM Zurich Research Laboratory and used for measurements presented in chapter 4 and 5 has been discussed. These silicon probes are similar to conventional V-shaped SFM cantilevers with a sharp tip of about 10 nm radius situated at the end of the cantilever beams. However, additionally depending on the design one or two resistive heater are integrated in the cantilever beam, which are lower doped than the rest of the beams and thus heat up when an electrical current runs through the heater. The heater typically produces an electrical power of 1-2 mW and reaches at heater temperature of up to 800-1000 °C. For the experiments presented in this study, however, typical heater temperatures of 200-400 °C for indentation experiments and of about 600 °C at most for the thermal imaging under vacuum conditions (see section 5.6) were used. Two different cantilever designs were applied in this study: A simple design with a single heater and a more sophisticated design with two heaters (one for data writing and one for reading). For the doping concentrations used the heater has its maximum electrical resistance at 550 °C, which is used to calibrate the heater temperature. To deduce the heater power and the temperature a 2 kΩ pre-resistor in series with the cantilever was used, which enabled to measure the electrical current and the resistance of the heater.

Chapter 4

High frequency nanoindentation of thin polymer films with pulse-heated SFM tips at elevated sample temperatures

4.1 Introduction

Whereas the indentation experiments with force-distance curves presented in chapter 2 were performed on a timescale of 1 second, bit writing in the "Millipede" is typically conducted on the micro-second scale. This short pulse duration is required for a product-relevant performance of the "Millipede" in order to achieve acceptable reading and writing times of the system and obviously the aim it to obtain shorter pulses to reach even higher data rates of the device. Thus, the thermomechanical properties of the polymer storage medium is of large interest on a time scale of micro-seconds. However, mechanical properties of thin polymer films on the nanoscale have been investigated only at low frequencies (see chapter 2) and high-speed indentation experiments have rarely been preformed [65]. Although pulsed-force mode measurements [30–34] are typically performed at higher frequencies of typically 1-2 kHz, the interaction forces are too small to create permanent deformations of the sample surface. Additionally, the transfer of results obtained with force-distance curves of 1 Hz to indentation experiments on the micro-second scale is difficult, because bulk mechanical properties of polymers are known to be strongly frequency dependent.

Different "Millipede" related studies have addressed the writing mechanism and the polymer medium at high indentation speeds using the heatable cantilevers [15,27,66,67], but all measurements have been conducted at ambient sample con-

ditions. However, the influence of the sample temperature is manifold: The mechanical properties of the polymer is changed and the stability of the indentations is reduced (see chapter 2) at elevated sample temperatures. The heat transfer between heater and sample is reduced due to the smaller temperature difference. Furthermore, the performance of the heatable cantilevers at elevated temperatures is supposed to deviate from ambient temperatures because of the reduced cooling effect of the surrounding air. Thus, in this chapter high-frequency nanoindentation experiments at elevated sample temperatures will presented, which shall address these questions.

4.2 Experimental setup

The measurements discussed in this chapter have been carried out with heatable cantilevers implemented in a commercial SFM (Dimension 3000 with Nanoscope IIIa Controller from Veeco). Additionally, the heating stage (Imaging Corp. and a controller from LakeShore, Model 330) used for the force-distance curves in chapter 2 has been used to conduct the experiments at elevated sample temperatures. There are multiple advantages of this approach:

- High-speed nanoindentation experiments could be conducted, while maintaining the convenient, user-friendly imaging and force-distance curve capability as well as the analysis software of a commercial SFM.
- The optical cantilever deflection system could be used for imaging in contact mode and for the measurement of force-distance-curves. During the imaging procedure the cantilever remained unheated and the usual contact mode imaging was performed using the laser signal. This imaging mode has been used for the analysis of the written indentations in section 4.4.4. An additional possibility is to generate a thermal image simultaneously during the contact mode imaging: For this purpose the cantilever was heated and the change of the cantilever voltage according to the sample topography is recorded during scanning. The latter procedure will be presented in section 4.3 in detail in oder to demonstrate the imaging capability of the heatable cantilevers.
- The indentation procedure was realized using the programming tool 'NanoScript' included in the microscope software, which is a script language with syntax similar to the programming language C and made it possible to move the tip in a controlled way to a desired location and set voltages as well as triggers.
- A so-called signal access module (SAM) delivered with the microscope provides access to signals like cantilever deflection, friction signal and piezo

voltages. Additionally voltages and triggers can be set with the nanoscript and can be accessed on special output channels of the SAM.

- Image and force-distance curve analysis tools worked out for the experiments in chapter 2 can be used for these experiments as well.
- The experience for the usage of the heating stage obtained during the indentation experiments of chapter 2 was very helpful. As it has already been stated in chapter 2 the piezo calibration is not affected by elevated sample temperatures and the temperature difference between heating platform and sample has been measured to be 2 °C at most.

In this section the adaption of the heatable cantilever tips to the microscope will be described and the imaging capability of these devices will be presented in the next section 4.3. The setup for the pulse-heated nanoindentation experiments will then be pointed out in section 4.4.1.

4.2.1 Adaption of the heatable cantilevers to the D3000 SFM

In contrast to the nanoindentation measurements of chapter 2, where commercial Tapping Mode tips have been used, now the heatable cantilevers discussed in chapter 3 are applied. It turned out, that it is not possible to use optical cantilever deflection detection system of the microscope with the SL1 type cantilevers, because not enough laser light is reflected from the relatively small cantilever back onto the position sensitive detector (PSD). The capacitive platform of the 3LD type cantilevers (see figure 3.1), however, is large enough to reflect back enough light for the use of the optical detection system. Thus, 3LD type cantilevers have been used for all measurements throughout this section. Although these cantilevers have two heaters (one for thermomechanical reading and one for writing) only the write heater located close to the tip has been used in these experiments, whereas the other heater has not been contacted.

In the D3000 SFM the tip is mounted on a special designed tip holder, which is attached to the tube piezo. Since the chip body of the heatable cantilevers is wider than the chip of commercial cantilevers and additional electrical connections for the heater are necessary for the operation, the tip holder of the microscope had to be reconstructed to fit the heatable cantilevers into the microscope. Figure 4.1 shows the reconstructed tip holder for the use of the heatable 3LD cantilevers on the left and the original tip holder used with commercial cantilevers in comparison. Special attention had to be paid, that the tip holder modifications did not exceed the height level of the tip in order to make sure, that actually the tip touches the sample surface and not parts of the modified tip holder like the connector clamps or the screws.

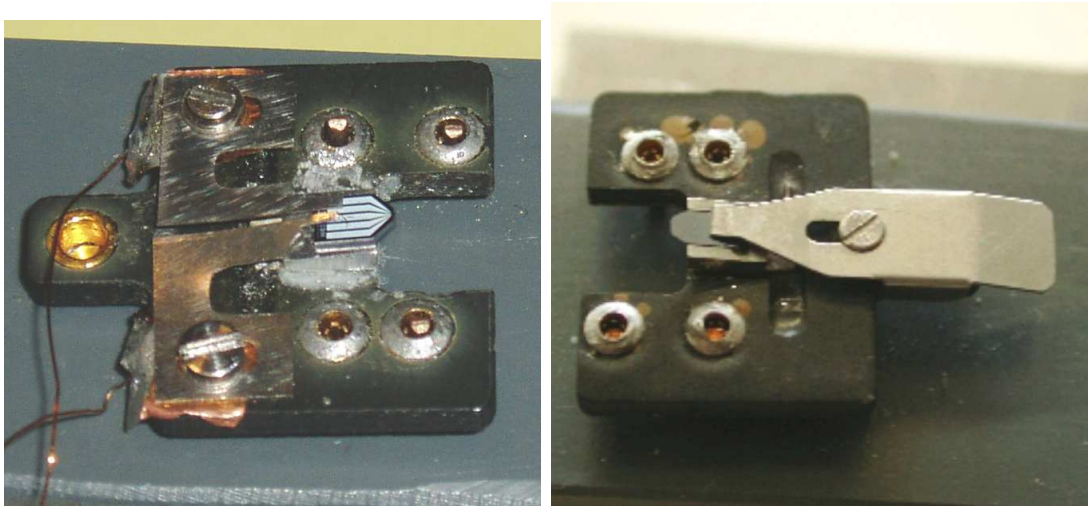

Figure 4.1: *Left:* Reconstructed tip holder for the use of the heatable 3LD cantilevers. *Right:* Original tip holder for the use of commercial cantilevers.

The size of the chip and the cantilever caused a second challenge while implementing the heatable cantilevers as figure 4.2 shows: Compared to commercial cantilevers the chip of the heatable cantilevers is rather thick and at the same time the cantilever is shorter than typical commercial cantilevers. Additionally, the original cantilever holder of the microscope is designed in such a way, that the cantilever is tilted about 13° with respect to the sample surface. If the heatable cantilevers had been used with this tilting angle, the laser beam would have pointed onto the edge of the cantilever chip and could not reach the cantilever itself. Thus, the tilting angle of the cantilever chip had to be changed and it was found, that the laser can be adjusted onto the cantilever and the beam is reflected onto the position sensitive detector with an tilt angle of 7°.

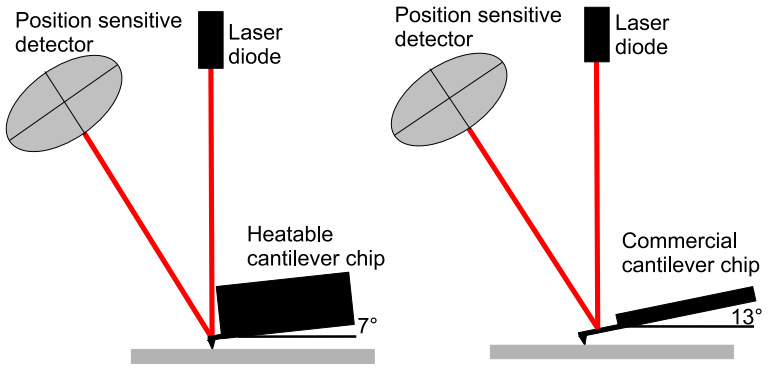

Figure 4.2: Schematic drawing of the optical beam path using the heatable cantilever chip (*left*) and a commercial cantilever chip (*right*).

4.3 Topography imaging with heated cantilever tips under ambient conditions

The modifications discussed in the previous section enable to use the heatable cantilever for thermomechanical sensing similar to the read procedure of the "Millipede" as discussed in chapter 1.1.1. In this section topography imaging using the thermal signal of the heatable cantilevers will be demonstrated.

In our case contact mode imaging using the deflection signal of the position sensitive detector for the feedback is conducted. Simultaneously, the cantilever is heated with a constant voltage applied to the circuit shown in figure 3.3. As the tip moves over the sample, the distance between heater and sample changes, which causes different heater temperatures. This in turn leads to a variation of the cantilever's electrical resistance and consequently to a variation of the electrical current and of the cantilever voltage. Thus, a thermal image can be generated from cantilever voltage data, which are recorded during scanning.

An example demonstrating the imaging capability using the thermal signal is shown in figure 4.3. A polymer blend of PMMA and SBS (Styrene-Butadiene-Styrene) is used as a sample, which forms a 2-phase structure as observed in the conventional Tapping Mode images at the top. These structures are well reproduced in the topography image of the contact mode scan on the bottom left using the optical detection signal for the feedback loop. The image at the bottom right is the simultaneously recorded thermal image generated from the cantilever voltages and obviously represents the sample topography. In section 5.6 experiments will be presented, where thermal properties of different materials are investigated, but in this experiment the imaging contrast results primarily from topography effects.

In the following sections of this chapter nanoindentation experiments will be discussed and the imaging will be done in contact mode with the tip not heated using the optical signal for the feedback, whereas the cantilever will be heated only during the indentation process.

4.4 Nanoindentations with a pulse-heated tip and electro-static force

In the last sections the adaption of the heatable cantilevers to the commercial SFM and the thermal imaging capability have been shown. Now, we will focus on the nanoindentation experiments with pulsed-heated tip and electro-static force. The interplay between the microscope's scan unit and the external pulse electron-

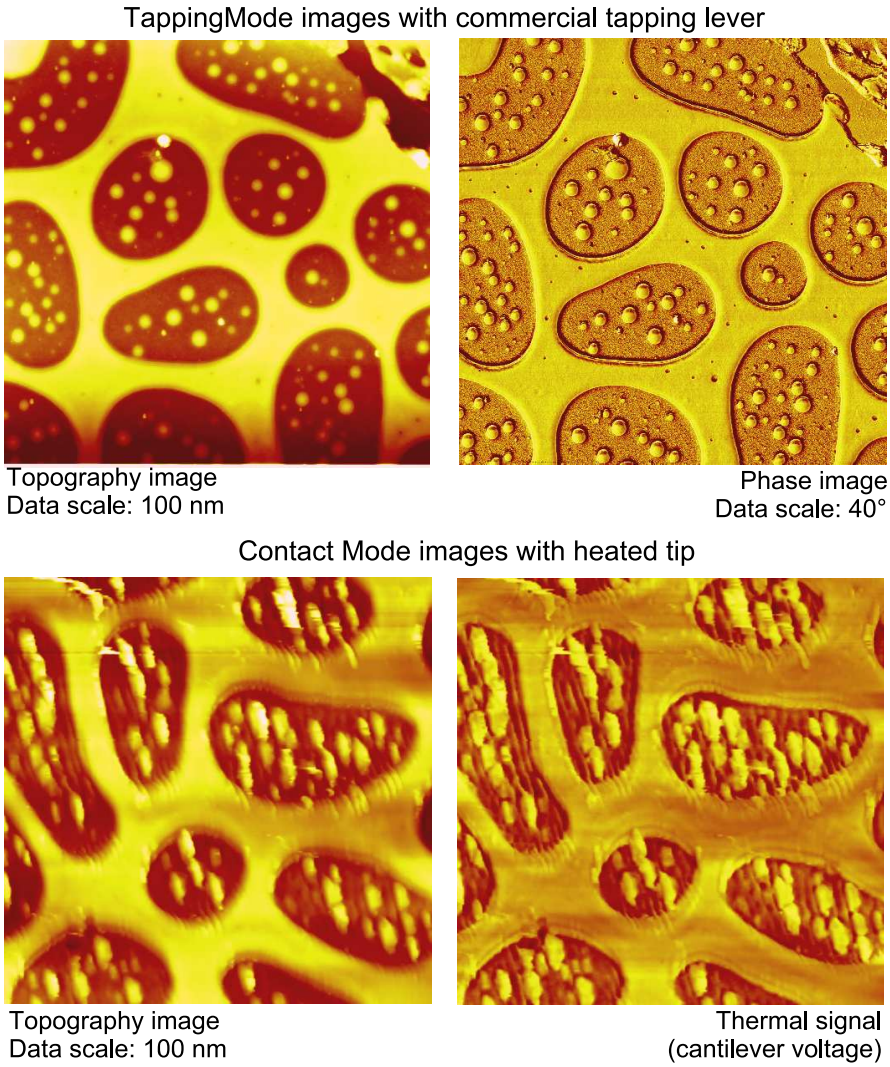

Figure 4.3: *Top:* Tapping Mode images of the SBS-PMMA sample. *Bottom:* Topography (left) and thermal image (*right*) measured in contact mode using the heatable cantilevers and the optical signal for the feedback loop. Size of all images: 15 μm.

ics for the indentation procedure was a special issue and will be discussed detailed in section 4.4.1. Additionally, a procedure for calibrating the electro-static force will be described in section 4.4.3. Nevertheless, the main attention will be paid to the experimental results: The measurements have been conducted on the two sample systems 35 nm PMMA on silicon and 80 nm SU8 on silicon, which have already been investigated with the force-distance curve based nanoindentations in chapter 2. Both sample have been measured at elevated sample temperature up to 120 °C (SU8) and 130 °C (PMMA).

4.4.1 Experimental implementation

In this section the experimental implementation of the indentation procedure and the measurement techniques will be shown. The basic principle of the high-speed indentation process is to bring the cantilever heater to a certain temperature and simultaneously apply an electrostatic potential to the sample. If the electrical potential of the cantilever $V_{\text{Cantilever}}$ and the sample V_{Sample} are different, an electro-static force acting between the cantilever and the sample will attract the cantilever towards the sample. This electro-static force will be proportional to the square of the voltage difference between heater and sample:

$$F_{\text{electro-static}} \propto |V_{\text{Sample}} - V_{\text{Cantilever}}|^2 \tag{4.1}$$

When bringing the heater to an elevated temperature the polymer material underneath the tip will be heated up as well and becomes softer. In combination with the electrostatic force the tip deforms the surface. If the extend of force in combination with heat is sufficient, the tip creates a permanent impression in the polymer. This procedure requires much shorter times for the indentation process than the indentation process using force-distance curves (chapter 2): Whereas the indentation process with force-distance curves is conducted with 1 Hz meaning, that the complete indentation cycle takes 1 second, the indentation experiments using the abovementioned procedure with the electro-static force pulses and the pulse-heated cantilever tip have all been conducted with a pulse duration of 10 μs.

Similar to the array of the indentations in figure 2.10 two dimensional grids of indentations have been created to study the effect of different combinations of heater temperature and electro-static force: The heater temperature has been varied along one axis by changing the input voltage of the cantilever circuit and the electro-static force has been varied along the other axis by changing the sample voltage. Thus, the effect of both parameters can be studied independently and the threshold of creating permanent indentations can be identified.

The indentation procedure has been implemented by making use of the 'Nanoscript' function built-in the standard software of the D3000 SFM. This tool is a script language with syntax similar to the programming language C and enables to controll the microscope directly. The following examples shall illustrate the possibilities given with this tool:

- The tip can be moved to the center of the scan field using the Nanoscript command `LithoCenterXY()`.
- The scan procedure for imaging can be stopped with the command `LithoScan(FALSE)` and started with `LithoScan(TRUE)`.
- Relative movement of the tip in x-direction by `dx` and in y-direction by `dy` at a speed of `rate` is conducted with the command `LithoTranslate(dx,dy,`

`rate)`. During the movement the SFM feedback can be switched off with the command `LithoFeedback(FALSE)` and switched on with `LithoFeedback(TRUE)`.

- To set voltages on different output channels of the SAM (Signal Access Module of the microscope) the command `LithoSet(channel,voltage)` is used, where `channel` represents the output channel and `voltage` the voltage to be set. However, it turned out that the voltages measured on the output channel deviate from the programmed voltages. Thus, the difference had to be corrected using a compensation function and additionally all relevant voltages have been stored using the oscilloscope, which enabled to save measurement data on an internal hard disk drive.

- A trigger for initiating the writing pulse and the data sampling with an oscilloscope is set with `LithoTrigger(line)`, where `line` denotes the output line used for the trigger.

- Pulses with a length `time` and pulse height `voltage` can be created with the command `LithoPulse(channel,voltage,time)`. However, it turned out that it was not possible to create pulses of 10 μs length with the command, because the SAM outputs are not sufficiently fast.

Thus, another method the pulses creation has been used: Figure 4.4 shows the electronic circuit used for the indentation process and figure 4.5 shows a flow chart of the pulse and array generation. The pulses are generated by setting the desired DC voltage on the SAM outputs and triggering a function generator (DS 345, Standford Research) to produce the TTL signal, which makes the analog switches to connects through the DC voltages to the cantilever and the sample respectively for the time of the TTL pulse duration. Thus, the pulse-height is determined by the DC voltages set by the nanoscript program, while the pulse duration is given by the TTL pulse length of the function generator. Hence, the pulse height can easily be set by the nanoscript language tool and consequently the electro-static forces and the heater temperatures can be varied with the nanoscript program.

The amplifiers for the cantilever voltages and the sample voltages have been inserted, because the output voltages of the SAM turned out to be not large enough in order to create the required pulse heights. Three signals have been measured with the oscilloscope (Wave Runner LT 350 by LeCroy): The input voltage V_{in} of the cantilever circuit (Analog DC out 2), the cantilever voltage $V_{\text{Cantilever}}$ and the voltage applied to the sample V_{Sample} (Analog DC out 1). The oscilloscope provided the possibility to save the data of all channels simultaneously on an internal hard disk drive. These data could be downloaded to an external computer via fire-wire interface. Thus, the data of each pulse have been save and could be used for the subsequent data analysis. Especially the heater temperature during each pulse could be calculated by taking the heater resistance versus temperature

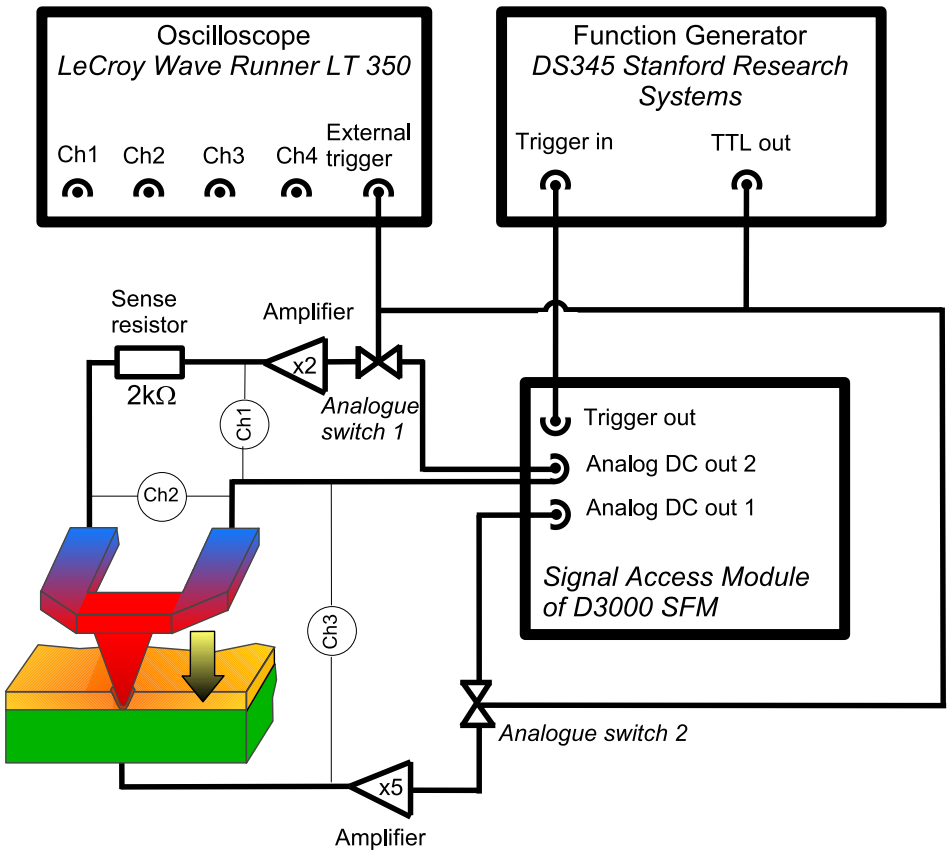

Figure 4.4: Cabling of the different components used for the nanoindentation experiments with pulse heated cantilever and electrostatic force. For clarity, the connections to the oscilloscope are omitted, but are marked in the sketch with circles and the labeling "Chx", where x denotes the channel on he oscilloscope.

curve obtained from an IV measurement into account (see section 4.4.2) and the electro-static force could be calculated with a calibration measurement, which is discussed in section 4.4.3.

An example for an indentation pulse is shown in figure 4.6. Both the input voltage of the cantilever circuit and the electro-static voltage is nearly constant during the pulse duration except for the over-shoot effect at the beginning of the pulses. On the other hand the cantilever voltage exhibits a clear dependence on time showing, that the heater temperature increases incessantly during the pulse time. One observes, that for small input voltages (and consequently relative low heater temperatures) the heater reaches a constant level during the pulse duration and comes in thermal equilibrium, whereas this is not the case any more for large input voltages (and consequently high heater temperatures). The performance of the cantilever during the pulsed indentation and the heater temperature determination will be discussed in detail in the next section.

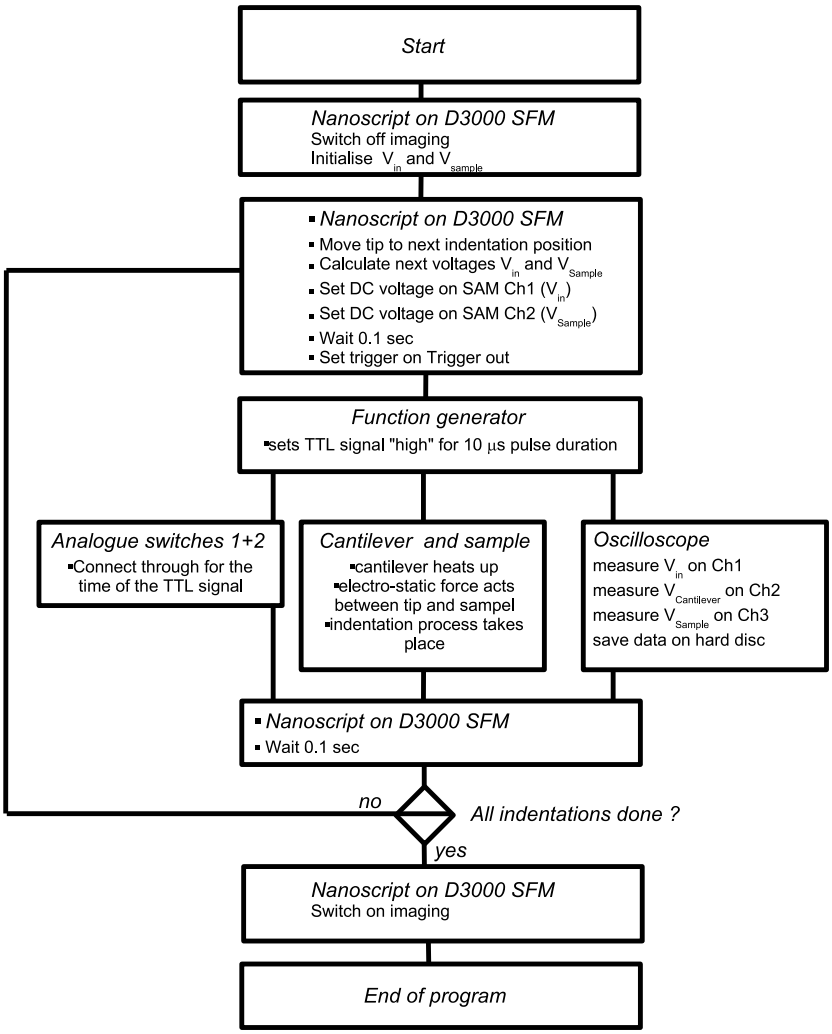

Figure 4.5: Flow chart of the indentation procedure. The input voltage of the cantilever circuit V_{in}, the cantilever voltage $V_{Cantilever}$ and the voltage applied to the sample V_{Sample} are set by the SAM and pulses of 10 μs are generated using electronic analog switches.

4.4.2 Cantilever performance during pulsed indentation

The determination of the heater temperature by an IV measurement and a temperature calibration has been shown in section 3.3. Usually the IV curve is measured with the tip not being in contact with the sample using a triangular input voltage as function of time at a frequency of 1 Hz. Since this is rather slow and the heater reaches the equilibrium temperature at each data point, we will refer to this measurement as the "DC IV-curve".

However, the situation changes, when the heater is pulse-heated during the indentation process and the tip is in contact with the sample. We have seen in the

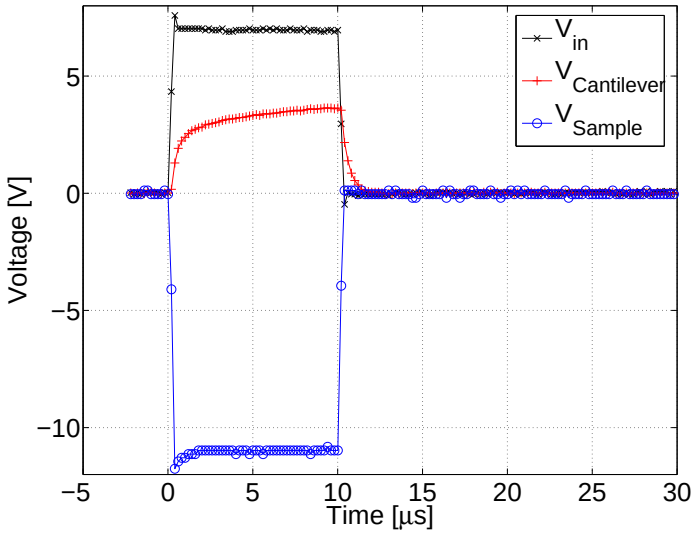

Figure 4.6: Example for an indentation pulse: The input voltage of the cantilever circuit V_{in} , the cantilever voltage $V_{Cantilever}$ and the voltage applied to the sample V_{Sample} are shown.

previous section that the heater does not reach the point of thermal equilibrium during the pulse duration at high input voltages. Additionally, with the tip in contact with the sample the cooling through the tip and the small air gap between heater and sample changes the cooling efficiency of the heater which leads to a changed IV characteristic.

To compare both cases, besides the conventional DC IV-curve an IV measurement has been conducted with the input voltage pulsed for 10 μs duration and the input pulse height ramped up to 10 V, which is high enough to reach the maximum of the heater resistance at 550 °C. The according cantilever voltage is measured simultaneously. Figure 4.7 shows four examples for pulses measured during this experiment.

- In the top left example the input voltage of about 2.5 V is rather moderate and the cantilever voltage is nearly constant for the pulse duration showing that the heater is in thermal equilibrium with the surrounding area.
- In the second example (top right) the input voltage is larger (V_{in} = 9.0 V) and the cantilever voltage increases during the entire pulse time. This behavior has already been observed in figure 4.6 of the previous section.
- Going to higher input voltages (V_{in} = 9.5 V) a saturation of the cantilever voltage can be observed (bottom left). In this case the heater reaches the maximum resistance at a heater temperature of 550 °C.
- At an input voltage of 10 V (bottom right diagram) the cantilever voltage

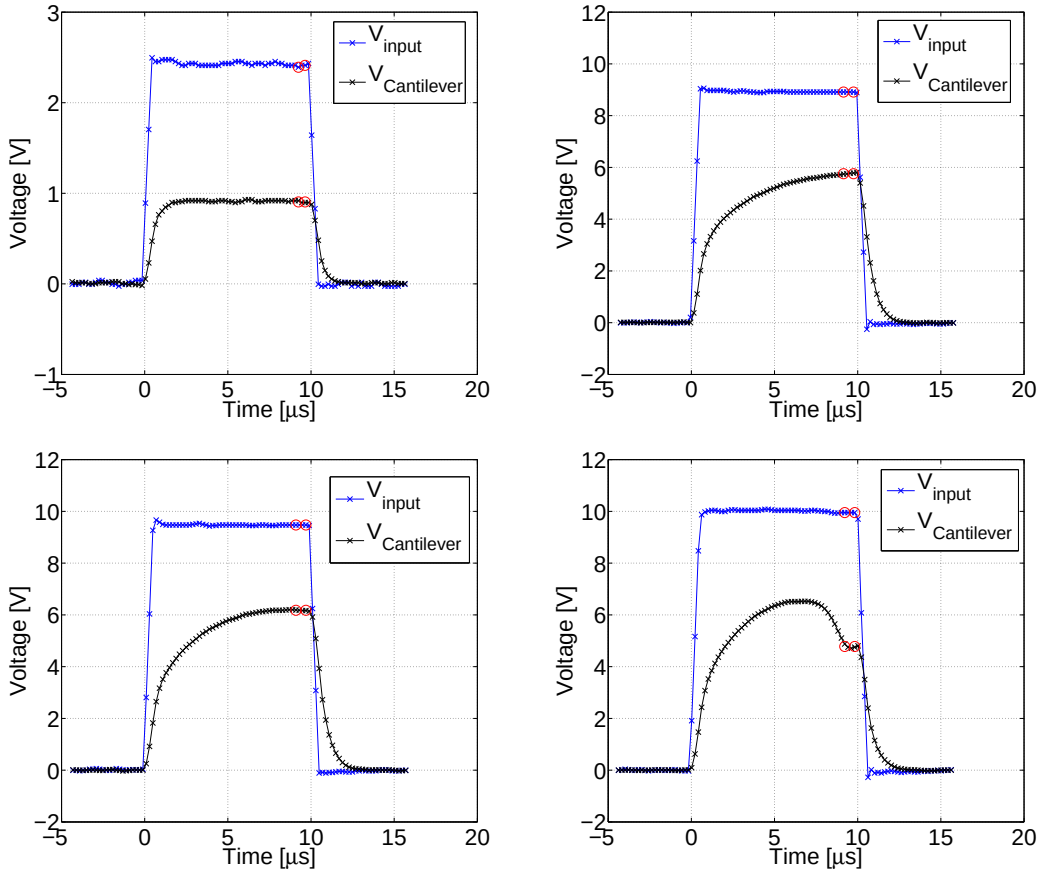

Figure 4.7: Examples of pulses measured during the pulsed IV characteristics measurement with the tip in contact with the sample (80 nm SU8 on silicon). The data points between the two symbols ∘ mark the range used for the IV curve shown in figure 4.8. Note the different ordinate scaling of the top left diagram.

shows a maximum after about 6 μs. This corresponds to the point of the maximum heater resistance and afterwards the resistance decreases, even though the heater temperature is further increased.

In order to conduct the heater temperature calibration it is important that the input voltages are high enough to reach the point of maximum cantilever resistance, which is known to occur at a temperature of 550 °C.

For the calculation of the IV curve and the temperature calibration the data between the markers ∘ in figure 4.7 are averaged. With the input voltage V_{in}, the cantilever voltage $V_{Cantilever}$ and the known sense resistor R_{Sense} of 2kΩ, the current and the heater power are calculated. The result of the entire IV curve measurement is shown in figure 4.8, where each data point is calculated from one pulse. The left graph shows the electrical current as function of the input voltages. The shape of both curves is similar to the example discussed in figure 3.3

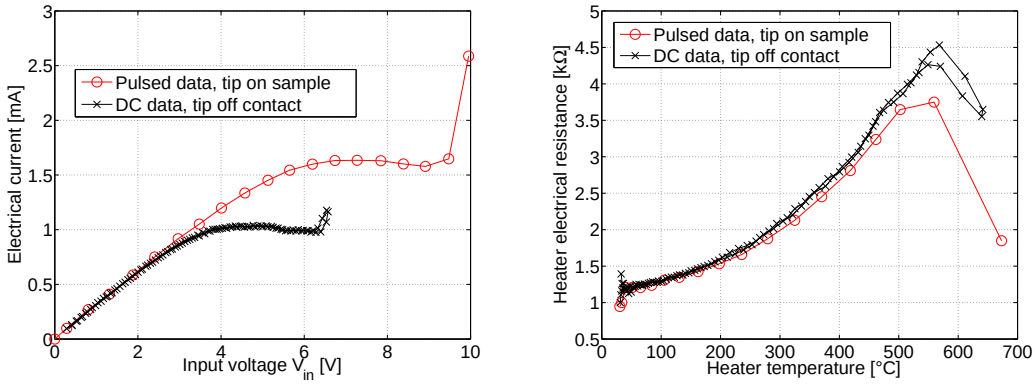

Figure 4.8: Comparison of the IV characteristics (*left*) and the heater electrical resistance versus heater temperature curve (*right*) derived from measurements with pulsed tip in contact with the sample (markers ∘) and from a DC-like IV curve measured with a ramping time 1 second and the tip being retracted from the sample (markers ×).

with the characteristic kink of the curve, where the heater temperature exceeds 550 °C. But one observes, that this kink is shifted to higher input voltages for the pulsed IV with the tip in contact with the sample, which comes from the additional cooling of the heater by the sample. The resistance versus heater temperature on the other hand match well because this relation does not depend on the cooling effects and is a function only of the heater's doping concentration. At higher temperature the curves deviate slightly presumably because only a few data points have been measured for the pulsed IV curve, which makes the determination of the kink inaccurate.

Since both kinds of IV curve measurements lead to the RT curve within the error margins, the heater temperature determination will be done using the DC IV curve, which is experimentally less intricate. For the cases where the heater does not reach the thermal equilibrium state and the temperature is increasing during the entire pulse duration the temperatures given in the following section denote the maximum of the heater temperature during the pulse duration, i.e. typically the temperature of heater when the input voltage is switched off after the 10 μs.

4.4.3 Electro-static force calibration

In section 4.4.1 it has been shown, how the heat and electro-static pulses are created and how the heater temperature is determined. Now, a calibration procedure will be discussed, which enables to determine the electro-static force associated with the voltage applied to the sample. As already stated previously the electro-

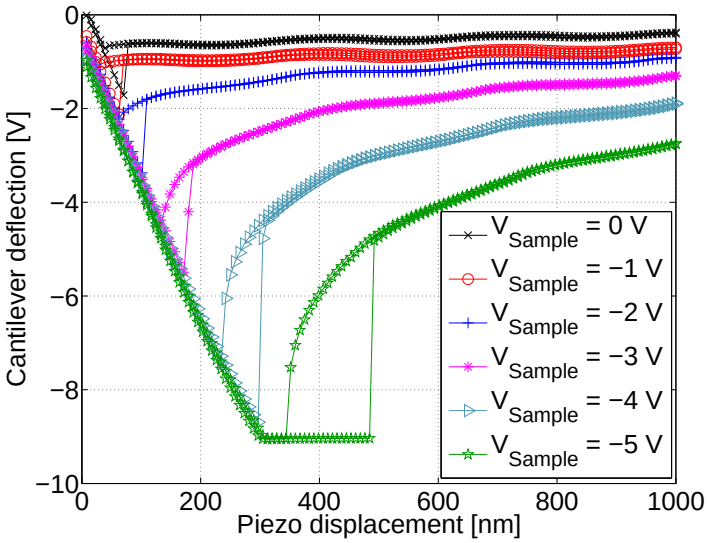

Figure 4.9: Force distance curves measured at different DC sample voltages. The shift of the snap-off position is used for the electro-static force calibration.

static force is proportional to the square of the voltage difference between heater and sample $F_{\text{electro-static}} \propto |V_{\text{Sample}} - V_{\text{Cantilever}}|^2$.

The electro-static force calibration is performed by measuring force-distance curves using the optical signal at different DC sample voltages. During the force-distance curve measurement the cantilever heater remains unheated. As the sample voltage is decreased to more negative values the snap-in and snap-off positions shift to the right as figure 4.9 shows. Thus, the tip snaps to or off the surface at larger piezo displacements. One also observes a bending of the cantilever in the off contact region, which is also originated from the electro-static force and could be used for the calibration. However, here the shift of the snap-off position as function of the applied sample voltage is used to determine the electro-static force: Multiplied with the cantilever's spring constant the shift of the snap-off postion is equal to the electro-static force. Figure 4.10 shows the electro-static force determined with this procedure as function of the DC sample voltage. As expected a 2nd order polynomial function describes the data measured well.

The force-distance curve measured at -5.0 V sample voltage in figure 4.9 exhibits, that the snap-off instability cannot be measured completely, because the position sensitive detector obviously saturates at the large cantilever deflections resulting from the high electro-static forces. Nevertheless, the position of the snap-off is still detectable, but force-distance curves cannot be measured at higher sample voltages. Depending on the particular cantilever and calibration the limit for the

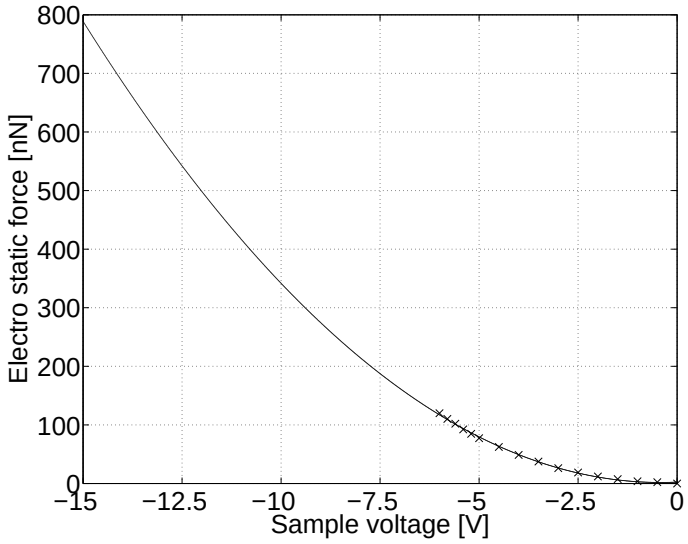

Figure 4.10: Electro-static force as function of the voltage applied to the sample.

force-distance curve measurement is at -5 to -8 V corresponding to electro-static forces between 50 and 150 nN. However, as we will see in the next chapter at a sample temperature of 30 °C electro-static forces between 150 and 550 nN are required to create a permanent impressions in a PMMA film with a typical heater temperature between 100 and 300 °C. Due to the saturation of the detector the calibration could not be measured with such high sample voltages. Hence, the measured calibration data have to be extrapolated. For the example of the calibration curve shown in figure 4.10 it was possible to measure force-distance curves with sample voltages between 0 and -6.0 V. The extrapolation to more negative sample voltages shows, that a sample voltage of about -9.4 V was necessary to generate an electro-static force of 300 nN.

For the calibration the cantilever is unheated and thus, no input voltage is applied to the cantilever circuit ($V_{\text{in}} = 0$). Consequently the cantilever is also at ground level ($V_{\text{Cantilever}} = 0$). However, during the indentation pulse the cantilever is at a certain voltage $V_{\text{Cantilever}}$. To calculate the according electro-static force the difference between sample and cantilever voltage has to be taken into account: $F_{\text{electro-static}} \propto |V_{\text{Sample}} - V_{\text{Cantilever}}|^2$. However, one has to be aware of one effect influencing the calibration procedure: For the duration of the indentation pulse an electrical current is running through the heater and a voltage drop across the heater occurs, which leads to a potential gradient along the heater with a potential at the one end of the heater being at $V_{\text{Cantilever}}$ and the other end at ground level. Consequently the electrostatic force acting between heater and sample is not symmetric at both sides of the heater. Instead the force is larger at the side being at $V_{\text{Cantilever}}$. For the data evaluation the electro-static force

has been calculated using half the value of the cantilever voltage to calculate the voltage difference between heater and sample. With this difference the electro-static force is calculated using the 2nd oder polynomial fit of the data obtained from the calibration experiment. As an example the electro-static force acting during the pulse shown in figure 4.6 shall be calculated: The sample voltage was V_{Sample}= -11 V and the maximum of the cantilever voltage was $V_{\mathrm{Cantilever}}$= 3.6 V. The difference is worked out to be $\Delta V = |V_{\mathrm{Sample}} - 0.5 \cdot V_{\mathrm{Cantilever}}|$ = -12.8 V. This corresponds to a force of 570 nN as one deduces from the extrapolated polynomial data fit in figure 4.10. The factor of 0.5 in the above equation has been determined experimentally and by simulation [68].

At elevated sample temperatures the temperature of the heater changes significantly and the cantilever voltage changes as well even though equal input voltages are applied. Consequently the difference between sample voltage and cantilever voltage also changes leading to changing electrostatic forces. Hence, the data of all pulses at different sample temperatures are stored with the oscilloscope, which enables to determine the electro-static force and the heater temperature of each indentation.

4.4.4 High frequency nanoindentation at room temperature

In the previous sections the experimental setup, the pulse generation and the electro-static force calibration have been discussed. Now, the nanoindentation experiments with a pulse-heated cantilever tip and electro-static force pulses will be presented with the sample not being heated. Since the entire microscope is situated inside a box to avoid disturbances, the lowest achievable sample temperature was 30 °C. As in chapter 2 a 35 nm thin PMMA and a 80 nm thin SU8 film both on silicon were investigated. The sample preparation of both samples has been discussed in section 2.4.

Figure 4.11 shows an example of indentations produced with 10 μs pulses on the 35 nm PMMA film on silicon at a sample temperature of 30 °C. The sample voltage has been varied linearly from 0 to -11.0 V in the vertical direction and in the horizontal direction the input voltage of the cantilever circuit has been varied from 2.8 to 7.0 V. The resulting heater temperatures ranged from 100 up to 316 °C and the electro-static forces from 116 up to 554 nN for the visible indentations.

Although the entire array consists of 16×16 pulses a clear threshold for the creation of permanent indentations is obvious and only 13 columns and 10 lines are visible: For heater temperatures smaller than 100 °C and forces smaller than 120 nN no permanent impressions are observable. In the experiments of this chapter all arrays were produced with 16×16 pulses. The numbering of the columns

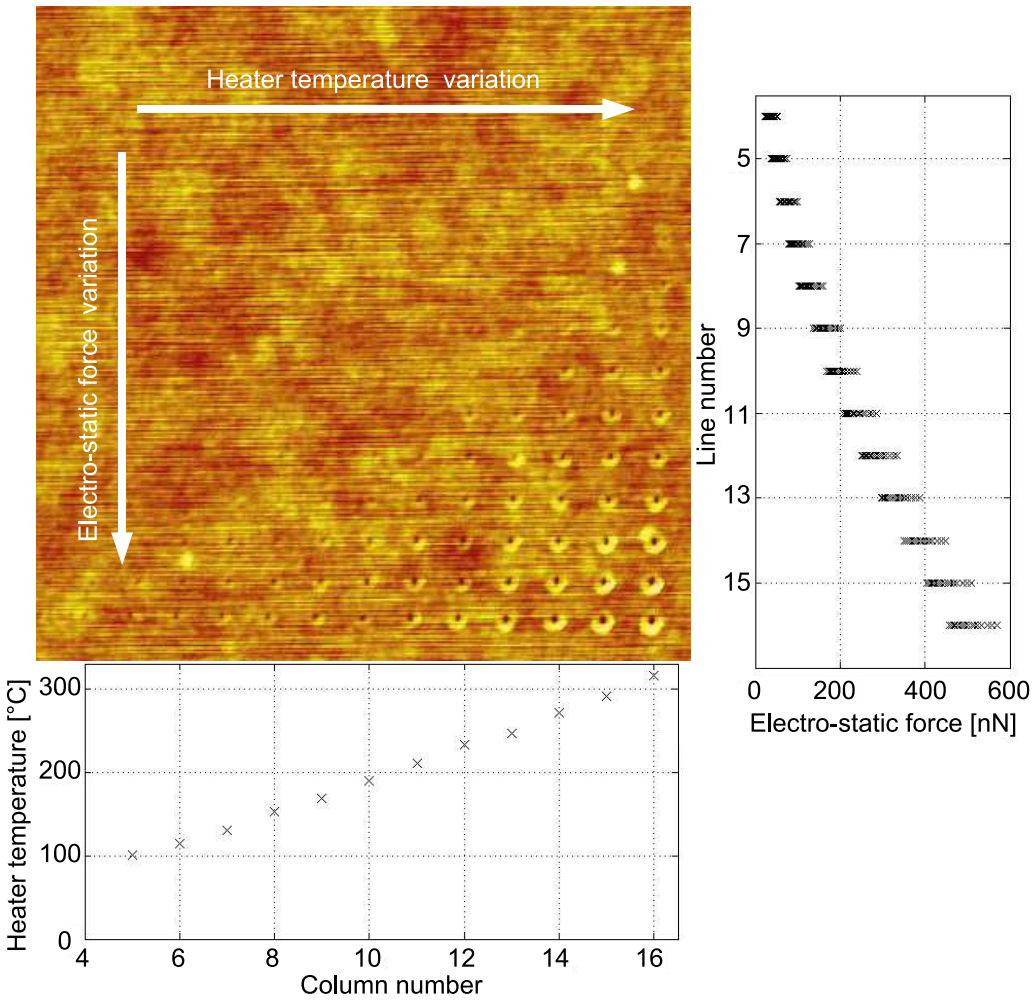

Figure 4.11: Example of an indentation array created with 10 μs pulses on the 35 nm PMMA film on silicon at a sample temperature of 30 °C. The electro-static forces and heater temperatures are shown in the graphs. Contact mode image scanned with unheated tip; Image size: 1.6 μm; Height scale: 10 nm ; Scan rate: 5 Hz per line

and lines will be done such that the columns are counted from left to right and the lines from top to bottom (see figure 4.11). I.e. the largest indentation at the bottom right is in column 16, line 16.

Although both the sample voltages and the input voltages of the cantilever circuit have been varied independently in the horizontal and vertical direction respectively, one observes from the right graph in figure 4.11, that the electro-static forces split up within a line. This originates from the fact, that although the sample voltage is kept constant within a line the voltage difference between sample and cantilever changes as the input voltage of the cantilever

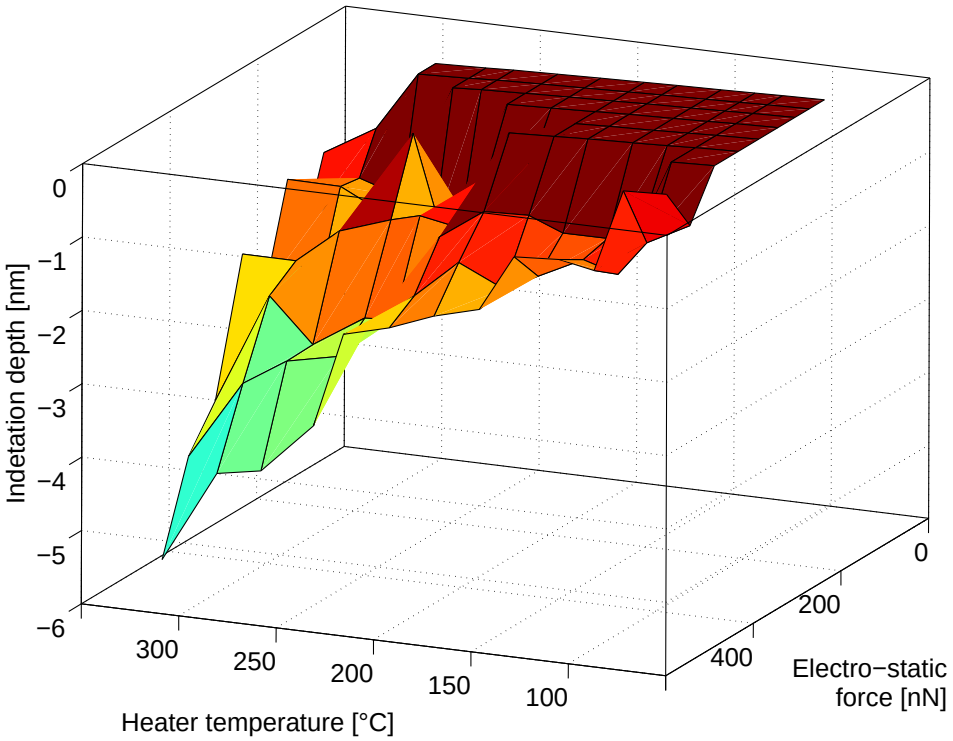

Figure 4.12: Depth of the indentations shown in figure 4.11 as function of heater temperature and electro-static force.

circuit and consequently the cantilever voltage is varied. Since the electro-static force is a function of both the sample voltage and the cantilever voltage $F_{\text{electro-static}} \propto |V_{\text{Sample}} - V_{\text{Cantilever}}|^2$, the electro-static force is not constant within an array line and increases with increasing heater temperature. This effect will be considered below and taken into account in the data analysis.

The indentation topography is analyzed with the program described in detail in chapter 2.6 (figure 2.22). Thus, it is possible to determine characteristic quantities like the indentation depth or rim height (among others). As figure 4.12 shows the indentation depth, which is measured as the vertical distance between the mean surface around each particular indentation and the deepest point of the indentation, increases with increasing heater temperature and electro-static force. In the following quantities concerning the parts of an indentation below the surface are negative and parts lying above the mean surface (e.g. the rim height) will be positive.

The comparison of indentations on PMMA and SU8 is shown in figure 4.13. Altough both measurements have been conducted with different tips and the electro-

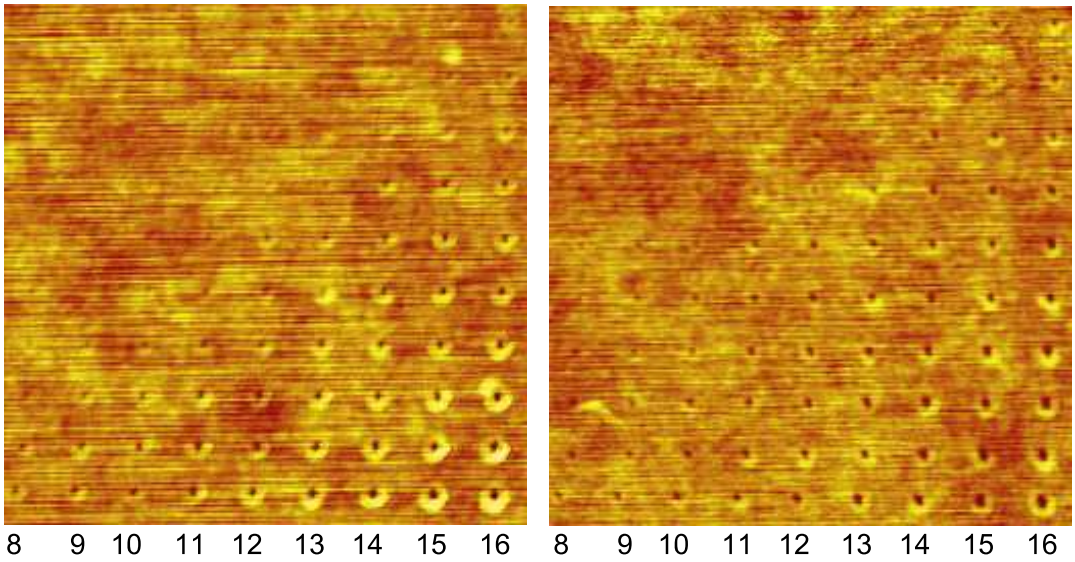

Figure 4.13: Comparison of indentations created with pulse-heated cantilever tip on 35 nm PMMA (*left*) and 80 nm SU8 (*right*) on silicon at a sample temperature of 30 °C. Image size: 1.0 μm; Height scale: 10 nm ; Scan rate: 5 Hz per line

static force was slightly higher on SU8 than on PMMA ($F_{\text{electro-static,SU8}} \leq 670\,\text{nN}$, $F_{\text{electro-static,PMMA}} \leq 554\,\text{nN}$) while the heater temperatures were equal, both images should be directly comparable, because one can assume that the implications originating from the different tips and the different electro-static forces are not as strong as those due to the different polymer properties: The indentations in the columns 8 to 11 of the lowest line (low heater temperatures, large electro-static forces) look similar on PMMA and SU8. The lateral dimensions are comparable and the rim formation is relatively moderate. With increasing heater temperature (column 12 to 16) a clearly enhanced pile-up effect is observed on PMMA, while on SU8 the rim remains rather small. Similar observations have already been made in the discussion of nanoindentation experiments with force-distance curves (see section 2.5.2.1, especially figure 2.11), where the pile-up effect of PMMA at higher temperatures was also much larger than on SU8.

4.4.5 High frequency nanoindentation at elevated sample temperatures

In the previous section high frequency nanoindentation experiments on unheated samples at 30 °C have been shown and the results have been discussed. Now, the measurements at sample temperatures between 30 and 130 °C will be described and the results analyzed. The experiments have been conducted with the range

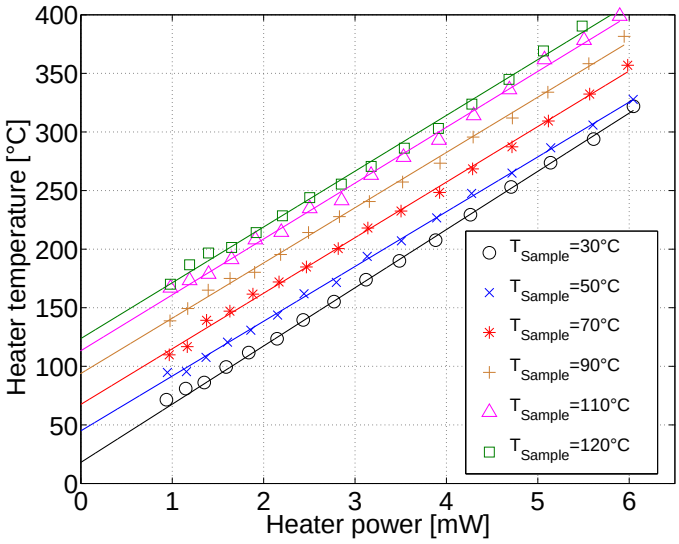

Figure 4.14: Heater temperature as function of power at different sample temperatures.

of both the input voltage of the cantilever circuit and the sample voltage remaining constant at each sample temperature (except at a sample temperature of 130 °C in the PMMA measurement slightly smaller writing parameter have been chosen). The heater temperature variation and the electro-static force variation, however, were not constant at different sample temperatures, because the electrical resistance of the heater and consequently the cantilever voltage ($V_{\mathrm{Cantilever}}$) is dependent on the temperature, which will change at different sample temperature. Thus, the performance of the heatable cantilevers will be investigated at first in section 4.4.5.1.

The indentation topography is analyzed from contact mode images scanned with unheated tip at the specific sample temperature. In section 4.4.5.2 the indentations on PMMA and SU8 at different sample temperatures will at first be analyzed qualitatively. In a second step typical topography quantities like the depth of the indentations will be considered quantitatively as function of the sample temperature, the heater temperature and the electro-static force.

4.4.5.1 Heatable cantilevers at elevated sample temperatures

Before the topography of the indentations created at elevated sample temperatures is addressed in the next section, the influence of different sample temperatures on the cantilever performance shall be investigated. One expects, that the cantilever heater is influenced by the heated sample in the following way: At

higher sample temperatures less cooling of the cantilever heater occurs and the cantilever heater will reach higher temperatures during the heating pulse even though the input voltage variation of the cantilever circuit remains constant at each sample temperatures. This is confirmed by the measurement shown in figure 4.14. The heater temperature as function of the electrical power produced by the heater at different sample temperatures is plotted. As expected the heater temperatures increase with increasing sample temperature. The data have been obtained from the stored oscilloscope traces of the experiment on the SU8 film. The indentations created with these pulses will be discussed in the next section 4.4.5.2. The electrical power P_{Heater} of the heater is calculated from the measured data V_{in} and $V_{\mathrm{Cantilever}}$ by $P_{\mathrm{Heater}} = V_{\mathrm{Cantilever}} \cdot I = V_{\mathrm{Cantilever}} \cdot (V_{\mathrm{in}} - V_{\mathrm{Cantilever}})/R_{\mathrm{Sense}}$ with $R_{\mathrm{Sense}} = 2\,\mathrm{k}\Omega$.

From these data it is possible to extrapolate the heater temperature with the tip in contact with the sample and no input voltage applied. The measured data are fitted with a linear function and extrapolated to zero heater power, $P_{\mathrm{Heater}} = 0\,W$, i.e. when the heater was not heated. These offset data are determined for each sample temperature and figure 4.15 shows the result in comparison to the case when the sample temperature and the heater temperatures would have been equal (dashed line) as one would expect assuming good thermal equilibration and contact between sample and cantilever. The expected and the measured data are in good agreement. Especially in the middle part for sample temperatures of 80 °C the data fit well. For sample temperatures below 60 and above of 100 °C a deviation by 10 °C from the expected behavior is observed. From this measurement one can conclude, that the heater temperature calibration of the cantilever is acceptable within an absolute error of $\pm\,10$ °C in the sample temperature range between 30 and 120 °C. However, the heater temperatures during the indentation experiments ranged up to 400 °C (figure 4.14). Extrapolation of the two linear lines leads to a heater temperature of 449 °C at a sample temperature of 400 °C, i.e. an absolute deviation of 49 °C, which corresponds to 13 % relative deviation. This deviation reflects the limit of the assumptions, measurement errors and fabrication tolerances. Comparing this with the assumed error of the heater temperature calibration of 30 % shows that in this case the deviation is smaller than expected. However, in the following we will retain the assumed 30 % error range.

4.4.5.2 Indentation topography at elevated sample temperatures

Now, the influence of the sample temperature on the topography of indentations made on the PMMA and on the SU8 film will be discussed and compared. Figure 4.16 gives an overview about the indentations arrays created at different sample temperatures on the 35 nm PMMA film. The influence of the sample tem-

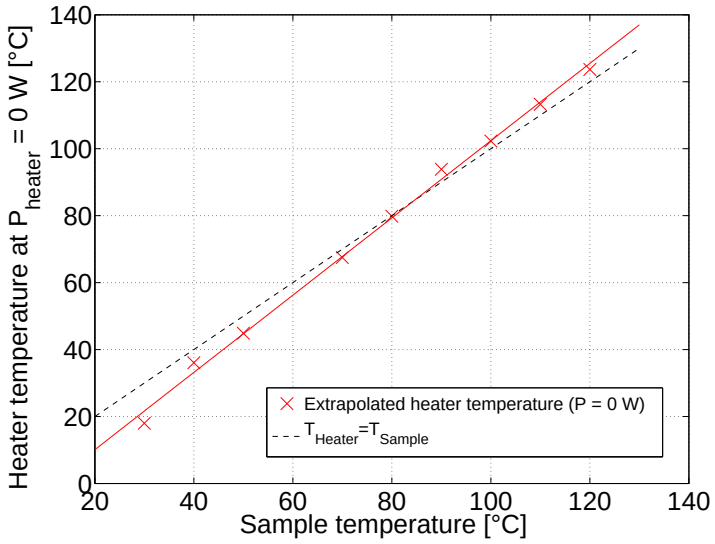

Figure 4.15: Extrapolated heater temperature as function of sample temperature.

perature is obvious: With increasing sample temperature the lateral size of the indentations becomes larger and the rim formation is clearly enhanced. At 125 and 130 °C, however, only a few indentations are visible and hardly any pile-up occurs.

The indentations on SU8 shown in figure 4.17 exhibit a clearly different behavior than those on PMMA: The influence of the sample temperature is much smaller and the indentations at high sample temperatures are laterally only slightly larger than those at 30 °C. The rim formation is also relatively small compared to the huge effect, which is observed on PMMA.

For the application of the indentation procedure in a data storage device like the "Millipede" (see section 1.1.1) the increased lateral indentation size on PMMA at elevated sample temperatures is not acceptable. This increase of the bit size would directly influence the data density and consequently the data capacity of the entire device. Although temperatures of above 100 °C during conventional operation are not realistic, 80 °C are typical device requirements and can for example occur when the device is placed inside a car behind the windscreen on a hot sunny sommer's day. Thus, the storage medium of choice for the "Millipede" product should not exhibit this clear increase of the lateral bit size. Alternatively the writing parameters (either force, heater temperature or writing time) could be adapted according to the specific environmental temperature. This in turn would add an additional component to the system and would make the device more complex. From this point of view and from the reduced rim formation SU8 seems to be the more adequate material for the storage medium. On the

other hand we have seen that the influence of the heater temperature is much smaller and thus the heating of the tip assists the indentation process much more efficiently on PMMA than on SU8, last but not least because of the presence of the glass transition of PMMA. Assuming that the high cross-linking density of SU8 is responsible for the reduced rim formation, it can be concluded that a highly cross-linked polymer with a glass transition temperature of $\approx 120\,^{\circ}\mathrm{C}$ would be ideal as a storage medium for thermomechanical data storage.

Furthermore, the measurements show, that it is difficult to maintain the high positioning accuracy for the reading and writing process at elevated sample temperatures: Both on PMMA and on SU8 the array grids at elevated sample temperature are distorted whereas they are rectangular at low sample temperatures. Supposably this comes from drift effects of the sample during the execution of the nanoscript and shows, that the sample was not completely stable. In our case this is no larger problem, because the entire array field is imaged, but for the reading procedure in the "Millipede" the positioning accuracy must be precise enough to address each indentation (bit) at various device temperatures. Although the "Millipede" device and the commercial SFM D3000 from Veeco are completely different designed and the comparison of both is not straightforwards (especially because completely different scanner techniques are used), nevertheless basic problems occurring at elevated environmental temperatures are experienced in these experiments and emphasize the enormous requirements concerning the "Millipede" scanner.

Quantitative analysis of indentations on PMMA and SU8

Unlike the force-distance curve measurements in chapter 2 where the indentation process could be observed "in situ" by analyzing the laser signal reflected by the cantilever, in these experiments one has to rely on the image topography scanned in contact mode after the creation of the indentations. So far the indentations produced at elevated sample temperatures on PMMA and SU8 have been analyzed qualitatively. Now, the topography of the indentations shown in figures 4.16 and 4.17 will be analyzed quantitatively. For this purpose the program described in detail in chapter 2.6 (figure 2.22) is used.

One has to be aware of several fundamental effects influencing the measurement of indentation topography:

- Due to convolution effects of the scanning tip and the sample topography the measured indentation topography will be afflicted with considerable deviations from the true sample surface, e.g. the indentation depth measured from the images might be significantly smaller than the true depth. Furthermore, the measured value depends on the shape of each particular tip:

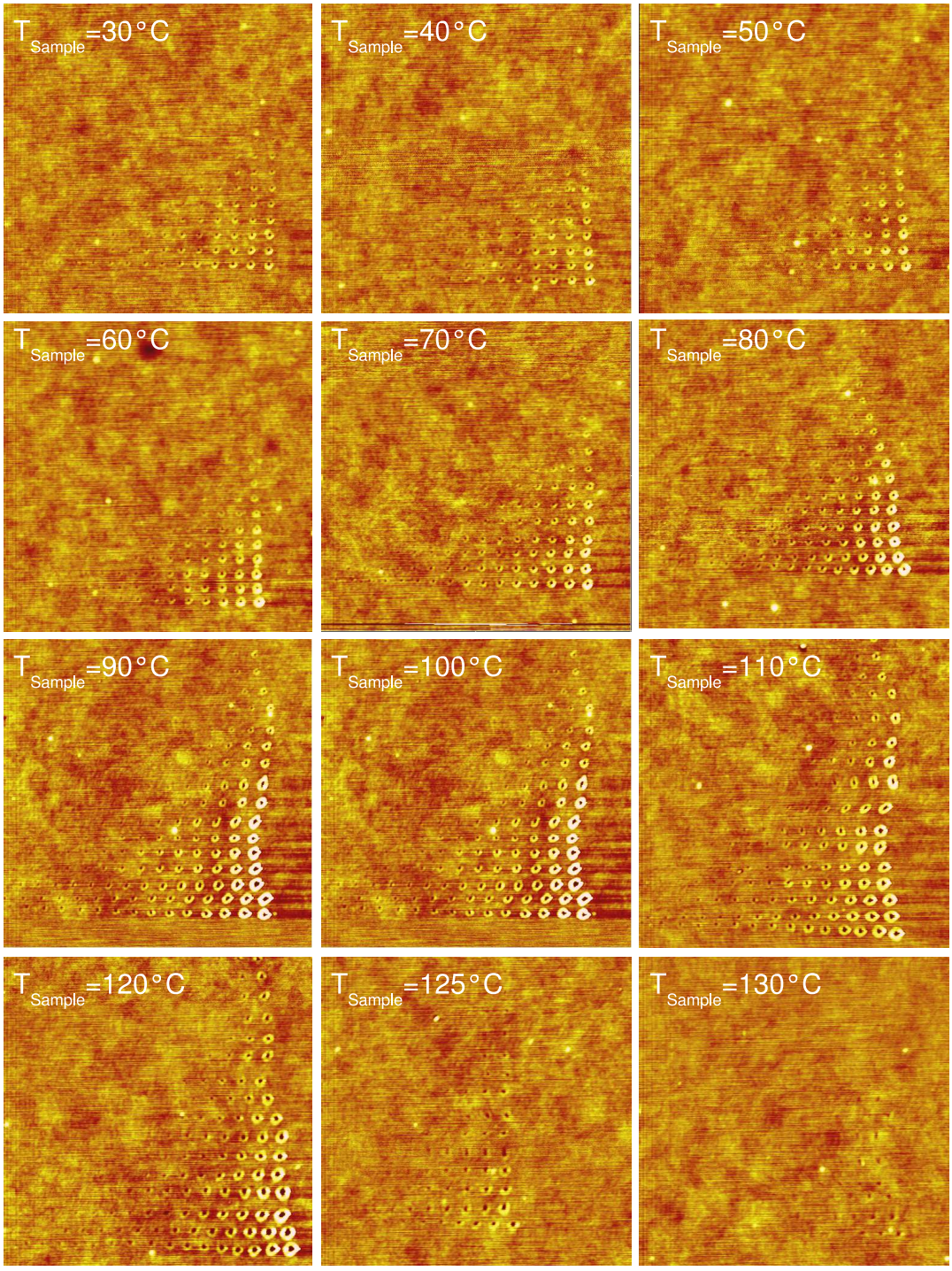

Figure 4.16: Contact mode images of indentations created on the 35 nm PMMA film on silicon at different sample temperatures. The heater temperature was varied in the horizontal direction and the electro-static force in the vertical direction. Image Size: 2 μm; Height scale: 10 nm; Line scan rate: 5 Hz

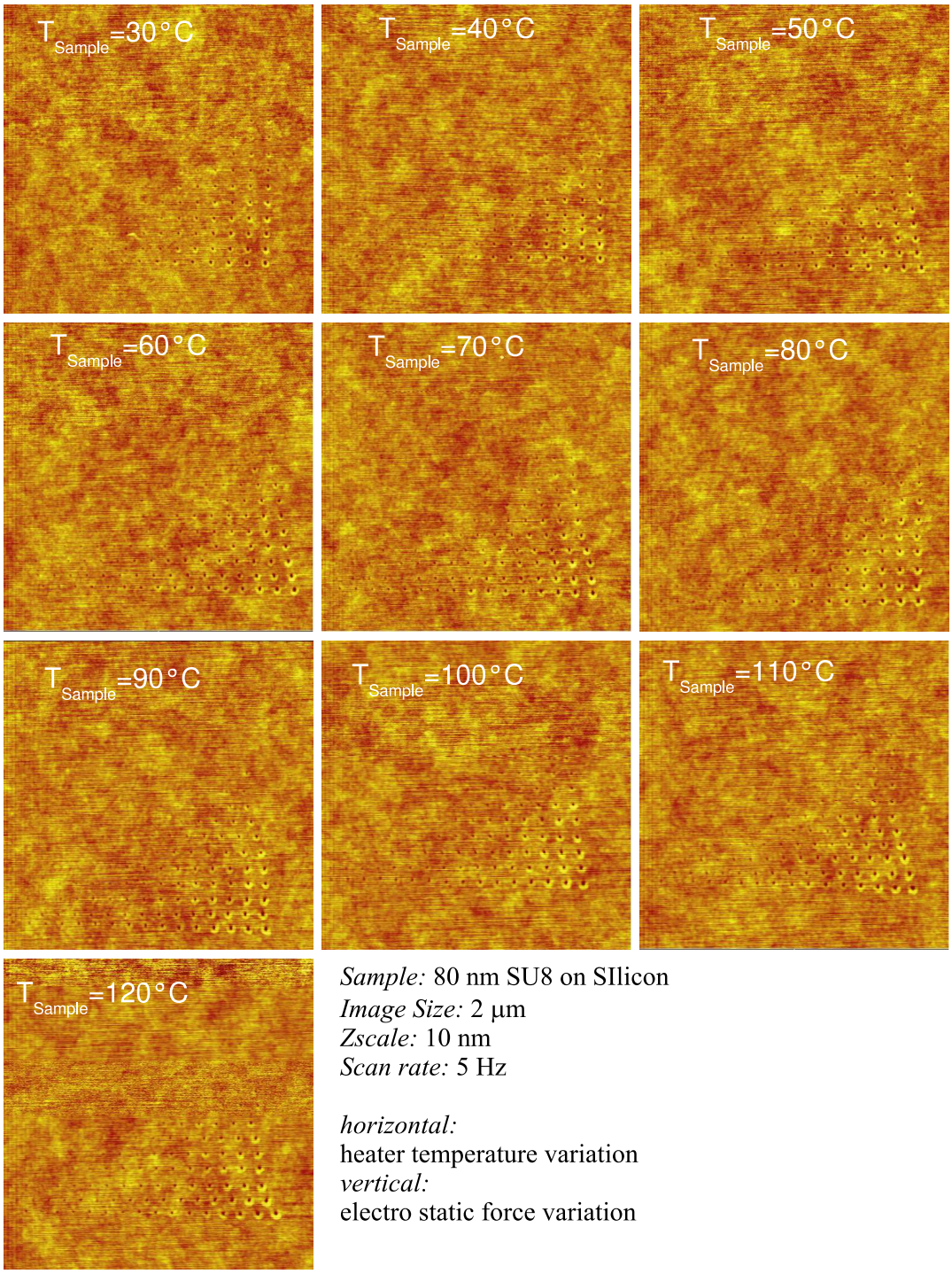

Figure 4.17: Contact mode images of indentations created on the 80 nm SU8 film on silicon at different sample temperatures.

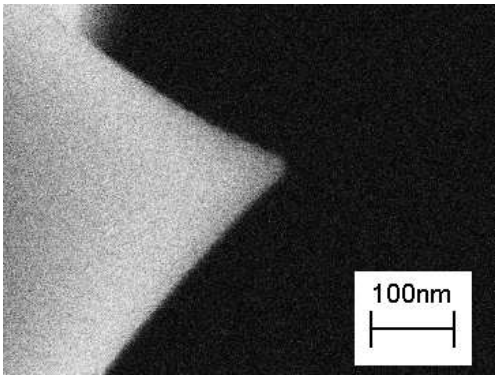

Figure 4.18: SEM image of the tip taken after usage for the indentation experiments and the imaging in Contact Mode on the PMMA sample.

Using a blunt tip for scanning will result in a value of the indentation depth being significantly smaller than using a sharp tip. However, in these experiments one is especially interested in the relative change of the indentation topography as function of the heater temperature, electro-static force and sample temperature and thus, the uncertainties in the measured values does not strongly affect the results.

- Relaxation processes of the indentations, which occur between the indentation procedure and imaging, will play a role and will change the sample topography (compare to section 2.6). Thus, during the experiment the aim was to keep the time for scanning short and a rather high line scan rate of 5 Hz was used, which led to a scanning time for one image with 512×512 pixels of about 1.7 minutes. Although this is considerably smaller than the relaxation times below the glass temperature observed in section 2.6, above the glass transition temperature of 115 °C relaxation processes have to be taken into account.

- Although in the SEM image of the tip taken after the experiment (see figure 4.18) no contamination is visible, it is generally challenging to conduct Contact Mode SFM imaging at elevated sample temperature (especially in and above the glass transition) because of possible tip contaminations which are not observable in the SEM, thermal drift effects and the compliance of the sample surface, which make it difficult to choose the appropriate deflection setpoint.

Thus, we will assume in the following, that the indentation depth was measured with an accuracy of ± 1 nm, which does not include the uncertainty originated from the tip-sample convolution effect.

Due to the strong temperature dependence of the indentations on PMMA we will at first investigate the data of PMMA and afterwards analyze the indentations

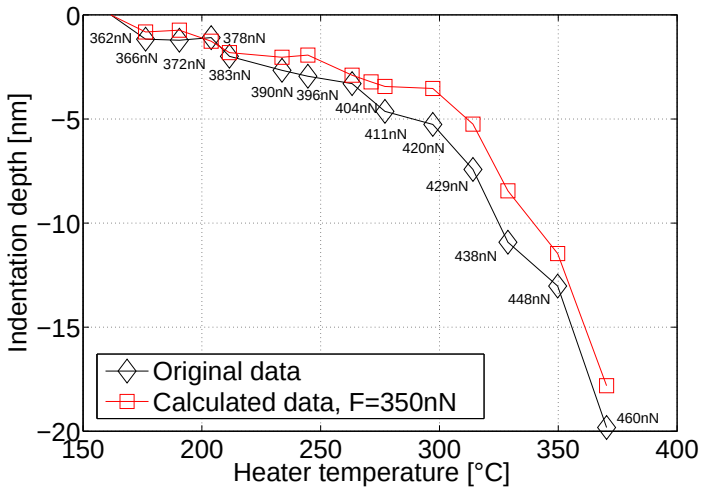

Figure 4.19: Depth of the indentations in the third line from the bottom in figure 4.16 as function of the heater temperature at a sample temperature of 100 °C. As the values show the electro-static force was not constant within an array line. Thus, the indentation depths for a constant force of 350 nN have been calculated using the Matlab function `CONTOUR` based on the measured 3-dimensional data. Sample: 35 nm PMMA on silicon

on SU8. We have already seen in figure 4.11 that the electro-static force is not constant within an array line, i.e. when the heater temperature is changed in the horizontal direction of the images shown in figure 4.16. Thus, the influence of the heater temperature on the indentation topography cannot be directly investigated within one horizontal line. However, since the indentations were created at each sample temperature as function of the electro-static force and heater temperature a 3-dimensional function of the topography related quantities can be determined as function of these variables. A first example has been shown for the indentation depths at 30 °C sample temperature in figure 4.11. Thus, it is possible to calculate traces of constant forces with an appropriate software tool. Here, the Matlab function `CONTOUR` [69] was used for this purpose, which enables to calculate lines of constant forces by linear interpolation of the measured data points.

An example is given in figure 4.19, where the depth of indentations in the third line from the bottom in figure 4.16 at a sample temperature of 100 °C is shown. The force values given vary between 362 and 460 nN, which corresponds to an increase of 27 %. In addition to the measured data the calculated data for a constant electro-static force of 350 nN are plotted, which shows, that there is indeed a significant difference between the measured data and the indentation depths calculated for a constant force. At lower sample temperatures between 30 and 80 °C, however, it is observed, that the influence of the varying electro-static forces is negligible.

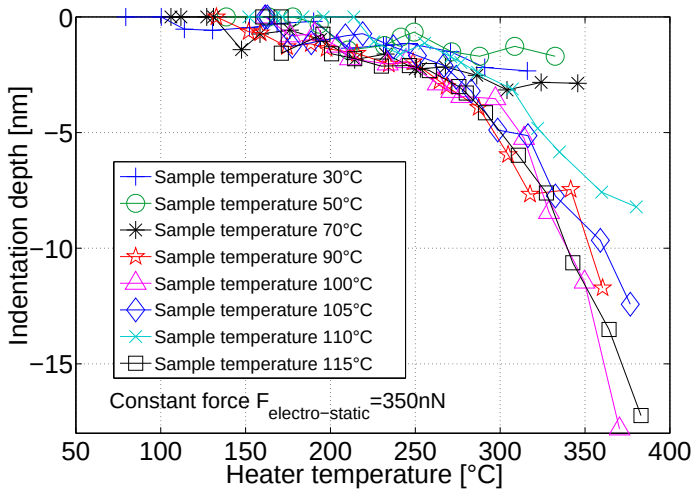

Figure 4.20: Indentation depth as function of the heater temperature at various sample temperatures and a constant electro-static force of F = 350 nN. Sample: 35 nm PMMA on silicon

Furthermore, in figure 4.19 one observes that the dependence of the indentation depth on the heater temperature is relatively small for heater temperatures of up to 300 °C: An indentation depth of 5 nm per 140 °C heater temperature increase is observed, which corresponds to a slope of ≈ 0.04 nm/K. At higher heater temperatures, however, the dependence is significantly larger and one obtains a slope of ≈ 0.19 nm/K. In order to get an understanding of this observation the indentation depths measured at different sample temperatures with a constant electro-static force of 350 nN shown in figure 4.20 shall be considered. This transition only occurs at sample temperatures higher than 90 °C, while at lower sample temperatures no kink is observable and the slope of the curve remains constant for the entire range of heater temperatures. Considering, for example, the indentation depths at a heater temperature of 350 °C an indentation depth of only 3 nm is measured at a sample temperature of 70 °C, whereas at 115 °C sample temperature the indentation depth is about 12 nm, thus a factor of 4 larger. Interestingly, the indentation depths for sample temperatures larger than 90 °C do not significantly depend on the sample temperature.

As the heat transferred to the sample is proportional to the temperature difference between heater and sample, the indentation depth as function of this temperature difference is plotted in figure 4.21. Again for sample temperature lower than 90 °C only little dependence of the indentation depth on the heater temperature is observed whereas for higher sample temperatures the strong increase of the indentation depths in observed.

A thorough analysis of the temperature field under the tip requires numerical models and is beyond the scope of this work. However, we can define an *effective*

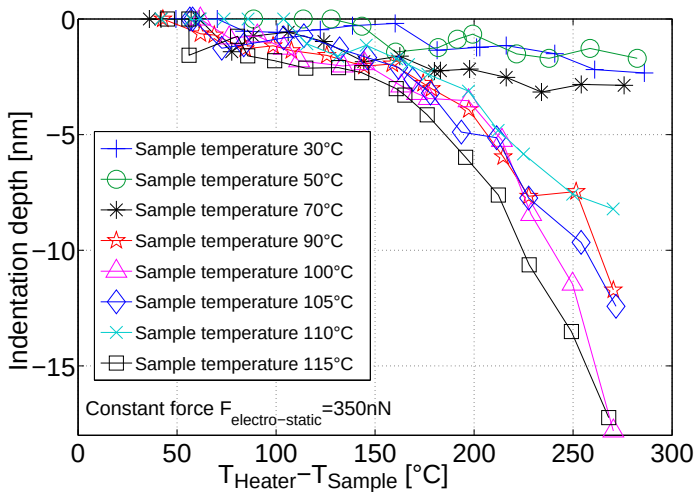

Figure 4.21: Indentation depth as function of the difference between heater temperature and sample temperature at a constant electro-static force of 350 nN and at various sample temperatures. Sample: 35 nm PMMA on silicon

local temperature associated with this field. This effective local temperature $T_{\mathrm{Sample,local}}$ can be estimated with the data of figure 4.21: We can assume, that this temperature is between the the global sample temperature and the heater temperature:

$$T_{\mathrm{Sample,local}} = T_{\mathrm{Sample,global}} + c \cdot (T_{\mathrm{Heater}} - T_{\mathrm{Sample,global}}) \tag{4.2}$$

where c is a factor describing the temperature increase around the tip sample contact $(0 < c < 1)$.

If we consider for example a constant indentation depth of 3 nm we measure a temperature difference between heater and sample of $T_{\mathrm{Heater}} - T_{\mathrm{Sample,global}} = 160\,^{\circ}\mathrm{C}$ at a sample temperature of 115°C. At a sample temperature of 70 °C the temperature difference is 230 °C to obtain an indentation depth of 3 nm. Since the electro-static force is constant the equal indentation depth of 3 nm can only be originated from equal surface temperatures. Thus, we get

$$T_{\mathrm{Sample,local}} = 115\,^{\circ}\mathrm{C} + c \cdot 160\,^{\circ}\mathrm{C} \tag{4.3}$$

and

$$T_{\mathrm{Sample,local}} = 70\,^{\circ}\mathrm{C} + c \cdot 230\,^{\circ}\mathrm{C} \tag{4.4}$$

Solving the system of equations leads to a factor of $c \approx 0.6$. Thus, we obtain a local surface temperature of $T_{\mathrm{Sample,local}} = 217\,^{\circ}\mathrm{C}$ at a heater temperature of 275 °C and a sample temperature 115 °C as well as for a heater temperature of 300 °C at 70 °C sample temperature. The type of data analysis was conducted

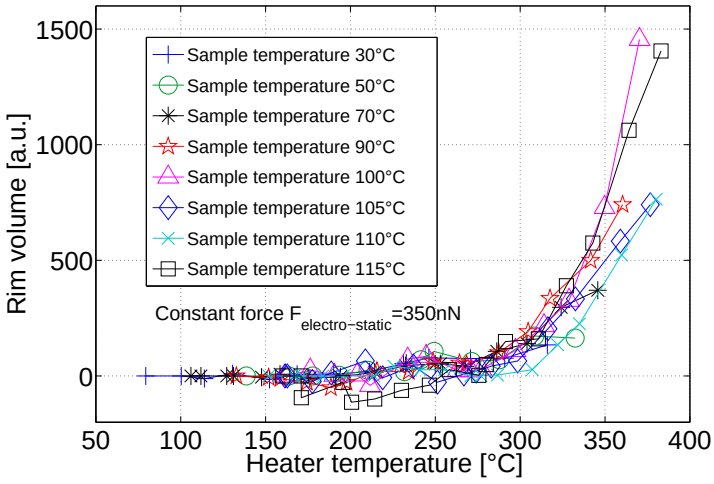

Figure 4.22: Rim volume as function of the heater temperature at various sample temperatures and a constant electro-static force of F = 350 nN. Sample: 35 nm PMMA on silicon

for several forces and data sets and it turns out that the factor of c is always in the range between 0.5..0.7. Thus, we can assume that the heater can increase the local sample temperature significantly above the transition temperature which is as we known from chapter 2 between 115 and 118 °C.

Although equation 4.2 can predict the local surface temperature at a given force and depth, it is not sufficient to explain the rim formation as shown in figure 4.22, where the volume of the rims is plotted as function of the heater temperature at an electrostatic force of 350 nN. The observations made concerning the indentation topography on PMMA will now be interpreted by taking the above considerations of the effective local sample temperature around the tip and the glass transition T_G of PMMA into account. Four different cases can be distinguished as schematically shown in figure 4.23: In case A the global sample temperature $T_{\text{Sample,global}}$ is below T_G and the heater temperature is too low to bring the polymer underneath the tip $T_{\text{Sample,local}}$ locally above T_G. In this case the polymer underneath the tip as well as the surrounding material is viscous and an indentation is formed mainly by compression of the polymer due to the force exerted by the tip. Since the material can hardly be transferred due to the high viscosity, the rim formation is moderate.

In case B the heater temperature is high enough to bring the polymer underneath the tip $T_{\text{Sample,local}}$ locally above T_G. Thus, there will be a boundary (indicated by the half circle in figure 4.23) between polymer material under the tip, which is above T_G and material below T_G in the surrounding. However, this radius of the boundary a_{boundary} between material being above and below T_G is similar to the

contact radius a_{contact} between tip and sample. Again, no large rim formation is possible.

In case C the global sample temperature $T_{\mathrm{Sample,global}}$ is below T_{G} and the heater temperature is high enough to bring the polymer underneath the tip $T_{\mathrm{Sample,local}}$ locally above T_{G}. Additionally, the radius of the boundary a_{boundary} between material being above and below T_{G} is larger than the contact radius a_{contact} between tip and sample. Thus, material transport to the surface is possible leading to a large rim formation as it is observed in figure 4.22.

In case D both the global sample temperature $T_{\mathrm{Sample,global}}$ is higher than T_{G} and the polymer underneath the tip $T_{\mathrm{Sample,local}}$ locally above T_{G}. No stable indentation can be formed as it is observed in figure 4.16. The entire material is easily deformable and no boundary between soft and viscous regions can be built up. The tip can easily penetrate into the polymer film, but at the same time the material is soft enough to relax and close the indentation as soon as the tip is removed. Consequently, no rim formation can be observed and the threshold of observable indentations is clearly shifted (see figure 4.16). Additionally, relaxation processes on a longer time scale have to be taken into account: As discussed in section 2.6 indentations are unstable at sample temperatures above T_{G} and relax with a time constant in the order of minutes. Since the performance of the nanoscript and the subsequent imaging takes several minutes, previously created indentations may have partially vanished between the indentation process and the subsequent imaging. As a consequence, data sets corresponding to case D (higher than 115 °C) are difficult to interpret and are not shown in the graphs.

The influence of the electro-static force on the indentation depth is shown in figure 4.24. Although the heater temperature is not constant due to the increasing sample temperature, the temperature difference between heater and sample $\Delta T = T_{\mathrm{Heater}} - T_{\mathrm{Sample}}$ is constant within an accuracy of 13 K. A clear depen-

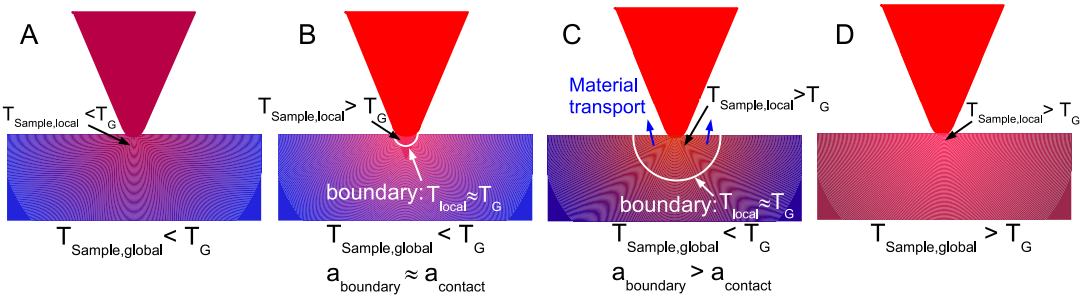

Figure 4.23: Schematic sketch of four different cases of assumed temperature distributions occurring in the indentation experiment on PMMA at different sample and heater temperatures.

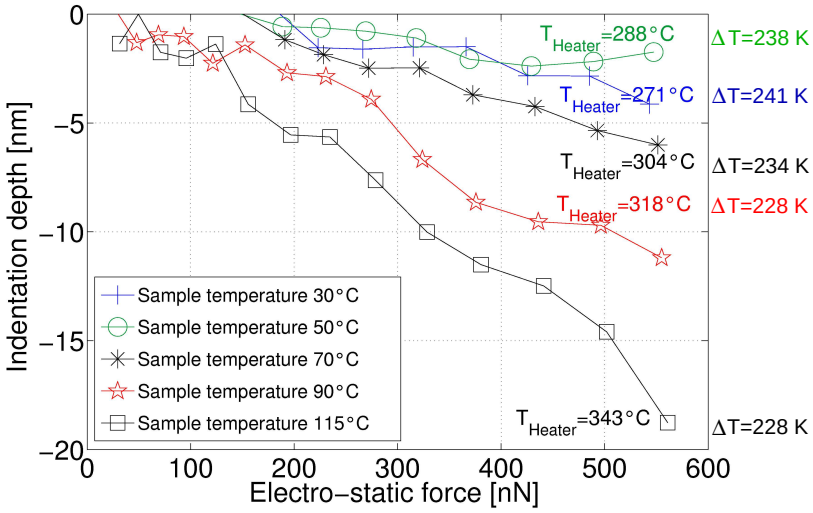

Figure 4.24: Indentation depth as function of the electro-static force at various sample temperatures. Due to the increase of the sample temperature the heater temperature is not constant. However, the temperature difference between heater and sample $\Delta T = T_{\mathrm{Heater}} - T_{\mathrm{Sample}}$ is constant within an accuracy of 13 K. Sample: 35 nm PMMA on silicon

dence of the indentation depth on the electro-static force as well as on the sample temperature can be ascertained.

So far we have focused on the PMMA sample, because of the strong temperature dependence and the presence of the glass transition on PMMA, which obviously leads to a large increase of the indentation depth as soon as the glass transition temperature is exceeded locally. We have already seen in the Contact Mode topography images in figure 4.17 that the sample temperature on SU8 plays a minor role. This observed difference between PMMA and SU8 can be readily explained by the fact that the sample temperature range reaches T_{G} of PMMA, but stays far below the T_{G} of SU8. Nevertheless, one observes a clear influence of the heater temperature on the lateral size of the indentation.

Figure 4.25 shows the indentation depth as function of the electro-static force at a constant temperature difference between heater and sample. In contrast to the equivalent measurement on PMMA (see figure 4.24) no significant influence of the heater and the sample temperature is observed and the influence of the force is much smaller than on PMMA (see figure 4.24) : If we consider for example the situation at a sample temperature of 90 °C an indentation depth of 11 nm at 560 nN is measured at a heater temperature $T_{\mathrm{Heater,PMMA}} = 318\,^{\circ}\mathrm{C}$, which corresponds to a gradient of $\approx 0.02\,\mathrm{nm/nN}$. On SU8, however, the heater temperature was even larger on PMMA ($T_{\mathrm{Heater,SU8}} = 378\,^{\circ}\mathrm{C}$). Nevertheless, we

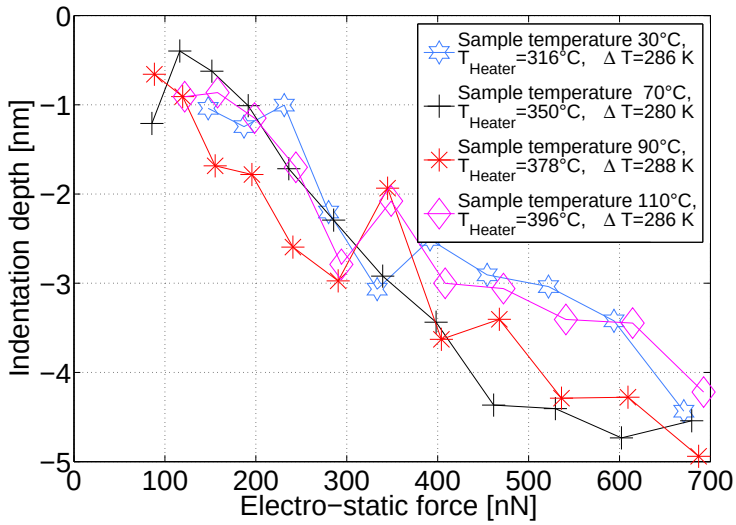

Figure 4.25: Indentation depth as function of the electro-static force at various sample temperatures. Due to the increase of the sample temperature the heater temperature is not constant. However, the temperature difference between heater and sample $\Delta T = T_{\text{Heater}} - T_{\text{Sample}}$ is constant within an accuracy of 8 K. Sample: 80 nm SU8 on silicon

find an indentation depth of only 5 nm at 700 nN being equivalent to a gradient of 0.007 nm/nN (see figure 4.25).

Figure 4.26 shows the indentation depths as function of the heater temperature at different sample temperatures. The forces applied ranged from 535 nN for the lower heater temperatures to 671 nN for the higher heater temperatures. Generally it would be possible to calculate the indentation depths for constant forces as it has been done in the case of PMMA. However, as we have already seen in figure 4.25 the influence of the electro-static force is rather small: with the gradient of 0.007 nm/nN the deviation of the indentation depth due to the increase of the force would be approximately 1 nm, which is about equal to the data noise and less than the measurement accuracy of ± 1 nm as stated above.

4.5 Chapter summary

In this chapter measurement using heatable cantilevers in a commercial SFM (D3000 by Veeco) have been shown. Both thermal imaging and high speed indentations were realized. Thermal topography imaging was demonstrated on a 2-phase polymer sample consisting of Styrene-Butadiene-Styrene and PMMA and the indentation measurements have been performed at elevated sample temper-

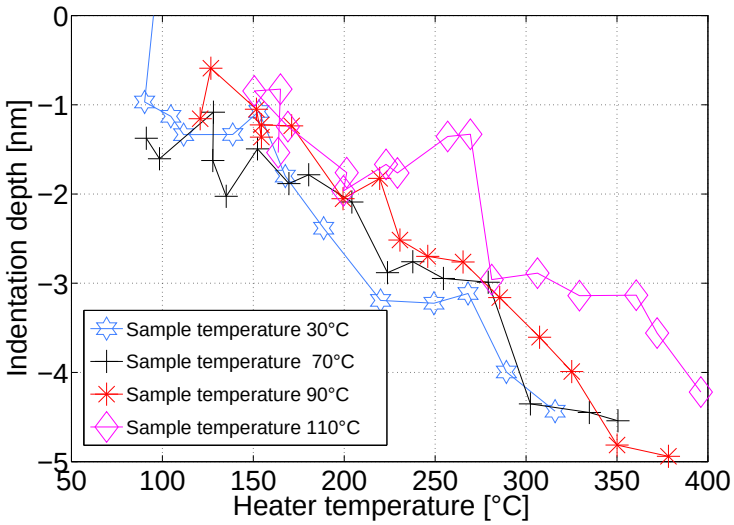

Figure 4.26: Indentation depth as function of the heater temperature at various sample temperatures. Electro-static forces of 535..671 nN were applied. Sample: 80 nm SU8 on silicon

atures on a 35 nm thin PMMA film and on a 80 nm SU8 film both on silicon. The indentation experiments were conducted at elevated sample temperatures between 30 and 130 °C. The indentation process was performed by heating the cantilever heater for 10 μs to temperatures of 80 to 400 °C and simultaneously applying an electro-static force of 20 to 550 nN. Arrays of indentations were created with varying heater temperature along the horizontal axis and changing electro-static forces along the vertical axis. These arrays were produced by making use of the so-called 'Nanoscript', which is a programming tool for the D3000/D3100 SFM similar to the programming language C. With this script language it was possible to move the tip to specific positions, to set voltages and triggers on the SAM (Signal Access Module) and to controll the entire process. The calibration procedure of the electro-static force is based on optical force distance curves measured at different DC voltages applied to the sample. With increasing sample voltage the snap-off position is shifted to larger forces needed to retract the tip from the sample making it possible to determine the electro-static force as function of the sample voltage.

Contact Mode images scanned with unheated tip using the optical deflection system have been analyzed both qualitatively and quantitatively. Whereas the influence of the sample temperature on the indentation topography on PMMA is large, on SU8 hardly any dependency of the topography on the sample temperature is observed. On PMMA both the lateral dimensions as well as the indentation depth and the rim volume increase significantly at higher sample temperatures. It has been shown, that the local sample temperature under the tip is responsible

for the indentation depth, whereas the boundary between regions being above and below T_{G} must be considered for interpretations of the rim formation.

Chapter 5

Heat transfer measurements on the nanoscale: Scanning Thermal Microscopy in vacuum

5.1 Introduction

In the previous section the heating capability of the thermal cantilevers was used to support the indentation process of the SFM tip into a polymer film. The thermal cantilever, however, can also be applied as an imaging sensor capable of high resolution scanning thermal microscopy (SThM). A first application of this type was demonstrated in section 4.3, where a thermal topography image scanned under ambient conditions was shown. Similar to the bit reading mechanism of the "Millipede" (see section 1.1.1) the thermal topography imaging capability was originated from the topography giving rise to changing distances between heater and sample. This resulted in variations of the cooling efficiency of the heater, which was used for the image generation. However, this measurement was qualitative rather than quantitative, mainly because the relative contributions of the heat transfer from the heater to the sample are not known. This, however, is a principal challenge in the field of Scanning Thermal microscopy (SThM): Although different types of thermal probes and measurement techniques have been developed and different types of samples such as integrated circuits [70], polymers [60, 71–77] or metals [78, 79] were investigated, quantitative measurements of thermophysical parameters, such as temperature, heat flux or thermal conductivity remain a problem. This is due to the fact that various paths contribute to the heat transfer between probe and sample and the relative amount of this heat transfer is difficult to determine. Under ambient conditions the heat transfer is dominated by heat conduction through air and additionally the water meniscus

caused by air humidity makes the measurements complicated. In vacuum, however, the measurement conditions are well defined and due to the absence of the air heat conduction, the direct measurement of the tip sample heat transfer can be conducted.

In this chapter, measurements shall be presented which address this issues: The heatable cantilevers discussed in chapter 3 were used in a vacuum chamber and both heat transfer measurements through the tip sample contact and thermal imaging under vacuum condition were conducted.

5.2 Heat transfer mechanisms

In this section an overview of the heat transfer mechanisms important for the operation of the thermal SFM cantilevers will be given. Figure 5.1 shows the different mechanisms under ambient conditions, which are involved when the heater platform is heated to several hundred degree Celsius:

- **Heat conduction through the cantilever legs:** Whereas the heater is at high temperatures, the chip base of the cantilever rests at room temperature. As the dimensions of the cantilever are large compared to the tip sample contact and silicon is a good thermal conductor, a large part of the heater energy is transferred to the chip base.
- **Heat conduction through the surrounding air:** A significant amount of heat is transferred to the surrounding air. If the cantilever is close to or in contact with the sample, the heat transfer to the sample is enhanced because the sample acts as a heat sink. As this mechanism is strongly dependent on the distance between heater and sample, it is used for the read operation of data bits in the "Millipede" (see section 1.1.1.1) and can be used for thermal imaging demonstrated in section 4.3. Besides thermal conduction through the air, convection could occur. However, for dimensions smaller than a few millimeters , convective cooling is negligible in comparison to heat conduction [15].
- **Radiative cooling:** This topic is interesting because the heater platform is only 300-500 nm away from the sample surface and thus near-field effects play a crucial role (see section 5.5.8).
- **Heat transfer through the tip sample point contact:** This mechanism is of main interest in this study and the experimental setup aim at separating this from the other contributions. Due to the small dimensions of the tip being significantly smaller than the phonon mean free path, confinement effects and reduced thermal conductivity of the tip are expected.

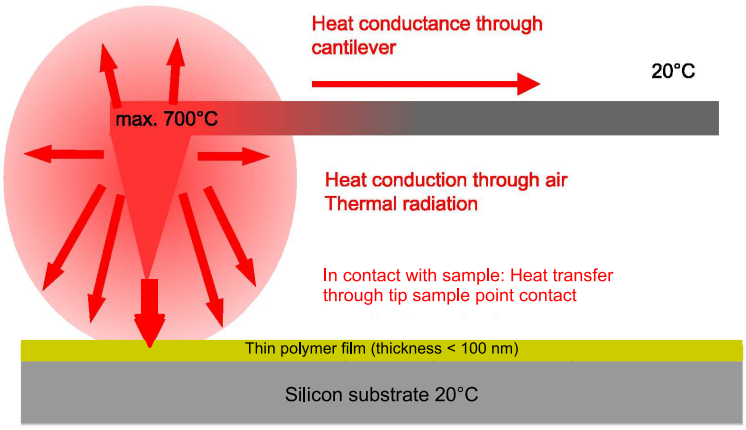

Figure 5.1: Heat transfer mechanisms under ambient conditions: Most of the heat energy is transferred through the air and the cantilever legs.

Furthermore, the mechanical coupling between tip and sample plays an important role and thus, the heat transfer to the sample will strongly depend on the pressure and on the contact area. Additionally, the thermal properties of the sample material influence the heat transfer: Similar to electro-magnetic or sound waves traveling from one medium to another, reflection and transmission of phonons occurs at the interface depending on the thermal properties and the sound velocities of each medium. Whereas in the case of electro-magnetic waves the effect is known as refraction, here it is called acoustic mismatch.
For the "Millipede" bit writing procedure the amount of energy transferred to the polymer film determines the temperature around the tip and thus the mechanical properties of the material. With the experiments presented in this chapter the direct measurement of the energy transfer is realized.

As heat conduction through the air and the cantilever legs are the dominant heat transfer paths under ambient conditions, it is difficult to measure the amount of energy transferred through the tip and the tip-sample interface. Furthermore, under ambient conditions a thin water film adsorbed on the sample surface is always present, which forms a meniscus between tip and sample and influences the heat transport.

Thus, in order to obtain defined conditions and to enable tip-sample heat transfer measurements, the heatable cantilevers were implemented in vacuum, where the heat conduction through the air is suppressed and only thermal conduction through the cantilever legs, thermal radiation and heat conduction through the tip sample contact occurs. The amount of heat transferred through the cantilever by heat conduction and by radiative cooling can be determined when the tip is not in contact with the sample. When the tip comes in contact additional cool-

ing through the tip sample contact occurs. Thus, by measuring approach curves similar to force-distance curves under vacuum conditions (i.e. at an air pressure of the order of 10^{-6} hPa) the heat transfer through the tip to the sample can be acquired.

In order to analyze the heat transfer problem, ideally all paths should be quantified. To distinguish between the different paths, experimental parameters were varied, which have influence on one or a subset of paths: distance dependence with the tip being out of contact, contact force when the tip is in contact with the sample, tip radius, sample material, heater temperature.

5.3 Experimental setup of the vacuum SFM

The measurements presented in this chapter were all carried out in a vacuum chamber, which was previously used for Scanning Tunneling Microscopy experiments [80]. The existing STM was reconstructed for use with the heatable 2-leg SFM cantilevers, which have been introduced in chapter 3. For this purpose the tip holder had to be re-designed, electrical connections for the cantilever had to be implemented and the 2 kΩ sense resistor had to be built-in to form a circuit as shown in figure 3.3. Since no optical detection system for the cantilever deflection was available in the vacuum chamber, only the thermal signal of the heater (i.e. the voltage drop across the heater, see figure 3.3) was used for the measurements.

A view into the vacuum chamber is shown in figure 5.2: The chip with a heatable SL1 type cantilever and the tip (1) is placed at the end of a tube piezo (3). The sample (2) is situated on a sample table (5), which can be moved laterally and makes it possible to select a location for the measurement. The piezo tube and the clamps (4), which provide electrical connections to the piezo and the heatable tip, are attached to a frame situated on tripod screws (6). The two tripod screws in the front shown in figure 5.2 are used for the manual coarse approach and the third screw at the back (not visible in the image) is controlled with a stepper motor for the fine approach.

The following steps are typically conducted to prepare and carry out a vacuum measurement:

- Both tip and sample are pre-characterized in an optical microscope and the tips are additionally imaged in the Scanning Electron Microscope (SEM). The samples are analyzed under ambient conditions in a commercial SFM (D3000 by Veeco) in Tapping Mode.
- For mounting tip and sample the vented vacuum chamber is opened by removing the main flange of the vacuum chamber. After mounting tip and

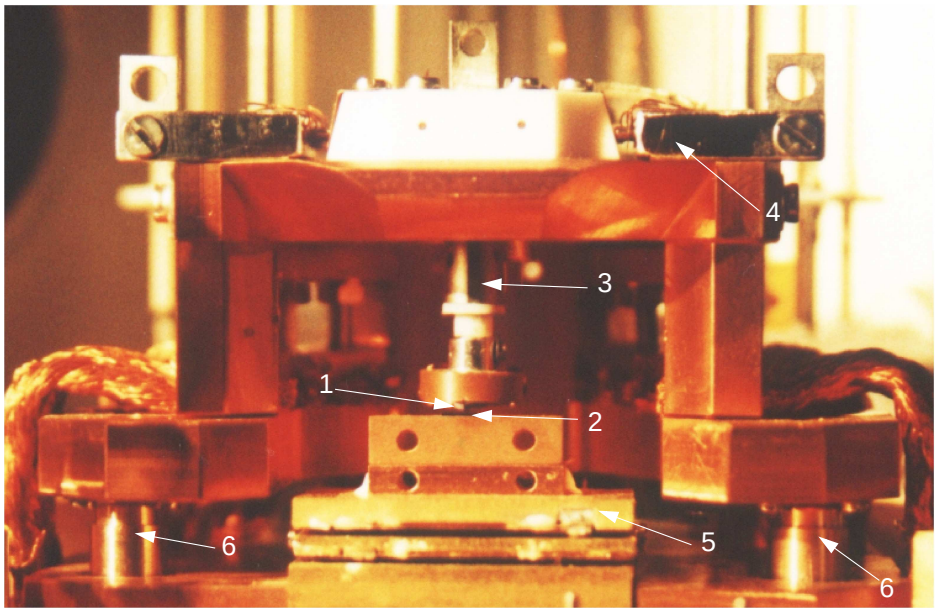

Figure 5.2: View into the vacuum chamber. The following components are marked: thermal cantilever / tip (1), sample (2), tube piezo (3), connector clamps for the tube piezo and the tip (4), movable sample table (5), tripod screws for the manual coarse-approach (6).

sample an IV curve measurement is performed to determine the electrical characteristics of the cantilever under ambient conditions.

- Then the tip approach to the sample is conducted. As the cantilever chip is mounted on a tripod frame, the tilt of the cantilever with respect to the sample surface is rather undefined. This challenge is enhanced by the small tip height of only about 500 nm and a width of the heater of several micro-meters resulting in a tolerance of the tilting angle of only $\approx \pm 2^\circ$ around the cantilever axis. With a larger tilt the cantilever legs or the heater touches the sample instead of the tip. Thus, the tip approach to the sample is a very crucial task and is conducted in two steps:

  1. For the coarse approach the tripod screws (6) in figure 5.2 are used in combination with the movable sample table (5) for the positioning of the sample with respect to the cantilever. During this operation both cantilever and sample are observed through a stereo microscope.

  2. In a second step of the approach procedure, the stepper motor controlled third tripod screw is used for the fine approach while continuously measuring approach curves, which are performed similar to the force-distance curves discussed in chapter 2. With a DC voltage applied as an input voltage the tip is moved vertically towards the

sample. As the tip approaches the surface the air conduction cooling is enhanced, which can be measured by monitoring the cantilever voltage. The snap-in can be detected in the same way. This procedure enables the tip to be brought into contact with the sample surface in a very controlled way without damaging the tip by uncontrolled movement. A detailed description of approach curves will be given in section 5.5.1.

- Once a proper adjustment is found, the tip is moved slightly away from the surface with the stepper motor and the chamber is closed by mounting the flange.
- Next, the vacuum chamber is evacuated. Like typical vacuum systems the pumping of the chamber is conducted in two steps. In the first step the chamber is evacuated with a rotary vane pump down to a pressure of 10^{-1} hPa and subsequently a turbomolecular pump is used to pump further down to pressures of 10^{-5} to 10^{-6} hPa as measured with a Bayert-Alpert gauge from Balzers.
- At pressures of 10^{-5} to 10^{-6} hPa the heat transfer through air is negligible and the experiments are carried out.
- IV curves are measured to determine the electrical characteristics of the cantilever under vacuum conditions.
- The tip is then re-approached to the sample surface again using the stepper motor, while performing approach curves.
- The measurements are then conducted.
- After finishing the experiments, the tip is retracted carefully from the sample and the chamber is vented with Nitrogen.
- When normal pressure is reached the flange can be removed again and the tip and sample can be removed.
- In most of the cases the tips are imaged in the Scanning Electron Microscope (SEM) again after the vacuum experiments.

To generate the signals necessary for the measurements (i.e. signals for the piezo tube and the supply voltages for the thermal cantilever) and for the data acquisition, a programmable 16-bit multi-channel ADC / DAC control device (ADwin Pro from Jäger Messtechnik GmbH) [81] was used. This ADwin Pro system is connected via a USB port to a Desktop PC and was programmed in *AD-Basic* [81] to conduct different measurement tasks: IV measurements (see section 5.4), thermal approach curves (see section 5.5.1), thermal imaging (see section 5.6). This system provides a very convenient interface to the mathematics software tool Matlab [69], which was used for data storage, data analysis, imaging processing and the display of the data.

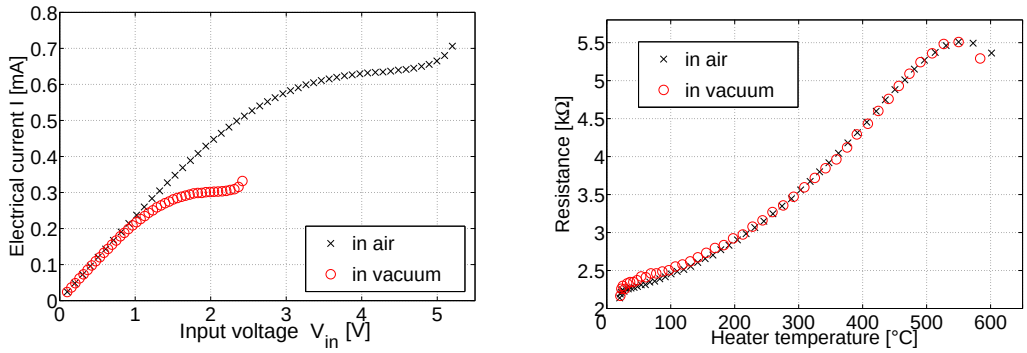

Figure 5.3: Heater electrical resistance versus input voltage (*left*) and heater electrical resistance versus heater temperature (*right*) under ambient conditions and in vacuum.

5.4 Electrical characteristics of heatable cantilevers in vacuum

Due to the different cooling mechanisms in air and vacuum the electrical characteristics of the cantilevers change significantly. Figure 5.3 shows the comparison of an IV characteristics obtained in air and in vacuum with the tip being far away from the sample. In vacuum, the cooling by air conduction is absent leading to smaller input voltages V_{in} to reach the characteristic kink, where the current increases significantly and which corresponds to the maximum of the heater resistance at 550 °C. On the other hand, the resistance versus temperature curve is in the first order independent of the cooling mechanisms and is a characteristic property of each individual cantilever. Thus, the curves measured in vacuum and air match (figure 5.3, *right*). These observations are analogous to the measurements with pulse-heated cantilevers and the tip in contact with the sample in section 4.4.2.

As discussed in chapter 3 a proportional relation between heater temperature and electrical power is assumed for the temperature calibration of the heater. The slope of this proportional relation is strongly affected by different cooling rates: In air a larger slope is measured than in vacuum, because more electrical power is required to reach a certain temperature due to the energy loss through the air cooling. This accounts for a lower thermal resistance $R_{\text{thermal}} = \Delta T / \Delta P$ of the entire system in air: In air the thermal resistance is determined to be $R_{\text{thermal,air}} = 2.0 \times 10^5\,\text{K/W}$, while in vacuum $R_{\text{thermal,vacuum}} = 9.5 \times 10^5\,\text{K/W}$ is measured from the temperature-power curves shown in figure 5.4. In section 5.5.2 the concept of thermal resistances will be introduced in more detail and thermal resistances for the various heat transport paths discussed in section 5.2 will be determined.

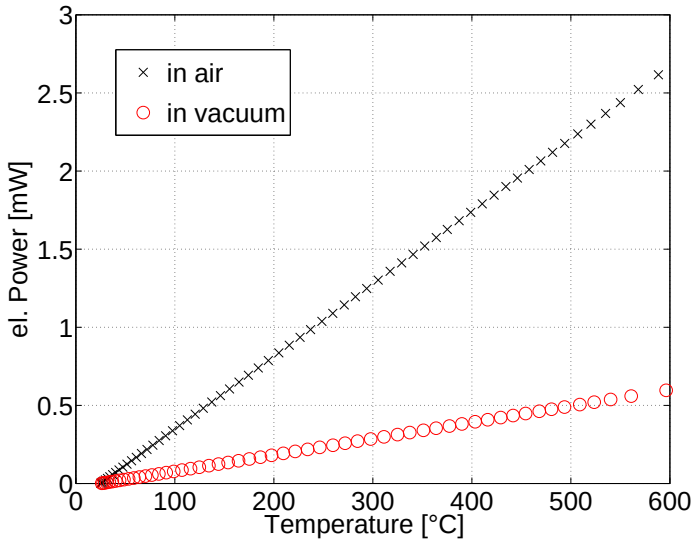

Figure 5.4: Comparison of the heater calibration under ambient conditions and in vacuum.

5.5 Heat transfer measurements with the vacuum SFM

5.5.1 Thermal approach curves

In order to measure the heat transfer from the heater through the tip to the sample, thermal approach curves were performed. Thermal approach curves are conducted in the same way as the force distance curves discussed in section 2.2 and shown in figure 2.1: The initial starting point of the tip is approx. 1 μm above the sample surface. The tip is then displaced towards the sample, resulting in an increase of the attractive tip-sample force. When this attractive force acting on the cantilever exceeds the stiffness of the cantilever, the tip snaps into contact with with the sample. Further displacement of the piezo results in an increase of the tip-sample force. After moving a pre-programmed distance, the piezo movement is reversed and the tip is retracted until it is released from the surface. All thermal approach curves presented in this study have been measured with a frequency of 1 Hz, i.e. the time for the complete approach and retract procedure was 1 second. During this approach and retract cycle the input voltage V_{in} is kept constant and the cantilever voltage V_{Lever} is recorded as a function of the cantilever position. In combination with the resistance versus heater temperature curve obtained from the temperature calibration procedure (see section 3.3) the heater temperature as function of the piezo displacement can be calculated.

Figure 5.5 shows a comparison of approach curves in air (*left*) and under vacuum conditions at at a pressure of $p = 8 \times 10^{-5}\,\mathrm{hPa}$ (*right*) both measured with a constant input voltage on a silicon sample. The start and end points of the approach curve are marked and the direction of the piezo displacement is labelled. Additionally, the snap in and snap off points are marked.

Under ambient conditions (figure 5.5, *left*) the cooling efficiency through the air conduction increases as the heater approaches the surface. This leads to a decreasing heater temperature as long as the tip is not in contact with the sample. In the contact region, however, the heater temperature is approximately constant, because the distance between heater and sample is fixed. The distance dependence of the heater temperature near the sample surface is exploited for the read procedure in the "Millipede" concept (see section 1.1.1.1). In the example shown in figure 5.5 (*left*) the tangent of the curve just before the tip snaps to the surface has a slope of $35\,\mathrm{K}/\mu\mathrm{m} = 0.035\,\mathrm{K/nm}$. This corresponds to a sensitivity of the thermal signal of $\frac{\partial}{\partial z} V_{\mathrm{Lever}} = 3.68 \times 10^{-5}\,\mathrm{V/nm}$.

In vacuum the distance dependent off-contact cooling effect is absent and the temperature is constant as long as the tip is not in contact with the surface (figure 5.5, *right*). At high heater temperatures of about 600 °C distance dependent radiative cooling becomes detectable, which will be presented and discussed in section 5.5.8. With the comparatively moderate heater temperatures of 311 °C used in figure 5.5 (*right*) the distance dependent radiative cooling is not measurable.

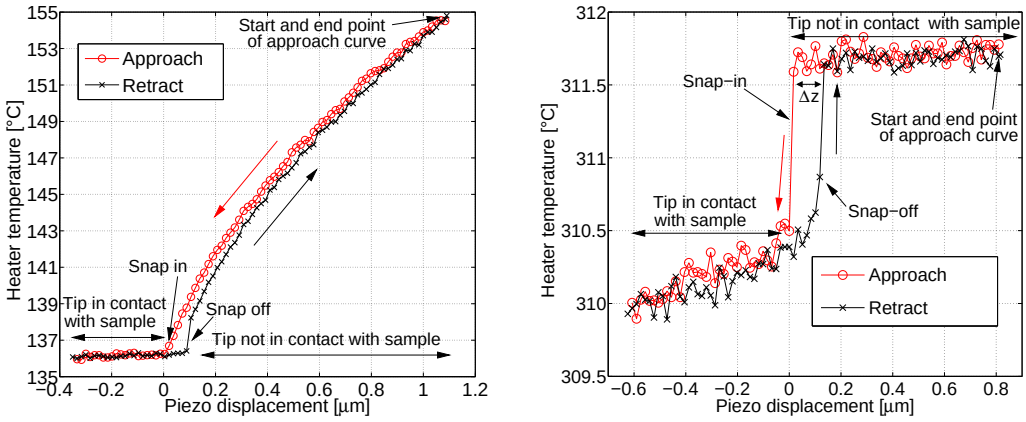

Figure 5.5: Thermal approach curves under ambient conditions (*left*) and in vacuum at a pressure of $p = 8 \times 10^{-5}\,\mathrm{hPa}$ (*right*) both measured on a silicon sample. The arrows denote the direction of the piezo movement. Note the different scales on the ordinate axis corresponding to a larger cooling effect under ambient conditions.

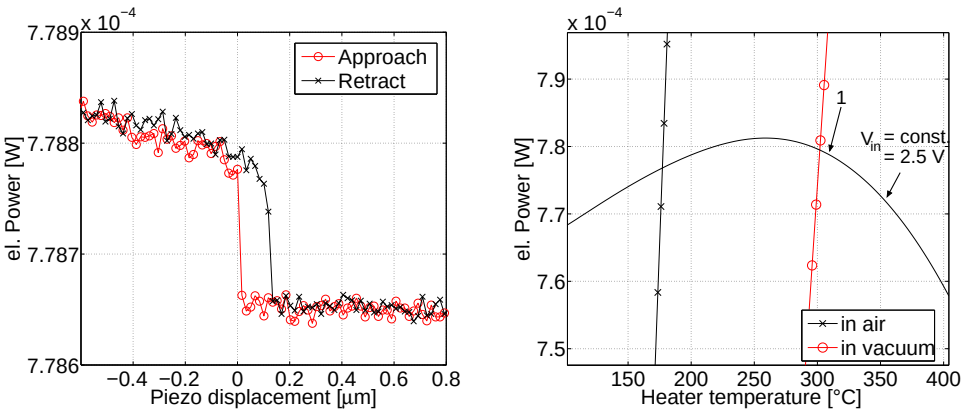

Figure 5.6: Distance dependence of heater power during a thermal approach curve in vacuum (*left*); Heater power as function of heater temperature for a constant input voltage of $V_{in} = 2.5$ V (*right*).

In the off-contact part of the approach curve in figure 5.5 (*right*) all heat produced in the heater is passed through the cantilever beams to the chip body, where the cantilever is mounted on. When the tip comes in contact with the sample, heat energy is additionally transferred from the heater through the tip to the sample and the heater is additionally cooled by the tip sample contact. Note, that in vacuum the heater temperature in contact depends on the piezo displacement, which is due to the fact that the contact radius increases as the contact pressure becomes larger. Furthermore, in the examples shown in figure 5.5 the overall temperature decrease in vacuum due to the tip-sample heat transfer is only 1.7 °C while in air the decrease of the temperature is approx. 18 °C even though the initial heater temperature is smaller in air than in vacuum. Thus, the cooling through the air is much more efficient than through the tip-sample contact as we will see in more detail in section 5.5.2, where the approach curves will be analyzed quantitatively.

Figure 5.6 shows the electrical power generated in the heater $P_{\mathrm{el,Heater}}$ during the approach cycle, which is calculated from the measured data V_{in} and $V_{\mathrm{Cantilever}}$ by $P_{\mathrm{el,Heater}} = V_{\mathrm{Cantilever}} \cdot I = V_{\mathrm{Cantilever}} \cdot (V_{\mathrm{in}} - V_{\mathrm{Cantilever}})/R_{\mathrm{Sense}}$. When the tip jumps into contact with the sample the power increases even though the temperature drops by 1.2 °C as is observed in figure 5.5. At first glance this observation is surprising, but can be explained considering the right part of figure 5.6. The heater power P as function of the heater temperature T is plotted for the constant V_{in} voltage of 2.5 V, which has been used for the approach curve measurement. Additionally, the straight calibration lines in air and in vacuum are shown. When the tip approaches the surface in the off contact region it has a temperature of 311.7 °C as observed in figure 5.5. This corresponds to point 1 in the right diagram of figure 5.6. Coming in contact with the sample the heater temperature drops

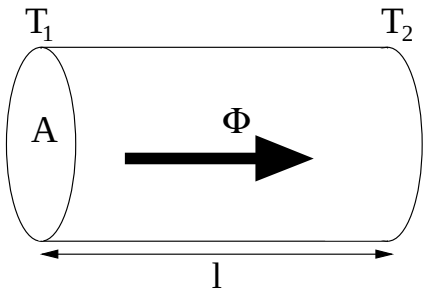

Figure 5.7: Quantities involved in Fourier's law.

to 310.5 °C. Since the slope of the $P-T$ curve at point 1 is negative, an increase of the power is observed in the approach curve.

Determination of adhesion from approach curves

An approach curve contains not only information about the heat transfer between heater and sample, but also about the adhesion force between tip and sample. Usually in a regular SFM setup with a laser detection system the adhesion is measured from the cantilever deflection at the snap-off point (see figure 2.1 in section 2.2), i.e. from the difference of the cantilever deflection at the snap-off and the undeflected cantilever in the off-contact region. In our case of the vacuum SFM no laser detection system is implemented and thus, the adhesion force has to be determined from the approach curves by measuring the piezo displacement Δz between snap-in and snap-off (see figure 5.5) and multiplying this with the cantilever's spring constant k

$$F_{\text{Adhesion}} \approx \Delta z \cdot k. \tag{5.1}$$

This neglects the fact, that the cantilever is deflected at the snap-in point and exerts a force pointing away from the sample. Since this is only a relatively small contribution the adhesion force can be determined with this method with sufficient precision and will be used in section 5.5.4 to determined the dependence of the heat transfer on the adhesion force.

5.5.2 Data analysis of approach curves in vacuum

To analyze the data of the thermal approach curves measured under vacuum conditions, one makes use of the concept of thermal resistances and Fourier's law, which is analogous to Ohm's law for the electrical case. Fourier's law states, that the heat flux density $\vec{\Phi}$ depends linearly on the temperature gradient ∇T:

$$\vec{\Phi} = k \cdot \nabla T \tag{5.2}$$

where k denotes the thermal conductivity of the material. For the simple case that two bodies of different temperatures T_1 and T_2 respectively are in contact with each other as shown in figure 5.7, Fourier's law simplifies to

$$\vec{\Phi} = k \cdot \frac{T_1 - T_2}{l} \vec{e} \tag{5.3}$$

with $\vec{e}$ being the unit vector pointing from one body to the other as indicated by the arrow in figure 5.7.

The specific thermal resistance ρ is related to the thermal conductivity by $\rho = k^{-1}$ and is given by

$$\rho = k^{-1} = \frac{T_1 - T_2}{l \cdot \Phi} = \frac{\Delta T}{l \cdot \Phi} \tag{5.4}$$

where the norm of the heat flux energy density Φ is given as

$$\Phi = W \,/\, (A\, t). \tag{5.5}$$

The absolute thermal resistance R_{th} is related to the specific thermal resistance by

$$\rho_{\mathrm{th}} = \frac{A}{l} R_{\mathrm{th}} \tag{5.6}$$

Thus, Fourier's law can be rewritten in terms of the absolute thermal resistance R_{th}:

$$R_{\mathrm{th}} = \frac{\Delta T}{P} \tag{5.7}$$

with P being the the energy transferred per time through the absolute thermal resistance R_{th}.

Now, the concept of thermal resistances will be applied to the case of the heatable cantilevers under vacuum conditions: In our case the heater is at an elevated temperature and heat is transferred through the cantilever to the chip body, that the cantilever is mounted on, and to the sample, if the tip is in contact with the sample. Both sample and chip are at room temperature RT. For the sample this is only true far away from the tip-sample contact whereas near this contact point an elevated temperature field will build up.

To calculate the thermal tip sample contact resistance $R_{\mathrm{th,Tip\text{-}Sample}}$, the approach curves are analyzed as shown in figure 5.8. When the tip is not in contact with the sample, heat is dissipated by heat conductance through the cantilever legs and thermal radiation. These two thermal resistances shall be combined to one thermal resistance $R_{\mathrm{th,Cantilever,Radiation}}$ and is calculated using Fourier's law:

$$R_{\mathrm{th,Cantilever,Radiation}} = \frac{T_{\mathrm{Heater,oc}} - \mathrm{RT}}{P_{\mathrm{Heater,oc}}} \tag{5.8}$$

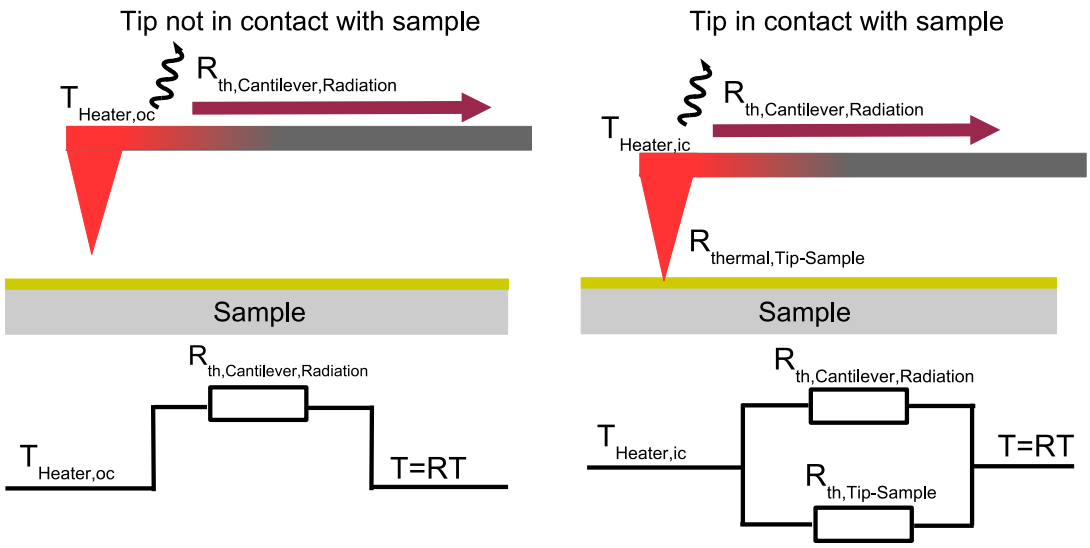

Figure 5.8: Analysis of thermal approach curves under vacuum conditions.

When the tip is in contact with the sample the heat is transferred through the combined thermal resistance of the cantilever legs and thermal radiation $R_{\mathrm{th,Cantilever,Radiation}}$ and the tip sample contact resistance $R_{\mathrm{th,Tip\text{-}Sample}}$, which form a parallel connection. As in the electrical case, the resistance is given by

$$\frac{1}{R_{\mathrm{th,Contact}}} \approx \frac{1}{R_{\mathrm{th,Cantilever,Radiation}}} + \frac{1}{R_{\mathrm{th,Tip\text{-}Sample}}} \tag{5.9}$$

This is an approximation, because the thermal resistance $R_{\mathrm{th,Cantilever,Radiation}}$ is assumed to be constant for the tip being in and off contact with the sample. Due to the temperature decrease of the heater when the tip comes in sample contact, the thermal radiation will decrease and therefore the combined thermal resistance $R_{\mathrm{th,Cantilever,Radiation}}$ will also change slightly. However, this change will be small, because the contribution of the radiation is small compared to the thermal conductance through the cantilever legs. Furthermore, the temperature drop of the heater is relatively small between in and off contact. Thus, the above assumption is justified and $R_{\mathrm{th,Cantilever,Radiation}}$ can be regarded to be constant. In chapter 5.5.8 the radiative heat transfer will be discussed in more detail and its relative contribution will be shown to be comparable small.

From equation 5.9 we obtain

$$R_{\mathrm{th,Tip\text{-}Sample}} \approx \left(\frac{1}{R_{\mathrm{th,Contact}}} - \frac{1}{R_{\mathrm{th,Cantilever,Radiation}}} \right)^{-1} \tag{5.10}$$

with $R_{\mathrm{th,Contact}}$ being

$$R_{\mathrm{th,Contact}} = \frac{T_{\mathrm{Heater,ic}} - \mathrm{RT}}{P_{\mathrm{Heater,ic}}} \tag{5.11}$$

The following example shall point out the calculation of the thermal contact resistance:

- The heater temperature in the off-contact region of the approach curve shown in figure 5.5 is $T_{\text{Heater,oc}} = 311.7\,^{\circ}\text{C}$ and $T_{\text{Heater,ic}} = 310.5\,^{\circ}\text{C}$ at the snap in.
- The corresponding heater powers are $P_{\text{Heater,oc}} = 7.7865 \times 10^{-4}\,\text{W}$ and $P_{\text{Heater,ic}} = 7.7877 \times 10^{-4}\,\text{W}$ (see figure 5.6).
- Thus, the combined thermal resistance of the cantilever legs and the thermal radiation is

$$R_{\text{th,Cantilever,Radiation}} = \frac{T_{\text{Heater,oc}} - \text{RT}}{P_{\text{Heater,oc}}} = 3.682 \times 10^{5}\,\text{K/W} \tag{5.12}$$

- The contact thermal resistance of the parallel connection is

$$R_{\text{th,Contact}} = \frac{T_{\text{Heater,ic}} - \text{RT}}{P_{\text{Heater,ic}}} = 3.666 \times 10^{5}\,\text{K/W}. \tag{5.13}$$

- With equation 5.10 the thermal contact resistance of the tip-sample contact is determined to be

$$\boxed{R_{\text{th,Tip-Sample}} = 8.5 \times 10^{7}\,\text{K/W}.}$$

Thus, it turns out that the thermal resistance of the cantilever is about 230 times smaller than the thermal resistance of the tip-sample contact and thus under vacuum conditions only

$$\frac{R_{\text{th,Tip-Sample}}}{R_{\text{th,Contact}}} \approx 0.004 = 0.4\,\% \tag{5.14}$$

of the energy produced in the cantilever heater is transferred to the sample in this example.

The error in the calculated thermal contact resistance, however, is large due to the large uncertainty in the temperature calibration. The error of the thermal resistance value is also afflicted with a large error and thus, we will assume an error of 30 % in the following.

From the analysis of the thermal approach curves and the results of the thermal resistances we can deduce the relative contributions of each path for the "Millipede" bit writing procedure when the heatable cantilevers are operated under ambient conditions. As discussed in section 5.4 (see figure 5.4) the overall thermal resistance of the heatable SL1 type cantilevers operated under ambient conditions is $R_{\text{th,Air,Cantilever,Rad,IV}} = 2.0 \times 10^{5}\,\text{K/W}$. This is deduced from the

IV-curve measurement under ambient conditions, which is conducted when the tip is far away from the sample. In this case heat is transferred through the cantilever legs, radiation and through the surrounding air. Since we have determined the combined thermal resistance of the cantilever legs and radiation from the vacuum measurement as shown above ($R_{\mathrm{th,Cantilever,Radiation}} = 3.682 \times 10^5\,\mathrm{K/W}$) we can calculate the contribution of the thermal conduction of the surrounding air:

$$\frac{1}{R_{\mathrm{th,Air,Cantilever,Radiation,IV}}} = \frac{1}{R_{\mathrm{th,Cantilever,Radiation}}} + \frac{1}{R_{\mathrm{th,Air,IV}}} \tag{5.15}$$

$$\frac{1}{R_{\mathrm{th,Air,IV}}} = \frac{1}{R_{\mathrm{th,Air,Cantilever,Radiation,IV}}} - \frac{1}{R_{\mathrm{th,Cantilever,Radiation}}} \tag{5.16}$$

With the above values we obtain a thermal resistance of $R_{\mathrm{th,Air,IV}} = 4.4 \times 10^5\,\mathrm{K/W}$.

During the bit writing, however, the heater is closer to the sample and cooling by thermal conduction through air conduction to the sample is enhanced. Thus, we take the thermal approach curve measured under ambient conditions into account: It is measured that the heater is at a temperature of 127.9 °C and has a power of 0.77 mW on the approach part just before the snap-in. At this point the heater is close to the sample such that it is comparable to the case of the bit writing and the tip is not in contact with the sample yet. Thus, the corresponding thermal resistance is $R_{\mathrm{th,snap\ in}} = \Delta T\,/\,P = 1.3 \times 10^5\,\mathrm{K/W}$. Again the contribution of the air cooling $R_{\mathrm{th,Air,snap\ in}}$ can be worked out:

$$\frac{1}{R_{\mathrm{th,snap\ in}}} = \frac{1}{R_{\mathrm{th,Air,snap\ in}}} + \frac{1}{R_{\mathrm{th,Cantilever,Radiation}}} \tag{5.17}$$

$$\frac{1}{R_{\mathrm{th,Air,snap\ in}}} = \frac{1}{R_{\mathrm{th,snap\ in}}} - \frac{1}{R_{\mathrm{th,Cantilever,Radiation}}} \tag{5.18}$$

and one obtains a value of $R_{\mathrm{th,Air,snap\ in}} = 2 \times 10^5\,\mathrm{K/W}$, which is about a factor of 2.2 smaller than $R_{\mathrm{th,Air,IV}} = 4.4 \times 10^5\,\mathrm{K/W}$, because the heater is close to the sample. Table 5.1 gives an overview of the thermal resistances involved in the heat transfer for the particular tip that was used in the experiments described in this section.

In the next section we will see that the thermal contact resistance on the 35 nm thin PMMA film is larger than that on the silicon sample, which was used so far (see figure 5.10): $R_{\mathrm{th,Tip\text{-}Sample,Polymer\ film}} = 2.0 \times 10^8\,\mathrm{K/W}$. Thus, from the thermal resistances one can conclude the relative contributions of the heat transfer during the bit writingIt turns out that $\approx$64.9% of the power produced in the heater is transferred through the air, $\approx$35.0% through the cantilever and only $<$0.1% flows through the tip sample contact and is used for the indentation process. For the "Millipede" reading process, however, a large heat transfer through the air is required in order to obtain a good sensitivity.

Thermal resistance	**Variable**	**Value [K/W]**
Thermal tip sample resistance on silicon	$R_{\text{th,Tip-Sample}}$	8.50×10^7
Thermal resistance of air (heater far away from sample)	$R_{\text{th,Air,IV}}$	4.4×10^5
Thermal resistance of air (heater close to sample)	$R_{\text{th,Air,snap in}}$	2×10^5
Combined thermal resistance of cantilever and radiation	$R_{\text{th,Cantilever,Radiation}}$	3.7×10^5

Table 5.1: Comparison of thermal resistances involved in the heat transfer from the heater through the tip to the sample and determined with the vacuum SFM for this particular tip used in the experiments of this section.

The thermal resistance of the tip sample contact, however, depends on various parameters such as mechanical and thermal properties of the tip and sample materials, tip radius and loading force. In the next sections different experiments will be shown which explore these aspects: Thermal contact resistances were measured with tips of different radii and apex angles in order to obtain an understanding of the influence of the tip size (section 5.5.5). Additionally, the thermal contact resistances of a continuously worn tip were measured and the adhesion between tip and sample was used as a measure of the contact radius between tip and sample (section 5.5.4). In the next section measurements on different samples such as the PMMA film on silicon and the silicon substrate will be presented in order to investigate the effect of different materials on the thermal tip-sample thermal contact resistance.

5.5.3 Thermal approach curves on PMMA and silicon

So far thermal approach curves measured on a silicon substrate have been considered. Now we will focus on thermomechanical properties of the 35 nm PMMA film on silicon and compare the results with the measurements on silicon. The PMMA sample used here is identical to the sample investigated in chapters 2 and 4 and the sample preparation has been described in section 2.4.

Figure 5.9 shows the comparison of approach curves measured on silicon and PMMA. Both measurements were conducted with the same tip and at comparable heater temperatures under vacuum conditions. Thus, the differences in the curves arise from the fact that PMMA and silicon exhibit different thermomechanical material properties. On silicon a relatively large jump of the heater temperature of $\Delta T_{\text{Heater}} = T_{\text{Heater,oc}} - T_{\text{Heater,ic}} = 267.8\,^{\circ}\text{C} - 266.8\,^{\circ}\text{C} = 1.0\,^{\circ}\text{C}$ at the snap in is observed, whereas on PMMA the drop is only about 0.3 - 0.4 °C. This difference

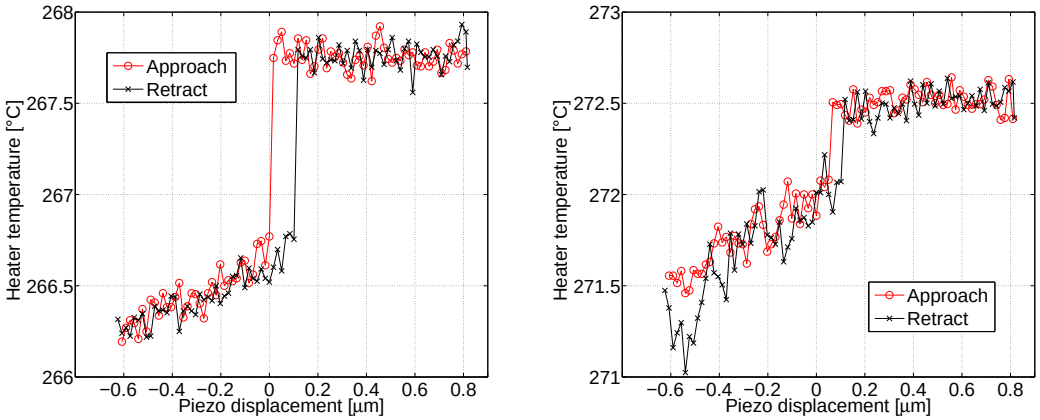

Figure 5.9: Comparison of thermal approach curves measured with the same tip on silicon (*left*) and PMMA (*right*).

originates from the higher thermal conductivity of silicon leading to a stronger cooling effect. However, one also has to take interface effects and different contact radii on both materials into account, which could also lead to different extents of the cooling effect. In section 5.5.3.2 the different contributions to the entire thermal contact resistance will be discussed and in section 5.5.3.3 the measured data will be correlated with a theoretical model.

5.5.3.1 Dependence of the thermal contact resistance on heater temperature

With the approach curves discussed in the last section the thermal contact resistances on both samples (silicon and PMMA) can be calculated in the same way as in the example in section 5.5.2. One question arising from this experiment is, whether the thermal contact resistances depend on the heater temperature.

To investigate this question thermal approach curves with different input voltages resulting in changing heater temperatures were measured on both samples. The result of this experiment is shown in figure 5.10. Plotted are the thermal contact resistances measured with the same tip on the PMMA film and on the silicon sample respectively, as a function of the heater temperature, which is determined at the point where the tip jumps into contact with the sample, i.e. right after the snap in.

One observes that the thermal contact resistance on PMMA depends significantly on the heater temperature whereas it is constant on silicon. A possible interpretation of this observation is the following: With increasing heater temperatures the PMMA material around the tip is heated up to higher temperatures and

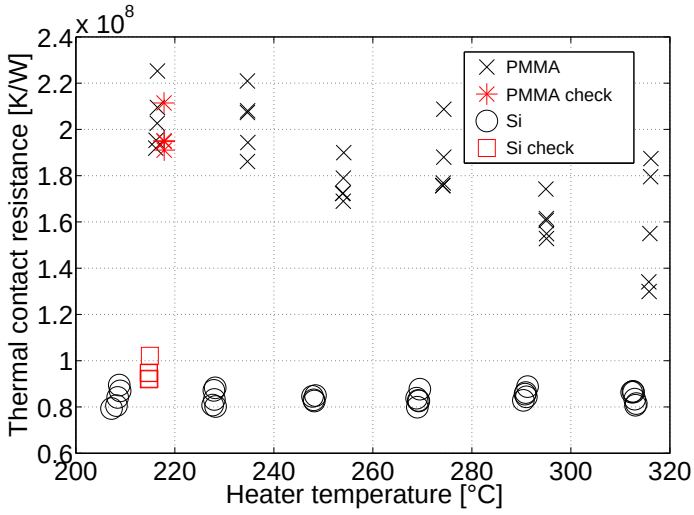

Figure 5.10: Comparison of thermal contact resistances on silicon and PMMA measured with the same tip. The data point marked with the symbols $*$ and $\square$ have been obtained after the measurements with higher heater temperatures in order to check the reproducibility.

becomes softer. This softening effect leads to an enhanced deformation of the surface resulting in an increasing contact area between tip and PMMA, which in turn causes the reduced thermal resistance at higher heater temperatures. On silicon, however, neither the material becomes soft nor the tip deforms the sample surface significantly and therefore the thermal resistances are independent from the heater temperature.

In order to check the reproducibility, the measurements with the lowest heater temperature (215 and 218 °C) have been repeated after the measurements with the higher heater temperatures (data plotted with the symbols $*$ and $\square$). These values show that the measurement is indeed reproducible and no significant tip wear or tip contamination occurred during the experiment.

The measurement shown in figure 5.10 furthermore demonstrates that different thermomechnical material properties lead to changing thermal contact resistances between tip and sample. This observation can be utilized in an imaging mode: Scanning the tip with constant input voltage over the sample surface leads to changing contact resistances, which can be used for the generation of an image. These varying contact resistances can originate from either topography effects as it will be shown in section 5.5.6 or due to different materials (see section 5.6).

In figure 5.10 the error bar are omitted for clarity. However, we have seen in section 5.5.2 that the determination of the thermal contact resistance is afflicted with an error of 30 % due to the large uncertainties of the heater temperature

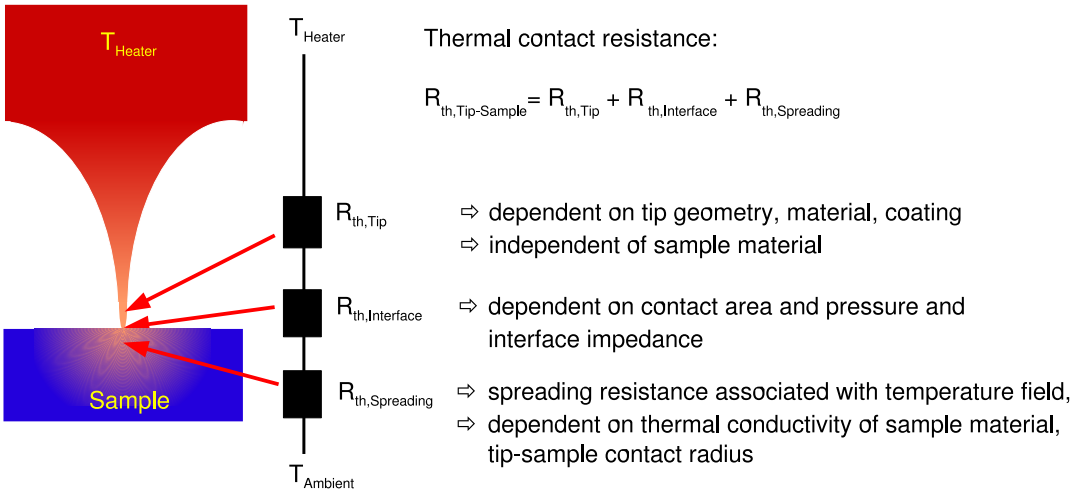

Figure 5.11: Schematic sketch of the thermal resistances involved in the thermal tip-sample contact resistance.

calibration. Thus, the absolute errors are large and for example for the highest heater temperatures the error intervals of the PMMA and silicon data overlap: On PMMA the lower limit of the error interval is at $0.91 \times 10^8\,\mathrm{K/W}$ and the upper limit of the error on silicon is at $1.04 \times 10^8\,\mathrm{K/W}$. However, since the same tip has been used for the measurements on PMMA and silicon and thus, the relative error have to be taken into account, which is - as we will see in the section 5.6.3.2 - by far smaller and allows the relative determination of the heater temperature with a resolution of better than 0.1 K.

5.5.3.2 Contributions to thermal tip sample contact resistance

As shown in figure 5.10 the thermal contact resistances on silicon are significantly smaller than those on PMMA: Assuming an absolute error of the heater temperature calibration of 30 % the mean thermal contact resistance on silicon is $R_{\mathrm{TS,Si}} = (8.6 \pm 2.6) \times 10^7\,\mathrm{K/W}$ and $R_{\mathrm{TS,PMMA}} = (2.0 \pm 0.6) \times 10^8\,\mathrm{K/W}$ on PMMA at low heater temperature of about 216 °C (see figure 5.10). Since the identical tip has been used in both experiments, one can exclude that the different thermal contact resistances originate from the tip. Thus, this effect must be due to the different thermal and mechanical properties of the two materials. In this section theoretical considerations concerning the thermal contact resistances will be discussed, which will be applied to the analysis of the measured data in the next section.

In the previous section the analysis of the approach curves using the concept of thermal contact resistances was explained. In fact, the thermal tip-sample

resistance $R_{\text{th,Tip-Sample}}$ is made up of different contributions as it is illustrated in figure 5.11 for the simple case that the tip is in contact with a sample, which is not covered with an additional layer:

- **The thermal resistance of the tip $R_{\text{th,Tip}}$:** The heat conductivity of the tip differs from bulk silicon material because of the geometric confinement at the tip apex [82]. I.e. the tips used in these experiments have a radius of 5-20 nm, but the mean free path of longitudinal acoustic phonons (LAP) have been measured to be about 300 nm for silicon [83]. Other studies [84] predict a substantial reduction of the heat transport near a heated source in a crystalline film, both having critical dimensions small compared to the LAP mean free path. Thus, phonon scattering at the tip walls will decrease the thermal conductivity at the very end of the tip. For an estimation of the thermal resistance of the tip predictions for the thermal resistivity of nano wires can be used [85]. Taking the varying diameter of the tip into account leads to a predicted thermal resistance of the tip of 10^6-10^7 K/W [15], which is confirmed by finite element simulations [86]. Additionally, further effects like the apex angle of the tip, impurities of the material and the oxide cap covering the silicon tip play a role. The oxide cap can theoretically be treated as a tunneling barrier for phonons [87] resulting in an additional thermal resistance of 10^7-10^8 K/W. Thus, the total thermal resistance of the tip is expected to be 10^7-10^8 K/W [15].

- **The interface thermal resistance $R_{\text{th,Interface}}$:** The interface between tip and sample makes up an additional thermal resistance: Similar to electro-magnetic or sound waves traveling from one medium to another, phonon reflection and transmission occurs at the interface depending on the media involved [88]. Additionally, the contact radius plays an important role, which in turn depends on the contact pressure and the mechanical material properties of tip and sample as well as on the their roughness. For a quantitative analysis the interface thermal resistance $R_{\text{th,Interface}}$ is written in the form:

$$R_{\text{th,Interface}} = \frac{r_{Int}}{\pi a^2} \tag{5.19}$$

  where r_{Int} is a constant describing the above mentioned phonon interface coupling and a is the radius of the tip sample contact. Whereas the contact radius can be determined using appropriate contact models such as the JKR model [89], the DMT model [90] or other contact models [91], values for the interface constant r_{Int} are difficult to obtain. Calculations lead to a value of $r_{Int} = 2.1 \times 10^{-9}\,\text{Km}^2/\text{W}$ [86] for an ideal silicon tip in contact with a PMMA sample. Experiments using large interface areas found $r_{Int} = 10^{-8}$ to $10^{-9}\,\text{Km}^2/\text{W}$ [92, 93]. However, experimental data with AFM tips necessary to analyze the thermal contact resistances in figure 5.10 have not been reported yet.

- **The spreading resistance of the sample surface $R_{\mathbf{th,Spreading}}$:** As figure 5.11 illustrates a temperature field builds up in the sample surface underneath the tip-sample contact. The so-called spreading resistance $R_{\mathrm{th,Spreading}}$ is associated with this temperature field and depends on the thermal conductivity k_{Sample} of the sample material and the contact radius a between tip and sample [94]:

$$R_{\mathrm{th,Spreading}} = \frac{1}{4\,k_{\mathrm{Sample}} \cdot a} \tag{5.20}$$

  If a film of thickness t is present on a substrate the spreading resistance can be calculated in the following way:

$$R_{\mathrm{th,Spreading}} = \frac{1}{4\,k_{\mathrm{Film}} \cdot a} - \frac{1}{2\pi \cdot k_{\mathrm{Film}} \cdot t} \ln\left(\frac{2}{1 + \frac{k_{\mathrm{Film}}}{k_{\mathrm{Substrate}}}}\right) \tag{5.21}$$

  where k_{Film} and $k_{\mathrm{Substrate}}$ denote the thermal conductivity of the film and the substrate material respectively.

Using the above model we can estimate the influence of different material parameters on the thermal contact resistances. Two parameters play a main role: the thermal conductivity and the Young's modulus. The thermal conductivity of the sample material determines the spreading resistance directly, whereas the Young's modulus has influence on the contact radius, which in turn affects the spreading resistances and the thermal interface resistance. The thermal conductivity of polymers, however, is known to be dependent on temperature and pressure. Thus, we have to take into account, that the thermal conductivity of the PMMA film underneath the tip [1] deviates from the bulk value measured under ambient conditions: The thermal conductivity of polymers is increased by a factor of up to 2 at a pressure of 1 GPa [95]. The literature value for the thermal conductivity of bulk PMMA at 100 °C and normal pressure is 0.25 W/mK [20] and consequently we have to take values of up to 0.5 W/mK into account.

One can estimate the spreading resistance on PMMA and on silicon: With an assumed contact radius of 5 nm we expect values of 0.9 to 1.9×10^8 K/W for the spreading resistance on PMMA using equation 5.21. In this example the second term in equation 5.21 is only a correction of $\approx 6\,\%$ and thus, we can conclude, that the influence of the substrate is small. On the silicon sample we expect a smaller contact radius of around ≈ 1 nm, because of the larger Young's modulus. A smaller contact radius would increase the spreading resistance. The thermal conductivity of silicon, however, is about a factor of 500 larger than that of

[1] A rough estimation of the pressure underneath the tip leads to 600 MPa, if typical values for the spring constant (0.1 N/m), the cantilever deflection (500 nm) and the contact area (5 nm) are assumed.

PMMA ($k_{\text{silicon}} = 130\,\text{W/mK}$, [96]) and thus, the spreading resistance on silicon is a factor of 100 smaller than on PMMA: $R_{\text{th,Spreading,silicon}} = 1.9 \times 10^6\,\text{K/W}$ as calculated with equation 5.20.

As shown in figure 5.11 the three thermal resistances are in series and thus, the sum of them gives the thermal tip-sample thermal resistance $R_{\text{th,Tip-Sample}}$

$$R_{\text{th,Tip-Sample}} = R_{\text{th,Tip}} + R_{\text{th,Interface}} + R_{\text{th,Spreading}} \tag{5.22}$$

As only the sum $R_{\text{th,Tip-Sample}}$ can be measured with thermal approach curves, the question arises as to which extent each of these thermal resistances contributes to the measured tip-sample thermal resistance. In the next section the concepts of the different thermal resistances will be applied to the data measured on silicon and PMMA in order to gain a deeper understanding.

5.5.3.3 Quantitative analysis of the thermal resistances on silicon and PMMA

In the last section theoretical considerations and estimations have been made or literature values have been given for the thermal resistances. In this section the measured data shall be correlated to the thermomechanical properties of both materials.

According to equation 5.22 the total thermal tip-sample resistance on silicon $R_{\text{TS,Si}}$ and PMMA $R_{\text{TS,PMMA}}$ respectively are given by

$$\begin{aligned} R_{\text{TS,Si}} &= R_{\text{Tip}} + R_{\text{Si,Int}} + R_{\text{Si,Spreading}} \\ &= R_{\text{Tip}} + \frac{r_{\text{Int,Si}}}{\pi \cdot a_{\text{Si}}^2} + \frac{1}{4 \cdot k_{\text{Si}} \cdot a_{\text{Si}}} \end{aligned} \tag{5.23}$$

$$\begin{aligned} R_{\text{TS,PMMA}} &= R_{\text{Tip}} + R_{\text{PMMA,Int}} + R_{\text{PMMA,Spreading}} \\ &= R_{\text{Tip}} + \frac{r_{\text{Int,PMMA}}}{\pi \cdot a_{\text{PMMA}}^2} + \frac{1}{4 \cdot k_{\text{PMMA}} \cdot a_{\text{PMMA}}} - \frac{\zeta}{2\pi \cdot k_{\text{PMMA}} \cdot t} \\ &= R_{\text{Tip}} + \frac{r_{\text{Int,PMMA}}}{\pi \cdot g^2 \cdot a_{\text{Si}}^2} + \frac{1}{4 \cdot k_{\text{PMMA}} \cdot g \cdot a_{\text{Si}}} - \frac{\zeta}{2\pi \cdot k_{\text{PMMA}} \cdot t} \end{aligned} \tag{5.24}$$

with

$$\zeta = \ln \frac{2}{1 + \frac{k_{\text{PMMA}}}{k_{\text{Si}}}} \quad \text{and} \quad a_{\text{PMMA}} = g \cdot a_{\text{Si}} \tag{5.25}$$

A value for ζ can be calculated because the thermal conductivity of silicon k_{Si} is much larger than that of PMMA and thus, $k_{\text{PMMA}}/k_{\text{Si}} \ll 1 \rightarrow \zeta \approx \ln 2 \approx 0.7$.

The two equations 5.23 and 5.24 make-up a system of equations, where the thermal conductivity of silicon ($k_{\mathrm{Si}} = 130\,\mathrm{W/mK}$) and the PMMA film thickness ($t = 35\,\mathrm{nm}$) are known. As discussed in the previous section the range of the thermal conductivity of PMMA can be assumed to be $k_{\mathrm{PMMA}} = 0.25..0.5\,\mathrm{W/mK}$. Estimations are given in the literature for the value of $r_{\mathrm{Int,PMMA}} = 2.1 \times 10^{-9}\,\mathrm{Km^2/W}$ [86] and for $R_{\mathrm{Tip}} = 10^7..10^8\,\mathrm{K/W}$ (see previous section). The contact radius between tip and sample on silicon and on PMMA can be calculated using appropriate contact models such as the JKR and DMT models. Since the radius of the tip used for this experiment is determined from an SEM image to be $7 \pm 3\,\mathrm{nm}$, we expect $a_{\mathrm{Si}} \approx 1..5\,\mathrm{nm}$ and $a_{\mathrm{PMMA}} \approx 1..25\,\mathrm{nm}$ ($g \approx 1..5$). However, values for the interface constant $r_{\mathrm{Int,Si}}$ are unknown and not yet reported. The following section will explore values for $r_{\mathrm{Int,Si}}$ and narrow down the limits for the other parameters.

The contact radii on silicon and PMMA a_{Si} and a_{PMMA} respectively can be calculated using the JKR and DMT models, which are usually applied to describe an AFM tip in contact with a sample surface. The DMT model [97] is used for an AFM tip being in contact with a hard sample such as silicon, whereas the JKR model [89] describes the case of an AFM tip in contact with a softer polymer sample such as PMMA [98]. According to the JKR model the contact radius $a_{\circ,\mathrm{JKR}}$ at zero load ($F = 0$) is given as

$$a_{\circ,\mathrm{JKR}} = \left(\frac{6\pi R_{\mathrm{Tip}}^2 w}{K}\right)^{1/3} \qquad \text{JKR} \tag{5.26}$$

and in the DMT model

$$a_{\circ,\mathrm{DMT}} = \left(\frac{\pi R_{\mathrm{Tip}}^2 w}{K}\right)^{1/3} \qquad \text{DMT} \tag{5.27}$$

where K is the reduced modulus, R_{Tip} is the radius of the AFM tip and w is the interfacial energy.

Thus, in order to determine the contact radii on both samples the effective moduli on silicon K_{Si} and PMMA K_{PMMA} have to be calculated and the interfacial energies w_{PMMA} and w_{Si} have to be determined.

The interfacial energies can be determined by taking the adhesion force into account, which is measured with every thermal approach curve (see section 5.5.1). In the DMT model the adhesion force is given by

$$F_{\mathrm{Adhesion,DMT}} = F_{\mathrm{Adhesion,Silion}} = 2\pi R_{\mathrm{Tip}} w_{\mathrm{Silion}} \tag{5.28}$$

and in the JKR model

$$F_{\mathrm{Adhesion,JKR}} = F_{\mathrm{Adhesion,PMMA}} = 1.5\pi R_{\mathrm{Tip}} w_{\mathrm{PMMA}}\,. \tag{5.29}$$

As the tip radius is known and the adhesion force is measured with the approach curves, the surface energies can be calculated: In the approach curves shown in figure 5.9 one observes a piezo displacement between snap-on and snap-off of 100 nm on silicon and 60 nm on PMMA. With the cantilever spring constant of 0.067 N/m one calculates an adhesion force of 7 nN on silicon and 4 nN on PMMA. Taking all measured approach curves into account leads to average adhesion values of $F_{\text{Adhesion,PMMA}} = 5.7\,\text{nN}$ and $F_{\text{Adhesion,silicon}} = 7.0\,\text{nN}$. Thus, using the equations 5.28 and 5.29 respectively the interfacial energies turn out to be $w_{\text{Si}} = 0.16\,\text{N/nm}$ and $w_{\text{PMMA}} = 0.17\,\text{N/m}$. However, one has to take rather large errors into account: For the determination of the adhesion force we have to consider that the the spring constant of the cantilever is afflicted with an error of about $\pm 50\,\%$ and the tip radius can be measured with an error of $\pm 3\,\text{nm}$. With the Gaussian law of error propagation the error of w is calculated with

$$\Delta w = \frac{\Delta F}{C\pi R_{\text{Tip}}} + \frac{F}{C\pi R_{\text{Tip}}^2}\Delta R_{\text{Tip}} \tag{5.30}$$

where $C = 1.5$ in case of the PMMA (JKR model) and $C = 2$ for silicon (DMT model). Thus, we end up with values of $w_{\text{Si}} = 0.16 \pm 0.15\,\text{N/nm}$ and $w_{\text{PMMA}} = 0.17 \pm 0.16\,\text{N/m}$ for the interfacial energies.

The reduced modulus K is defined as

$$\frac{1}{K} = \frac{3}{4}\left(\frac{1-\nu_{\text{Tip}}^2}{E_{\text{Tip}}} + \frac{1-\nu_{\text{Sample}}^2}{E_{\text{Sample}}}\right) \tag{5.31}$$

where E_{Tip} and E_{Sample} are the Young's moduli and ν_{Tip} and ν_{Sample} the Poisson's ratios of the sample material and the tip material respectively. With $E_{\text{PMMA}} = 3.3\,\text{GPa}$ and $\nu_{\text{PMMA}} = 0.36$ [20] and $E_{\text{silicon}} = 100\,\text{GPa}$ and $\nu_{\text{silicon}} = 0.42$ [96, 99] the effective moduli on PMMA and silicon are $K_{\text{silicon}} = 81\,\text{GPa}$ and $K_{\text{PMMA}} = 4.9\,\text{GPa}$. With these values the contact radii on silicon and PMMA can be calculated with equations 5.26 and 5.27. One obtains values of $a_{\text{Si}} = 0.7 \pm 0.6\,\text{nm}$ and $a_{\text{PMMA}} = 3.2 \pm 1.9\,\text{nm}$. The error has been calculated using the Gaussian law of error propagation:

$$\Delta a = \frac{1}{3}\left(\frac{c\pi R_{\text{Tip}}^2 w}{K}\right)^{-\frac{2}{3}}\left(\frac{2\pi c R_{\text{Tip}} w}{K}\right)\Delta R_{\text{Tip}} + \frac{1}{3}\left(\frac{c\pi R_{\text{Tip}}^2 w}{K}\right)^{-\frac{2}{3}}\left(\frac{\pi c R_{\text{Tip}}^2 w}{K}\right)\Delta w \tag{5.32}$$

where c=1 on silicon (DMT model) and c=6 on PMMA (JKR model).

Whereas the Young's modulus of silicon exhibits only a small temperature dependence and shall be assumed to be constant, the value of $E_{\text{PMMA}} = 3.3\,\text{GPa}$ only holds for room temperature and we have to take elevated temperatures of the PMMA into account. With increasing temperatures the material becomes softer and E_{PMMA} will decrease. Figure 5.12 *left* shows the dependence of the

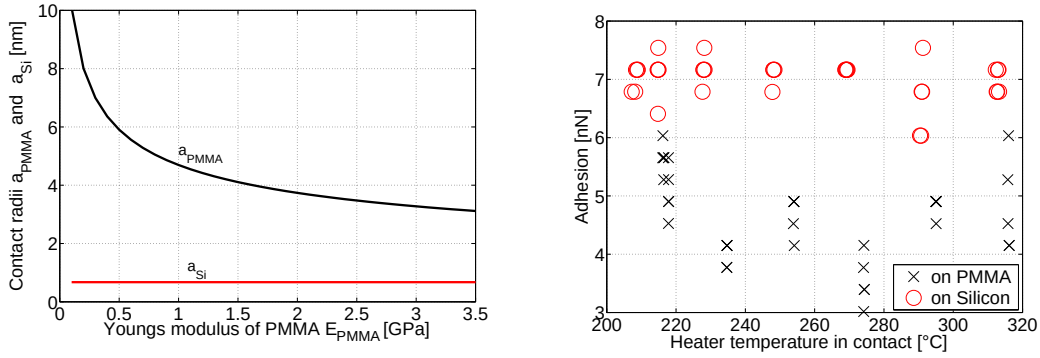

Figure 5.12: *Left:* Calculated contact radii on silicon and PMMA as function of Young's modulus. *Right:* Measured adhesion values as function of the heater temperature.

contact radius a_{PMMA} on the Young's modulus. As expected the contact radius on PMMA increases with decreasing E_{PMMA} up to more than 10 nm. The according factor $\mathrm{g} = a_{\mathrm{PMMA}} / a_{\mathrm{Si}}$ ranges from 4.6 to about 10 and thus taking the upper and lower limit of $a_{\mathrm{Si,upper\ limit}} = 1.3\,\mathrm{nm}$ and $a_{\mathrm{Si,lower\ limit}} = 0.1\,\mathrm{nm}$ into account we end up with a possible range of the contact radius on PMMA between 0.46 nm and 13 nm. From this one would expect that the adhesion force would increase at higher temperatures. The measurement, however, does not support this expectation: Figure 5.12 *right* shows that the adhesion force on PMMA does not increase at elevated heater temperature. One can conclude, that the temperature effect on the adhesion and thus on the contact radius is rather small. Before we carry on and investigate values of the general constants $r_{\mathrm{Int,Si}}$, $r_{\mathrm{Int,PMMA}}$ and R_{tip}, the parameters determined so far are summarized in table 5.2.

Now, values for the interface constant $r_{\mathrm{Int,Si}}$ shall be explored in the following. Considering equation 5.23

$$\begin{aligned} R_{\mathrm{TS,Si}} &= R_{\mathrm{Tip}} + \frac{r_{\mathrm{Int,Si}}}{\pi \cdot a_{\mathrm{Si}}^2} + \frac{1}{4 \cdot k_{\mathrm{Si}} \cdot a_{\mathrm{Si}}} \\ &= (8.6 \pm 2.6) \times 10^7\,\mathrm{K/W} \end{aligned} \tag{5.33}$$

one expects the thermal tip sample contact resistance $R_{\mathrm{TS,Si}}$ to depend linearly on the interface constant $r_{\mathrm{Int,Si}}$. The slope is dependent on the contact radius a_{Si} and the offset is a function of both the contact radius a_{Si} and the thermal resistance of the tip R_{Tip}. As we have to take the error intervals for the contact radius and the thermal resistance of the tip into account, we end up with nine straight lines describing the possible values for the interface constant $r_{\mathrm{Int,Si}}$: Figure 5.13 shows the straight lines for the different calculated contact radii $a_{\mathrm{Si}} = 0.7\,\mathrm{nm}$ (mean value), $a_{\mathrm{Si}} = 0.1\,\mathrm{nm}$ (lower limit) and $a_{\mathrm{Si}} = 1.3\,\mathrm{nm}$ (upper limit) and for different thermal resistances of the tip $R_{\mathrm{Tip}} = 5.5 \times 10^7\,\mathrm{K/W}$ (mean value),

Parameter	**Value**	**Method**
$R_{\mathrm{TS,Si}}$	$(8.6 \pm 2.6) \times 10^7\,\mathrm{K/W}$	Measurement Figure 5.10
$R_{\mathrm{TS,PMMA}}$	$(2.0 \pm 0.6) \times 10^8\,\mathrm{K/W}$	Measurement Figure 5.10
Tip radius R_{Tip}	$7 \pm 3\,\mathrm{nm}$	SEM image
Contact radius on silicon a_{Si}	$0.7 \pm 0.6\,\mathrm{nm}$	DMT model
Interfacial energy of silicon w_{Si}	$0.16 \pm 0.15\,\mathrm{N/m}$	DMT model
Contact radius on PMMA a_{PMMA}	$3.2 \pm 1.9\,\mathrm{nm}$ (at RT) 0.46...13 nm (T-dependent)	JKR model Figure 5.12
Factor $\mathrm{g} = a_{\mathrm{PMMA}} \,/\, a_{\mathrm{Si}}$	4.6...10	Figure 5.12
Interfacial energy of PMMA w_{PMMA}	$0.17 \pm 0.15\,\mathrm{N/m}$	JKR model
Effective module K_{Si}	81 GPa	calculated from bulk literature values
Effective module K_{PMMA}	4.9 GPa at 20 °C	calculated from bulk literature values

Table 5.2: Overview of the parameters calculated or measured in this section. Whereas tip radius and contact radii are values valid only for the particular tip used in this measurement, the interfacial energies and the effective modules are only material dependent.

$R_{\mathrm{Tip}} = 10^7\,\mathrm{K/W}$ (lower limit) and $R_{\mathrm{Tip}} = 10^8\,\mathrm{K/W}$ (upper limit). Additionally, the measured value of the thermal contact resistance of $R_{\mathrm{TS,Si}} = (8.6 \pm 2.6) \times 10^7\,\mathrm{K/W}$ is plotted with the solid line (mean value) and dashed lines (upper and lower limits).

Considering the mean values ($a_{\mathrm{Si}} = 0.7\,\mathrm{nm}$, $R_{\mathrm{Tip}} = 5.5 \times 10^7\,\mathrm{K/W}$) the calculated straight line (symbols □) intersects with the measured mean value (solid horizontal line, $R_{\mathrm{TS,Si}} = 8.6 \times 10^8\,\mathrm{K/W}$) at point A, which corresponds to a value of the interface constant of $r_{\mathrm{Int,Si,mean}} = 4.3 \times 10^{-11}\,\mathrm{Km^2/W}$. Again, the error interval is large: The upper limit of the interface constant turns out to be $r_{\mathrm{Int,Si,ul}} = 5.3 \times 10^{-10}\,\mathrm{Km^2/W}$ (Point B). The lower limit, however, cannot be specified, because the offset of the calculated straight line with $a_{\mathrm{Si}} = 0.1\,\mathrm{nm}$ and $R_{\mathrm{Tip}} = 1.0 \times 10^8\,\mathrm{K/W}$ is above the upper limit of the measured data (Point C) and thus, the interface constant would be negative, which physically would not make sense. Thus, we can conclude, that the interface constant for the tip on silicon determined with this method has a mean value of $r_{\mathrm{Int,Si,mean}} = 4.3 \times 10^{-11}\,\mathrm{Km^2/W}$, but the interval of possible values ranges from 0 to $r_{\mathrm{Int,Si,ul}} = 5.3 \times 10^{-10}\,\mathrm{Km^2/W}$.

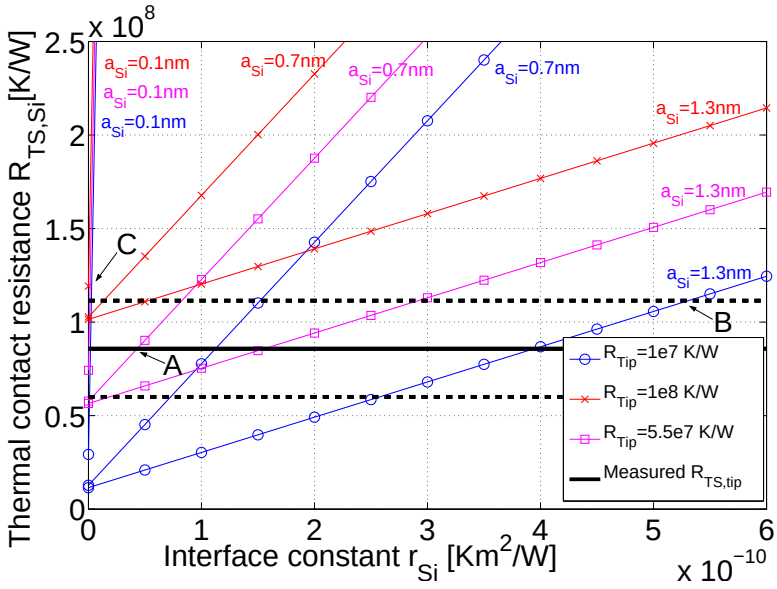

Figure 5.13: Calculated thermal resistances as function of the interface constant r_{Si} for different thermal resistances of the tip R_{Tip} and different contact radii a_{Si} in comparison with the measured data. The mean value of the measured data is plotted as a solid line and the dashed lines show the error interval assuming an error of 30 % due to the error of the temperature calibration.

As the slope of the straight lines is always positive, it is intuitive, that the offset of the calculated straight lines cannot be larger than the measured data, because otherwise one would not obtain any intersection points with the measured data. Thus, we can use this to determine the upper limit of the thermal resistance of the tip. Setting $r_{\mathrm{Int,Si}} = 0$ (offset condition) and resolving equation 5.33 leads to

$$R_{\mathrm{Tip}} = R_{\mathrm{TS,Si}} - \frac{1}{4 \cdot k_{\mathrm{Si}} \cdot a_{\mathrm{Si}}}. \tag{5.34}$$

With the measured value $R_{\mathrm{TS,Si}} = (8.6 \pm 2.6) \times 10^7\,\mathrm{K/W}$ we can calculate the upper limit of the tip thermal resistance as a function of the contact radius, which is shown in figure 5.14. Plotted is the upper limit of R_{Tip} versus the contact radius a_{Si} using equation 5.34 with $R_{\mathrm{TS,Si}} = 11.1 \times 10^7\,\mathrm{K/W}$ (upper limit). This is in good agreement with the expectations described in section 5.5.3.2.

For the determination of the interface constant $r_{\mathrm{Int,PMMA}}$ the same method as used for determining $r_{\mathrm{Int,Si}}$ can be applied: Again we expect a proportional relation between $R_{\mathrm{TS,PMMA}}$ and $r_{\mathrm{Int,PMMA}}$ with the slope being dependent on the contact radius a_{Si} and the offset being a function of R_{Tip}, k_{PMMA} and a_{Si} (see equation 5.24):

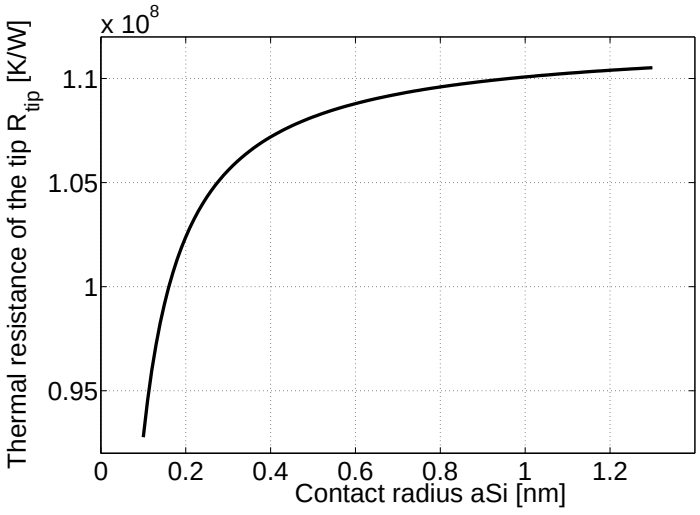

Figure 5.14: Upper limit of the thermal resistance of the tip R_{Tip} as function of the contact radius a_{Si} calculated with equation 5.34.

$$\begin{aligned} R_{\mathrm{TS,PMMA}} &= R_{\mathrm{Tip}} + \frac{r_{\mathrm{Int,PMMA}}}{\pi \cdot a_{\mathrm{PMMA}}^2} + \frac{1}{4 \cdot k_{\mathrm{PMMA}} \cdot a_{\mathrm{PMMA}}} - \frac{\zeta}{2\pi \cdot k_{\mathrm{PMMA}} \cdot t} \\ &\approx R_{\mathrm{Tip}} + \frac{r_{\mathrm{Int,PMMA}}}{\pi \cdot a_{\mathrm{PMMA}}^2} + \frac{1}{4 \cdot k_{\mathrm{PMMA}} \cdot a_{\mathrm{PMMA}}} \\ &= (2.0 \pm 0.6) \times 10^7\,\mathrm{K/W} \end{aligned} \tag{5.35}$$

The approximation can be made, because the last term in the first line is only a small correction of a few percent describing the influence of the substrate as we have already seen in the section 5.5.3.2.

However, the situation in this case is more complex than it has been for the interface constant on silicon: Whereas $R_{\mathrm{TS,Si}}$ is a function of three variables (R_{Tip},a_{Si} and $r_{\mathrm{Int,Si}}$), now additionally the thermal conductivity of the polymer k_{PMMA} is not known exactly. As we already know ranges of possible values for R_{Tip},a_{PMMA} and k_{PMMA}, we can consider the upper and lower limits of $R_{\mathrm{TS,PMMA}}$: As equation 5.35 shows, an upper limit of $R_{\mathrm{TS,PMMA}}$ is given for large values of R_{Tip} and small values for a_{PMMA} and k_{PMMA}. Thus, we set $R_{\mathrm{Tip}} = 11.1 \times 10^7\,\mathrm{K/W}$, $a_{\mathrm{PMMA}} = 0.46\,\mathrm{nm}$ and $k_{\mathrm{PMMA}} = 0.25\,\mathrm{W/(mK)}$. Accordingly, we obtain the lower limit of $R_{\mathrm{TS,PMMA}}$ by taking the lower limit of R_{Tip} and the upper limit of a_{PMMA} and k_{PMMA} into account: $R_{\mathrm{Tip}} = 4.1 \times 10^7\,\mathrm{K/W}$, $a_{\mathrm{PMMA}} = 7.0\,\mathrm{nm}$ and $k_{\mathrm{PMMA}} = 0.5\,\mathrm{W/(mK)}$.

In figure 5.15 the straight line for the case of the lower limit and the measured data as well as the error interval is plotted. From the intersection point of the

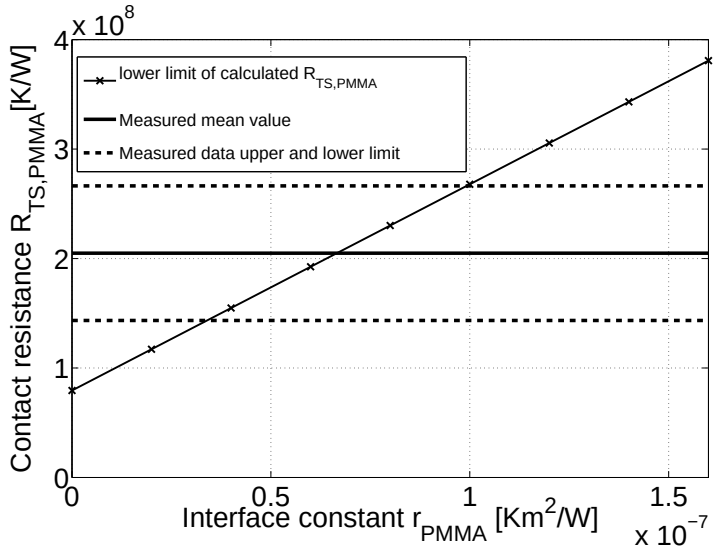

Figure 5.15: Thermal resistances as function of interface constant r_{PMMA} calculated with equation 5.35. The solid line denotes the measured mean value of $R_{\mathrm{TS,PMMA}}$ and the dashed line indicate the error interval.

calculated straight line with the upper limit of the measured data one concludes that the upper limit of the interface constant on PMMA is $r_{\mathrm{Int,PMMA,ul}} = 1.0 \times 10^{-7}\,\mathrm{Km^2/W}$. The straight line of the upper limit, however, is not plotted because the offset is too large to fit into the diagram and thus, the intersection point would be at negative interface constances $r_{\mathrm{Int,PMMA,ll}}$. Hence, with this measurement it is not possible to determine a value for the lower limit of $r_{\mathrm{Int,PMMA,ll}}$.

5.5.4 Adhesion dependence of thermal contact resistances

In the previous section the measurement of the heat transfer from the heater through the tip to different materials (silicon and PMMA) has been investigated and the measurements were correlated with a theoretical model. However, the uncertainties of the parameters involved were large and thus, another approach will be used in this section to investigate the values, which influence the tip sample heat transfer: The idea is to wear a particular tip continuosly in a targeted way and thus, to increase the tip size in a controlled manner. With increasing tip size one expects increasing contact radius and consequently increasing adhesion force. Simultaneously an increasing contact radius leads to a reduced thermal resistance as we have seen in the previous section. Hence, measuring the adhesion force enables one to deduce the contact radius and to correlate it with the thermal resistance.

The experiment was conducted in the following way: Approach curves were measured under vacuum conditions on the silicon sample. After every five approach

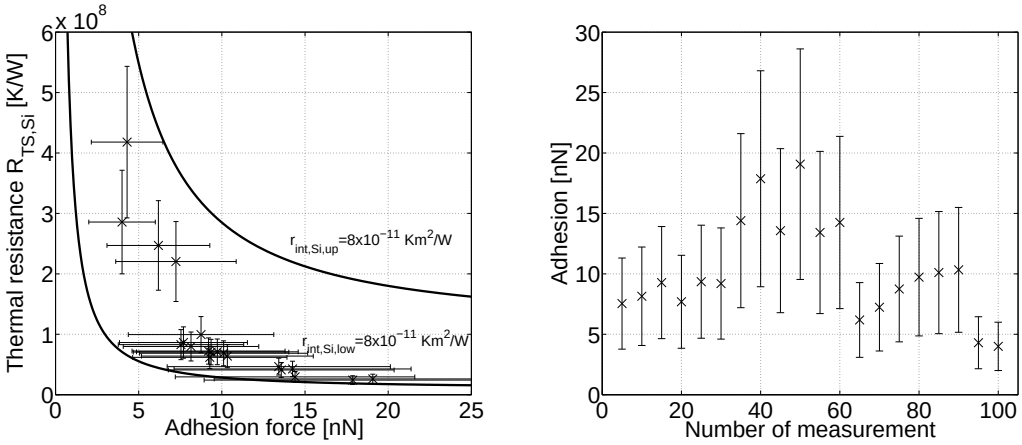

Figure 5.16: *Left:* Dependence of thermal resistance on the adhesion force during a wear-out experiment by continuously scanning the tip on silicon. *Right:* Adhesion force as function of the number of approach curve. Surprisingly a continuous increase of the adhesion is not observed. Instead the adhesion reached a maximum after 50 measurements and decreased afterwards.

curves the tip was dragged laterally over the surface with a force of approx. 100 nN. This has been done by 'scanning' 150 to 200 fields (each of them consisting of only 5 scan lines of 4.4 μm length).

Figure 5.16 (*left*) shows the thermal tip-sample contact resistance as function of the adhesion force measured on the silicon sample with over-all 100 approach curves. The data plotted are the average values of the adhesion force and the thermal contact resistance of every five approach curves taken after each tip blunting procedure. The adhesion force has been determined from the difference between the snap in and the snap off points of the approach curves as discussed in section 5.5.1. A clear dependence of the thermal tip-sample contact resistance as function of the adhesion force can be identified as the thermal contact resistance decreases significantly at higher adhesion forces.

These experimental data can be used for a further investigation of the interface constant $r_{\mathrm{int,Si}}$: Whereas the limits of the thermal resistance of the tip R_{Tip} and for the interfacial energy w_{Si} are known, the lower limit of $r_{\mathrm{int,Si}}$ could not be

Calculated $R_{\mathrm{TS,Si}}$	Upper limit	Lower limit
Contact radius on silicon a_{Si}	Lower limit	Upper limit
Thermal resistance of the tip R_{Tip}	1×10^7 K/W	11.1×10^7 K/W
Interfacial energy of silicon w_{Si}	0.01 N/m	0.31 N/m

Table 5.3: Overview of the parameters used for the theory curves plotted in figure 5.16 (*left*).

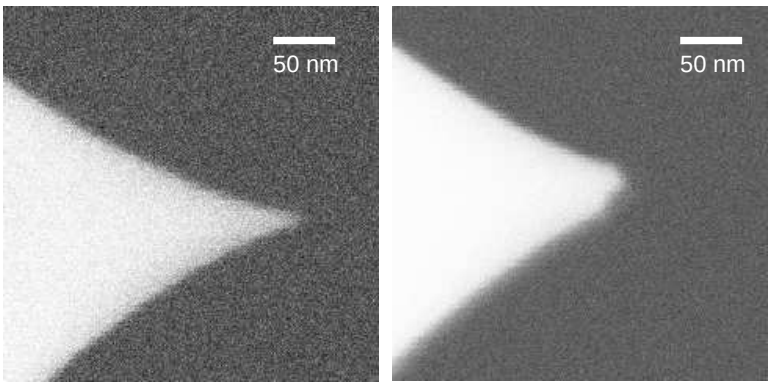

Figure 5.17: SEM of the tip used in the wear-out experiment before (*left*) and after (*right*) the measurement

determined in the previous section. Thus, two limiting cases for the parameters R_{Tip} and w_{Si} are considered here and $r_{\mathrm{int,Si}}$ is adapted such that the measured data fit into the upper and lower limit of the error range.

Figure 5.16 (*left*) shows these two limiting curves, which are calculated with equation 5.33. For the upper curve the upper limit of the thermal resistance of the tip and the lower limit of the contact radius is used. Analogously for the lower curve, the lower limit of R_{Tip} and the upper limit of a_{Si} are used. In order to obtain a relationship between the adhesion force and the contact radius equations 5.27 and 5.28 are combined leading to

$$a_{\mathrm{Si}} = \left(\frac{F^2_{\mathrm{Adhesion}}}{4\pi w_{\mathrm{Si}} K} \right)^{1/3} \tag{5.36}$$

Thus, the upper limit of a_{Si} is given by the lower limit of w_{Si} and vice versa. The parameters used for both scenarios are summarized in table 5.3. For both scenarios the interface constant $r_{\mathrm{int,Si}}$ is the only remaining fit parameter. It turns out that for both the upper and lower curve a single value of the interface constant can be used: $r_{\mathrm{int,Si}} \approx 8 \times 10^{-11}\,\mathrm{Km^2/W}$ as shown in figure 5.16 (*left*). Thus, this experiment enables one to obtain a more accurate value for this parameter than has been possible with the measurement discussed in the previous section.

In figure 5.16 (*right*) the adhesion forces are plotted as function of the number of approach curves. Surprisingly, the adhesion does not increase continuously as one would expect. Instead the adhesion reaches a maximum after about 50 approach curves and decreases afterwards. SEM images of the tip have been made before and after the approach curves and wear experiments in the vacuum SFM (figure 5.17). The tip size has obviously increased, but it seems as if a part has chipped off at the bottom side of the tip. Thus, possibly the tip has been blunted during

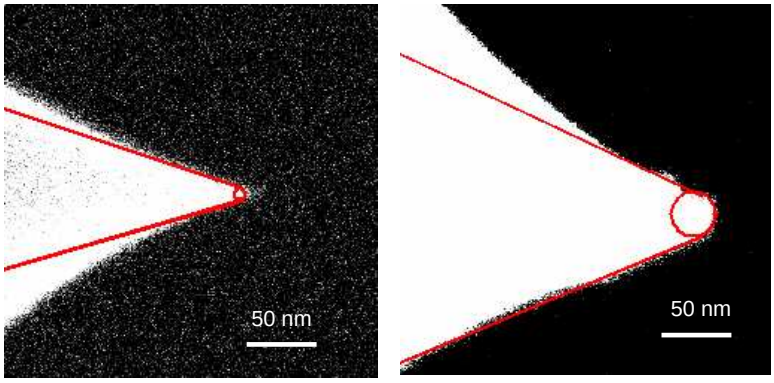

Figure 5.18: SEM images of different tips used in the vacuum SFM for the measurement of thermal contact resistance. A sharp tip of 10 nm diameter and an apex angle of 34 ° (*left*) and a blunt tip of 40 nm tip diameter and a apex angle of 48 ° (*right*).

the first 50 approach curves as expected and then the tip size has decreased again because of the spalling. This explains, why the adhesion force did not increase continuously in figure 5.16 (*right*).

5.5.5 Dependence of thermal contact resistances on tip geometry

In this section the dependence of the thermal contact resistance on the tip geometry is investigated. Tips of different radii were used in the vacuum chamber and the thermal contact resistances was measured on silicon. Before the measurement in the vacuum SFM the tips were imaged in the Scanning Electron Microscope (SEM) in order to determine tip size and geometry.

The tip radius plays a crucial role, because it influences all three contributions to the measured thermal contact resistance. The tip thermal conductivity is assumed to depend on the tip radius as well as the contact radius, which in turn influences the interface thermal resistance and the spreading resistance. A sharp tip with a small tip radius results in a small contact area and consequently in a larger thermal interface resistance $R_{\mathrm{th,Interface}}$ and a larger spreading resistance $R_{\mathrm{th,Spreading}}$, whereas a blunt tip will exhibit a larger contact radius and the total thermal resistance of a blunt tip is therefore expected to be smaller. The apex angle is investigated because it possibly influences the phonon scattering at the tip walls and thus, the thermal resistance of the tip $R_{\mathrm{th,Tip}}$.

In figure 5.18 examples of two different tips illustrate how the tip diameter and apex angle were determined. A circle fitting the tip and two tangents fitting

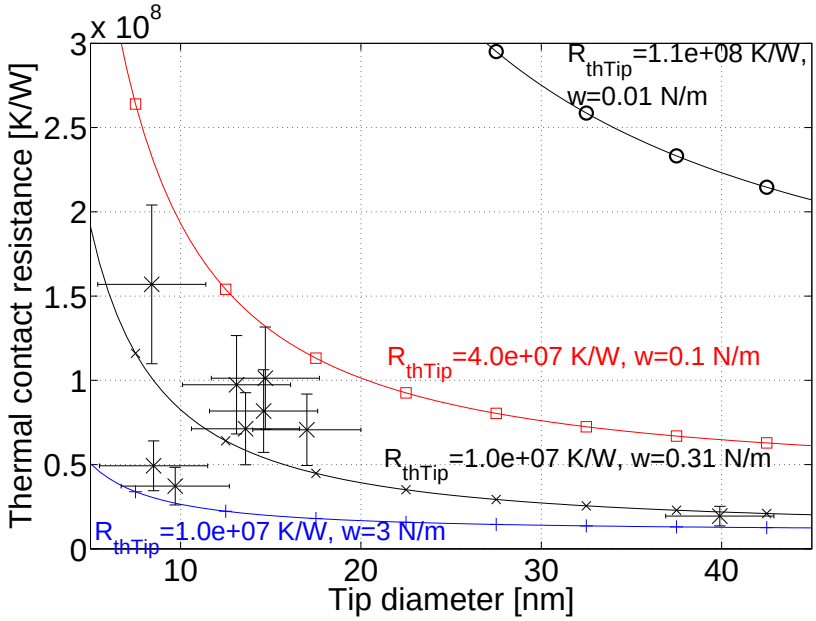

Figure 5.19: Dependence of thermal resistance on tip diameter measured on silicon.

the walls of the cone were plotted on the SEM image by visual judgment. The circle's diameter as well as the angle between the two tangents were determined with appropriate software. As a result for the tip on the left side a diameter of 10 nm and an apex angle of 35 ° is obtained. The second tip is significantly blunter and has a diameter of 40 nm and an apex angle of 48 °. With this method the accuracy of the tip diameter should be on the order of ±3 nm depending on the image quality. This means, that for a tip of 10 nm diameter the relative errors are about ±30 %. The measurement of the angle is afflicted with an error of ±10 °, because of the uncertainties in the tangent positioning.

In figure 5.19, the thermal contact resistances of different tips measured on the silicon sample are plotted as function of the tip diameter. The data are rather noisy and the scatter is quite large. Nevertheless, four calculated curves are plotted in addition to the measured data using the model described in section 5.5.3.2 with different parameters: Again the limiting cases are considered using the values of $r_{\mathrm{Si}} = 8 \times 10^{-11}\,\mathrm{Km^2/W}$, $w_{\mathrm{Si}} = 0.16 \pm 0.15\,\mathrm{N/m}$ and $R_{\mathrm{Tip}} = 1...11.1 \times 10^7\,\mathrm{K/W}$ as determined in the previous sections. The two black curves (plotted with the symbols ∘ and ×) represent the upper and lower limits with the parameters indicated in the diagram. The lower curve plotted with symbols × describes the lower limit of the measured data points well except the two data points in the lower left corner, which do not fall into the calculated range. The parameters have been varied such that these two values also fall this area (blue curve, symbols +). It turns out that an interfacial energy of 3 N/m is required in order

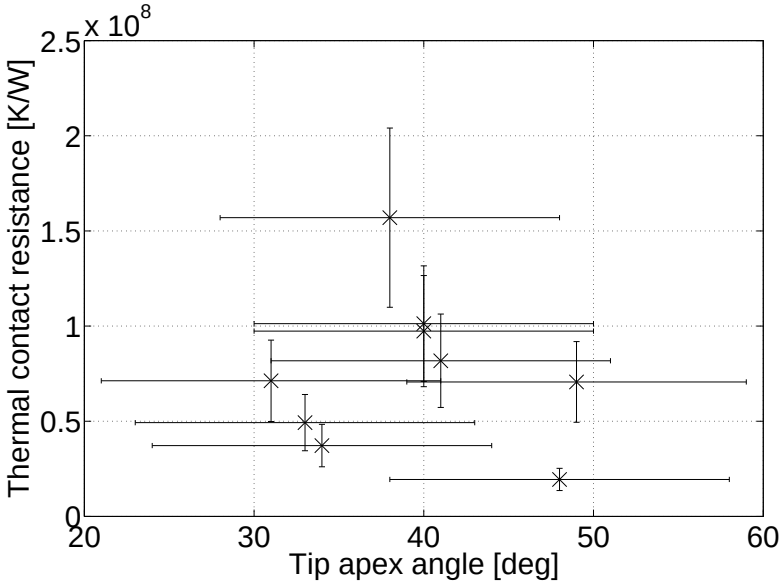

Figure 5.20: Dependence of thermal resistance on tip apex angle on silicon.

to meet this requirement, which is about a factor 10 larger than the calculated value using the DMT model. Thus, presumably the tips leading to these two data points do not obey our model because possibly other effects have occurred during the measurement: Perhaps the oxide cap covering the tip is thinner than usual or tip contaminations influence the measurement. Additionally, impurities inside the tip could enhance phonon scattering and reduce the thermal conductivity. The actual tip shape and the roughness at the very end of the tip are also not very well defined and cannot be resolved in the SEM. For a better understanding measurements of a larger number tips would be desirable and a better control of the tip shape and material would desirable, which was not possible within the framework of this study. Nevertheless, the majority of the data points obey the theoretical model well.

The calculated upper curve (symbols $\circ$) is much higher than the experimental data. Thus, one can conclude that $w_{\mathrm{Si}} = 0.01\,\mathrm{N/m}$ is too low whereas $R_{\mathrm{Tip}} = 1.1 \times 10^8\,\mathrm{K/W}$ is too large. Consequently, these values have been changed such that the calculated curve fit to the upper limit of the measured data. One ends up with the red curve (symbols $\square$), which is calculated with $R_{\mathrm{Tip}} = 4 \times 10^7\,\mathrm{K/W}$ and $w_{\mathrm{Si}} = 0.1\,\mathrm{N/m}$.

Figure 5.20 shows the measurement of the thermal contact resistance as function of the apex angle of the tip. No correlation can be ascertained and thus, one can conclude that the apex angle does not influence the thermal conductivity of the tip.

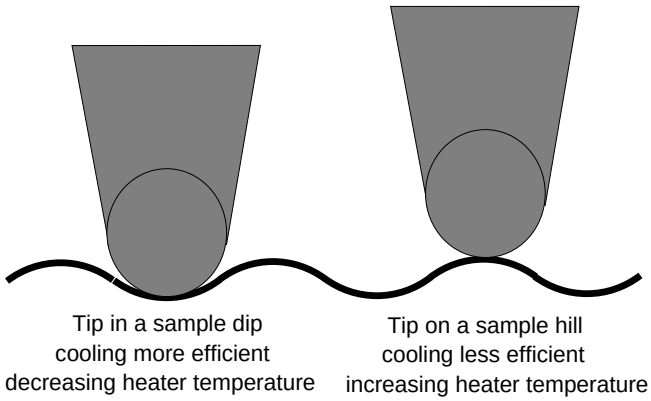

Figure 5.21: Schematic sketch of the topography effect leading to thermal imaging contrast on the silicon sample: As the tip scans over the sample in Contact Mode, the contact area changes leading to different cooling efficiencies and consequently to a varying heater temperature and electrical resistance. This in turn changes the cantilever voltage, which is amplified and recorded for the image generation.

5.5.6 Surface analysis of the silicon sample

So far we have assumed that the sample is homogeneous and the measurement of the thermal contact resistance was expected to be independent from the specific location. In order to investigate the surface of the silicon sample, images have been scanned using a commercial SFM (D3000 from Veeco) in Tapping Mode under ambient conditions and with a heatable tip under vacuum conditions in Contact Mode. Both measurements are shown in figure 5.22.

Similar to the thermal imaging described in section 4.3 the thermal image measurement was conducted by scanning the tip across the sample with the applied input voltage kept constant. However, in contrast to thermal imaging in air, where a variation of the distance between heater and sample causes the imaging contrast, under vacuum conditions changing contact resistances lead to the imaging capability. In this case the sample consists of a single material and the thermal image resembles the sample topography due to changing contact areas between tip and sample as sketched in figure 5.21. Changing cooling efficiencies give rise to a variation of the heater temperature, which in turn leads to a variation of the heater electrical resistance and of the cantilever voltage V_{Lever}, which is amplified and recorded for the image generation.

The thermal image in figure 5.22 (*left*) reveals, that the silicon surface is inhomogeneous, which possibly originates from thickness variations of the native oxide. Consequently the thermal contact resistance depends strongly on the location. Regions of low heater temperature (dark colored) and spots of high heater temperature (bright spots) can clearly be distinguished. The Tapping Mode image

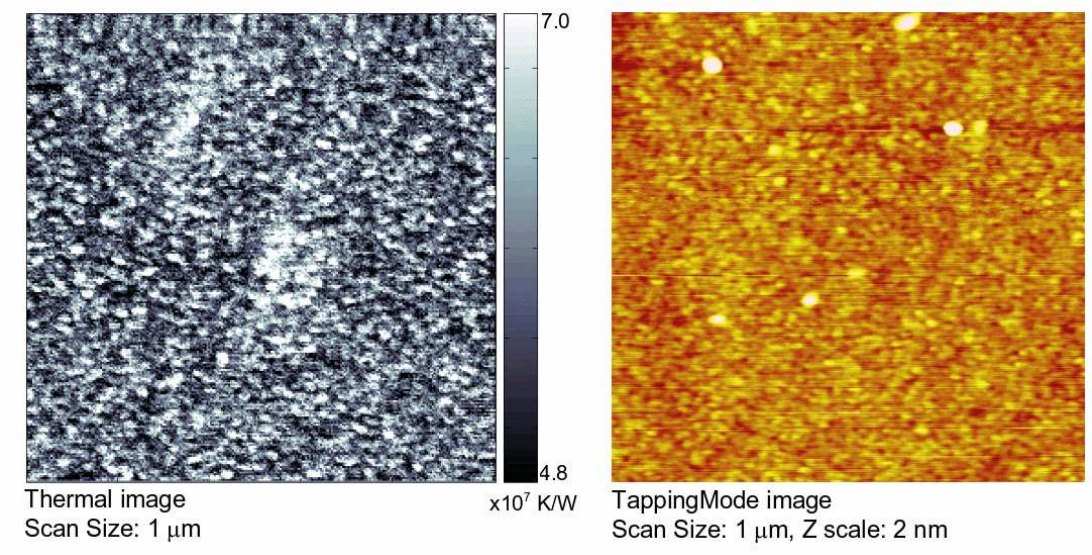

Figure 5.22: Thermal image obtained under vacuum conditions with a heatable cantilever (*left*) and Tapping Mode image scanned under ambient conditions using a commercial SFM tip (*right*) on the silicon sample. The thermal contact resistance variation corresponds to a heater temperature range between 308.3 and 310.2 °C.

scanned under ambient conditions in figure 5.22 (*right*) shows the same granularity, which means, that the thermal contrast correlates with the topography. This in turn means, that the approach curve measurement is influenced by the area, where the measurement took place. Although the amplified cantilever voltage was measured during the scanning procedure, it is possible to derive the heater temperature variation and the thermal contact resistance variation in the image. One obtains a heater temperature variation between 308.3 and 310.2 °C and a range of the thermal contact resistances from 4.8 to 7.0×10^7 K/W. Thus, the variation of the thermal resistance caused by the sample topography is in the range of 2.2×10^7 K/W. In section 5.6 it will be shown in detail, how these calculations were performed.

This location dependence explains the large scatter of the thermal resistances measured with different tips in section 5.5.5: With different tips the location of the approach curve measurements could not be controlled and each tip was used at another location.

Since it was encouraging to obtain thermal images with high lateral and thermal resolution under vacuum conditions as demonstrated on the silicon sample in figure 5.22, this method was applied to another more defined sample. In section 5.6 further thermal imaging experiments will be presented and the detailed experimental setup as well as data analysis will be described.

Parameter	**Value**	**Method**
Thermal resistance of the tip R_{Tip}	1 to $10\times 10^7\,\mathrm{K/W}$	Literature
(for tip diameters	$<11.1\times 10^7\,\mathrm{K/W}$	figures 5.13,5.14
between 8 and 40 nm)	1 to $4\times 10^7\,\mathrm{K/W}$	figure 5.19
Interface constant $r_{\mathrm{Int,Si}}$	$< 5.3 \times 10^{-10}\,\mathrm{Km^2/W}$	figure 5.13
	$\approx 8 \times 10^{-11}\,\mathrm{Km^2/W}$	figure 5.16
Interface constant $r_{\mathrm{Int,PMMA}}$	$< 1.0 \times 10^{-7}\,\mathrm{Km^2/W}$	figure 5.15
	$2.1 \times 10^{-9}\,\mathrm{Km^2/W}$	Literature

Table 5.4: Overview of the parameters involved in the theoretical model considered in this section.

5.5.7 Discussion and conclusions of this section

In this section three different types of experiments have been described in order to determine the parameters involved in the theoretical considerations made in section 5.5.3.3: The thermal contact resistance has been measured on different samples (silicon and a PMMA film), because these materials exhibit different thermomechanical properties. In a second experiment the tip was continuously blunted by dragging it over the silicon sample and the thermal contact resistance was measured as function of the adhesion force. As a third experiment ten different tips with varying tip diameters (between 7 and 40 nm) were used for the measurement of the thermal contact resistance.

With each of these experiments the range of one or several parameters could be determined or narrowed down by taking contact models like the DMT and JKR model into account. Table 5.4 summarizes the results of these investigations.

However, the error intervals remain large and that no value for the lower limits of interface constant $r_{\mathrm{Int,PMMA}}$ could be obtained. This is due to the fact, that initial quantities needed for the data analysis cannot be determined with higher accuracy. Namely three parameters play a key role: the tip radius, the cantilever spring constant and the temperature calibration of the cantilever heater. The tip radius measurement is afflicted with an error of ± 3 nm and for the spring constant an error of 50 % is assumed. This is due to the fact that the geometry of this type of cantilevers is rather complex and no analytical calculations can be made. Furthermore, the experimental setup did not provide a laser system, which would have enabled to measure the cantilever spring constant on a reference cantilever. The error of the heater temperature calibation is about 30 % as stated in chapter 3.3. All these uncertainties sum up to the large errors in the determination of the parameters.

Besides the technical problems, systematic inaccuracies have to be taken into account: The calculation of the effective moduli with bulk values is possibly

inaccurate. Whereas the bulk values hold for macroscopic samples it could be the case that these material parameters deviate on the nanoscale, especially the Young's moduli and the thermal conductivities. In the case of the PMMA film, the complex interplay between heat and pressure make the data analysis more complicated than in the case of the silicon as the thermal conductivity of polymers is temperatures and pressure dependent. Thus, the contact radius is afflicted with large uncertainties and consequently the interface thermal resistance as well as the spreading resistance.

Despite these challenges, the results of this section are promising because the expected ranges of the parameters given in the literature are for the first time experimentally confirmed on the nanoscale. Especially the upper limit of the thermal resistance of the tip correlates well with the literature values and a value for the interface constant on silicon $r_{\mathrm{Int,Si}}$ could be obtained. One can state that the model of the thermal resistances described in section 5.5.3.2 is experimentally confirmed and that the parameters fit into the expected ranges. It is worth noticing that the interface resistances are difficult to measure on the macroscale,too. For example, no measurements of pure Si-SiO_2 has been published. In all measurements addressing this issue a metal contact is involved, which means that an average silicon-metal and a Si-SiO_2 junction is measured.

Determination of the surface temperature

With the results obtained in the previous section it is possible to calculate the temperature of the sample surface underneath the tip and the tip temperature itself, which is of special interest, because the the mechanical properties of the polymer material are strongly dependent on the temperature. On the one hand, one would like to reach a sufficiently high polymer temperature to soften it. On the other hand, degradation processes occur at higher temperatures, which would lead to a destruction of the polymer.

We have seen in section 5.5.3 that the thermal contact resistance measured with approach curves is made up of different contributions (thermal resistance of the tip, thermal resistance of the tip sample interface and thermal spreading resistance inside the sample material). All these contributions depend in the thermomechanical properties of both the tip and the sample and thus the surface temperature will strongly depend on the sample.

Prior to the temperature calculation is the determination of the various thermal resistances on both samples: With an interface constant of $r_{\mathrm{Int,Si}} = 8 \times 10^{-11}\,\mathrm{Km^2/W}$ and a contact radius of a_{Si} =0.7 nm on silicon one obtains a thermal interface resistance of $R_{\mathrm{Int,Si}} = 5.2{\times}10^7\,\mathrm{K/W}$ (61 %) and a spreading resistance of $R_{\mathrm{Spreading,Si}} = 2.8\ {\times}10^6\,\mathrm{K/W}$ (3 %). The measured mean value of the entire con-

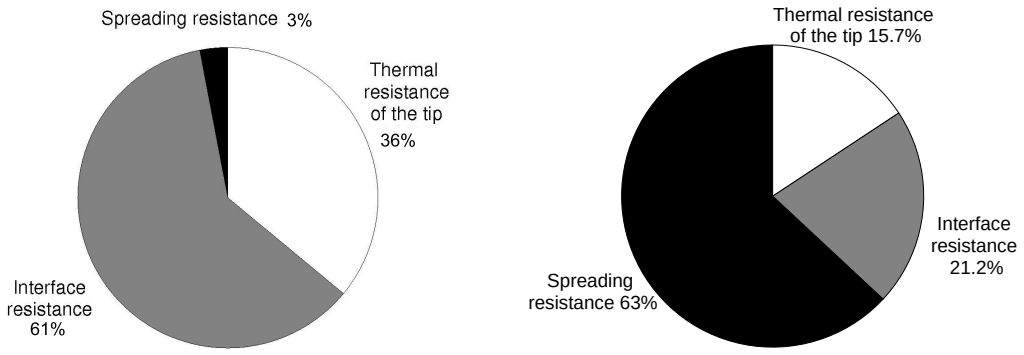

Figure 5.23: Relative contribution of the individual thermal resistances on silicon (*left*) and on PMMA (*right*).

tact resistance is $R_{\mathrm{TS,Si}} = 8.6{\times}10^7\,\mathrm{K/W}$ (see figure 5.10 and table 5.2) and thus, the thermal resistance of the tip is $R_{\mathrm{Tip}} = 3.1{\times}10^7\,\mathrm{K/W}$ (36 %).

On PMMA the situation changes completely: Due to the large uncertainties of the parameters (especially of the interface constant $r_{\mathrm{Int,PMMA}}$, the contact radius and the thermal conductivity) it is difficult to determine the interface and the spreading resistance exactly. Assuming an interface constant of $r_{\mathrm{Int,PMMA}} = 2.1{\times}10^{-9}\ \mathrm{Km^2/W}$ leads to a contact radius of 4 nm calculated with the above thermal resistance of the tip of $R_{\mathrm{Tip}} = 3.1{\times}10^7\,\mathrm{K/W}$ and the measured mean value of $R_{\mathrm{TS,PMMA}} = 2.0{\times}10^8\,\mathrm{K/W}$. The spreading resistance turns out to be $R_{\mathrm{Spreading,PMMA}} = 1.25{\times}10^8\,\mathrm{K/W}$ ($\approx 63\,\%$) calculated with a thermal conductivity of $k_{\mathrm{PMMA}} = 0.5\ \mathrm{W/(mK)}$ and an interface resistance of $R_{\mathrm{Int,PMMA}} = 4.2{\times}10^7\,\mathrm{K/W}$ ($\approx 21.2\,\%$). The relative contributions to the thermal tip sample contact resistances on both samples are illustrated in figure 5.23.

For the calculation of the sample surface temperature we consider the thermal resistances and the temperatures as sketched in figure 5.24. At a heater temperature of T_{Heater} the power flowing through the tip sample contact is given by

$$P = \frac{T_{\mathrm{Heater}} - T_{\mathrm{Ambient}}}{R_{\mathrm{TS}}} \tag{5.37}$$

and accordingly the sample temperature is given by

$$P = \frac{T_{\mathrm{Heater}} - T_{\mathrm{Surface}}}{R_{\mathrm{Tip}} + R_{\mathrm{Interface}}} \tag{5.38}$$

$$\Longrightarrow T_{\mathrm{Surface}} = T_{\mathrm{Heater}} - P \cdot (R_{\mathrm{Tip}} + R_{\mathrm{Interface}}) \tag{5.39}$$

Thus, for silicon at a heater temperature of $T_{\mathrm{Heater}} = 200\,^{\circ}\mathrm{C}$ and a thermal contact resistance of $R_{\mathrm{TS,Si}} = 8.6{\times}10^7\,\mathrm{K/W}$ one obtains a power of $P_{\mathrm{Si}} = 2\,\mu\mathrm{W}$ transferred

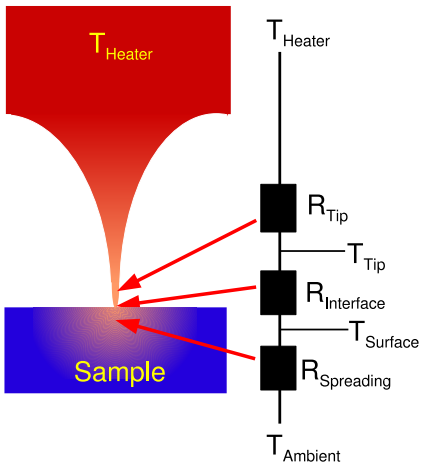

Figure 5.24: Schematic sketch explaining the procedure of determining the surface temperature.

through the tip sample contact. With equation 5.39 a surface temperature of $T_{\mathrm{Surface,Si}} = 31\,^{\circ}\mathrm{C}$ is calculated. Hence, the increase of the surface temperature is only 6 °C. This is mostly due to the very small spreading resistance in silicon originated from the high thermal conductivity. Conducting a similar calculation for the tip temperature leads to $T_{\mathrm{Tip,Si}} = 138\,^{\circ}\mathrm{C}$. This shows, that the largest temperature drop occurs at the interface between tip and sample.

On PMMA, the surface temperature is considerably larger because of the small thermal conductivity of PMMA: With the same calculation as for silicon and the values given above, one obtains a power of $P_{\mathrm{PMMA}} = 0.88\,\mu\mathrm{W}$ transferred through the tip sample contact and a surface temperature $T_{\mathrm{Surface,PMMA}} = 136\,^{\circ}\mathrm{C}$. The tip temperature turns out to be $T_{\mathrm{Tip,PMMA}} = 173\,^{\circ}\mathrm{C}$. Thus, in this case the largest temperature drop occurs inside the sample.

5.5.8 Radiative heat transfer

For the quantitative analysis of thermal approach curves as discussed in section 5.5.2 the heat conductance through the cantilever legs and the thermal radiation were combined to a single thermal resistance, when the tip is not in contact with the sample. Now, we will estimate the amount of energy transferred by thermal radiation using the Stefan-Boltzmann law, which states that two bodies of temperature T_1 an T_2 facing each others exchange radiative energy given as:

$$S = \frac{\pi^2 k_{\mathrm{B}}^4}{60\hbar^3 c^2}\left(T_1^4 - T_2^4\right) = \Theta\left(T_1^4 - T_2^4\right) \tag{5.40}$$

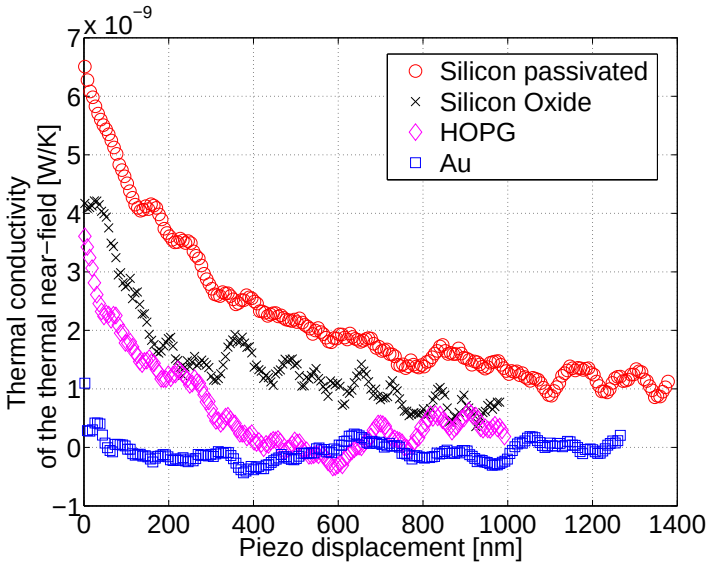

Figure 5.25: Radiative heat transfer measured on different materials with a heater temperature of $\approx$ 600 °C.

with the cooling power per area S , the Boltzmann factor k_B, Planck's constant $\hbar$ and c the speed of light. The factor Θ is calculated to $\Theta = 5.7 \times 10^{-8}\,\mathrm{W/(m^2K^4)}$. In section 5.5.2 we have seen that the combined thermal resistance of the cantilever and the thermal radiation is $R_{\mathrm{th,Cantilever,Radiation}} = 3.682 \times 10^5\,\mathrm{K/W}$ at a heater temperature of 310.5 °C. Using the Stefan-Boltzmann law and a heater size of $6{\times}4\,\mu$m leads to a thermal radiation conductivity of $1{\times}10^{-9}\,\mathrm{W/K}$, which corresponds to a thermal radiation resistance of $R_{\mathrm{th,Radiation}} = 9.5 \times 10^8\,\mathrm{K/W}$. Hence, the combined thermal resistance of the cantilever and the thermal radiation $R_{\mathrm{th,Cantilever,Radiation}}$ is clearly dominated by the contribution of the thermal resistance of the cantilever and the radiation part is negligible.

Radiative cooling results from propagating electro-magnetic waves. Here, the distance between heater and sample ranges between 0.5 and 2.0 μm which is in the range of the radiation wave length and therefore near-field effects have to be taken into account. It has theoretically been shown that radiation cooling can be dominated by evanescent modes in the near-field, which exponentially decay and which do not propagate [100–102]. Whereas the far-field radiation is not distance dependent, in the near-field the cooling efficiency is predicted to be distance dependent. In the approach curves presented so far, however, no distance dependence of the off-contact part was observed (see figures 5.9 and 5.5). According to the theory of thermal near-field radiation the cooling efficiency scales with T^2 and thus, the cooling effect becomes detectable at higher heater temperatures as figure 5.25 confirms: Plotted is the distance dependent near-field thermal conductivity calculated from the off-contact parts of approach curves.

A heater temperature of about 600 °C was used and curves are plotted such that the snap in positions are located at zero piezo displacement. Thus, the closer the heater moves to the sample the higher becomes the thermal radiative conductivity.

Besides the distance dependence, one also observes a strong sample material dependence. Whereas passivated silicon exhibits a very strong distance dependence of the radiative thermal conductivity above Gold (Au), hardly any change is observed.

5.6 Thermal imaging with the vacuum SFM

In section 5.5.3 we have seen that it is possible to distinguish thermal properties of different materials (i.e. a PMMA film on silicon and a silicon wafer) by measuring thermal approach curves. A first thermal image scanned under vacuum conditions with a heatable cantilever tip has been presented in figure 5.22 and supported the understanding of the results of the thermal contact resistance measurement with different tips.

In this section further measurements shall be described, which explore the imaging capability with heatable tips under vacuum conditions in more detail and more quantitatively. The aim of these experiments is to investigate the limits of the thermal imaging capability with this method and to measure the thermal conductivity of different materials within a single image. While the thermal imaging capability in the image of the silicon substrate in figure 5.22 mainly originates from topography effects, a sample with little topography has been chosen in order to minimize topography effects and to make sure that the thermal contrast is due to different material properties. As a sample, which fulfills these requirements, a 3 nm thin amorphous hafnium oxide HfO_2 film on silicon has been imaged. This sample exhibits regions, where the hafnium oxide film is interrupted and 'native' silicon oxide of 1-2 nm thickness is formed.

Hafnium oxide is of technical importance because it is a possbile material for future gate dielectrics in highly integrated electronic circuits [22]. So far silicon oxide is used for this purpose, but with further miniaturization of the devices the thickness of the isolation layer between the gate electrode and the source-drain channel decreases, which leads to undesired tunneling effect. Thus, new materials are under investigation for the isolating layer such as hafnium oxide, which have a high dielectric constant and prevent the tunneling effect.

The amorphous hafnium oxide HfO_2 film on silicon has been prepared in the following way [103]: The growth of the HfO_2 film on a silicon wafer was made in a molecular beam epitaxy (MBE) system. After cleaning with a Piranha

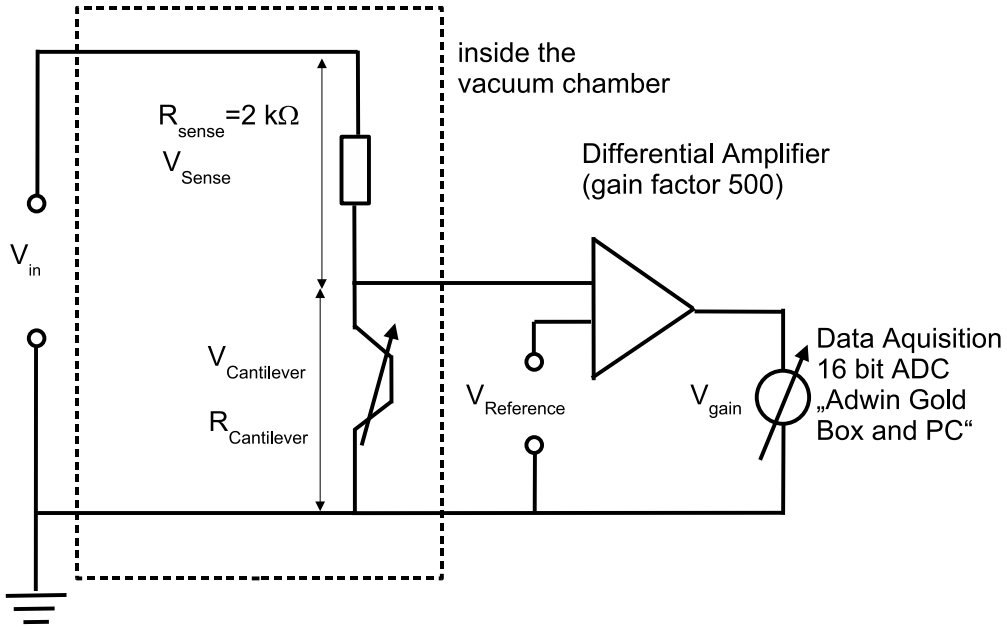

Figure 5.26: Electrical circuit used for the vacuum imaging experiments.

solution (H_2O_2 : H_2SO_4) , the wafer was introduced into the UHV degas module and annealed for 5 min at 1000 °C. Next, the wafer was cooled to 350 °C and the surface was exposed simultaneously to Hf and O (atomic oxygen) until the desired thickness was reached, typically 3 nm. Although the intention was to produce a homogeneous film, the resulting film exhibits regions, where the HfO_2 is interrupted. In these fields silicon oxide is formed as soon as the sample is removed from the MBE system and is brought into ambient conditions. Thus, the resulting sample was a 2-phase system consisting of a 3 nm HfO_2 layer and a 1-2 nm silicon oxide layer on a silicon substrate. The right image in figure 5.27 shows a Tapping Mode SFM image of the sample scanned under ambient conditions in a commercial SFM (Dimesion D3000, Veeco).

5.6.1 Experimental setup for the thermal vacuum imaging

Prior to the actual thermal imaging, approach curves are measured in order to find the piezo displacement necessary to bring the tip into contact with the sample. These approach curves are measured with the same constant input voltage as the subsequent imaging. The approach curves additionally support the data analysis as will be shown in section 5.6.3. As a next step the tip is brought into contact with the sample by applying the piezo voltage which had been determined in the

approach curve measurement. Then the imaging procedure is started and the tip is raster-scanned with a constant input voltage. In contrast to the approach curve measurements, where the cantilever voltage $V_{\mathrm{Cantilever}}$ has been measured, now the differentially amplified voltage V_{Gain} is recorded for each pixel (amplification factor 500). Thus, the electrical circuit has been modified slightly as figure 5.26 shows. Actually at each pixel the V_{Gain} voltage is sampled three times and the average value is saved for the display of the image. In order to increase the thermal contrast imaging has been conducted with higher heater temperature ($\approx$ 615 °C) than used for the thermal contact resistance measurements (200 °C to 350 °C).

As a laser deflection system was not implemented in the vacuum chamber, thermal imaging was realized in the constant height mode. Thus, the force acting between tip and sample was not controlled during imaging. As already observed in previous approach curve measurements, the heater temperature is dependent on the piezo displacement and thus on the force acting between tip and sample. Thus, the uncontrolled way of imaging the sample could possibly cause variations of the heater temperature due to topography induced changes in contact pressure. However, since the topography of the sample is small ($\approx$2 nm) as deduced from the Tapping Mode image in figure 5.27, the change of the heater temperature originated from varying contact pressures is neglectable, if the image plane is parallel to the sample surface. To achieve this the typical tilt of the sample with respect to the piezo tube axis has been compensated during scanning, which has been done by measuring the snap off positions of approach curves performed at different sample positions prior to imaging. During the scanning procedure a 1st order plane fit of these snap off positions was used to adjust the piezo voltages and keep the cantilever force approximately constant. With this method it is avoided that the tip looses contact with the sample and a constant contact pressure can be assumed, which means, that the thermal contrast in the image is due to variations of the thermal properties of the sample.

5.6.2 Experimental results of thermal vacuum imaging

The left image in figure 5.27 shows a thermal image of the HfO_2 film obtained with a heatable SL1 type cantilever under vacuum conditions. A constant DC input voltage V_{in} has been used to bring the heater to a temperature of about 615 °C during scanning. The spots of the interrupted HfO_2 layer are clearly visible and the structures are comparable to the Tapping Mode image on the right hand side of figure 5.27.

The original scan field has a size of 512×512 pixels. To remove turnaround artefacts at the end of each scan line the image shown is a section of 368×368 pixels. Although the voltages applied to the piezo as well as the stored number

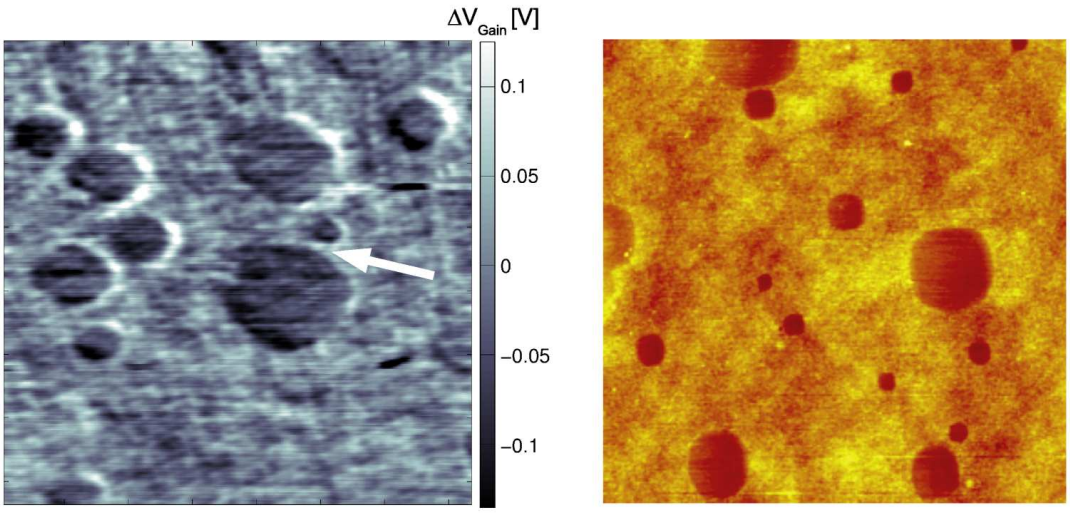

Figure 5.27: *Left:* Thermal image of the HfO_2 film on silicon scanned with a heater temperature of about 615 °C under vacuum conditions. The arrow marks the separation of two spots, which are ≈ 25 nm apart from each other. Image size: 1.6×1,8 μm; *Right:* Tapping Mode image of the same sample scanned under ambient conditions with a commercial SFM. Image size 2 μm, Height scale 5 nm

of pixels were equal for the slow and fast scan axis, the image size is not exactly quadratic (height: 1.6 μm, width: 1,8 μm), because the piezo scanner exhibited a small distortion in vertical and horizontal direction and thus the calibration in both directions was different.

The raw data have been processed with a line-by-line regression subtraction. To avoid artefacts only data outside the spots have been taken into account for the calculation of the regression line. Additionally, the image has been low pass filtered using a sliding average window of 5×5 pixels.

A lateral resolution of better than 25 nm can be deduced from the fact that the two spots marked by the arrow in the image are separated by approx. 25 nm. One recognizes that the contrast at the edges of the fields is strongly enhanced corresponding to a higher heater temperature, which presumably comes from a reduced contact area between tip and sample when the tip moves up the edge.

One observes a variation of the amplified voltage $\Delta V_{\mathrm{Gain}} \approx 0.2\,\mathrm{V}$. This variation can be converted into a heater temperature change of 0.1 K. The procedure leading to this result as well as the calculation of the corresponding variation of the thermal contact resistance will be described in the following section 5.6.3.

5.6.3 Rescaling of thermal vacuum imaging

In the previous section thermal imaging of an interrupted HfO_2 film has been presented and features like the resolution and artefacts have been discussed. Now, the thermal image will be analyzed more quantitatively: The temperature of the heater will be determined as well as its temperature variation during imaging. From that, the variation of the thermal contact resistance can be deduced.

At first glance the conversion of the measured amplified gain voltage V_{Gain} into the corresponding heater temperature seems to be straightforward: Since the reference voltage $V_{\mathrm{Reference}}$ could be measured, the voltage of the cantilever $V_{\mathrm{Cantilever}}$ should be simple to calculate using the formula

$$V_{\mathrm{Gain}} = (V_{\mathrm{Cantilever}} - V_{\mathrm{Reference}}) \cdot F_{\mathrm{Gain}} \Rightarrow V_{\mathrm{Cantilever}} = \frac{V_{\mathrm{Gain}}}{F_{\mathrm{Gain}}} + V_{\mathrm{Reference}} \quad (5.41)$$

with F_{Gain} being the amplification factor. The electrical resistance of the cantilever is given by

$$R_{\mathrm{Cantilever}} = V_{\mathrm{Cantilever}} \cdot \frac{R_{\mathrm{Sense}}}{(V_{\mathrm{in}} - V_{\mathrm{Cantilever}})} \quad (5.42)$$

and using the RT-characteristics should lead to the heater temperature.

Unfortunately, this procedure cannot be applied in this case mainly because of instabilities of the differential amplifier: It turns out, that the amplifier does not keep the reference voltage constant with the required precision. Instead another way has been used and will be described in the following.

5.6.3.1 Temperature of the tip heater during thermal imaging

First the temperature of the heater during imaging shall be determined. This can be done by taking an approach curve into account. Figure 5.28 shows an approach curve measured on the HfO_2 film with the same tip and the same input voltage as the thermal image in figure 5.27. The initial offset of the piezo displacement for the imaging procedure has been chosen as marked by the arrow, which corresponds to an initial heater temperature between 611.2 and 611.4°C. As already observed in previous approach curves a hysteresis effect between approaching and retracting occurs, which makes it difficult to decide, at which temperature the heater was during imaging.

Furthermore, a second uncertainty comes into play regarding the conversion of the approach curve data: During the approach curve measurement the $V_{\mathrm{Cantilever}}$ voltage is measured, while the input voltage V_{in} is kept constant. With these

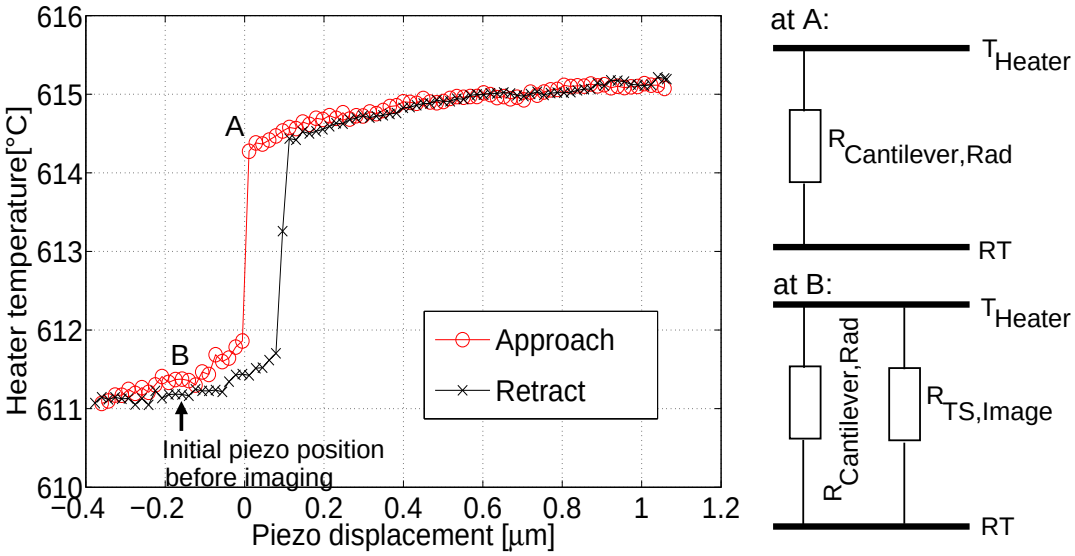

Figure 5.28: *Left:* Thermal approach curve measured on HfO_2 with the same input voltage used during the scanning of the thermal image shown in figure 5.27. Marked is the piezo position before the imaging has been started. *Right:* Equivalent circuit diagram of the thermal resistances.

quantities and the sense resistance of 2 kΩ the cantilever resistances is calculated and the RT characteristics of the cantilever is used to determine the heater temperature. So far, moderate input voltages and thus moderate heater temperatures have been used for the approach curve measurements of section 5.5. For these temperatures below 550 °C the RT curve is unique, but it splits up into two branches for temperatures higher than 550 °C as used for imaging (see figure 5.29) due to annealing effects within the heater as discussed in section 3.3. This makes it difficult to determine at which absolute temperature the heater was during the scan procedure. A difference of 7.0 K between the two branches in the RT curve of figure 5.29 for a given heater resistances is observed.

The hysteresis effects of both the approach curve and the RT-curve lead to an overall uncertainty in the absolute heater temperature of 7.2 K ranging from 611.2 to 618.4 °C.

Additionally, the absolute uncertainty of the heater temperature determination has be taken into account: As stated in section 3.3 an error of 30 % for the temperature calibration is assumed, which corresponds to 175.5 °C in this case. Thus,

$$T_{\mathrm{Heater,image}} = 615 \pm 176\,^{\circ}\mathrm{C}.$$

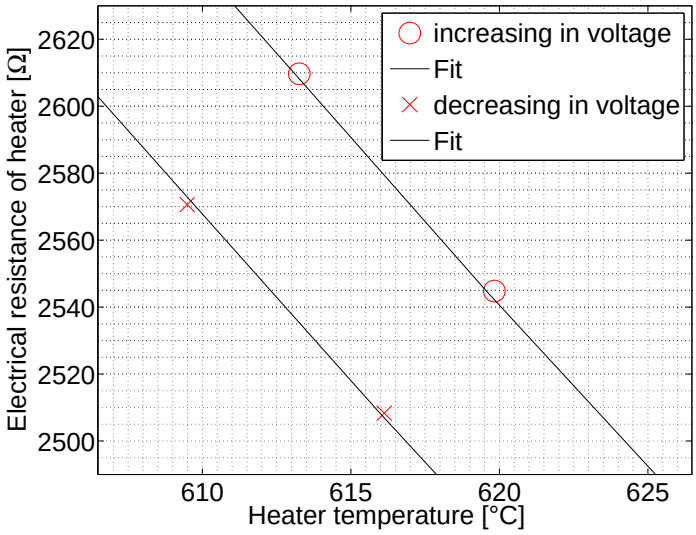

Figure 5.29: Zoom into the RT curve of the cantilever used for the thermal image shown in figure 5.27

5.6.3.2 Variation of the heater temperature during the imaging procedure

Now the variation of the heater temperature during the imaging procedure shall be determined:

- From figure 5.27 a variation of the amplified gain voltage of $\Delta V_{\mathrm{Gain}} = 0.2\,\mathrm{V}$ is observed.
- Since an amplification factor of $F_{\mathrm{Gain}} = 500$ is used, the variation of the cantilever voltage is

$$\Delta V_{\mathrm{Cantilever}} = V_{\mathrm{Cantilever,+}} - V_{\mathrm{Cantilever,-}} = \Delta V_{\mathrm{Gain}} \,/\, F_{\mathrm{Gain}} = 0.4\,\mathrm{mV}. \quad (5.43)$$

- The cantilever voltage of $V_{\mathrm{Cantilever}} = 2.4677\,\mathrm{V}$ corresponds to the heater temperature at the marked piezo position in the approach curve in figure 5.28. Thus, the cantilever voltages in the thermal images ranges from

$$V_{\mathrm{Cantilever,-}} = V_{\mathrm{Cantilever}} - 0.5 \cdot \Delta V_{\mathrm{Cantilever}} = 2.4675\,V \quad (5.44)$$

  to

$$V_{\mathrm{Cantilever,+}} = V_{\mathrm{Cantilever}} + 0.5 \cdot \Delta V_{\mathrm{Cantilever}} = 2.4679\,V. \quad (5.45)$$

- With these two values the corresponding heater resistances $R_{\text{Cantilever,+}}$ and $R_{\text{Cantilever,-}}$ can be calculated using equation 5.42 and then the well-known procedure of determining the heater temperature with the RT-characteristics can be conducted: The input voltage was V_{in} =4.4 V and a sense resistance of 2 kΩ was used and thus the electrical resistances of the cantilever are $R_{\text{Cantilever,+}} = 2554.6\,\Omega$ and $R_{\text{Cantilever,-}} = 2553.7\,\Omega$ respectively. Hence, the variation of the cantilever resistance was $\Delta R = 0.9\,\Omega$.
- To convert this into the corresponding heater temperature variation, the slope of the RT characteristics shown in figure 5.29 is used. The slope of both branches is equal and is calculated to be $S = 9.7\,\Omega/\text{K}$. With the resistance variation in the thermal image of $\Delta R = 0.9\,\Omega$ a variation of the heater temperature of

$$\boxed{\Delta T_{\text{Heater,image}} = \Delta R/S = 0.1\,\text{K}}$$

is calculated.

5.6.3.3 Variation of the thermal contact resistance during imaging

The temperature variation of the heater is due to variations of the thermal tip-sample contact resistance $R_{\text{TS,Image}}$ during the imaging procedure. In this section a calculation shall be carried out, which determines the variation of the thermal contact resistance in the thermal image.

The cantilever voltages during imaging are known from the above mentioned calculations and thus, the heater power range can be worked out. Together with the heater temperatures it is possible to derive the total thermal resistances at point B marked in 5.28. At this point the heat energy is transferred through the tip-sample contact, the cantilever legs and thermal radiation. The latter two can be combined to a single thermal resistance $R_{\text{Cantilever,Rad}}$, which forms a parallel connection with the tip-sample contact resistance. It is assumed, that the thermal imaging contrast is based only on variations of the tip-sample contact resistances, while $R_{\text{Cantilever,Rad}}$ remains constant.

This is not exactly correct, because as the tip snaps into contact with the sample, the heater comes closer to the surface and the radiation cooling will be stronger resulting in a smaller thermal resistance $R_{\text{Cantilever,Rad}}$. To investigate the extent of this effect the bending of the cantilever during the snap-in has to be estimated. This is done by considering the adhesion hysteresis of the approach curve, which is approximately 100 nm. This distance is approximately equal to the cantilever bending just before the tip snaps off the surface on the retracting part of the approach curve. Typically the cantilever deflection at the snap-in is much smaller than at the snap-off and we can assume that the cantilever is deflected by at most

100 nm at the snap-in. From the approach curve a temperature change about 0.3 °C at a distance change of 100 nm can be deduced. The effect may be a bit larger because of the obviously increasing slope of the approach curve near the sample surface. The total temperature difference of the heater between the points A and B is ≈ 3°C. Thus, one can deduce that this difference is made up of the enhanced radiation cooling, which leads to a temperature reduction of 0.3 °C, and 2.7 °C originated from the tip-sample contact cooling. This estimation shows, that the tip-sample contact cooling is the dominant effect and the enhanced radiation in contact plays a secondary role.

In detail, the calculation of the thermal tip-sample contact resistance $R_{\mathrm{TS,Image}}$ during imaging is performed in the following way:

1. As the cantilever voltage range is known (see equation 5.44 and 5.45), the heater power range during imaging can be calculated using the following equation

$$P_{\mathrm{Heater}} = V_{\mathrm{Cantilever}} \cdot I = V_{\mathrm{Cantilever}} \cdot \frac{V_{\mathrm{in}} - V_{\mathrm{Cantilever}}}{2k\Omega}. \tag{5.46}$$

   with I being the electrical current. With the cantilever voltages previously determined $V_{\mathrm{Cantilever,\text{-}}} = 2.4675\,\mathrm{V}$ and $V_{\mathrm{Cantilever,+}} = 2.4679\,\mathrm{V}$ the corresponding heater powers are $P_{\mathrm{Heater,+}} = 2.3841\,\mathrm{mW}$ and $P_{\mathrm{Heater,\text{-}}} = 2.3842\,\mathrm{mW}$ resulting in a power variation of $\Delta P_{\mathrm{Heater}} = 0.1\,\mathrm{mW}$.

2. In the previous section the heater temperature variation in the image has been calculated to be 0.1 K. From the approach curve in figure 5.28 a heater temperature at the marked imaging piezo position of $T_{\mathrm{Heater,image}} = 611.37\,^{\circ}\mathrm{C}$ is deduced and thus, the heater temperatures during imaging range from $T_{\mathrm{Heater,image,\text{-}}} = 611.32\,^{\circ}\mathrm{C}$ to $T_{\mathrm{Heater,image,+}} = 611.42\,^{\circ}\mathrm{C}$.

3. Since the heater power and the heater temperature are determined, the total thermal resistances are calculated using equation 5.7:

$$R_{\mathrm{Contact,Total,+}} = \frac{T_{\mathrm{Heater,+}} - \mathrm{RT}}{P_{\mathrm{Heater,+}}} = 2.4597 \times 10^5\,\mathrm{K/W} \tag{5.47}$$

   and

$$R_{\mathrm{Contact,Total,\text{-}}} = \frac{T_{\mathrm{Heater,\text{-}}} - \mathrm{RT}}{P_{\mathrm{Heater,\text{-}}}} = 2.4559 \times 10^5\,\mathrm{K/W}. \tag{5.48}$$

   respectively.

One should be aware, that the total thermal contact resistance $R_{\mathrm{Contact,Total,}\pm}$ is actually made up of two contributions as the equivalent circuit diagram in the right part of figure 5.28 shows: At point A the radiation and the heat transfer

through the cantilever legs are combined to $R_{\mathrm{Cantilever,Rad}}$ and at point B additionally the tip-sample contact resistance $R_{\mathrm{TS,Image}}$ forms a parallel connection with $R_{\mathrm{Cantilever,Rad}}$.

Thus, the above calculated total thermal contact resistances of the heater during imaging $R_{\mathrm{Contact,Total,\pm}}$ are given by

$$\frac{1}{R_{\mathrm{Contact,Total,+}}} = \frac{1}{R_{\mathrm{Cantilever,Rad}}} + \frac{1}{R_{\mathrm{TS,Image,+}}} \tag{5.49}$$

and

$$\frac{1}{R_{\mathrm{Contact,Total,-}}} = \frac{1}{R_{\mathrm{Cantilever,Rad}}} + \frac{1}{R_{\mathrm{TS,Image,-}}}. \tag{5.50}$$

The combined thermal resistances of radiation and the heat transfer through the cantilever at point A in figure 5.28 is worked out to be $R_{\mathrm{Cantilever,Rad}} = 2.4684 \times 10^5\,\mathrm{K/W}$ using equation 5.7 with values of $T_{\mathrm{Cantilever,Rad}} = 614.3\,^{\circ}\mathrm{C}$ for the heater temperature and $P_{\mathrm{Cantilever,Rad}} = 2.3874\,\mathrm{mW}$ for the power generated by the heater at point A. The tip-sample contact resistances in the thermal image turn out to be $R_{\mathrm{TS,Image,+}} = 6.979 \times 10^6\,\mathrm{K/W}$ and $R_{\mathrm{TS,Image,-}} = 4.850 \times 10^6\,\mathrm{K/W}$ respectively. Thus, a variation of the tip-sample contact resistance of

$$\boxed{\Delta R_{\mathrm{TS,Image}} = 2.13 \times 10^6\,\mathrm{K/W}}$$

is derived.

5.6.4 Material contrast in the thermal image

An interesting question resulting from the thermal image of figure 5.27 is whether the imaging contrast originates from different thermal properties of silicon oxide and hafnium oxide. In this case the mean thermal tip-sample contact resistance inside and outside of the spots are expected to be different and it would be possible to estimate values for the thermal conductivity of the two materials relative to each other. On the other hand, if the mean values were not different, then one would have to conclude, that the thermal imaging contrast is mainly due to topography effects at the edges of the spots similar to the thermal image of the silicon surface of figure 5.22. Thus, by analyzing the data of the thermal image, a deeper understanding of the thermal imaging capability can be gained.

5.6.4.1 Statistical analysis of the thermal image

At first, histograms of the thermal contact resistance data inside (i.e. on the silicon oxide) and outside the spots (i.e. on the hafnium oxide) shall be compared.

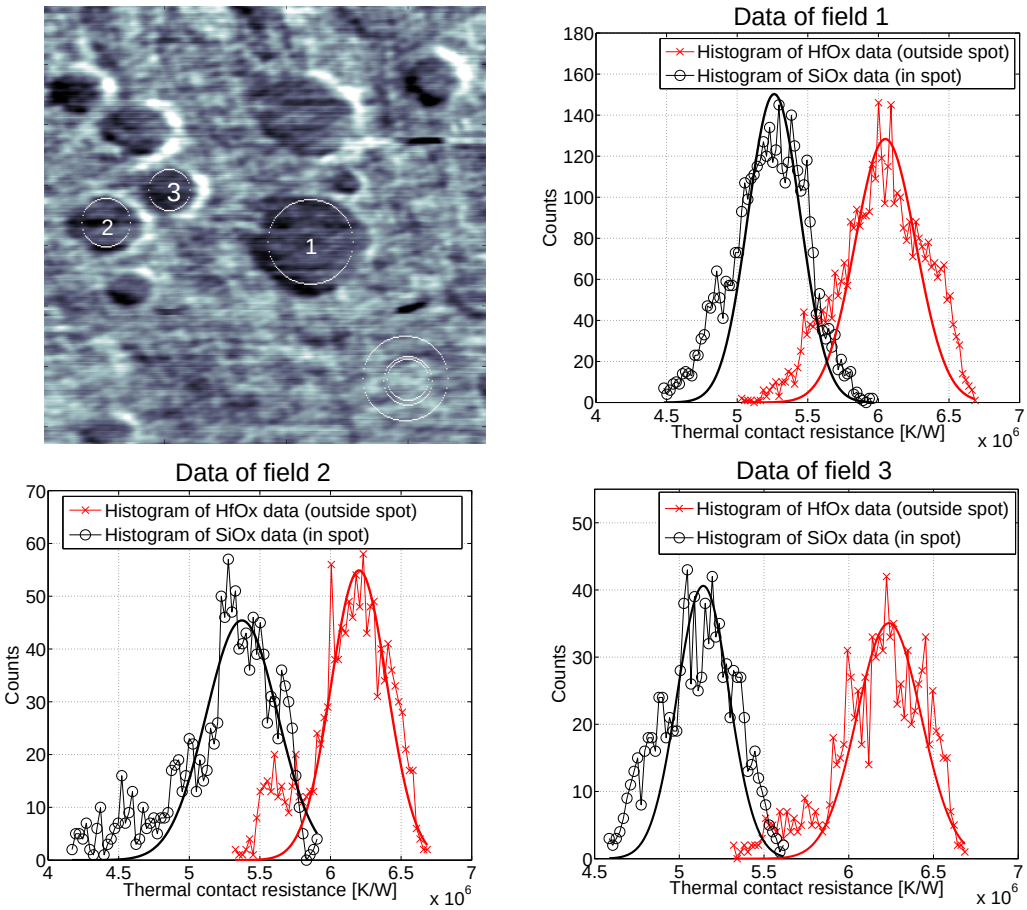

Figure 5.30: Thermal image with three fields marked with circles which are analyzed with the histograms also shown in the figure.

For this purpose three fields have been selected as shown in figure 5.30. The considered areas are marked and numbered in the image. Along with the data inside a spot, a reference field on the HfO_2 film with the same number of data points has been selected and analyzed. In the diagrams of figure 5.30 both sets of data are taken into account separately to plot the histograms. In all three cases the two histograms can be distinguished, which shows that indeed the mean values measured of the silicon oxide and the HfO_2 differ. For each spot the average and the standard deviation of the mean value are calculated and table 5.5 summarises the results.

Global averages of thermal contact resistances on both phases

So far only single spots in figure 5.30 have been analyzed. In the next section a model will be presented, which will be applied to calculate the thermal conduc-

Region	1	2	3
Number of data points	3905	1293	941
On silicon oxide			
Average $R_{\mathrm{TS,Image}}$ [10^6 K/W]	5.225	5.255	5.113
Standard deviation of mean $R_{\mathrm{TS,Image}}$ [10^3 K/W]	4.2	10.0	7.0
On HfO_2			
Average $R_{\mathrm{TS,Image}}$ [10^6 K/W]	6.023	6.130	6.176
Standard deviation of mean $R_{\mathrm{TS,Image}}$ [10^3 K/W]	4.8	7.8	8.7

Table 5.5: Average thermal contact resistances and according standard deviations obtained from the area marked in the thermal image shown in figure 5.30.

tivity of the hafnium oxide film relative to the silicon oxide. To gain best possible accuracy for this model the global average of the thermal contact resistances have to be taken into account, which will be determined in this section.

For the calculation of the global average of the thermal contact resistances on the hafnium oxide and on the silicon oxide only parts of the thermal image have been taken into account as shown in figure 5.31: Obvious scan artefacts e.g. at the edges of the spots are omitted in the analysis. Figure 5.31 (*middle*) shows the areas of data, which have been used for the average thermal contact resistance on the hafnium oxide film. For the average thermal contact resistance on the silicon oxide the areas shown in figure 5.31 (*right*) have been taken into account.

Figure 5.32 shows the histogram of the data obtained on the HfO_2 film and on the silicon oxide. Both distributions overlap, but nevertheless can clearly be distinguished. The average thermal contact resistance on the HfO_2 film is

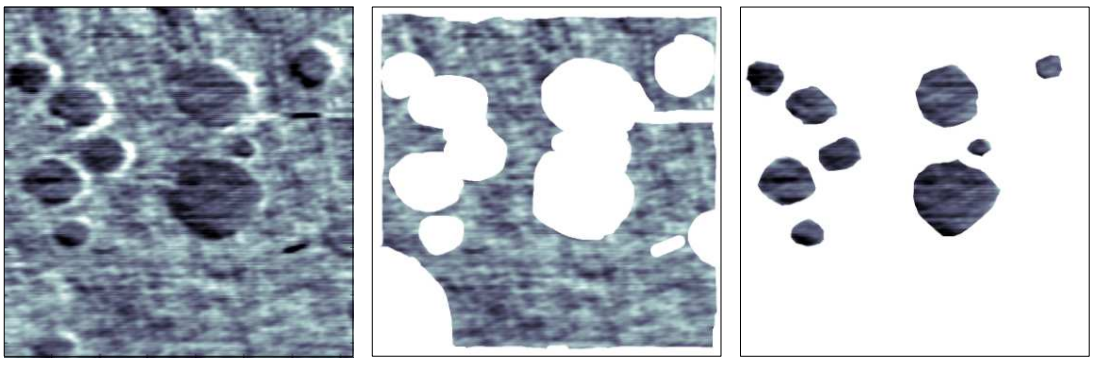

Figure 5.31: *Left:* Thermal image of the hafnium oxide / silicon oxide sample; *Middle:* Exclusion mask for the calculation of the global thermal contact resistances on the hafnium oxide; *Right:* Exclusion mask for the calculation of the global thermal contact resistances on the silicon oxide.

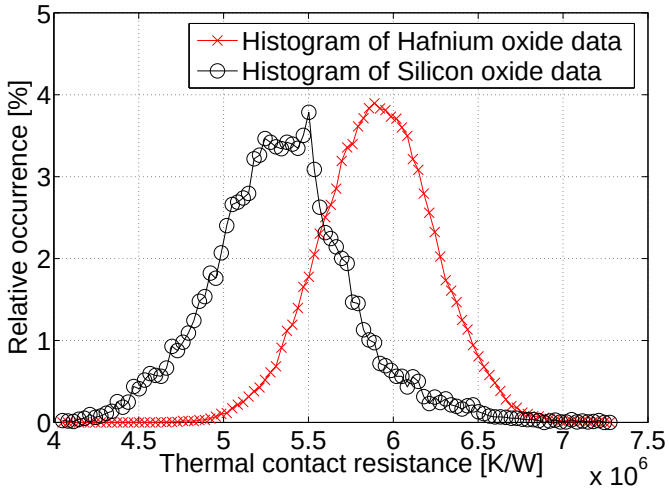

Figure 5.32: Histogram of the thermal contact resistances obtained from the thermal image with the exclusion masks shown in figure 5.30.

determined to be $5.909\times10^6\,\mathrm{K/W}$ and on silicon oxide $5.343\times10^6\,\mathrm{K/W}$. Table 5.6 summarises the data. Using the average thermal contact resistance on both phases of the thermal image, an estimation of the thermal conductivity of the hafnium oxide relative to the silicon oxide will be given in the next section.

	On silicon oxide	On HfO_2 film
Number of data points	17777	81676
Average $R_{\mathrm{TS,Image}}$	$5.343\times10^6\,\mathrm{K/W}$	$5.909\times10^6\,\mathrm{K/W}$
Standard deviation of mean $R_{\mathrm{TS,Image}}$	$3.1\times10^3\,\mathrm{K/W}$	$1.2\times10^3\,\mathrm{K/W}$

Table 5.6: Summary of the average and standard deviation of the thermal resistances obtained on HfO_2 film and on silicon oxide.

5.6.4.2 Determination of the thermal conductivity of the hafnium oxide layer

With the results for the thermal contact resistances obtained in the last section, the thermal conductivity of the hafnium oxide layer can be calculated using a simple model which shall be described in this section.

We have already seen in section 5.5.3.2 that the thermal contact resistance which is measured with our method, is made up of different contributions: The thermal resistance of the tip $R_{\mathrm{th,Tip}}$, the interface thermal resistance $R_{\mathrm{th,Interface}}$ and the spreading resistance of the sample surface $R_{\mathrm{th,Spreading}}$. These three resistances are in series and the sum of them gives the thermal tip-sample contact resistance

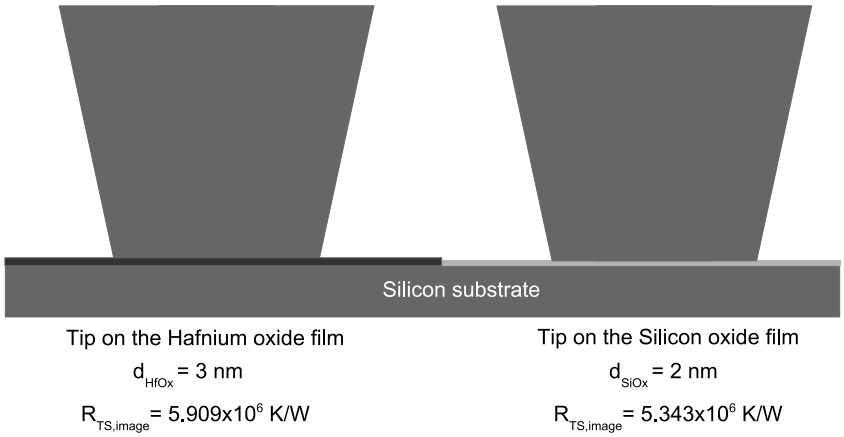

Figure 5.33: Schematic sketch of the heatable tip scanning the hafnium oxide sample. *Left:* Tip is on top of the 3 nm hafnium oxide film and the tip-sample thermal contact resistance is 5.909×10^6 K/W; *Right:* Tip is on top of the 2 nm thin self-passivated silicon oxide film and the tip-sample thermal contact resistance is 5.343×10^6 K/W.

$R_{\text{th,Tip-Sample}} = R_{\text{th,Tip}} + R_{\text{th,Interface}} + R_{\text{th,Spreading}}$. This only holds for the simple case that the tip is in contact with a sample, which is not covered by an additional layer such as a polymer film (PMMA or SU8) or an oxide layer (HfO_2 or silicon oxide).

Here, the thermal resistance of the hafnium oxide R_{HfO_2} and the silicon oxide layer R_{SiOx} respectively have to be taken into account as additional thermal resistances. Additionally, a second interface occurs between the oxide layers and the silicon substrate, which will be denoted with the variables $R_{\text{Int,HfO}_2\text{,Si}}$ and $R_{\text{Int,SiOx,Si}}$ respectively.

Figure 5.33 shows a schematic sketch of the heatable tip scanning a region on the hafnium oxide (*left*) and one on the silicon oxide (*right*). Since the diameter of the contact area turns out to be large (about 50 nm, see below) in comparison to the layer thickness (2 nm on silicon oxide and 3 nm on the HfO_2 film), spreading effects in the oxide layers can be neglected and only the thermal conductivity of the layer is taken into account. The above mentioned formula can be re-written in the following way for both cases shown in figure 5.33. If the tip scans the HfO_2 film, the thermal contact resistance $R_{\text{TS,Image,HfOx}}$ is given by:

$$R_{\text{TS,Image,HfO}_2} = R_{\text{Tip}} + R_{\text{Int,Tip,HfO}_2} + R_{\text{HfO}_2} + R_{\text{Int,HfO}_2\text{,Si}} + R_{\text{Spreading,Si}} \quad (5.51)$$

With the tip scanning on the silicon oxide, the thermal tip sample contact resistance $R_{\text{TS,Image,SiOx}}$ is given by:

$$R_{\text{TS,Image,SiOx}} = R_{\text{Tip}} + R_{\text{Int,Tip,SiOx}} + R_{\text{SiOx}} + R_{\text{Int,SiOx,Si}} + R_{\text{Spreading,Si}} \quad (5.52)$$

$R_{\mathrm{TS,Image,HfO_2}}$	Thermal resistance measured on the HfO_2 film in the thermal image
$R_{\mathrm{TS,Image,SiOx}}$	Thermal resistance measured on the silicon oxide film in the thermal image
R_{Tip}	Thermal resistance of the SFM tip
$R_{\mathrm{Int,Tip,HfO_2}}$	Thermal resistance of the interface between tip and HfO_2 film
$R_{\mathrm{Int,Tip,SiOx}}$	Thermal resistance of the interface between tip and silicon oxide film
$R_{\mathrm{HfO_2}}$	Thermal resistance of the HfO_2 film
R_{SiOx}	Thermal resistance of the silicon oxide film
$R_{\mathrm{Int,HfO_2,Si}}$	Thermal resistance of the interface between the HfO_2 film and the silicon substrate
$R_{\mathrm{Int,SiOx,Si}}$	Thermal resistance of the interface between the silicon oxide film and the silicon substrate
$R_{\mathrm{Spreading,Si}}$	Thermal spreading resistance in the silicon substrate

Table 5.7: Summary of the variables used for the calculation of the thermal resistance of the HfO_2 film.

The variables and their meaning are listed in table 5.7. We are especially interested in the thermal resistance of the hafnium oxide layer $R_{\mathrm{HfO_2}}$. According to theoretical considerations [88] one can assume that the interface resistances on the hafnium oxide and on silicon oxide are equal $R_{\mathrm{Int,Tip,SiOx}} \approx R_{\mathrm{Int,Tip,HfO_2}}$ and that the interface resistances between the oxide layers and the silicon substrate are equal $R_{\mathrm{Int,SiOx,Si}} \approx R_{\mathrm{Int,HfO_2,Si}}$. Subtraction of equation 5.52 from equation 5.51 leads to

$$\Delta R_{\mathrm{TS,Image}} = R_{\mathrm{TS,Image,HfO_2}} - R_{\mathrm{TS,Image,SiOx}} = R_{\mathrm{HfO_2}} - R_{\mathrm{SiOx}} \tag{5.53}$$

We also have to take into account, that both layers have different thicknesses and hence equation 5.53 is re-written in terms of the specific thermal resistances $\rho_{\mathrm{HfO_2}}$ and ρ_{SiOx} respectively, which are given by

$$\rho_{\mathrm{HfO_2}} = R_{\mathrm{HfO_2}} \cdot \frac{A_{\mathrm{HfO_2}}}{d_{\mathrm{HfO_2}}} \quad \text{and} \quad \rho_{\mathrm{SiOx}} = R_{\mathrm{SiOx}} \cdot \frac{A_{\mathrm{SiOx}}}{d_{\mathrm{SiOx}}} \tag{5.54}$$

where $A_{\mathrm{HfO_2}}$ and A_{SiOx} denote the contact area of the tip on the HfO_2 layer and on the silicon oxide layer respectively. $d_{\mathrm{HfO_2}}$ and d_{SiOx} represent the thicknesses of the HfO_2 layer and the silicon oxide layer respectively. Equation 5.53 can be re-written as follows:

$$\Delta R_{\mathrm{TS,Image}} = \frac{\rho_{\mathrm{HfO_2}} \cdot d_{\mathrm{HfO_2}}}{A_{\mathrm{HfO_2}}} - \frac{\rho_{\mathrm{SiOx}} \cdot d_{\mathrm{SiOx}}}{A_{\mathrm{SiOx}}} \tag{5.55}$$

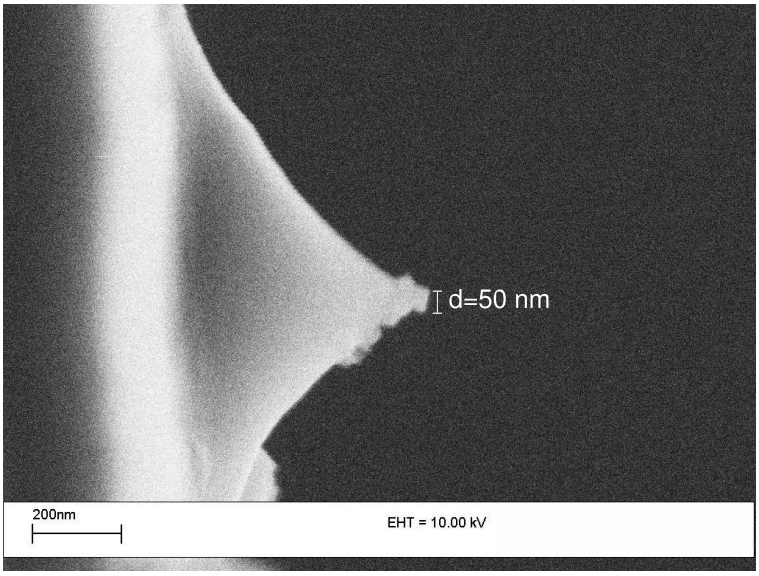

Figure 5.34: SEM image of the tip used for the thermal image (see figure 5.27) of the HfO_2 sample. The SEM image has been taken after the tip was used for the vacuum measurement. Obviously the tip has been blunted by the scanning procedure and a had the shape of a frustum. The size of the flat end turns out to be about 50 nm in diameter.

Thus, the specific thermal resistivity of HfO_2 is:

$$\rho_{HfO_2} = \frac{A_{HfO_2}}{d_{HfO_2}} \cdot \left(\Delta R_{TS,Image} + \frac{\rho_{SiOx} \cdot d_{SiOx}}{A_{SiOx}} \right) \tag{5.56}$$

With this equation the specific thermal resistivity of HfO_2 can be calculated if the values of all relevant quantities can be determined: The film thickness of the hafnium is known to be $d_{HfO_2} = 3\,\text{nm}$ [103] and the thickness of the self-passivated silicon oxide is typically $d_{SiOx} = 2\,\text{nm}$ [104]. In the last section, a thermal contact resistance of $R_{TS,Image,HfOx} = 5.909 \times 10^6\,\text{K/W}$ on the hafnium oxide film and $R_{TS,Image,SiOx} = 5.343 \times 10^6\,\text{K/W}$ on the silicon oxide has been determined. Thus, the difference is $\Delta R_{TS,Image} = 5.7 \times 10^5\,\text{K/W}$.

Furthermore, the contact area of the tip with the sample is needed. Considering the Scanning Electron Microscope (SEM) image of the tip taken after the experiment (figure 5.34) one observes that the tip clearly has been blunted and the resulting diameter of the tip end is about $d_{Tip} \approx 50\,\text{nm}$. Thus, we can assume the contact area to be equal to the flat end of the tip. The contact area both on the hafnium oxide and on the silicon oxide can be calculated to be

$$A = A_{HfO_2} = A_{SiOx} = \pi \left(\frac{d_{Tip}}{2} \right)^2 = 2 \times 10^{-15}\,\text{m}^2 \tag{5.57}$$

Finally, for the calculation of the thermal conductivity of the HfO_2 film the thermal conductivity is required. A literature value for bulk silicon oxide of $\sigma_{SiOx} = \rho_{SiOx}{}^{-1} = 1.4\,W/(Km)$ [105, 106] can be found. The specific thermal conductivity of the HfO_2 film of

$$\boxed{\sigma_{HfO_2} = \rho_{HfO_2}{}^{-1} = 0.86\,W/(Km)}$$

is calculated.

It is somewhat difficult to determine the accuracy of this result. Due to the systematic error of the heater temperature calibration, this result will also be afflicted with at least an error of 30 %. However, further systematic uncertainties come into play: The assumption of equal interface resistances on hafnium and silicon oxide has to be checked. Both the contact area and the interface constants on both phases could possibly cause uncertainties. Additionally, different roughnesses of both materials could also influence the result. As a rough estimation one can assume that this value is afflicted with an error of 50 %. Nevertheless, the result is in remarkably good agreement with another study, which determined the thermal conductivity of microcrystalline hafnium oxide films to be 1.2-1.3 W/(Km) at a temperature of 300 K [106].

5.7 Chapter summary

In this chapter Scanning Thermal Microscopy (SThM) measurements under vacuum conditions were presented. For this purpose the heatable SL1 type cantilevers introduced in chapter 3 were used in a vacuum chamber at pressures of 10^{-5} hPa in order to eliminate heat transfer through air and through the water meniscus typically present under ambient conditions.

In the first experimental part of the chapter, heat transfer mechanisms of the heatable cantilevers were investigated: The main focus has been put on the heat transfer from the heater located in the cantilever through the tip to the sample using the concept of thermal resistances. The dependence of the thermal resistance on the thermomechanical properties of different samples, different tip geometries and on the adhesion force was investigated. The various measurements enabled the correlation of the experimental data with a theoretical model and the determination of various parameters involved in the model. With these results it was possible to identify the different contributions of the heat transfer mechanisms present under ambient conditions during the "Millipede" bit writing process: It turns out, that less than 0.1 % of heater power is transferred through the tip to the sample while 35 % is dissipated through the cantilever legs and 64 % is lost into the surrounding air. These measurements additionally enabled

to calculate the sample surface temperature of $T_{Surface,PMMA} = 136\,°C$ on PMMA and $T_{Surface,Si} = 31\,°C$ on silicon. Furthermore, radiative near-field heat transfer has been shown to be strongly distance and material dependent as predicted by theoretical models.

Besides thermal heat transfer experiments thermal imaging with a lateral resolution of 50 nm and a thermal resolution of 0.1 K was demonstrated on a 2-phase sample system consisting of a 3 nm thin HfOx sample and a native 1-2 nm thin silicon oxide sample. The regions of different materials have clearly been distinguished by statistical means and the data analysis led to values of the thermal conductivity of the hafnium oxide being in the expected range.

Chapter 6

Outlook

The results obtained in this study, the experimental techniques and the data analysis could serve as a starting point for further research in the field of thermomechanics on the nanoscale.

Although force-distance curves with the SFM are widely used nowadays, surprisingly little work has been reported at elevated sample temperatures [50, 51]. Especially the properties of polymers on the nanoscale are of interest, because they are of technological and scientific interest and the required temperatures are significantly lower than e.g. for metals and thus, experimentally well accessible. Since the frequency dependence of thin PMMA films was recently investigated at room temperature with SFM force-distance curve measurements [65], the combination of both heat and frequency could possibly lead to a thorough understanding of mechanical properties on the nanoscale. Furthermore, the relaxation processes of indentations created at various sample temperatures and frequencies could be investigated in a similar manner as in the experiments shown in section 2.6.

One limitation of the force-distance curves with the SFM is that this experimental technique is so far restricted to relative measurements with a single tip, because as shown in section 2.3.2 the SFM tips used in this study break at 1.5-2 μN. Hence, robust SFM tips with a well-defined shape would be desirable, which are not available so far and cannot not be manufactured in a reproducible way today. Experimental data obtained with such tips in combination with theoretical models and computer simulations would be necessary for a thorough understanding of the indentation process.

The thermal vacuum SFM certainly offers the largest potential for further research and development both in technological and scientific respect. Since hardly any scanning thermal microscopy measurements have so far been performed under vacuum conditions [79] the measurements of this study are to some extend pioneering and the possible potential of this technique are manifold.

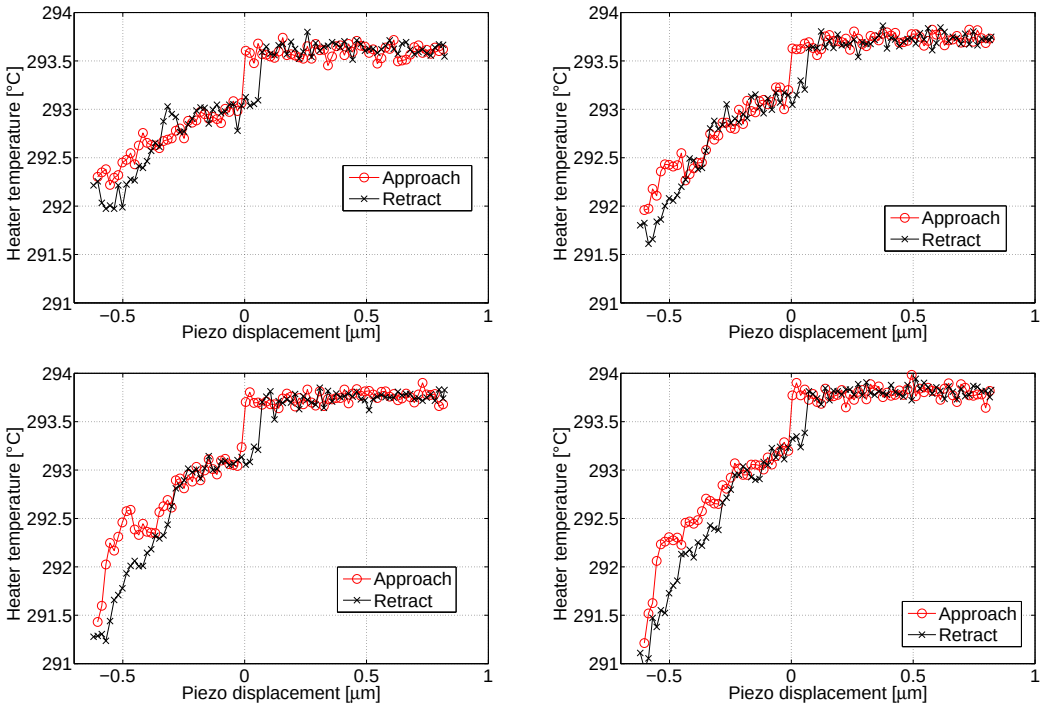

Figure 6.1: Series of four approach curves measured at the same location on PMMA. The change of the contact part of the curves is persumably originated from a permanent surface modification.

One interesting topic would be the investigation of the polymer surface after the approach curve measurements. As one has seen in chapter 4 a threshold exists for combinations of contact pressure and tip temperature for the creation of permanent surface deformations. The penetration of the tip into the polymer film, however, should cause an enhanced heat transfer which should be measurable with approach curves. Hence, considering a sequence of thermal approach curves gives a first hint for surface modifications caused by the tip as shown in figure 6.1. A series of four approach curves measured at the same location on the 35 nm PMMA film on silicon is presented. The increase of the heater cooling in the contact part from curve to curve is a clear hint that the surface is permanently deformed or the polymer material is damaged. For the investigation of the polymer surface at the location of the approach curve measurement thermal imaging capability of polymer samples under vacuum conditions would be necessary. This, however, is difficult to realize mainly due to the very high heater temperature of more than 600 °C necessary for imaging under vacuum conditions. Although the surface temperature is significantly smaller at these high heater temperatures, the polymer material is destroyed at these high heater temperatures making imaging impossible. Alternatively, contact mode imaging using an optical detection system would also allow to image the sample surface,

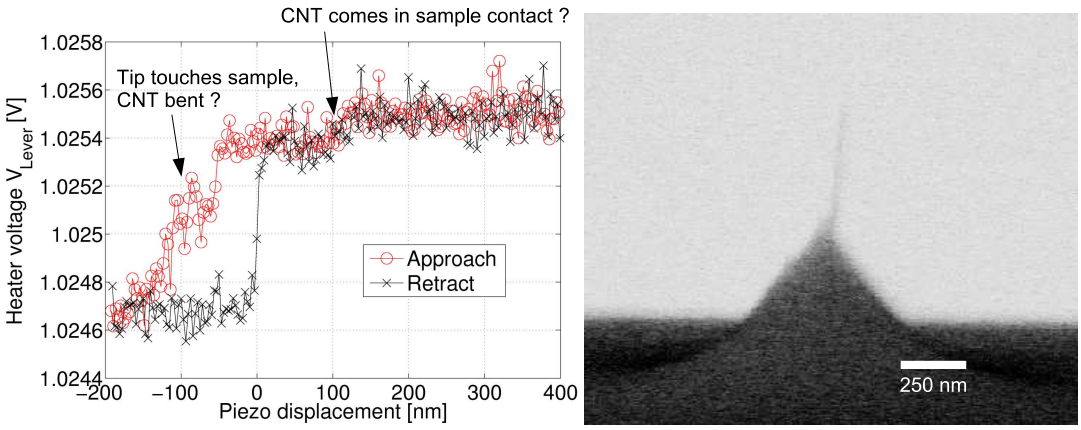

Figure 6.2: Thermal approach curve measured with a carbon nanotube attached to the tip of a heatable cantilever.

but unfortunately at the present stage now optical detection system was implemented in the vacuum chamber and it was not possible to install one within the framework of this study.

The data analysis of the approach curves measured under vacuum conditions could also be further developed. The approach curves measured in this study have merely been analyzed in the off-contact part and at the snap-in position. The contact region, however, has so far not been taken into account and contains certainly valuable information: The slope of the contact part is supposed to be a function of the heater temperature, the tip radius, the polymer material and the possibly of the polymer film thickness and thus, the analysis of the data in this respect could lead to more complete understanding of the thermomechanics of the tip sample contact.

The experimental results obtained in this study are unfortunately afflicted with large errors, which is mainly due to the large uncertainties of the heater calibration procedure and therefore, a more precise method would be desirable. More important would progress concerning fundamental challenges of the data analysis: The determination of the thermal resistance of the hafnium oxide film is based on the knowledge of the thermal resistance of the silicon oxide assuming that the interface resistances between the films and the silicon substrate are equal. This assumption can to some extend be justified with theoretical models [88] but experimental investigation of this assumption would be desirable.

Besides experimental refinements and further developments of the techniques used in this study a huge variety of experiments using the heatable cantilevers is imaginable. Numerous topics could be addressed with the thermal vacuum SFM: One example is presented in figure 6.2 (*left*), which shows a thermal approach curve

measured using a tip with a multi-wall carbon nanotube (MWCNT) attached to its end (see figure 6.2 *right*). Thus, as the CNT comes into contact with the sample, heat is transferred from the heater through the tip and the CNT to the sample making it in principle possible to directly determine the thermal conductivity of the CNT. In the experiment shown it is unfortunately unclear, which kink in the approach curve is originated from the CNT and form the tip itself. However, nanoindentation experiments under ambient conditions show that the thermal resistance of these tip is significantly smaller than that of conventional tips [107].

A similar experiment could be conducted to measure the thermal conductivity of single molecules by combining the thermal approach curve measurements presented in this study with force spectroscopic techniques: Force spectroscopy experiments with conventional SFM tips are performed by bringing the tip in contact with the sample surface, where single macro-molecules (e.g. DNA molecules) are deposited on. These molecules are bound with one end to the tip and with the other end to the sample. As the tip is retracted form the surface, the molecule is unfolded by the force acting on it and the unfolding process can be studied. With the thermal vacuum SFM setup these unfolding experiments could be conducted with the heatable cantilevers and the heat would be transferred through a single molecule to the sample. Similar to the above mentioned CNT experiment the thermal conductivity of the molecule could be determined.

As the results of the thermal imaging under vacuum conditions are very encouraging this technique could be further improved and applied to other samples such as nanostructures (e.g. to the gold clusters shown in Appendix A or samples with oriented polymer molecules (e.g. block-copolymers), self-assembled monolayer and CMOS structures.

Besides using the heatable cantilevers in contact mode other operation modes would offer main advantages. Especially the digital pulsed-force mode (DPFM) could lead to an improvement of the experimental technique: In DPFM the piezo is modulated with a frequency of 1-2 kHz in perpendicular direction to the sample and several thermal approach curves would be recorded at every pixel. Especially the drift effects of the differential amplifier discussed in section 5.6.3 would be circumvented, because the entire approach curve could be measured at each pixel and used for the calculation of the thermal contact resistance data. Further, wear induced by a sliding tip during imaging in contact mode could be reduced.

First measurements using the heatable cantilever in PFM have been conducted on the PMMA-Polystyrene (PS) polymer blend, a similar sample as the PMMA-SBS polymer blend discussed in section 4.3, in order to demonstrate the feasibility of this method: Figure 6.3 shows the topography image obtained from the optical deflection signal and the simultaneously recorded thermal image. This image was generated from the thermal signal of the cantilever heated using a DC input

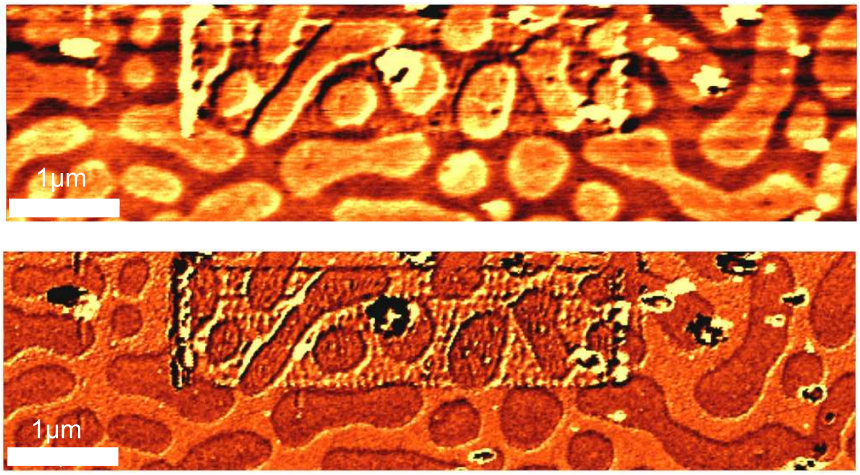

Figure 6.3: Topography image (*top*) obtained from the optical deflection signal and image generated from the simultaneously recorded thermal signal (*bottom*) measured in Pulsed Force mode with a DC voltage applied to the cantilever circuit.

voltage to the cantilever circuit. Since this image is a zoom out of a region previously scanned, surface modifications can be observed by the frame visible in the image. Besides material deposition at the edges of the smaller scan frame, ripple formation can be ascertained, which has already been reported using the heatable cantilevers in contact mode in previous studies [15,108]. In this case the thermal signal resembles the sample topography just like the contact mode image shown in figure 4.3 due to the distance dependence of the heater temperature. However, performing such PFM measurements under vacuum conditions or on flat samples with very little topography would lead to thermal information of the sample surface on the nanoscale.

This technique could even be extended: Whereas the input voltage to the cantilever circuit is kept constant in the above mentioned experiment one could also think of a kind of pump-probe experiment by switching on and off the heater. As several approach curves are typically measured at each pixel, the first curve could be performed with the heater switched on in order to effectuate any kind of surface modification (e.g. deformation or softening). The following curves could be used to analyze this modification with the heater being switched off. By performing these measurement with different modulation frequencies of the piezo it could be even possible to determine time scale of heat diffusion processes on the nanoscale. Similar experiments could be performed in Tapping Mode on even shorter time scales, because the cantilever is excited in resonance. For the 3LD cantilever this means a resonance frequency of about 60 kHz, which corresponds to a oscillation time of about 15 μs.

Besides the possibility to perform thermal conductivity and calorimetry measurements on the nanoscale the heatable cantilevers have been demonstrated to serve as a tool for nano lithography. In a recent study [109] these cantilevers have been used for dip pen lithography. The large advantage is that ink can be used which is solid at room temperature and becomes fluid at elevated temperatures. Thus, by heating the tip ink can locally and selectively be deposited. With this novel technique structure sizes of 100 nm were demonstrated [109] and it is certainly possible to create smaller structures with this method. Furthermore, so far deposition of octadecylphosphonic acid (OPA) on mica has been shown and extending this method to other materials and substrates would be desirable.

Chapter 7

Summary

In the present study a variety of experiments concerning the nanoscale thermomechanical properties of several materials were presented. The interplay of thermal and mechanical material properties was investigated on the nanoscale by conducting Scanning Force Microscopic (SFM) measurements on heated samples and using heatable SFM cantilever tips at elevated sample temperatures and under vacuum conditions. These heatable SFM cantilever tips are manufactured at the IBM Research Laboratory in Zurich (Switzerland) and are used for investigations of a novel data storage concept called "Millipede", which uses these heatable tips to create tiny indentations in thin polymer films to store data with ultra-high density. As the present study was conducted in cooperation between the IBM Laboratory in Zurich and the Department of Experimental Physics at the University of Ulm (Germany), these not commercially available cantilever tips could be used for the experiments described in this work. On the one hand, investigations concerning possible data storage media for the "Millipede" were performend and hence, research closely linked to a possible product was conducted. On the other hand, basic physical research in the field of Scanning Thermal microscopy (SThM) was carried out. Mainly thin polymer films (Polymethylmethacrylate and SU8 epoxy photo resists) with a thickness of less than 100 nm were investigated, but also silicon substrates as well as a 3 nm thin hafnium oxide layer on silicon were analyzed.

In the first experiment, the thermomechanical properties of a 35 nm thick PMMA film in comparison with a 80 nm SU8 epoxy photo resist, both on a silicon substrate, were investigated with force distance curve measurements using a commercial microscope (Dimension D3100 from Veeco) and conventional Tapping Mode SFM cantilever tips. The indentation experiments were performed at elevated sample temperatures between 100 and 130 °C using a heating stage. The maximum forces were in the range of up to 4 μN leading to permanent impressions in the polymer films of lateral diameters between 100 and 300 nm.

From the force penetration curves, which were calculated by combining force distance curves and a calibration measurement on silicon (calibration force curve, CFC), characteristic quantities like the indentation depth, remanence depth, hysteresis energy and penetration slope among others were analyzed as a function of the sample temperature and of the applied force. Whereas PMMA undergoes the glass transition in this specific temperature range and all quantities were clearly temperature dependent, the temperature dependence on the SU8 sample was significantly smaller. Nevertheless, the observed temperature dependence on PMMA is smaller than expected from the change of the mechanical properties in the glass transition.

The thermal stability of the permanent indentations created on PMMA with the force distance curve measurements was investigated by continuously scanning the indentations in Tapping Mode and analysis of the indentation depth. A temperature dependent relaxation process was identified, which clearly shows the glass transition of the polymer between 115 and 118 °C.

Two types of experiments were conducted using SFM cantilevers manufactured with lithographic methods at the IBM Zurich Research Laboratory, which have integrated heater making it possible to perform measurements with heated tips. These silicon probes are similar to conventional V-shaped SFM cantilevers with a sharp tip of about 10 nm radius situated at the end of the cantilever beams. In addition, depending on the design, one or two resistive heater are integrated in the cantilever beam, which are lower doped than the rest of the beams and heat up when an electrical current passes through the heater. The heater uses an electrical power of up to 1-2 mW and reaches heater temperature of 800-1000 °C at most. For the experiments presented in this study, however, typical heater temperatures of 80-400 °C were used for indentation experiments and of up to 600 °C for thermal imaging under vacuum conditions. For the doping concentrations used, the heater has its maximum electrical resistance at 550 °C, which is used to calibrate the heater temperature. To deduce the heater power and temperature a 2 kΩ resistor was used in series with the cantilever enabling the measurement of the electrical current and the resistance of the heater.

In the first experiment using the heatable cantilevers both thermal topography imaging and high speed indentations was realized. To do this, the heatable cantilevers were implemented in the above-mentioned commercial microscope Dimension D3100/3000 SFM from Veeco. Thermal topography imaging relies on the distance dependence of the heater temperature at changing distances to the sample surface and was demonstrated on a 2-phase polymer sample consisting of Styrene-Butadiene-Styrene and PMMA. The indentation measurements have been conducted at sample temperatures between 30 and 130 °C on a 35 nm thick PMMA film and on a 80 nm SU8 film both on silicon. The indentation process was performed by heating the cantilever heater for 10 μs to temperatures of 80

to 400 °C and simultaneously applying an electro-static force of 20 to 550 nN. To investigate the influence of the heater temperature and the electro-static force on the indentation topography, arrays of indentations were created with varying heater temperature along the horizontal axis and changing electro-static forces along the vertical axis. These arrays were produced by making use of the so-called 'Nanoscript', which is a programming tool for the D3000 SFM similar to the programming language C. With this script language it was possible to move the tip to specific positions, to set voltages and triggers on the SAM (Signal Access Module) and to control the entire process. The calibration procedure of the electro-static force is based on optical force distance curves measured at different DC voltages applied to the sample. With increasing sample voltage the snap-off position is shifted to larger cantilever forces needed to retract the tip from the sample making it possible to determine the electro-static force as function of the sample voltage.

Contact mode images of the indentations scanned with an unheated tip using the optical deflection system have been analyzed both qualitatively and quantitatively. Whereas the influence of the sample temperature on the indentation topography on PMMA is large, on SU8 hardly any dependency of the topography on the sample temperature is observed. On PMMA both the lateral dimensions as well as the indentation depth and the rim volume increase significantly at higher sample temperatures.

The main part of the present study focuses on Scanning Thermal Microscopy (SThM) measurements under vacuum conditions. For this purpose the heatable cantilevers were implemented in a vacuum chamber and operated at pressures of 10^{-5} hPa in order to eliminate heat transfer through air and through the water meniscus typically present under ambient conditions. With this setup the heat transfer from the heater through the tip to different samples was investigated and thermal imaging was realized.

The heat transfer mechanisms were investigated by performing thermal approach curves similar to force distance curves on a 35 nm thick PMMA film on silicon and on a silicon substrate. The heat transport through the tip sample contact is observable by the additional cooling of the heater when the tip comes into contact with the sample. The approach curves were quantitatively analyzed using the concept of thermal resistances and thermal conductivities, which describe the amount of heat energy transferred through a certain area at a given temperature difference per unit of time. The dependence of the thermal tip sample contact resistance on the thermomechanical properties of different samples, different tip geometries and on the adhesion force was investigated. These measurements enabled the correlation of the experimental data with a theoretical model and to determine the various parameters used in this model. With these results it was possible to identify the different contributions of the heat transfer mechanisms

present under ambient conditions during the "Millipede" bit writing process: It turned out, that less than 0.1 % of the heater power is transferred through the tip to the sample while 35 % is dissipated through the cantilever legs and 64.9 % is lost into the surrounding air.

These measurements allowed to deduce the sample surface temperatures on different samples during the thermal approach curve measurements in vacuum. Due to varying thermomechanical properties of the materials the surface temperatures deviate significantly. For example for a heater temperature of 200 °C a surface temperature of $T_{Surface,PMMA} = 136\,°C$ on PMMA and $T_{Surface,Si} = 31\,°C$ on silicon was calculated.

Besides the thermal conductivity through the cantilever and the tip-sample contact, radiative heat transfer was observed. In addition to distance independent thermal far-field radiation distance dependent near-field radiation occurs, which results from the coupling of non-propagating evanescent waves, if the distance between heater and sample is comparable to the radiation wavelength ($\approx 1\,\mu$m). This near-field radiation could be observed from the distance dependent heater temperature in the off-contact part of thermal approach curves measured with heater temperatures of more than 600 °C.

Finally, thermal imaging with a lateral resolution of 50 nm and a thermal variation of the heater of 0.1 K was demonstrated on a 2-phase sample system consisting of a 3 nm thin hafnium oxide film and a native 1-2 nm thin silicon oxide. Changing thermal contact resistances on different samples gave rise to a heater temperature variation, which resulted in a measurable cantilever voltage change. This in turn permitted the variation of the thermal contact resistance and the heater temperature to be calculated. The materials could clearly be distinguished by statistical means and the quantitative data analysis led to a value of the thermal conductivity of the thin film hafnium oxide of $0.86 \pm 0.43\,$W/(Km) which is in good accordance with other studies.

Zusammenfassung

In der vorliegenden Studie wurden verschiedene Experimente zur Untersuchung von thermo-mechanischen Eigenschaften unterschiedlicher Materialien auf der Nanoskala durchgeführt. Die Wechselwirkung von thermischen und mechanischen Materialeigenschaften wurde mittels rasterkraftmikroskopischer Techniken auf geheizten Proben und mittels heizbarer Rasterkraftmikroskopiespitzen untersucht. Diese am IBM Forschungslabor Zürich hergestellten heizbaren Spitzen dienen zur Untersuchung und Entwicklung eines neuartigen Datenspeicherkonzeptes ("Millipede"), bei dem nanometrische Indentationen auf dünnen Polymerfilmen erzeugt werden und somit Daten mit bisher unerreichter Dichte gespeichert werden können. Da die vorliegende Arbeit im Rahmen einer Kooperation zwischen dem IBM Forschungslabor Zürich und der Abteilung Experimentelle Physik der Universität Ulm durchgeführt wurde, standen diese kommerziell nicht erhältlichen Meßsonden für die hier gezeigten Messungen zur Verfügung. Einerseits wurden in dieser Studie Untersuchungen von möglichen Speichermedien für das "Millipede"-Konzept angestellt und somit relativ produktnahe Forschungs- und Entwicklungsarbeit geleistet, andererseits wurden grundlegend neue physikalisch-technische Entwicklungen auf dem Gebiet der thermischen Rastersondenmikroskopie vorangetrieben. Deshalb standen Untersuchungen von dünnen Polymerfilmen (Polymethylmethacrylat PMMA und SU8 Epoxid Photolack) mit einer Schichtdicke von unter 100 nm im Vordergrund, aber auch Siliziumsubstrate sowie eine 3 nm dünne Hafniumoxidschicht wurden analysiert.

Zunächst wurden grundlegende thermo-mechanische Eigenschaften eines 35 nm dünnen PMMA-Films auf Silizium im Vergleich mit einem 80 nm dünnen SU8-Film auf Silizium mittels Kraft-Distanz-Kurven untersucht. Dazu wurden konventionelle Tapping Mode Spitzen in einem kommerziellen Rasterkraftmikroskop (Dimension D3100/3000 von Veeco) eingesetzt. Für diese Indentationsexperimente wurde die Probe mittels einer Heizplatte auf Temperaturen von 100 bis 130 °C gebracht. Maximalkräfte von bis zu 4 μN wurden verwendet, um permanente Indentationen von lateralen Dimensionen zwischen 100 und 300 nm zu erzeugen.

Die Kraft-Eindring-Kurven, die aus der Kombination der Kraft-Distanz-Kurve mit einer Kalibriermessung berechnet werden, wurden hinsichtlich der charak-

teristischen Größen wie Eindringtiefe, Remanenztiefe, Hystereseenergie und Eindringsteigung u. a. als Funktion der Probentemperatur und Kraft ausgewertet. Während sich PMMA im betreffenden Temperaturbereich im Glasübergang befindet und alle Größen eindeutig temperaturabhängig sind, ist der Einfluß der Probentemperatur auf SU8 signifikant geringer. Gleichwohl ist die beobachtete Temperaturabhängigkeit auf PMMA geringer als aufgrund der sich im Glasübergang stark ändernden mechanischen Moduln zu erwarten wäre.

Die thermische Stabilität der Indentationen auf PMMA wurde durch kontinuierliches Abbilden der Probentopographie im Tapping Mode untersucht und die Lochtiefe als Funktion der Zeit und Probentemperatur ausgewertet. Ein klar temperaturabhängiger exponentieller Relaxationsprozess konnte identifiziert werden, der es ermöglicht, den Glasübergang zu bestimmen. Im Fall der hier verwendeten PMMA Probe lag dieser zwischen 115 und 118 °C.

Die weiteren Experimente wurden mit den bereits angesprochenen heizbaren Meßsonden durchgeführt, die im IBM Forschungslabor Zürich mit lithographischen Methoden hergestellt werden. Diese aus Silizium gefertigten Sonden sind gängigen V-förmigen Cantilevern ähnlich und haben eine scharfe Spitze von etwa 10 nm Radius am Ende der Cantileverbalken. Zusätzlich sind je nach Design ein oder zwei Heizer in die Cantileverbalken integriert. Diese Heizer sind geringer dotiert als die übrigen Bereiche der Balken und heizen sich deshalb auf, wenn ein elektrischer Strom fließt. Der Heizer kann elektrische Leistungen von bis zu 1-2 mW und Maximaltemperaturen von 800-1000 °C erreichen. In den hier gezeigten Experimenten wurden jedoch Heizertemperaturen von 200-400 °C für Indentationsversuche und 600 °C für thermische Rastersondenmikroskopie unter Vakuumbedingungen verwendet. Die Abhängigkeit des elektrischen Widerstands des Heizers von der Temperatur ermöglicht eine Bestimmung der Heizertemperatur, da für die benutzten Dotierkonzentrationen ein Maximum des elektrischen Widerstands bei 550 °C bekannt ist. Die elektrische Leistung des Heizers und der elektrische Widerstand wurden mittels eines 2 kΩ Vorwiderstandes in Serie mit dem Cantilever gemessen, um die Temperaturbestimmung zu ermöglichen.

Im ersten Teil, in dem die heizbaren Cantilever zum Einsatz kamen, wurden sowohl verschiedene Hochgeschwindigkeits-Nanoindentationsexperimente durchgeführt als auch ein thermisches Bildgebungsverfahren der Probentopographie realisiert. Dafür wurden die heizbaren Cantilever im oben erwähnten kommerziellen Rasterkraftmikroskop Dimension D3100/3000 von Veeco implementiert. Das thermisches Abbilden der Probentopographie beruht auf der Abstandsabhänigkeit der Heizertemperatur zur Probenoberfläche und wurde auf einem 2-Phasen-Probensystem bestehend aus Styrol-Butadien-Styrol und PMMA realisiert. Die Indentationsexperimente wurden bei Probentemperaturen zwischen 30 und 130 °C auf einem 35 nm dünnen PMMA Film und auf einem 80 nm SU8 Film auf Silizium durchgeführt. Der Indentationsprozess wurde durch Aufheizen des Can-

tileverheizers für 10 μs auf Temperaturen von 80 bis 400 °C bei gleichzeitigem Anlegen einer elektrostatischen Kraft von 20 bis 550 nN realisiert. Um den Einfluß der Heizertemperatur und der elektrostatischen Kraft auf die Topographie der Indentationen zu untersuchen, wurden zweidimensionale Indentationsfelder erzeugt. In horizontaler Richtung wurde dazu die Heizertemperatur variiert und vertikal die elektrostatische Kraft verändert. Zur Erstellung dieser Gitterstrukturen wurde das sogenannte 'Nanoscript' benutzt, das eine Programmiersoftware ähnlich der Programmiersprache C für das D3000/D3100-Rasterkraftmikroskop darstellt. Diese Skriptsprache ermöglicht es, die Spitze gezielt zu positionieren, Spannungen und Trigger auf einem zum Mikroskop gehörenden Zusatzgerät (SAM - Signal Access Module) zu setzen und so den Gesamtprozess zu steuern. Die Kalibrierung der elektrostatischen Kraft erfolgte mittels optischer Kraft-Abstands-Kurven, die bei verschiedenen Gleichspannungen an der Probe gemessen wurden. Mit zunehmender Spannung an der Probe verschiebt sich der Abrißpunkt zu größeren Cantileverkräften, was eine Bestimmung der elektrostatischen Kraft ermöglicht.

Die Indentationen wurden im Kontakt-Modus mit ungeheizter Spitze unter Ausnutzung des konventionellen optischen Detektionssystems abgebildet. Die auf diese Weise erhaltenen Bilder wurden sowohl qualitativ als auch quantitativ analysiert. Während die Probentemperatur großen Einfluß auf die Topographie der Indentationen auf PMMA hat, ist bei SU8 kaum eine Abhägigkeit von der Probentemperatur festzustellen. Sowohl die lateralen Dimensionen als auch die Indentationstiefen und das Auswurfvolumen nehmen bei hohen Probentemperaturen signifikant zu.

Der Hauptteil der Arbeit befaßt sich mit thermischer Rasterkraftmikroskopie unter Vakuumbedingungen. Zu diesem Zweck wurden die heizbaren Cantilever in einer Vakuumkammer bei einem Druck von 10^{-5} hPa implementiert, um sowohl Wärmeleitung durch die Luft als auch den typischerweise unter Normalbedingungen vorhandenen Wassermeniskus auszuschließen. Mit diesem Versuchsaufbau wurden Wärmeübertragsmessungen des Spitze-Probe-Kontaktes durchgeführt sowie ein auf thermischen Effekten beruhendes Bildgebungsverfahren realisiert.

Der Wärmeübertrag vom Heizer durch die Spitze in die Probe wurde mittels sogenannter thermischer Abstandskurven untersucht, die den bekannten Kraft-Distanz-Kurven ähnlich sind. Thermische Abstandskurven wurden auf einem Silziumsubstrat und dem 35 nm PMMA Film gemessen. Der Wärmetransport durch die Spitze zur Probe konnte anhand des zusätzlichen Kühlungseffektes beobachtet werden, der auftritt sobald die Spitze in Kontakt mit der Probe kommt. Die Datenanalyse erfolgte mittels des Konzeptes der thermischen Widerstände. Die Abhängigkeit des thermischen Spitze-Probe-Kontaktwiderstandes von thermo-mechanischen Eigenschaften verschiedener Probenmaterialien, verschiedener Spitzengeometrieen und von der Adhäsionskraft wurden untersucht. Diese Messungen ermöglichten es, die Meßdaten mit den Vorhersagen eines theo-

retischen Modells zu vergleichen und verschiedene Parameter des Modells zu bestimmen.

Anhand der Resultate konnten die verschiedenen Beiträge der Wärmeübertragsmechanismen unter Normalbedingungen quantitativ bestimmt werden. Man kann daraus schließen, dass beim Schreibvorgang im "Millipede" weniger als 0.1 % der elektrischen Heizleistung zum lokalen Aufheizen des Probenmaterials unter der Spitze verwendet wird, während 35 % durch die Cantileverbalken zum Siliziumchip transportiert wird, auf dem der Cantilever befestigt ist, und 64.9 % der elektrischen Leistung über Wärmeleitung durch die Luft verloren geht.

Weiterhin konnten die Oberflächentemperaturen verschiedener Proben während der Messung der thermischen Abstandskurven bestimmt werden. Aufgrund der stark unterschiedlichen thermo-mechanischen Eigenschaften der untersuchten Silizium- und PMMA-Proben ergeben sich signifikant unterschiedliche Oberflächentemperaturen. Bei einer Heizertemperatur von beispielsweise 200 °C berechnet man eine Oberflächentemperatur von 136 °C auf PMMA und von 31 °C auf Silizium.

Neben den Wärmeübertragsmechanismen durch den Spitze-Probe-Kontakt und durch die Cantileverbalken konnte auch Wärmestrahlung beobachtet werden. Außer abstandsunabhängiger Fernfeldstrahlung nach dem Stefan-Boltzmann-Gesetz tritt bei Abständen zwischen Heizer und Probe, die im Bereich der Strahlungswellenlänge liegen ($\approx 1\,\mu$m), auch eine abstands- und materialabhängige Strahlungskühlung auf, die auf Nahfeldeffekten beruht und aus evaneszenten, nicht propagierenden Wellen besteht. Diese kann anhand der abstandsabhängigen Heizertemperatur einer thermischen Abstandskurve außerhalb des Kontaktbereiches nachgewiesen werden.

Neben den Wärmeübertragsmessungen mittels thermischer Abstandskurven konnte ein thermisches Bildgebungsverfahren mit einer lateralen Auflösung von besser als 50 nm und einer Heizertemperaturvariation von etwa 0.1 K realisiert werden. Das dabei verwendete 2-phasige Probensystem bestand aus einem 3 nm dünnen Hafniumoxidfilm und einem 1-2 nm dünnen, spontan gewachsenen Siliziumoxidfilm. Für die Messung wurde eine konstante elektrische Spannung an die Serienschaltung aus Cantileverheizer und 2 kΩ-Vorwiderstand angelegt. Die Spitze wurde im Scan-Modus der konstanten Höhe über die Probe gerastert und die differenziell verstärkte Cantileverspannung an jedem Bildpunkt gemessen. Aufgrund verschiedener thermischer Kontaktwiderstände variiert die Heizertemperatur und damit die Cantileverspannung auf verschiedenen Materialien, woraus sich ein Bild der Cantileverspannung ergibt. Dieses läßt sich wiederum in eine Variation der Heizertemperatur und des thermischen Kontaktwiderstands umrechnen. Die quantitative Analyse der Meßdaten zeigt, dass sich die Meßwerte auf beiden Materialien statistisch klar unterscheiden und führt zu einer thermischen Leitfähigkeit des Dünnfilm-Hafniumoxids von $0.86 \pm 0.43\,\mathrm{W/(Km)}$, die in guter Übereinstimmung mit anderen Studien ist.

Appendix A

Proof for the penetration of the PMMA film by the tip

The measurements of force-distance curves at sample temperatures above the glass transition and with forces larger than 3 μN (see figure 2.12 in section 2.5.2.2) shows a characteristic vertical peak at the turnaround point of the FPC (see figure 2.12 in section 2.5.2.2). This vertical peak most likely shows that the tip penetrates through the PMMA film and reaches the silicon substrate. In this chapter an alternative way based on lithographic techniques to prove this interpretation will be considered.

As figure A.1 illustrates the idea is to use the penetrated PMMA film as a mask

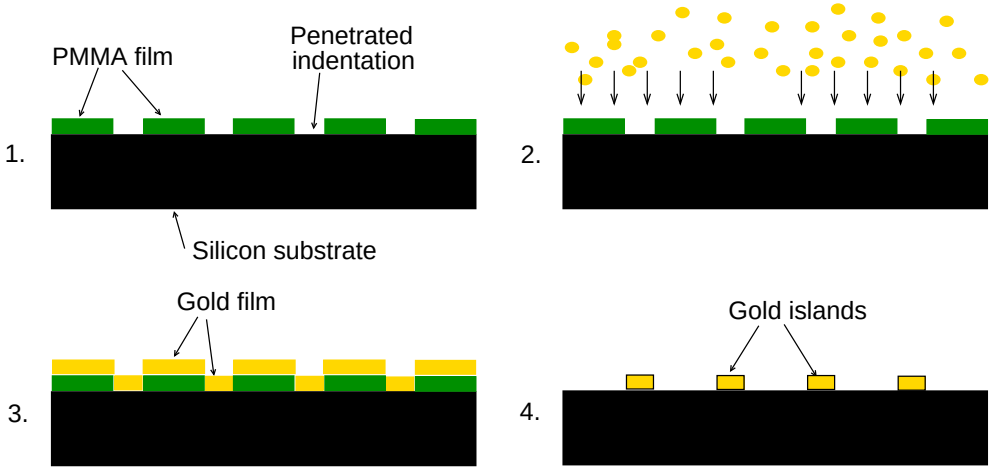

Figure A.1: Procedure illustrating the creation of small Gold islans on the silicon substrate proving that the tip indeed had reached the silicon substrate during the indentation process.

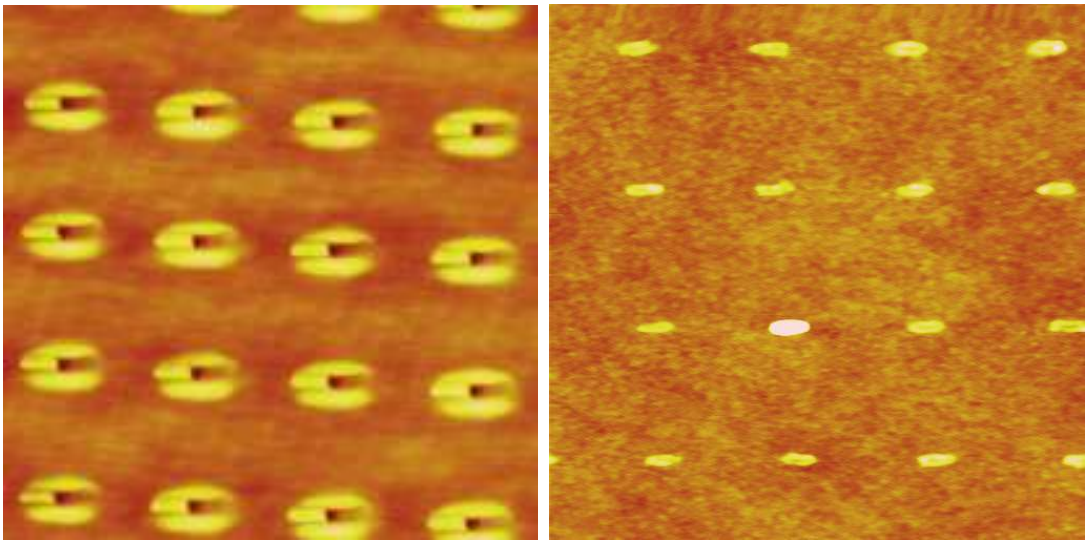

Figure A.2: *Left:* Array of indentations created with maximum forces of $\approx 6\,\mu$N in a 35 nm thin PMMA film on silicon. *Right:* As a result of the procedure described in the text Gold islands with dimensions of 140 nm $\times$ 50 nm $\times$ 5 nm remain on the silicon substrate. Both image sizes: 1.8 μm, Height scale: 20 nm (*left*) and 10 nm (*right*)

for the creation of Gold islands at the locations where the indentations have been situated. In detail the following procedure has been conducted:

1. An array of indentation is created in 35 nm thin PMMA film on silicon with high forces (about 4-6 μN) at room temperature.
2. A thin Gold film of about 100 nm thickness is sputtered onto the PMMA sample.
3. A lift-off process is conducted using an alkaline remover for photo resists and subsequent ultra-sonic bath for 2 minutes at 60 °C. With this lift-off step the double layer of Gold and PMMA is removed completely from the silicon except at the positions of the indentation, where Gold has reached the substrate, small Gold island of about the indentation diameter remain.

Figure A.2 shows on the left a Tapping Mode image of a 20×20 array of indentations created with FPC measurements at room temperature. After the conduction of the abovementioned sputter and lift-off procedure the Gold islands shown in figure A.2 on the right result. The size of the islands is measured from the SFM image to be about 140 nm×50 nm×5 nm (Width × Length × Height). Due to convolution effects the true lateral dimensions are probably smaller. The asymmetric shape of the island could also result from convolution effects, if the imaging tip would also be asymmetric.

Appendix B

Estimation of the deformation energy with the Hertzian model

The elastic deformation energy of the surface when the tip indents into the polymer film can be estimated using Hertzian contact theory [110]. According to this theory the penetration depth δ of the tip as function force F exerted by the tip of radius R is given by

$$\delta = F^{2/3} \left[\frac{1}{K^2 R} \right]^{1/3} \tag{B.1}$$

K is the so-called effective modulus and is given by

$$\frac{1}{K} = \frac{3}{4} \left(\frac{1 - \nu^2_{\text{Polymer}}}{E_{\text{Polymer}}} + \frac{1 - \nu^2_{\text{silicon}}}{E_{\text{silicon}}} \right) \tag{B.2}$$

where E_{Polymer} and E_{silicon} are the Young's Moduli and ν_{Polymer} and ν_{silicon} the Poisson's ratio of the sample material and the tip material respectively. Formula B.1 can be rewritten to give

$$F = \delta^{3/2} (K^2 R)^{1/2} = K \sqrt{R} \delta^{3/2} \tag{B.3}$$

The deformation energy is given by W:

$$W = \int F \mathrm{d}\delta \tag{B.4}$$

Inserting of formula B.3 leads to

$$W = \int_0^{\delta_{\max}} \delta^{3/2} K \sqrt{R} \, \mathrm{d}\delta = K \sqrt{R} \int_0^{\delta_{\max}} \delta^{3/2} \mathrm{d}\delta = \frac{2}{5} K \sqrt{R} \, \delta_{\max}^{5/2} \tag{B.5}$$

where $\delta_{\max}$ denotes the maximum tip pentration depth.

In our case of a silicon tip indenting a polymer film, we can assume the silicon tip to be much harder than the polymer, i.e. $E_{\text{silicon}} \gg E_{\text{PMMA}}$. Hence,

$$K = \frac{4E_{\text{PMMA}}}{3(1-\nu^2_{\text{PMMA}})} \tag{B.6}$$

With the literature values of $E_{\text{PMMA}} = 3.3 \times 10^9\,\text{N/m}^2$ [20] and $\nu = 0.4$ [16] for PMMA the effective modulus is calculated to $K = 5.2 \times 10^{-9}\,\text{N nm}^{-2}$. From the SEM image in figure 2.5 we can deduce a tip radius of about 20 nm. Thus, for the elastic deformation energy a value of $W = 421.1\,\text{keV}$ is calculated with formula B.5. This estimation only takes the elastic deformation energy into account, but the plastic and viscoelastic energies are not considered. Thus, this estimation give a lower limit of the energies involved in the indentation process. Thus, the calculated value is slightly too high, but at least the range of the measured values corresponds with the measured quantity. For more precise calculations a more adequate model and a better knowledge about the material properties would be required.

Bibliography

[1] G. Binnig and H. Rohrer. Scanning tunneling microscopy. *Helvetica Physica Acta*, 55:726–735, 1982.

[2] G. Binnig, C.F. Quate, and Ch. Gerber. Atomic force microscope. *Phys. Rev. Lett.*, 56(9):930–933, March 1986.

[3] D.M. Eigler and E.K. Schweizer. Positioning single atoms with a scanning tunneling microscope. *Nature*, 344:524–526, 1990.

[4] Leon Abelmann (University of Twente), Takahiro Onoue, Martin Siekman, Rogelio Murillo, and Cock Lodder. Magnetic probe recording, February, 28th - March 1st, 2005. Presentation on "International Probe Storage Workshop III" at IBM Research Laboratory, Zurich.

[5] S. Hong (Samsung), H. Ko, D.-K. Min, J. H. Jung, H. Park, C. Parkand S. Buehlmann, Y. W. Nam, Y. Kim, K. No, H. C. Shin, and H. J. Shin andN. Park. Resistive Probe Storage: R/W Mechanism, February, 28th - March 1st, 2005. Presentation on "International Probe Storage Workshop III" at IBM Research Laboratory, Zurich.

[6] Ken Eldredge (HP). A planar electrostatic motor for probe strorage, February, 28th - March 1st, 2005. Presentation on "International Probe Storage Workshop III" at IBM Research Laboratory, Zurich.

[7] U. Dürig, P. Vettiger, and G. K. Binnig. The "Millipede" - more than one thousand tips for future AFM data storage. *IBM J. RES. DEVELOP.*, 44(3), 2000.

[8] P. Vettiger, G. Cross, M. Despont, U. Drechsler, U. Dürig, B. Gotsmann, W.Häberle, M.A. Lantz, H.E. Rothuizen, R. Stutz, and G.K. Binnig. The "Millipede" - nanotechnology entering data storage. 1(1):39–55, March 2002.

[9] Bharat Bhushan. *Handbook of Nanotechnology*, chapter E31. Springer, 2004.

[10] U. Drechsler, N. Bürer, M. Despont, U. Dürig, B. Gotsmann, F. Robin, and P. Vettiger. Cantilevers with nano-heaters for thermomechnical storage application. *Microelectronic engineering*, 67-68(2):397–404, 2003.

[11] H. Pozidis, W. Häberle, D. Wiesmann, U. Drechsler, M. Despont, T.R. Albrecht, and E. Eleftheriou. Demonstration of thermomechnical recording at 641 Gbit / in^2. *IEEE Trans. Magn.*, 40(4 pt.2):2531–2536, 2004.

[12] Taken from www.zurich.ibm.com by courtesy of Evangelos S. Eleftheriou, IBM Research GmbH Zurich, Säumerstrsse 4, CH-8803 Rüschlikon.

[13] H. J. Mamin and D. Rugar. Thermomechanical writing with an atomic force microscope tip. *Appl. Phys. Lett.*, 61:1003–1005, 1992.

[14] Courtesy of Evangelos S. Eleftheriou, IBM Research GmbH Zurich, Säumerstrsse 4, CH-8803 Rüschlikon.

[15] Bernd Gotsmann and Urs T. Dürig. *Applied scanning probe methods II*, chapter Nano-thermomechanics: Fundamentals and application in data storage devices. Springer, to be published 2006.

[16] H.G. Elias. *Makromoleküle*. Hüthig & Wepf Verlag Basel Heidelberg New York, 4 edition, 1981.

[17] P.C. Hiemenz. *Polymer Chemistry - The Basic Concepts*. Marcel Dekker, 1984.

[18] P.J. Flory. *Statistical mechanics of chain molecules*. Interscience Publishers a division of John Wiley & Sons, 1969.

[19] Strobl. *Polymers*. Oxford University Press, 1986.

[20] J. Brandrup and E.H. Immergut. *Polymer Handbook*. Wiley-Interscience Publications, 2 edition.

[21] M. Pietralla. *Advanced Functional Molecules and Polymers, Volume 4, Physical properties and applications*, volume 4, chapter Conduction of heat in polymers, pages 99–121. Overseas publishers association, 2001.

[22] J. Mannhart and D.G. Schlom. Oxide- Tausendsassas für die Mikoelektronik. *Physik Journal*, June:45–51, 2005.

[23] R.J. Colton, A. Engel, J.E. Frommer, H.E. Gaub, A. Gewirth, R. Guckenberger, J. Rabe, W.M. Heckl, B. Parkinson, and Rabe. *Procedures in Scanning Probe Microscopies*. John Wiley & Sons, 1 edition, 1998. Seite 159.

[24] Bharat Bhushan. *Handbook of Nanotechnology*. Springer, 2004.

[25] Veeco, Digital Instruments GmbH, Janderstrasse 9, 68199 Mannheim, Germany.

[26] O.Marti and J. Cholchero nd J. Mlynek. Combined scanning force and friction microscopy of mica. *Nanotechnology*, 1:141–144, 1990.

[27] Bharat Bhushan. *Handbook of Nanotechnology*, chapter C17,D26. Springer, 2004.

[28] U.D. Schwarz, H. Blum, H. Hölscher, W. Allers, and R. Wiesendanger. *The physics of sliding friction*, chapter Friction in the low-load regime: Studies on the presure and direction dependence of frictional forces by means of friction force microscopy, pages 369–402. Kluwer Academic Publishers, 1996.

[29] H.U. Krotil. *CODYMode®:Scanning Force Microscopy: The current Measurement of Adhesion, Friction and Viscoelasticities*. Shaker Verlag, 1 edition, 2000.

[30] Armin Rosa-Zeiser, Eva Weilandt, Sabine Hild, and Othmar Marti. The simultaneous measurement of elastic, electrostatic and adhesive properties by scanning force microscopy: pulsed-force mode operation. *Meas. Sci. Technol.*, 8:1333–1338, 1997.

[31] Armin Rosa-Zeiser. *Der Pulsed Force Mode als kraftmikroskopische Untersuchungsmethode für unterschiedlich gefüllten Naturkautschuk bei linearer Deformation*. PhD thesis, Universität Ulm, June 1997.

[32] Alexander Gigler and Othmar Marti. *SPMs beyond imaging*, chapter Pulsed Force Mode SFM. P. Samori, to be published 2005.

[33] P.M. Spizig. Dynamische Rasterkraftmikroskopie. Master's thesis, 2002. PhD thesis, Universität Ulm.

[34] Atomic Force Microscopy Digital Pulsed Force Mode, Witec GmbH, HörvelsingerWeg 6 , D-89081 Ulm, Germany.

[35] P. Maivald, H.J. Butt, S.A.C. Gould, C.B. Prater, B. Drake, J.A. Gurley, V.B. Ellings, and P.K. Hansma. Using force modulation to image surface elasticities with the atomic force microscope. *Nanotechnology*, 2:103–106, 1991.

[36] M. Radmacher, R.W. Tillmann, and H.E. Gaub. Imaging viscoelasticity by force modulation with the atomic force microscope. *Biophysical Journal*, 64:735–742, 1993.

[37] E. Meyer, H. Heinzelmann, P. Grütter, T. Jung, T. Weisskopf, H.R. Hidber, R. Lapka, H. Rudin, and J. Güntherodt. *J. Microscopy*, 152:269, 1988.

[38] B. Cappella and G. Dietler. Force-distance curves by atomic force microscopy. *Surface Science Reports*, 34, 1999.

[39] J. Domke and M. Radmacher. Measuring the elastic properties of thin polymer films with the atomic force microscope. *Langmuir*, 14:3320–3325, 1998.

[40] M. Heuberger, G. Dietler, and L. Schlapach. Mapping the local young's modulus by analysis of the elastic deformations occuring in atomic force microscopy. *Nanotechnology*, 5:12–23, 1994.

[41] S.A. Chizhik, Z. Huang, V.V. Gorbunov, N.K. Myshkin, and V.V. Tsukruk. *Langmuir*, 14:2606–2609, 1998.

[42] Mark R. VanLandingham, John S. Villarrubia, Will F. Guthrie, and Greg F. Meyers. Nanoindentation of polymers: An overview. *Recent Advances in Scanning Probe Microscopy, Proceedings of the 220th American Chemical Scociety National Meeting*, 44(3), August 2000.

[43] E. Boschung, M. Heuberger, and G. Dietler. Energy dissipation during nanoscale indentation of polymers with an atomic force microscope. *Appl. Phys. Lett.*, 64(14), April 1994.

[44] D. Drechsler. *Rasterkraftmikroskopische Untersuchungen zu materialspezifischen Eigenschaften von Polymeren und ihren Blendsystemen.* PhD thesis, Universität Münster, Germany, 1998.

[45] R. M. Overney, C. Buenviaje, R. Luginbühl, and F. Dinelli. Glass and structural transitions measured at polymer surfaces on the nanoscale. *Journal of thermal analysis and calorimetry*, 59:205–225, 2000.

[46] C. Buenviaje, F. Dinelli, and R. M. Overney. *Interfacial Properties on the submicron scale*, chapter Glass transition measurements of ultrathin polymer films. American Chemical Society, 2000.

[47] F. Dinelli, C. Buenviaje, and R. M. Overney. Glass transitions of thin polymeric films: Speed and load dependence in lateral force microscopy. *Journal of chemical physics*, 113(5):2043–2048, 2000.

[48] S.S. Sills, R. M. Overney, W. Chau, V.Y. Lee, R.D. Miller, and J. Frommer. Interfacial glass transition profile s in ultrathin, spin cast polymer films. *Journal of chemical physics*, 120(11):5334–5338, 2004.

[49] C. Buenviaje, F. Dinelli, and R. M. Overney. *Interfacial Properties on the submicron scale*, chapter Glass transition measurements of ultrathin polymer films. American Chemical Society, 2000.

[50] V.N. Bliznyuk, H.E.Assender, G.A.D. Briggs, and Y. Tsukahara. Surface glass transition temperature of amorphous polystyrene measured by SFM. *submitted to Appl. Phys. Lett.*

[51] V.N. Bliznyuk, H.E.Assender, and G.A.D. Briggs. Surface glass transition temperature of amorphous polymers. a new insight with SFM. *Macromolecules*, 35, 2002.

[52] Molecular Imaging, 4666 S. Ash Avenue, Tempe, Arizona 85282 U.S.A.

[53] Lake Shore Cryotronics Inc., 575 McCorkle Blvd., Westerville OH 43082, U.S.A.

[54] Andreas Kleiner. Thermal stability of nanometric polymer structures. Master's thesis, September 2003. Diploma thesis, Universität Ulm.

[55] S. Ge, Y. Pu, H.F. Zhang, M.Rafailovich, J.Sokolov, C. Buenviaje, R. Buckmaster, and R.M. Overney. *Phys. Rev. Let.*, 85(11):2340, 2000.

[56] K. Weishaupt, H. Krbecek, M. Pietralla, H. D. Hochheimer, and P. Mayr. Pressure dependence of the elastic constants of Poly(methylmethacrylate). *Polymer*, 36(17):3267–71, 1995.

[57] S.-R. Ge, A. Takahara, and T.Kaiiyama. *Langmuir*, 11:1341, 1995.

[58] S. Theobald, W.Pechold, and B.Stoll. The pressure and temperature dependence of the relaxation processes in poly(methylmethacrylate). *Polymer*, 42(1):289–295, 2001.

[59] F. Yang and J.C.M. Li. Impression recovery of PMMA. *J. Mat. Res.*, 12(10):2809–2814, 1997.

[60] H.M. Pollock and A. Hammiche. Micro-thermal analysis: techniques and applications. *Journal of Physics D: Applied Physics*, 34:R23–R53, 2001.

[61] K. Edinger, T. Gotszalk, and W. Ranglow. Novel high resolution scanning thermal probe. *J. Vac. Sci. Technol.B*, 19(6):2856–2860, 2001.

[62] Li Shi and Arun Majumdar. Recent revelopments in micro and nanoscale thermoetry. *Microscale thermophysical Engineering*, 5:251–265, 2001.

[63] personal communication with M. Despont, IBM Research GmbH Zurich, Säumerstrsse 4, CH-8803 Rüschlikon.

[64] S.M. Sze. *Physics of semiconductor devices.* John Wiley and Sons, 1981.

[65] Michael Holzwarth. Frequency dependence of viscoelastic properties of polymers. *Diploma thesis, Universität Ulm*, June 2005.

[66] Scott Sills, R. M. Overney, Bernd Gotsmann, and Jane Frommer. Strain shielding and confined plasticity in thin polymer films: Impacts on thermomechanical data storage. *Tribology Letters*, 19(1):9–15, 2005.

[67] Mark A. Lantz, Bernd Gotsmann, Urs T. Dürig, and Peter Vettiger. Carbon nanotube tips for thermomechanical data storage. *Applied Physics Letters*, 83(6):1266–1268, 2003.

[68] personal communication with B. Gotsmann, IBM Research GmbH Zurich, Säumerstrsse 4, CH-8803 Rüschlikon.

[69] Matlab, The language of technical computing, The MathWorks, Inc., 3 Apple Hill Drive, Natick, MA 01760-2098, UNITED STATES.

[70] A. Majumdar, J. Lai, M. Chandrachood, O. Nakabeppu, Y. Wu, and Z. Shi. Thermal imaging by atomic force microscopy using thermocouple cantilever probes. *Rev. Sci. Instrum.*, 66(6):3584–3592, 1995.

[71] M. Song, D.J. Hourston, D.B. Grandy, and M. Reading. An application of micro-thermal analysis to polymer blends. *Journal of applied polymer science*, 81:2136–2141, 2001.

[72] V.V. Tsukruk, V.V. Gorbunov, and N. Fuchigami. *Thermochimica Acta*, 395:151–158, 2003.

[73] H.M. Pollock, A. Hammiche, M. Song, D.J. Hourston, and M. Reading. Interfaces in polymeric systems as studied by c.a.s.m. *J. Adhesion*, 67:217–234, 21998.

[74] D.M. Price, M. Reading, and T.J. Lever. Applications of micro-thermal analysis. *Journal of Thermal analysis and calorimetry*, 56:673–679, 1999.

[75] D.M. Price, M. Reading, A. Hammiche, and H.M. Pollock. New adventures in thermal analysis. *Journal of Thermal analysis and calorimetry*, 60:723–733, 2000.

[76] D.M. Price, M. Reading, R.M. Smith, H.M. Pollock, and A. Hammiche. Localised evolved gas analysis by micro-thermal analysis. *Journal of Thermal analysis and calorimetry*, 64:309–314, 2001.

[77] D.S. Fryer, P.F. Nealey, and J.J. de Pablo. Thermal probe measurements of the glass transition temperature for ultrathin polymer films as a function of thickness. *Macromolecules*, 33, 2000.

[78] O. Nakabeppu and T. Suzuki. Microscale temperature measurement by scanning thermal microscopy. *Journal of thermal analysis and calorimetry*, 69:727–737, 2002.

[79] W. Müller-Hirsch, A. Kraft, M.T. Hirsch, J. Parisi, and A. Kittel. Heat transfer in ultrahigh vacuum scanning thermal microscopy. *J. Vac. Sci. Technol. A*, 17(4):1205–1210, 1999.

[80] Othmar Züger. *Scanning Tunneling Microscopy on Gallium single crystal surfaces close to the melting temperature.* PhD thesis, ETH Zurich, Switzerland, 1992.

[81] Jäger Computergesteuerte Messtechnik GmbH, Rheinstraße 2-4, 64653 Lorsch, Germany.

[82] Gang Chen. Phonon heat conduction in nanostructures. *International Journal of Thermal Sciences*, 39:471–480, 2000.

[83] Y.S. Ju and K.E. Goodson. Phonon scattering in silicon films of thickness below 100 nm. *Applied Physics Letters*, 74:3005–3007, 1999.

[84] P.G. Sverdrup, Y.S. Ju, and K.E. Goodson. Sub-continuum simulations of heat conduction in silicon-on-insulator transistors. *Journal of heat transfer*, 123:130–137, 2001.

[85] Sebastian G. Volz and Gang Chen. Molecular dynamics simulation of thermal conductivity of silicon nanowires. *Applied Physics Letters*, 75(14):2056–2058, 1999.

[86] William Paul King. *Thermomechanical formation of polymer nanostructures.* PhD thesis, Stanford University, 2002.

[87] Kelly R. Patton and Michael R. Geller. Thermal transport through a mesoscopic weak link. *Physical review B*, 64:155320–1– 155320–7, 2001.

[88] E.T. Swartz and R.O. Pohl. Thermal boundary resistance. *Review of Modern Physics*, 61(3):605– 668, 1989.

[89] K. L. Johnson, K. Kendall, and A. D. Roberts. Surface energy and the contact of elastic solids. *Proc. R. Soc. Lond. A.*, 324:301–313, 1971.

[90] D. S. Dugdale. *J. Mech. Phys. Solids*, 8:100–104, 1960.

[91] K.L. Johnson. *Contact mechanics.* Cambridge University press, 1984.

[92] Chuan Hu, Michael Kiene, and Paul S. Ho. Thermal conductivity and interfacial thermal resistance of polymeric low k films. *Applied Physics Letters*, 79(25):4121–4123, 2001.

[93] S. Govorkov et al. *Review of Scientific Intruments*, 68:3828–3834, 1997.

[94] M. M. Yovanovich, J. Richard Culham, and Pete Teertstra. Analytical modeling of spreading resistance in flux tubes, half spaces andcompound

disks. *IEEE Transactions on Components, packaging and manufacturing technology, Part A*, 21(1):168–176, 1998.

[95] R. G. Ross, P. Andersson, B. Sundqvist, and G. Backstrom. Thermal conductivity of solids and liquids under pressure. *Reports on progress in physics*, 10:1347–1402, 1984.

[96] C. J. Glassbrenner and G. A. Slack. Thermal conductivity of silicon and germanium from 3k to the melting point. *Physical Review*, 134(4A), 1964.

[97] B. V. Derjaguin, V. M. Muller, and Yu. P. Toporov. Effect of contact deformations on the adhesion of particles. *J. Colloid Interface Sci.*, 53(2):314–325, nov 1975.

[98] K. L. Johnson and J. A. Greenwood. An adhesion map for the contact of elastic spheres. *J. Colloid Interface Sci.*, 192:326–333, may 1997.

[99] www.goodfellow.com.

[100] D. Polder and M. van Hove. Theory of radiative heat transfer between closely spaced bodies. *Physical review B*, 4(10), 1971.

[101] J.B. Pendry. Radiative exchange of heat between nanostructures. *J. Phys. Condens. Matter*, 11:6621–6633, 19992.

[102] Jean-Philippe Mulet, Karl Joulain, Remi Carminati, and Jean-Jacques Greffet. Enhanced radiative heat transfer at nanometric distances. *Microscale thermophysical engineering*, 6:209–222, 2002.

[103] personal communication with C. Rossel, IBM Research GmbH Zurich, Säumerstrsse 4, CH-8803 Rüschlikon.

[104] O. Marti, B. Drake, S. Gould, and P.K. Hansma. Atomic resolution force microscopy of graphite and the "native oxide" on silicon. *J.Vac.Sci. Technol. A*, 6(2), 1988.

[105] Mihai G. Burzo, Pavel L. Komarov, and Peter E. Raad. *5th International Conference on Thermal, Mechanical and Thermo-mechanical Simulation and Experiments in Micro-electronics and Micro-systems (EUROSIME 2004), Brussels, Belgium*, chapter Non-contact Thermal Conductivity Measurements of Gold Covered Natural and Isotopically-Pure Silicon and Their Respective Oxides. EUROSIME 2004, May 10-12, 2004.

[106] S.-M. Lee, D.G. Cahill, and T.H. Aallen. Thermal conductivity of sputtered oxide films. *Phys. Rev.B*, 52:253, 1995.

[107] Mark A. Lantz, Bernd Gotsmann, Urs T. Dürig, Peter Vettiger, Yoshikazu Nakayama, Tetsuo Shimizu, and Hiroshi Tokumoto. Carbon nanotube tips

for thermomechanical data storage. *Applied physics letters*, 83(6):1266–1268, 2003.

[108] Bernd Gotsmann and Urs T. Dürig. Thermally activated nanowear modes of a polymer surface induced by a heated tip. *Langmuir*, 20:1495–1500, 2004.

[109] P.E. Sheehan, L.J. Withman, W.P. King, and B.A. Nelson. Nanoscale deposition of solid inks via thermal dip pen nanolithography. *Appl. Phys. Lett*, 85(9):1589–1591, August 2004.

[110] Heinrich Hertz. Über die Berührung fester elastischer Körper. *J. Reine Angew. Mathematik*, 92:156–171, 1882.

[111] M. Hinz. Stabilitätsuntersuchungen von nanometrischen Polymerstrukturen zur Datenspeicherung. *Diploma thesis, Universität Ulm, Germany*, 2001.

[112] M.Hinz, A.Kleiner, S.Hild, O.Marti, U.Dürig, B.Gotsmann, U.Drechsler, T.R. Albrecht, and P.Vettiger. Temperature dependent nano indentation of thin polymer films with the scanning force microscope. *European Polymer Journal*, 40(5):957–964, May 2004.

Nomenclature

AFM Atomic force microscope synonymously Scanning force microscope

CCD charge coupled devices, chip sensitive to light used in cameras for image recording

CFC Calibration force curve

DMT Contact model named after its developers [97]

DPFM Digital Pulsed Force Mode [**?**]

DSC Differential scanning calorimetry

EFM Electrical force microscopy

FDC Force distance curve

IC Integrated circuit

JKR Contact model named after its developers [89]

LAP Longitudinal acoustic phonon

MBE Molecular beam epitaxy

MFM Magnetic force microscopy

MWCNT Multi-wall Carbon Nanotube

PDA personal digital assistant, mobile computer

PFM Pulsed force mode [?]

PMMA Polymethylmethacrylate

PS-PMMA Mixture of two different polymers Polystyrene and PMMA making up a 2-phase sample surface

PSD Position sensitive detector, device used in an SFM for the detection of the cantilever deflection

SAM Signal access module, part of D3000 SFM to access various signals

SBS-PMMA Mixture of two different polymers Styrene-Butadiene-Styrene and PMMA making up a 2-phase sample surface

SD Smart digital, standard for mobile data storage devices

SFM Scanning force microscope synonymously Atomic force microscope

SThM Scanning thermal microscopy

STM Scanning tunneling microscope [1]

TGA Thermo gravimetry analysis

List of Figures

1.1 Schematic sketch of the "Millipede" concept and Scanning Electron Microscope (SEM) image of the "Millipede" cantilever array . . . 3
1.2 Diagram of "Millipede" capacity as function of pit spacing and diagram of "Millipede" data rates during the write process as function of total power consumptions . . . 4
1.3 Schematic sketch of the thermomechanical bit writing process. Graphs from [12]. . . . 5
1.4 Example of bits written with different parameters using a heatable cantilever . . . 6
1.5 Schematic sketch of the thermomechanical bit reading process. Graphs from [12]. . . . 7

2.1 Sketch of force distance curves . . . 13
2.2 Example for an FDC and a CFC . . . 14
2.3 Example for an FPC with quantities of interest . . . 15
2.4 The heating platform used for the measurement of force-distance curves at elevated sample temperature . . . 16
2.5 SEM image of a Tapping Mode tip . . . 18
2.6 Molecular structure of PMMA . . . 19
2.7 DSC-Curve of bulk PMMA . . . 20
2.8 *Left:* Individual monomer unit of SU8; *Right:* Monomer unit of SU8 in the polymer . . . 21
2.9 DSC (*left*) and TGA measurement (*right*) of SU8 . . . 21
2.10 Example of an array of 10×10 indentations in a 35 nm PMMA film on silicon at 100 °C sample temperature. . . . 22
2.11 Comparison of the topography of indentations created with constant maximum force at different sample temperatures on the PMMA and the SU8 film. . . . 23
2.12 10 FPC measured at 130 °C sample temperature with maximum forces exerted by the tip between 0.4 and 4.0 μN. . . . 24
2.13 10 FPC measured at 100 °C sample temperature with maximum forces exerted by the tip between 0.4 and 4.0 μN. . . . 25

2.14 Penetration depth as function of the cantilever force. 26
2.15 Remanence depth as function of the cantilever force at different temperatures. 27
2.16 Hysteresis energy as function of the penetration depth. 28
2.17 Slope of the loading curve as function of the temperature at different maximum cantilever deflections. 29
2.18 Example for FPCs measured on SU8 at a sample temperature of 100 °C (*left*) and 120 °C (*right*). 30
2.19 Maximum penetration depth and remanence depth as function of cantilever force on SU8. 31
2.20 Hysteresis energy as function of remanence depth on SU8. 32
2.21 Sequence of four Tapping Mode images measured at 120 °C 33
2.22 User interface of the topography analysis program. 34
2.23 Time evolution of indentations at 115 °C 35
2.24 Relaxation time constants τ at different temperatures 36
2.25 Percentage decrease of the indentation depth on PMMA 37

3.1 Two different types of heatable cantilevers used in this study . . . 41
3.2 SEM image of a tip 42
3.3 Electrical circuit for measuring the cantilever IV characteristics . 43
3.4 Typical temperature dependence of the heater resistance. 44

4.1 Reconstructed tip holder for the use of the heatable 3LD cantilevers and original tip holder for the use of commercial cantilevers. 50
4.2 Schematic drawing of the optical beam path using the heatable cantilever chip and a commercial cantilever chip. 50
4.3 Tapping Mode and thermal contact mode images of the SBS-PMMA sample 52
4.4 Cabling of the different components used for the nanoindentation experiments with pulse heated cantilever and electrostatic force. . 55
4.5 Flow chart of the indentation procedure 56
4.6 Example for an indentation pulse: The input voltage of the cantilever circuit V_{in} , the cantilever voltage $V_{Cantilever}$ and the voltage applied to the sample V_{Sample} are shown. 57
4.7 Examples of pulses measured during the pulsed IV characteristics measurement with the tip in contact with the sample 58
4.8 Comparison pulsed and DC-like IV characteristics and RT-curve . 59
4.9 Force distance curves measured at different DC sample voltages . 60
4.10 Electro-static force as function of the voltage applied to the sample. 61
4.11 Example of an array of indentations created with 10 μs pulses on the 35 nm PMMA film on silicon. 63
4.12 Depth of the indentations shown in figure 4.11 as function of heater temperature and electro-static force. 64

4.13 Comparison of indentations created with pulse-heated cantilever tip on the PMMA and SU8 samples at room temperature 65
4.14 Heater temperature as function of power at different sample temperatures. 66
4.15 Extrapolated heater temperature as function of sample temperature. 68
4.16 Contact mode images of indentations created on the 35 nm PMMA film on silicon at different sample temperatures. 70
4.17 Contact mode images of indentations created on the 80 nm SU8 film on silicon at different sample temperatures. 71
4.18 SEM image of the tip taken after usage for the indentation experiments and the imaging in Contact Mode on the PMMA sample. . 72
4.19 Measured data and recalculated indentation depths as function of the heater temperature at 100 °C sample temperature. 73
4.20 Indentation depth as function of the heater temperature at various sample temperatures and a constant electro-static force of F = 350 nN. Sample: 35 nm PMMA on silicon 74
4.21 Indentation depth as function of the difference between heater temperature and sample temperature at a constant electro-static force of 350 nN and at various sample temperatures. Sample: 35 nm PMMA on silicon 75
4.22 Rim volume as function of the heater temperature at various sample temperatures and a constant electro-static force of F = 350 nN. Sample: 35 nm PMMA on silicon 76
4.23 Schematic sketch of the assumed temperature distribution occurring in the indentation experiment at different sample and heater temperatures. 77
4.24 Indentation depth as function of the electro-static force at various sample temperatures on PMMA. 78
4.25 Indentation depth as function of the electro-static force at various sample temperatures on SU8. 79
4.26 Indentation depth as function of the heater temperature at various sample temperatures on SU8. 80

5.1 Sketch of heat transfer mechanisms 85
5.2 View into the vacuum chamber 87
5.3 Heater performance under ambient conditions and in vacuum . . . 89
5.4 Comparison of the heater calibration under ambient conditions and in vacuum. 90
5.5 Thermal approach curves under ambient conditions and in vacuum 91
5.6 Distance dependence of the heater power during a thermal approach curve in vacuum 92
5.7 Quantities involved in Fourier's law. 93
5.8 Analysis of thermal approach curves under vacuum conditions. . . 95

5.9 Thermal contact resistances on silicon and PMMA 99
5.10 Thermal contact resistances on silicon and PMMA 100
5.11 Schematic sketch of the thermal resistances involved in the thermal tip-sample contact resistance. 101
5.12 Calculated contact radii on silicon and PMMA as function of Young's modulus and measured adhesion values as function of the heater temperature. 107
5.13 Calculated thermal resistances as a function of interface constant r_{Si} for different thermal resistances of the tip R_{Tip} and different contact radii a_{Si} in comparison with the measured data. 109
5.14 Upper limit of the thermal resistance of the tip R_{Tip} as function of the contact radius a_{Si} calculated with equation 5.34. 110
5.15 Thermal resistances as function of interface constant r_{PMMA} calculated with equation 5.35. The solid line denotes the measured mean value of $R_{\mathrm{TS,PMMA}}$ and the dashed line indicate the error interval. 111
5.16 Dependence of thermal resistance on the adhesion force and adhesion force as function of number of approach curve 112
5.17 SEM of the tip used in the wear-out experiment before and after the measurement 113
5.18 SEM images of a sharp and a blunt tip used in the vacuum SFM for the measurement of thermal contact resistance 114
5.19 Dependence of thermal resistance on tip diameter measured on silicon. 115
5.20 Dependence of thermal resistance on tip apex angle on silicon. . . 116
5.21 Schematic sketch of the topography effect leading to thermal imaging contrast on the silicon sample. 117
5.22 Thermal image and Tapping Mode image of the silicon sample . . 118
5.23 Relative contribution of the individual thermal resistances on silicon (*left*) and on PMMA (*right*). 121
5.24 Schematic sketch explaining the procedure of determining the surface temperature. 122
5.25 Radiative heat transfer measured on different materials with a heater temperature of $\approx 600\,^{\circ}\mathrm{C}$. 123
5.26 Electrical circuit used for the vacuum imaging experiments. 125
5.27 Thermal image of the HfO_2 film on silicon 127
5.28 Thermal approach curve on HfO_2 with the same input voltage as for the thermal image shown in figure 5.27. 129
5.29 Zoom into the RT curve of the cantilever used for the thermal image 130
5.30 Thermal image with the analyzed fields marked with circles and according histograms. 134
5.31 Exclusion masks for the calculation of the global thermal contact resistances. 135

5.32 Histogram of the thermal contact resistances obtained from the thermal image with the exclusion masks shown in figure 5.30. . . . 136
5.33 Schematic sketch of the heatable tip scanning the hafnium oxide sample. 137
5.34 SEM image of the tip used for the thermal image of the hafnium oxide sample. 139

6.1 Series of four approach curves measured at the same location on PMMA. The change of the contact part of the curves is persumably originated from a permanent surface modification. 144
6.2 Thermal approach curve measured with a carbon nanotube attached to the tip of a heatable cantilever. 145
6.3 Topography image (*top*) obtained from the optical deflection signal and image generated from the simultaneously recorded thermal signal (*bottom*) measured in Pulsed Force mode with a DC voltage applied to the cantilever circuit. 147

A.1 Procedure illustrating the creation of small Gold islans on the silicon substrate proving that the tip indeed had reached the silicon substrate during the indentation process. 157
A.2 Array of indentations created on a PMMA film with force-distance curves and Gold islands resulting from the procedure described in the text. 158

Issue of statement

Hereby, I declare, that I have conducted the work of this study self-dependently and that I have only used the resources stated. Parts, which are literally or analogously taken from other sources, are referenced. The study has not been submitted in this or similar way in another dissertation.

Some parts of the present study,however, have already been published elsewhere: I have measured parts of the data presented in chapter 2 during the time of my diploma thesis, which I also conducted in the Department of Experimental Physics at the University of Ulm in collaboration with the IBM Research Laboratory Zurich (ZRL). These data have already been published in [111, 112]. Since these measurements fit very well into the subject of this thesis and provide a good starting point for the experiments described in the following chapters, I decided to show these data in this study again.

Data presented in section 2.6 were measured by A.Kleiner (Department of Experimental Physics, University of Ulm) during the time of his diploma thesis from September 2002 to September 2003 under my supervision and have been published in [54].

The DSC and TGA measurements in chapter 2 were conducted by Mrs.Asbach at the University of Ulm, which I am thankful for.

All sketches shown in chapter 1.1.1.1 have been taken from the IBM web site (www.zurich.ibm.com) by courtesy of Evangelos S. Eleftheriou. The graphs in figure 1.2 were made Evangelos S. Eleftheriou and he allowed me to present these data in this thesis, what I am grateful for.

Several techniques and devices used in this study have actually not been developed by myself. I could rather make use of developments made by other colleagues which I am very grateful for: The heatable cantilevers used in this study have been developed, produced, tested and applied at the Micro and nano mechanics group of the science and technology department at the IBM Research Laboratory Zurich. The colleagues there also developed the ideas for the temperature calibration of the heater temperature (see section 3.3) and the calibration of the electro-static force shown in section 4.4.3.

The technique for the high-frequency nano-indentation (see 4.4.1) using the Signal Access Module of the D3000 SFM in combination with the Nanoscript and analogue switches has been developed by G.C.Cross, U.Dürig and B.Gotsmann while setting up another experiment at the ZRL.

The vacuum chamber used for the heat transfer experiments described in chapter 5 has been setup by U.Dürig and O.Züger and has originally been designed and used as a high-vacuum Scanning Tunneling Microscope (STM). U.Dürig reconstucted the tip holder for the use of the heatable cantilever. He also placed the microscope unit into the vacuum chamber after it had been stored outside the chamber for years and first tests and experiments of the electronics, software and tip holder had been made.

The majority of the Scanning Electron Microscopy images have been made at the ZRL by various people, e.g. B.Gotsmann, U.Drechsler, D.Jubin, M.Despont.

B.Gotsmann and M.A.Lantz actually measured the data presented in the section of the thermal radiation heat transfer shown in chapter 5.5.8 as well as the approach curve measured using the carbon nanotube in section 6. The CNT was attached to the heatable tip by Tetsuo Shimizu and Hiroshi Tokumoto (Nanotechnology Research Institute, National Institute of Advanced Industrial Science and Technology, Tsukuba Central-4, Higashi 1-1-1, Tsukuba, Ibaraki 305-8562, Japan), which I am thankful for.

Marcell Ott (by that ime Department of Organic Chemistry III, University Ulm) had the idea and conducted the sputtering and lift-off technique for the gold clusters presented Appendix A. The Pulsed Force mode images in combination with the thermal signal presented in chapter 6 were measured in cooperation with Alexander Gigler, Department of Experimental Physics, University Ulm.

Martin Hinz

October 2005

Acknowledgements

I appreciated the help of many people and without their support this work would have not been possible.

Definitely the most important person I worked together with is Bernd Gotsmann from the IBM Research Laboratory (ZRL). He guided and supported me during the entire time and provided help in all questions. Especially the vacuum experiments would not have been such successful without his help. I am incredible thankful for having had such a good supervisor.

I am grateful to Prof. O. Marti for giving me the possibility to conduct this PhD thesis in his department, for his help in physical questions and for always making the stays at the ZRL possible.

I am grateful to the entire Micro and nano mechanics group of the science and technology department at the IBM Research Laboratory Zurich. Several times I had the chance to be guest in this group and I appriciated the time there a lot. These stays in Rüschlikon were always very fruitful and I could learn a lot. I am specially grateful to Urs T. Dürig, Mark A. Lantz and Armin Knoll, who all contributed a lot to this study. Urs let me use the vacuum chamber for the heat transfer and thermal vacuum imaging experiments and supported the experiment in physical and technical questions. He always helped whenever some equipment of the setup broke and was the contact person for the entire cooperation time during my Diploma and the PhD thesis. Mark contributed a lot to the vacuum experiment and had many good ideas. He also proof-read the thesis, which I am thank ful for. Armin helped with the application of the heatable cantilever in the DI and the data analysis. A special thank to Ute Drechsler and Michel Despont for the fabrication of the heatable cantilevers and the samples. Many thanks to Paul Rossell for providing the hafnium oxide film sample. I would also like to acknowledge the managers at the ZRL Peter Vettiger, Thomas A. Albrecht and Johannes Windeln for supporting my stays at the ZRL. I would like to thank Evangelos S. Eleftheriou for allowing me to use the graphs of figure 1.2, which were made by him and for allowing me to use graphs in chapter 1.1.1.1 from the IBM web site www.zurich.ibm.com.

At the Department of Experimental Physics of the University of Ulm I would like to thank my colleagues of supporting me and making this department to a place of work and joy (and table tennis): My PhD colleagues Alexander Gigler, Michael Holzwarth, Frank Sperka, Nichola Maghelli, Manuel Gonçalves, Andreas Boger, Carl Stefan (Charly) Imhof, Holger Schieferdecker, Alexander Schmatulla. Thanks to Andreas Kleiner for working together with me during his diploma thesis and allowing me to present some of his data in this thesis. Special thanks go to Wolfram Ibach for writing the indentation analysis software and to Prof. Martin Pietralla and Sabine Hild for always having time for discussions and answering questions.

Thanks to Tamara Stadter for always having an encouraging word and Mrs. Asbach for doing DSC and TGA measurements as well as Mr. Asbach and Mr. Heise for help concerning both physical and administrative questions. Andreas Ziegler (Sektion Elektronenmikroskopie, Ulm University) introduced me to the use of the SEM and helped whenever questions or problems occurred. I also would like to thank Marcell Ott who had the idea with the gold clusters, which is presented Appendix A. He also conducted the sputtering and the lift-off procedure of the samples.

A special thank goes to the members of the electrical and mechanical workshops both in Ulm and in Rüschlikon, who contributed a lot to the experimental setups used in this thesis.

I want to especially thank my girlfriend Jutta Krasenbrink for her steady support and encouragement, also for her understanding in cases when scientific research had priority. Last but not least I am grateful to my parents, who always supported my study and the PhD thesis a lot.

Lebenslauf



Persönliche Angaben

Name	Martin Hinz
Geburtsdatum, -ort	02.12.1973 in Bonn am Rhein
Familienstand	ledig
Staatsangehörigkeit	deutsch und schweizerisch

Schulbildung

09 / 1984 - 05 / 1993	Immanuel-Kant Gymnasium, Tuttlingen, Abitur

Zivildienst

08 / 1993 - 10 / 1994	Zivildienst beim Bund für Umwelt- und Naturschutz Deutschland e.V. (BUND), Kreisgruppe Tuttlingen

Studium und Promotion

10 / 1994 - 09 / 1996	Grundstudium Physik (Diplom) an der Universität Ulm, Vordiplom
10 / 1996 - 06 / 1997	Studium Physik an der Universität Leeds (GB), Abschluss Bachelor of Science
10 / 1997 - 02 / 2002	Hauptstudium Physik (Diplom) an der Universität Ulm, Abschluss Diplom-Physik
seit 04 / 2002	Promotion in der Abteilung Experimentelle Physik, Universität Ulm

Ulm, Oktober 2005

Martin Hinz